INCREASED HYDROGEN UPTAKE OF ZIRCONIUM BASED CLADDINGS AT HIGH BURNUP

by
ADRIENN BARIS

A thesis submitted to the University of Birmingham for the degree of DOCTOR OF PHILOSOPHY

School of Metallurgy and Materials
University of Birmingham
March 2019

ABSTRACT

In light water reactors the fuel is encapsulated in Zr-based claddings that withstand the harsh environment (neutron bombardment, high temperature and water under pressure); without absorbing too many neutrons to sustain the chain reaction in the reactor core. Relatively high corrosion resistance of Zr is achieved when alloyed (e.g. with Sn, Fe, Cr, Ni, or Nb). Some elements form second phase particles (SPPs) and provide protection against rapid corrosion. The cladding undergoes compositional and microstructural changes, such as irradiation-induced SPP dissolution. Zr oxidizes at the metal-oxide interface by diffusion of the oxidizing species through the oxide layer. Therefore, a protective inner barrier oxide is essential to prevent the metal from fast reaction with different species. Hydrogen is released as a by-product of the oxidation, and by the radiolysis of the coolant. If H enters the metal it precipitates as brittle Zr-hydrides degrading the cladding's mechanical properties. The H-uptake is a critical safety issue. Although, extensive literature is available on this topic, there are some aspects that need better understanding. Increasing H-uptake of certain cladding types at high burnups was reported. The causes are not yet fully understood.

To better understand the causes of increased H-uptake at high burnups, an extremely high burnup cladding (9 cycle LK3/L Zircaloy-2) from boiling water reactor provided the basis of the study. The same type of cladding after different service times was examined revealing the compositional and microstructural evolution. Two types of cladding from pressurized water reactor with medium burnup were studied to separate the reactor- and alloy-specific parameters from the generic ones.

FIB tomography was used for the 3D reconstructions of the microstructure; EPMA and ChemiSTEM for the micro- and nanometric chemical analysis.

It is revealed that regardless of alloy- and reactor-type, crack-free oxide and the absence of large hydrides in the vicinity of the metal-oxide interface; undulated interface; and presence of SPPs are among the essential factors for the cladding's high performance.

It is demonstrated that the oxidation of the hydrides at the metal-oxide interface induces crack formation in the oxide, reducing its protectiveness.

High level of SPP dissolution, large hydride phases in the metal and high level of porosity in the oxide at the interface, straight metal-oxide interface, stoichiometric oxide, increased Ni concentration in the inner oxide, segregation of Fe, Ni, Sn and slightly Cr in the metal grain boundaries, Sn segregation at the interface oxide are identified as the causes of increased H-uptake of the LK3/L cladding at high burnups. Although all of these factors are present after 9 cycles, the cladding does not show extremely fast oxidation and H-uptake even beyond the designed service time.

ACKNOWLEDGEMENTS

First of all, I would like to express my sincere gratitude to my supervisor at PSI, Dr. Sousan Abolhassani, who guided me patiently for four years to find good directions in my research, and who always supported me. This work would not have been possible without her immense knowledge in the field and her valuable advices for the thesis writing. I greatly appreciate her positive attitude both at a professional and personal level. She kept smiling and encouraging me even during hard times; this helped me to overcome every difficulties I faced in these years. I feel very lucky to have a supervisor like her.

I would like to thank my supervisors at Birmingham, Dr. Yu-Lung Chiu and Prof. Hugh Evans, for their insightful comments and suggestions throughout the PhD work and for the support and help in the writing of this thesis. I could not have imagined a better group of supervisors and it was a pleasure to work with all three of them.

I would like to thank the Nuclear Fuels group for the great working environment and all the opportunities to participate in various scientific events and conferences that helped to widen my knowledge and perspective.

I would like to thank *swissnuclear* for the financial support of this project. Westinghouse Electric Co., KKL, KKG are thanked for providing the investigated materials. This project is a partner of the MUZIC-3 collaboration which I thank for the very stimulating discussions and for broadening my perspective and deepening my understanding of the topic.

Many thanks to Matthias Martin, Robin Grabherr, Stephane Portier, and Andrej Bullemer for making possible all my measurements in the Hotlab through providing access to the instruments

and sample preparation tools. I am grateful to Dr. Elisabeth Müller for her patience and kind help whenever I had some trouble with the FIB or TEM. She was always available to help or answer any questions with a high professional level. I wish to thank Dr. Robin Schäublin for his support in the ChemiSTEM measurements at ETH Zürich, and for giving very useful advices that considerably improved the quality of the results. I thank Jinsen Tian for assistance during the ChemiSTEM measurements at the University of Birmingham even during his PhD thesis write-up.

I thank my friends and groupmates at PSI - Dipa, Barbi, Jonny, Aaron, Harry, and Weijia - for making the working days even more fun and that they were always available for some coffee break and chatting.

I cannot express enough my appreciation to my beloved Shantanu for making life easier with his understanding and easy-going attitude, for the emotional support, for the good advices and motivation all the time. I would like to thank my family for the emotional support and patience in these years, and that I could always count on them.

TABLE OF CONTENTS

LIST OF ABBREVATIONS

LWR	Light Water Reactor
BWR	Boiling Water Reactor
PWR	Pressurized Water Reactor
KKL	Kernkraftwerk Leibstadt (Leibstadt Nuclear Power Plant)
KKG	Kernkraftwerk Gösgen (Gösgen Nuclear Power Plant)
HPU	hydrogen-pickup, hydrogen uptake
HPUF	hydrogen pickup fraction
SPP	secondary phase particle, second phase particle
GB	grain boundary
HCP	hexagonal close-packed
BCC	body-centred cubic
BCT	body-centred tetragonal
FCC	face-centred cubic
FCT	face-centred tetragonal
PB ratio	Pilling-Bedworth ratio
TSSD	terminal solid solubility limit of dissolution
TSSP	terminal solid solubility limit of precipitation
PCI	Pellet-Cladding Interaction
FEG	Field Emission Gun
SEM	Scanning Electron Microscope
ESEM	Environmental Scanning Electron Microscope
FIB	Focused Ion Beam
3D FIB	Three-Dimensional Focused Ion Beam
SIMS	Secondary Ion Mass Spectroscopy
EPMA	Electron Probe Micro-Analysis
TEM	Transmission Electron Microscope
STEM	Scanning Transmission Electron Microscope
SE	Secondary Electron
BSE	Backscattered Electron
HAADF	High-Angle Annular Dark Field

DF	Dark Field
BF	Bright Field
EDS	Energy Dispersive X-ray Spectroscopy
WDS	Wavelength Dispersive Spectroscopy
APT	Atom Probe Tomography
XANES	X-ray Absorption Near Edge Structure
XRD	X-ray Diffraction
DFT	Density Function Theory
M/O	metal-oxide

LIST OF DEFINITIONS

Burnup: A measure of how much energy is extracted from a primary nuclear fuel source. It is most commonly defined as the fission energy release per unit mass of fuel.

MWd/kgU: Megawatt-days/kilogram Uranium – Unit of burnup. Indicates that how much of energy is extracted from the fuel source (e.g. uranium pellet).

Medium burnup: In this thesis samples with the range of ~40-55 MWd/kgU burnup are considered as medium burnup.

High burnup: In this thesis samples with the range of ~ 55-75 MWd/kgU are considered as high burnup.

Extreme high burnup: In this thesis samples above 85 MWd/kgU are considered as extreme high burnup.

Cycle: The measure of time that a cladding has served in the reactor. Each cycle is 11 months, in the reactors studied in this project and the reactor is shut down for service for approximately one month per year. The burnup increases with the number of cycles.

Crud: “Chalk River Unidentified Deposits” or CRUD is the deposit on the surface of cladding during the service.

Slice-and-view: Image batch collecting process in SEM/FIB systems that uses subsequent slicing and imaging of the material by FIB and SEM.

Image segmentation: An image processing method for 3D visualization. The process of partitioning a digital image into multiple regions by assigning a label to every pixel that have similar characteristics. In this thesis the different phases of the material were the basis of the segmentation.

Bounding box (of a 3D reconstruction): In Avizo: “the bounding box of an object is the smallest rectangular, axis-aligned volume in 3D space that encompasses the object”.

ChemiSTEM: A technology developed by FEI (part of Thermo Fisher Scientific) providing high resolution compositional and microstructural information (i.e. EDS mapping is paired with imaging) using Scanning Transmission Electron Microscopy.

QMap: For each pixel of the ChemiSTEM map a full EDS spectrum is collected and saved. QMap is a quantified ChemiSTEM map.

LIST OF PUBLICATIONS

Papers with content that is included partially or entirely in the thesis:

Baris, A., Restani, R., Grabherr, R., Chiu, Y.L., Evans, H.E., Ammon, K., Limbäck, M. and Abolhassani, S., 2018. Chemical and microstructural characterization of a 9 Cycle Zircaloy-2 cladding using EPMA and FIB Tomography. *Journal of Nuclear Materials*, *504*, pp.144-160.

Baris, A., Abolhassani, S., Chiu, Y.L. and Evans, H.E., 2018. Observation of crack microstructure in oxides and its correlation to oxidation and hydrogen uptake by 3D FIB Tomography–case of Zr-ZrO2 in reactor. *Materials at High Temperatures*, *35*(1-3), pp.14-21.

Baris, A., Abolhassani, S., Gabherr, R., Restani, R., Schäublin, R., Chiu, Y.L., Evans, H.E., Ammon, K., and Limbäck M., 2018. Causes of increased hydrogen uptake of Zircaloy-2 cladding at high burnups – A comparative stud of the chemical composition of a 3 cycle and a 9 cycle cladding. *TopFuel 2018, Conference Proceeding*

Abolhassani, S., Baris, A., Hawes, J., Grabherr, R., Colldeweih, A., Bertsch, J., Chollet, M., Kuri, G., Martin, M., Portier, S., Ammon, K., Ledergerber, G., Limbäck, M., 2019. Towards an improved understanding of the mechanisms involved in the increased hydrogen uptake and corrosion at high burnups in zirconium based claddings. Submitted to *19th ASTM International Symposium on Zirconium in the Nuclear Industry*.

Relevant papers that are not included in the thesis:

Colldeweih, A.W., Baris, A., Spätig, P. and Abolhassani, S., 2019. Evaluation of mechanical properties of irradiated zirconium alloys in the vicinity of the metal-oxide interface. *Materials Science and Engineering: A*, *742*, pp.842-850.

1. INTRODUCTION

A brief background of the work is presented here including a short description of the basics of the light water nuclear reactors, their water chemistry and the irradiation induced damage of the material; together with the motivation and aims of the thesis. The structure of the thesis is also described.

1.1. Background of light water nuclear reactors

Zirconium (Zr) based alloys are used as fuel cladding in light water nuclear reactors (LWR) such as boiling water reactors (BWR) and pressurized water reactors (PWR) [1], [2]. Light water reactors are thermal nuclear reactors that use normal water as coolant and neutron moderator [3], [4]. The heat is produced by controlled nuclear fission which takes place in the reactor core. The reactor core contains the nuclear fuel (e.g. UO2 pellets made of fissile uranium-235) inside the claddings, and the control element (e.g. control rods made of Cd or Hf which can capture and stop the neutrons if needed). The claddings are about 4 m long and hundreds of them are assembled in groups inside the core. The produced heat is used to increase the temperature of the water in order to generate steam that is used to drive the turbine. The turbine is connected to the generator providing electricity that is conducted to the populated and industrial areas. The steam goes through a condenser system that cools down the steam and turns it to water so that the water can be conducted back to the reactor core [3], [4].

In Figure 1-1 the basic schematics of the BWR and PWR is shown. The major difference between them is that in BWR the steam is generated directly in the reactor vessel, while PWR uses a secondary loop steam generator that is separated from the main reactor vessel.

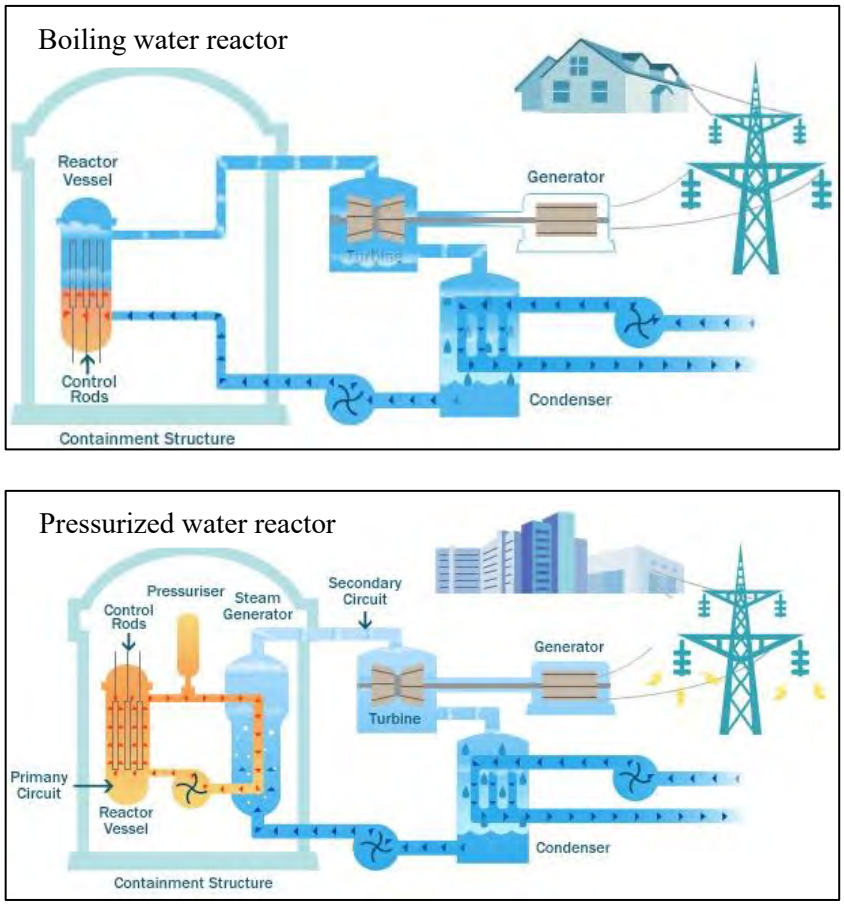

Figure 1-1 Basic schematics of BWR and PWR nuclear reactors [5].

1.2. Brief description of the differences between BWR and PWR

In order to give a short overview of the two types of LWRs the most important differences are presented, such as the operating pressure and temperatures, and the water chemistry. BWRs operate at relatively high pressure in order to keep the water in a liquid state at higher temperatures: it uses around 7 MPa and 280 °C inlet and 330 °C outlet temperature during operation [6]. The pressure in PWRs is more than twice as in BWR namely 15 MPa. The inlet and outlet temperatures are 290 °C and 325 °C respectively [6]. The water chemistry changes with time and the nature of additions and water pH depend on the type of reactor; and is different

from one reactor to another; however there are some general recommendations [7]. The goal is to optimize the performance, control the corrosion and minimize the build-up of nuclear activity. In some cases water chemistry is used to regulate the reactor power [7], [8], [9], [10].

BWR requires pure water with low conductivity and low level of impurities [9]. Although, high purity coolant is required in BWRs, some elements have shown beneficial effect when they are added in small quantity and under controlled conditions, such as Zn, Fe, H, and noble metals (e.g. Pt) [9]. Due to the presence of dissolved oxygen and hydrogen peroxide from the radiolysis of the water, the BWR environment is oxidizing [9]. The oxidizing environment can promote stress corrosion cracking of the stainless steel reactor components and pipes, and to supress this effect H is injected in the coolant [9]. This shifts the electrochemical potential to higher negative levels. However, H addition can increase the "shutdown radiation fields" as it induces structural changes in the oxide layer formed in the inner system surfaces [9]. Small amount of Zn is therefore a common additive and it is introduced to supress the activity transport to out-of-core components by stopping the absorption of radionuclides by oxides on system surfaces [8], [9]. Some guidelines for BWR water chemistry from EPRI is presented in Table 1-1 from reference [7], showing that Cu, Fe and O are injected in the water normally in small quantities. About 20-100 ppb oxygen helps to minimize the corrosion and corrosion release in the feed water system [11].

In PWR, normally boric acid is added to the coolant in order to control the core reactivity [8], [10]. However, boric acid shifts the pH towards the acidic region, therefore LiOH is introduced to counterbalance this effect, and in this way the corrosion and the corrosion-product transport can be minimized [8], [10]. The recommended range of concentrations is presented in Figure

1-2 from reference [7]. Furthermore, chlorides and fluorides are also common additives as presented in Table 1-2 from the same reference. Generally overpressure of hydrogen is applied (25-30 cc/kg) in order to supress radiolytic oxygen formation and keep oxygen below 5 ppb.

Table 1-1 EPRI recommendations for BWR water chemistry [7].

Control parameter	Frequency of measurement	Achievable value	Action levels 1	2	3
Reactor feedwater / condensate during power operation					
Feedwater conductivity (μS/cm at 25 °C)	continuously	≤0.06	>0.07		
Condensate conductivity	continuously	≤0.08	>0.10		>10
Feedwater total copper (ppb)	weekly integrated	≤0.10 ≤0.30	>0.50 >0.50		
Feedwater total iron (ppb)	weekly integrated	≤2.0	>5.0		
Feedwater dissolved oxygen (ppb)	continuously	20-50	<10 >200		

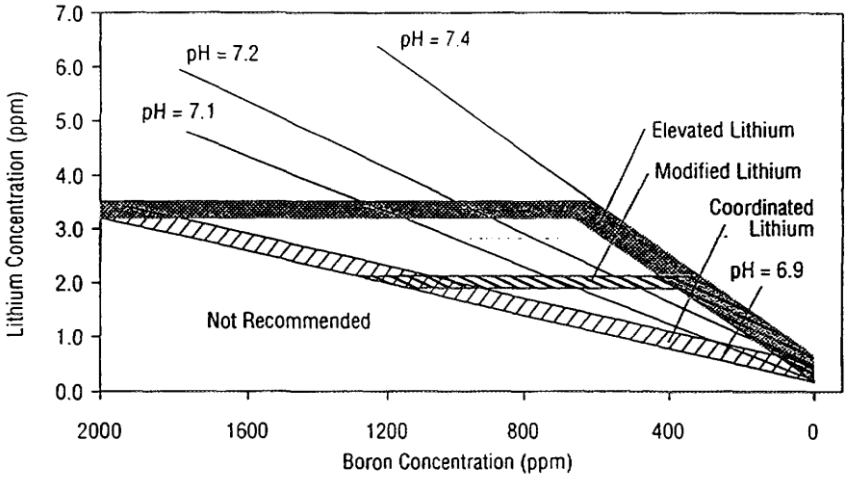

Figure 1-2 Recommendations for B and Li concentrations in the coolant from EPRI for PWR [7].

Table 1-2 EPRI recommendations for PWR water chemistry [7].

Hydrogen (cm^3) (STP)/kg H_2O [a)]	25 - 50
chlorides (mg/kg)	< 0.15
fluorides (mg/kg)	< 0.15
dissolved oxygen (mg/kg)	< 0.01
lithium (mg/kg)	consistent with station lithium program

[a)] STP, standard temperature and pressure (0 °C, atm)

1.3. Background of Zr based claddings

As the cladding serves as the first barrier between the reactor coolant and the fuel it has to be resistant to the severe environment of the reactor in order to operate safely. Un-alloyed Zr has high affinity for O and oxidises rapidly [12]. Alloying elements (usually Sn, Fe, Cr, Ni, Nb) improve the oxidation resistance and mechanical properties of Zr. Some of these elements have a relatively high solid solubility limit (e.g. Sn) and some are practically insoluble in the Zr matrix (e.g. Fe, Cr, Ni) therefore they form secondary phase precipitates (SPPs) [12].

Besides the good mechanical and satisfactory corrosion properties, Zr alloys also provide low neutron absorption cross-section which is indispensable for the efficient operation of the reactor.

However, after a long residence time the cladding degrades [12]. In general, the life-limiting factors of the cladding are: oxidation, hydrogen uptake (H-uptake), irradiation-induced SPP dissolution, and the subsequent consequences of such degradations as well as the dimensional modifications to the cladding [12], [13], [14], [15], [16], [17].

The material is bombarded by fast neutrons in reactor causing structural damage mostly by elastic interactions between the neutrons and the material's atoms [12]. The energy is transferred to the target atom moving the atom from its original place, i.e. forming vacancies,

interstitials, and charged defects in the oxide [12]. The displaced atom could have enough energy to induce further displacements; this is called collision cascade. Dislocation loops are also formed; depending on their Burgers-vectors <a> type or <c> type loops are observed [18]. In the oxide the formed defects are charged due to the ionic nature of the Zr-O bonding. The displacement energies (for Zr and O) are expected to be higher than in the metal, therefore the caused radiation-damage would also be different [12].

The above mentioned irradiation-induced damage will not be studied in this thesis.

It has been shown that the presence of SPPs in the Zr based alloys improves the oxidation properties of the material compared to the SPP-free material [19]. During the irradiation the SPPs dissolve. This affects the further oxidation properties, and the material will be less protective against rapid oxidation.

Oxidation of Zr occurs at the metal-oxide interface; therefore the oxidizing species have to migrate through the already formed oxide layer to form zirconia (ZrO_2) at the metal-oxide interface [12], [20]. Furthermore, cracks are produced in the oxide during the formation of the oxide layer [21]. Hydrogen is produced by the corrosion process and a part of the formed hydrogen penetrates through the oxide layer and reaches the metal [12], [22]. This process is called H-uptake or H-pickup (HPU). Once the hydrogen content of the metal reaches the solubility limit, Zr-hydrides form which are brittle phases and therefore they deteriorate the mechanical properties of the cladding [23], [24]. Both processes result in a reduced protection capability of the cladding. Therefore, HPU and oxidation became the topic of intense research with the aim to improve the understanding of the mechanisms behind the oxidation and HPU.

It is also worth mentioning that during the service, due to the chemical additions to the coolant and also due to the corrosion of pressure vessel and stainless steel pipes, or other components,

crud (or: Chalk River unidentified deposits) is formed on the surface of the claddings and it is composed of metal oxides such as Fe_2O_3 (hematite), Fe_3O_4 (magnetite), FeOOH (goethite), or (Ni,Co)xFe_3-xO_4 (spinel) [25], [26]. Crud is an unwanted deposition as it can increase the corrosion of the cladding. The crud is not the topic of this work and the reader can refer to many publications in this field [25], [26], [27], [28].

One of the main difficulties in the examination to understand the behaviour of the cladding materials is the number of influencing parameters, such as the microstructure of the oxide layer, irradiation-induced dissolution of the SPPs, the distribution of the dissolved elements, etc. In addition, samples extracted from nuclear reactors are highly radioactive. Therefore, special processes, safe and well-equipped laboratories are needed starting from the transportation of the rods until the investigation of the small cladding segments. This is an expensive and time-consuming process.

1.4. Motivation and aim of the thesis

Although large amount of data are available in the literature on the oxidation and HPU behaviour of different Zr alloys, most of these are autoclave studies which do not necessarily describe the in-reactor behaviours. In fact, significant differences are observed in the cladding behaviour (oxidation and HPU) once it is exposed to the reactor conditions. Therefore, the best approach to better understand the HPU and oxidation behaviour is the investigation of claddings served in reactors.

Due to the special needs of equipment and the difficulties of handling and storing highly radioactive materials only limited number of studies are available in the current literature.

There are only few studies on the changes in the behaviour of a certain cladding from low to high or extremely high burnups, e.g. [14], [13], [29]. In one of these studies [13] it was demonstrated that the HPU changes with the time spent in the reactor and that it increases in certain cladding alloys (e.g. LK3/L type Zircaloy-2 in BWR) towards high burnups. The term "increased H-uptake" refers to this phenomenon. However, it must be noted that not all alloys show this behaviour. This implies that knowing the early and/or mid-life behaviour of a given cladding may not provide the complete information regarding the late-life behaviour of the cladding, without the complete understanding of the mechanism of the HPU. The reason behind the increased HPU has not yet been well explained and it needs further studies.

The study of Abolhassani et al. [13] suggested some possible parameters which could influence the HPU; such as: certain microstructural and compositional changes (e.g. SPP dissolution); nature of the oxide layer and its resistance to crack formation; microstructure and morphology of the metal-oxide interface; etc. This study gave the starting point of this current thesis work. Therefore, one of the main aims of the thesis is to examine the suggested parameters and to find additional parameters which could be responsible for the increased HPU at high burnups.

Also, it is well-established that the microstructure and the composition are changing dynamically during service. It is also known that they affect the oxidation and HPU of the cladding. Therefore, an improved knowledge of the microstructure and composition of the cladding during service conditions might help to identify the decisive parameters resulting in the HPU increase.

For this reason the thesis aims to:

- Study the evolution of the microstructure and the chemical composition of the LK3/L Zircaloy-2 (see composition and other details in Table 1-3 and Table 1-4) BWR cladding from low to extreme high burnups.
    - For this reason, a 3 cycles, a 6 cycle and a 9 cycle LK3/L claddings were studied and compared by Electron Probe Micro Analysis (EPMA) and FIB tomography. ChemiSTEM was also applied on the un-irradiated, the 3, 7, and 9 cycle claddings.
- Establish the link between the observed microstructural and compositional changes and the changes in HPU and oxidation behaviour of the cladding.
- Identify those parameters which could be responsible for the increased HPU at high burnups.
- Separate reactor- and alloy-specific parameters from those generic ones.
    - In order to achieve this aim, the thesis includes the study of two PWR claddings as well: a 4 cycle Zircaloy-4 and a 3 cycle Zr-2.5Nb samples (see composition and other details in Table 1-3 and Table 1-4). These samples are studied with EPMA and FIB tomography, and compared to the results of the BWR claddings.

It must be noted that this latter aim is rather a difficult task. The approach was based on the study of different claddings from a completely different reactor environments and compositions. Chapter 7 contains the comparison of practically all the core results that are obtained, from the whole thesis. Despite the fact that the samples selected are very different, and some aspects cannot be directly compared, Chapter 7 attempts to compare as many aspects as possible, e.g. the element distribution in different parts of the samples; the presence or

absence of SPPs; the segregation of certain elements at similar sites of the segment in both PWR and BWR claddings; the microstructural aspect, i.e. crack and hydride volume fractions; etc. It is worth noting already here that in order to provide a complete comparison, all possible aspects were discussed.

The thesis work has been performed mainly at Paul Scherrer Institute where a well-equipped Hot Laboratory is available for the investigation of highly radioactive materials while a C-lab provides tools for sample preparation and microscopy investigations of lower activity samples. Some TEM experiments were carried out at the University of Birmingham and at ETH Zürich. The thesis aims to provide some information which is missing in the literature and to improve the understanding of the in-reactor cladding behaviour up to extremely high burnups necessary for the safer late-life operation of the cladding (as well as for the development of new alloys with better resistance for HPU and oxidation).

The composition of the claddings that are investigated in this study is shown in. The heat treatment is also presented. In the case of the LK3/L sample: log A parameter is the cumulative annealing parameter and it is described as $A = \sum t_i e^{\frac{-Q}{RT_i}}$ [30], [31], where i is the i^{th} heat treatment (after the last β-quench) at T_i (K) temperature for t_i (h) time, R is the gas constant and Q is the activation energy for precipitate growth [31], here equal to 63 000 cal/mol [29], [32]. The samples that are studied and some of the important parameters throughout the thesis are presented in Table 1-3 and Table 1-4.

In this thesis the term “cycle” is used in order to describe the service time of the claddings. Each cycle is 11 months, in the reactors studied in this project and the reactor being down for service for approximately one month per year [33]. Furthermore, burnup is also given for each materials that are studied. The burnup is a measure of how much energy is extracted from a primary

nuclear fuel source (e.g. uranium pellet). It is most commonly defined as the fission energy release per unit mass of fuel, i.e. its unit us MWd/kgU (Megawatt-days/kilogram Uranium). In this thesis, the different levels of burnup is defined as follows: Medium burnup: samples with the range of ~40-55 MWd/kgU burnup are considered as medium burnup. High burnup: samples with the range of ~55-75 MWd/kgU are considered as high burnup. Extreme high burnup: samples above 85 MWd/kgU are considered as extreme high burnup.

Table 1-3 The composition and heat treatment of the claddings that are investigated in this study. SRA: stress relieve annealed, PRX: partially recrystallized condition [13].

Cladding	Sn (wt%)	Fe (wt%)	Cr (wt%)	Ni (wt%)	Nb (wt%)	O (ppm)	Si (ppm)	H (ppm)	Heat treatment
LK3/L Zircaloy-2	1.34	0.18	0.11	0.05	-	1320	70		log A= -14.2
Zircaloy-4	1.20	0.22	0.107	-	-	1730	-	8	504 °C SRA
Zr-2.5Nb	-	0.07	-	-	2.5	1170	60	10	500 °C PRX

Table 1-4 The samples that are studied in the thesis and important parameters [13].

Sample	Residence time (cycle)	Reactor	Segment elevation (mm)	Burnup (MWd/kgU)	Oxide thickness (μm)	H content at closest measured elevation (ppm)
LK3/L Zircaloy-2	3	BWR (Leibstadt)	2011	44.6 (peak)	4.4 (mean)	44 (at elevation of 2002 mm)
	6		2014.5-2019	66.9 (peak)	14 (mean)	202(at elevation of 2002 mm)
	7		1928	67.6 (peak)	21 (mean)	339 (at elevation of 2000 mm)
	9		2039	89 (peak)	46 (mean)	595 (at elevation of 2045 mm)
Zircaloy-4	4	PWR (Gösgen)	1468	51.5	59 (rod max)	209 (at elevation of 1561 mm)
Zr-2.5Nb	3		869	41.4	16 (rod max)	70 (from one data point)

1.5.Structure of the thesis

In Chapter 2 an overview of the current knowledge about the Zr alloys and their oxidation and HPU properties are presented. The effect of irradiation is given in the end of the chapter. The alloys and the characterization techniques used are briefly described in Chapter 3. The LK3/L type Zircaloy-2 cladding is characterized in great details therefore the description of the microstructural and compositional evolution of this alloy is divided into two chapters. Chapter 4 describes the microstructural evolution of the cladding, presenting the FIB tomography results and additional SEM observations on the 3, 6, and 9 cycle claddings and TEM micrographs on the un-irradiated, the 3, and 9 cycle samples. Chapter 5 presents the EPMA analysis of the 3, 6,

and 9 cycle LK3/L samples, and also includes the ChemiSTEM results on the un-irradiated, the 3, 7, and 9 cycles LK3/L Zircaloy-2 samples. Chapter 6 presents the microstructural (FIB tomography) and chemical results (EPMA) obtained from two selected PWR claddings, namely the 4 cycle Zircaloy-4 and the 4 cycle Zr-2.5Nb samples. Chapter 7 deals with the comparison of the results obtained from different alloys, used in different reactors, i.e. discusses all results that are presented in the thesis in order to distinguish between the reactor- and alloy-specific characteristics from those which are general. The interpretation of the results and the conclusions drawn are presented at the end of each chapter. In the end of the thesis a short Discussion and Conclusion is given providing the most important findings.

2. LITERATURE BACKGROUND

In this chapter an overview of the relevant literature is given. First, the development and history of the Zr-based alloys are summarized followed by more detailed description of the oxidation and hydrogen uptake (H-uptake) of Zr alloys, under both out- and in-reactor conditions. The most important processes influencing the oxidation and H-uptake will also be reviewed and finally the effect of irradiation discussed.

2.1. Brief introduction to the development of Zr-based alloys

The intense research on the Zr-based alloys and its usage for commercial purpose started in the early 1950's [1], [2]. One of the aims was to develop fuel cladding materials for nuclear reactors which operate at high temperatures, different water chemistries and severe irradiation conditions. Successful fuel cladding materials need to be safe and efficient with improved oxidation and H-uptake properties, better irradiation creep resistance and irradiation growth, higher strength, etc. [1]. By the middle of the 1960's Zr-based alloys became the primary cladding materials replacing the previously more widely used stainless steel for water-cooled reactors [1].

The main reason for choosing Zr as the base cladding material in nuclear reactors is the combination of low neutron absorption cross-section and good mechanical properties of Zr [1]. Furthermore, when it is alloyed the mechanical properties (creep behaviour, resistance against stress corrosion cracking) are further improved [1]. Pure Zr has high affinity for both O and H however when alloyed (e.g. with Sn, Nb, Fe, Cr, Ni) its corrosion behaviour is significantly improved.

The composition ranges of the typical Zr alloys for nuclear reactor applications are shown in Table 2-1. Zircaloy-2 is one of the first family of alloys developed and used in commercial BWRs.

Zircaloy-4 was developed from Zircaloy-2 in order to reduce the HPU in PWR. Ni is removed as it is claimed to be one of the responsible factors for the increased HPU of the material [2], [34]. Furthermore, higher Fe and narrower range of allowed Cr content describes this alloy.

Another development is the low-tin Zircaloy-4 where the Sn content is reduced and the aim is to reduce corrosion. It is widely used in PWRs today together with ZrNb type alloys. The ZrNb alloys were developed in Russia where the main focus was mostly on the effect of Nb addition instead of Sn [35]. ZrNb alloys have good mechanical properties (strength, creep resistance) and show reduced corrosion and H-pickup fraction (HPUF) (compared to the Zircaloy type alloys) but this latter is highly dependent both on the composition and the environment of the alloy [35]. It is worth noting that ZrNb binary alloys show poor corrosion resistance in oxidizing environments, such as in BWRs.[1]

[1] It is worth noting that an active search for alternative cladding materials started which is mainly driven by the increased hydrogen evolution and the quick reduction of the ductility in Zr-based claddings under the scenario of loss of coolant accident (LOCA) [184]. The development of the so called "accident tolerant" claddings (e.g. advanced steels, Mo based alloys, SiC) have not yet reached the level to provide similar or even better properties and further benefits during accidents. The discussion about these new materials is out of the scope and topic of this thesis therefore it will not be discussed here.

Table 2-1. The nominal composition of some of the Zirconium based alloys with Zr in balance [12], [36].

Alloy	Sn (wt%)	Fe (wt%)	Cr (wt%)	Ni (wt%)	Nb (wt%)	O (wt%)	Si
Zircaloy-2	1.2-1.7	0.07-0.20	0.05-0.15	0.03-0.08	-	0.12 typical	
LK3/L Zircaloy-2	1.34	0.18	0.11	0.05	-	1320	70
Zircaloy-4	1.2-1.7	0.18-0.24	0.07-0.13	-	-	0.12 typical	
Low-tin Zircaloy-4	1.2-1.35	0.2	0.1	-	<0.01		0.01
Zr-2.5Nb					2.4-2.8	0.13	
M5		0.06			1.0	0.125-0.135	
ZIRLO	0.9-1.3	0.07-0.14			0.8-1.4	0.1-0.16	

The above mentioned alloys were developed mostly in an empirical way and the deeper understanding of the role of the different alloying elements is rather a continuous process helped by different out-of-reactor and in-reactor experiments. In the following a brief description is presented about the current understanding of the effect of the different alloying elements on the oxidation and HPU processes.

Zr has a hexagonal close-packed (HCP) crystal structure (α-phase) up to 867 °C where it changes to the β-phase with body-centred cubic (BCC) structure [37]. Alloying elements Sn and O have a high solid solubility limit in the Zr matrix (see phase diagrams in Figure 2-1). They are α stabilizers and able to increase the phase transition temperature of Zr. O increases the yield strength of the metal in the range of 0.11-0.16 wt%. Above this value the ductility of the material decreases significantly [35].

In the absence of other alloying elements, Sn helps to inhibit the corrosion and to reduce the harmful effect of N impurities in the material. Sn improves the mechanical properties (yield

strength, creep) [38]. However, in the case of Zircaloy-2 the Sn content should not exceed 1.5 wt% or it greatly lowers the corrosion resistance of the alloy [39].

Fe, Cr, Ni and Nb are β-phase stabilizers [35]. Figure 2-2 shows the phase diagrams of these systems. Fe, Cr and Ni have very low solid solubility in the Zr matrix and therefore they precipitate as SPPs [40]. In ternary or quaternary alloys, and also in Zircaloys, they form different types of SPPs: such as Zr_2(Fe, Ni) and Zr(Fe, $Cr)_2$ which are ternary intermetallics.

The creep resistance and the tensile properties of the material are also greatly improved by Cr addition [41], [42]. Nb has a higher solubility in the β-phase and is slightly soluble in the α-phase of Zr (1.1 wt% at 600 °C) [43]. It improves the mechanical properties of the metal, counterbalances the detrimental effects of different impurities [38]. Furthermore, ZrNb alloys also have a high corrosion resistance and low H-uptake [44].

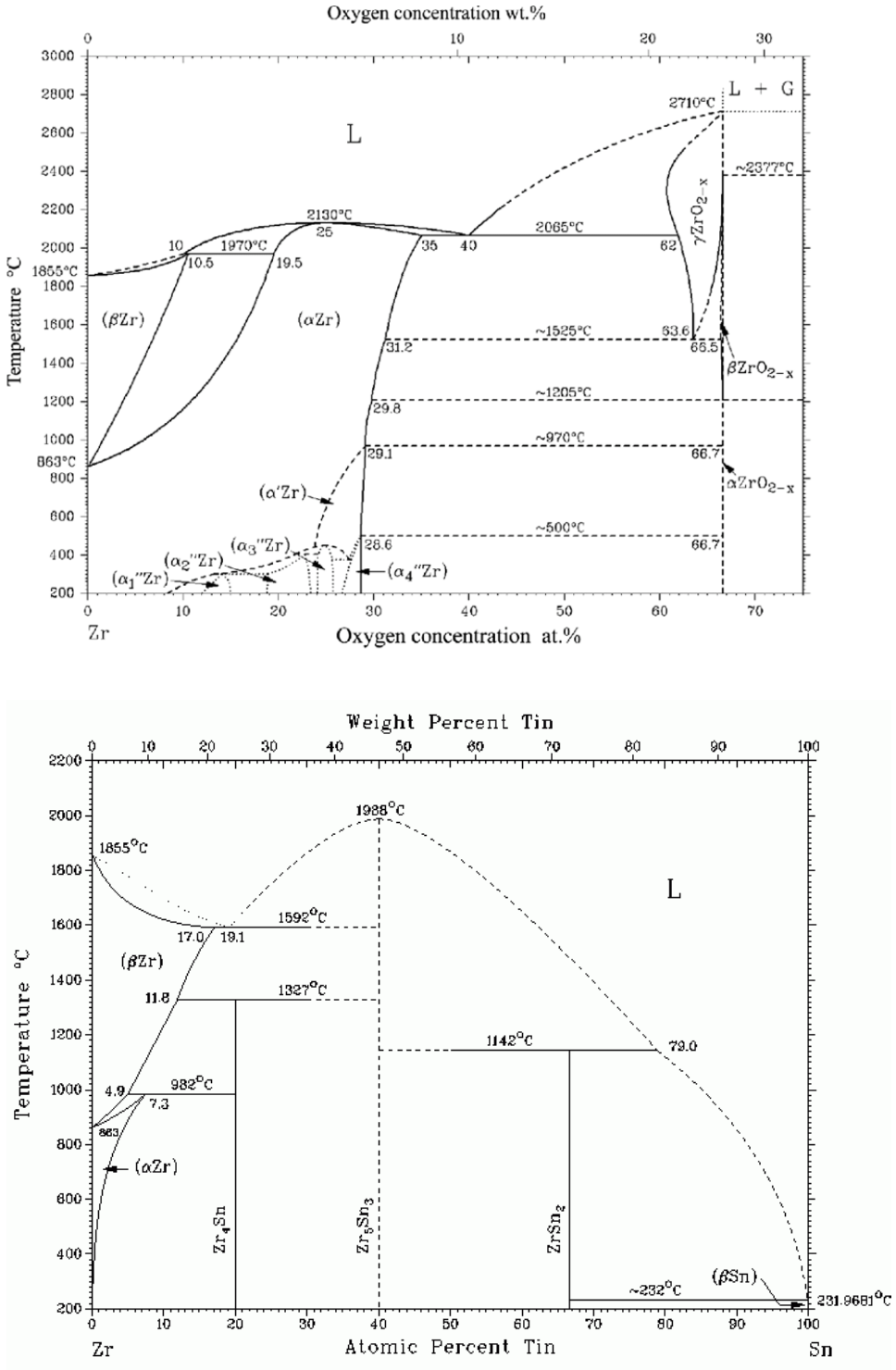

Figure 2-1. Zr-O and Zr-Sn binary phase diagrams [45], [46].

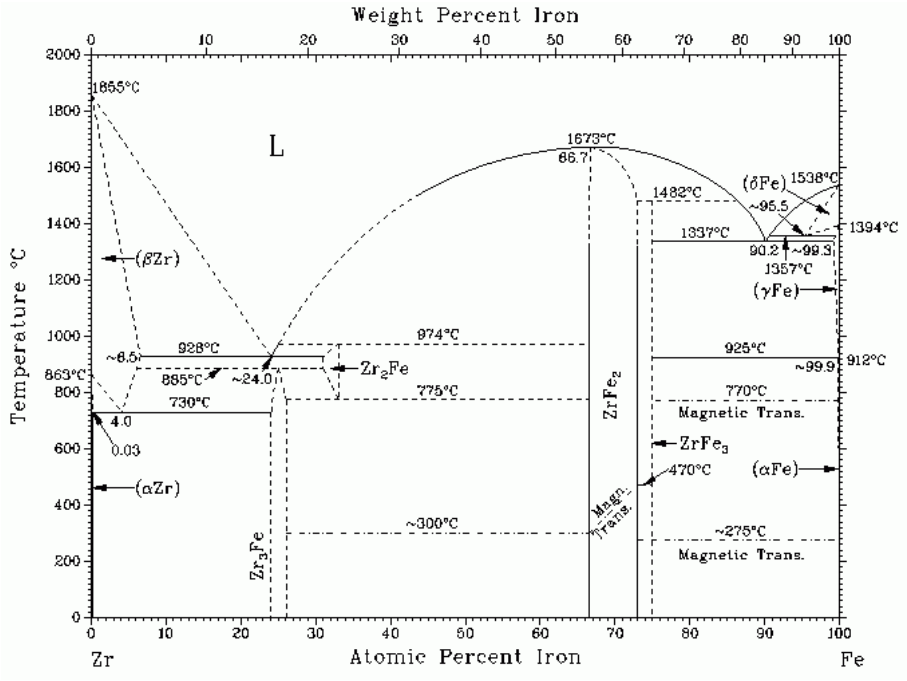
Weight Percent Iron
Temperature °C
Atomic Percent Iron
Zr
Fe
L
1855°C
1673°C
66.7
1482°C
(δFe)
1538°C
~95.5
1394°C
1337°C
90.2
~99.3
1357°C
(γFe)
(βZr)
974°C
928°C
~6.5
885°C
~24.0
Zr2Fe
775°C
730°C
4.0
0.03
(αZr)
ZrFe2
925°C
~99.9
912°C
770°C
Magnetic Trans.
ZrFe3
470°C
(αFe)
Magn. Trans.
~300°C
~275°C
Magnetic Trans.
Zr3Fe

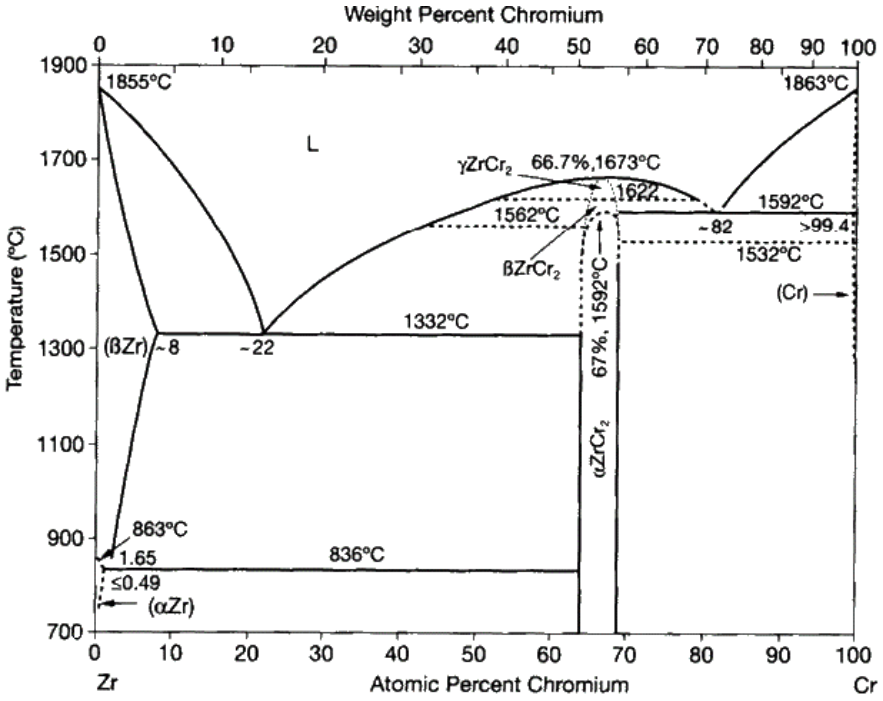
Weight Percent Chromium
Temperature (°C)
Atomic Percent Chromium
Zr
Cr
L
1855°C
1863°C
γZrCr2 66.7%,1673°C
1622
1562°C
1592°C
~82
>99.4
1532°C
βZrCr2
(Cr)
1332°C
(βZr)
~8
~22
67%, 1592°C
αZrCr2
863°C
1.65
836°C
≤0.49
(αZr)

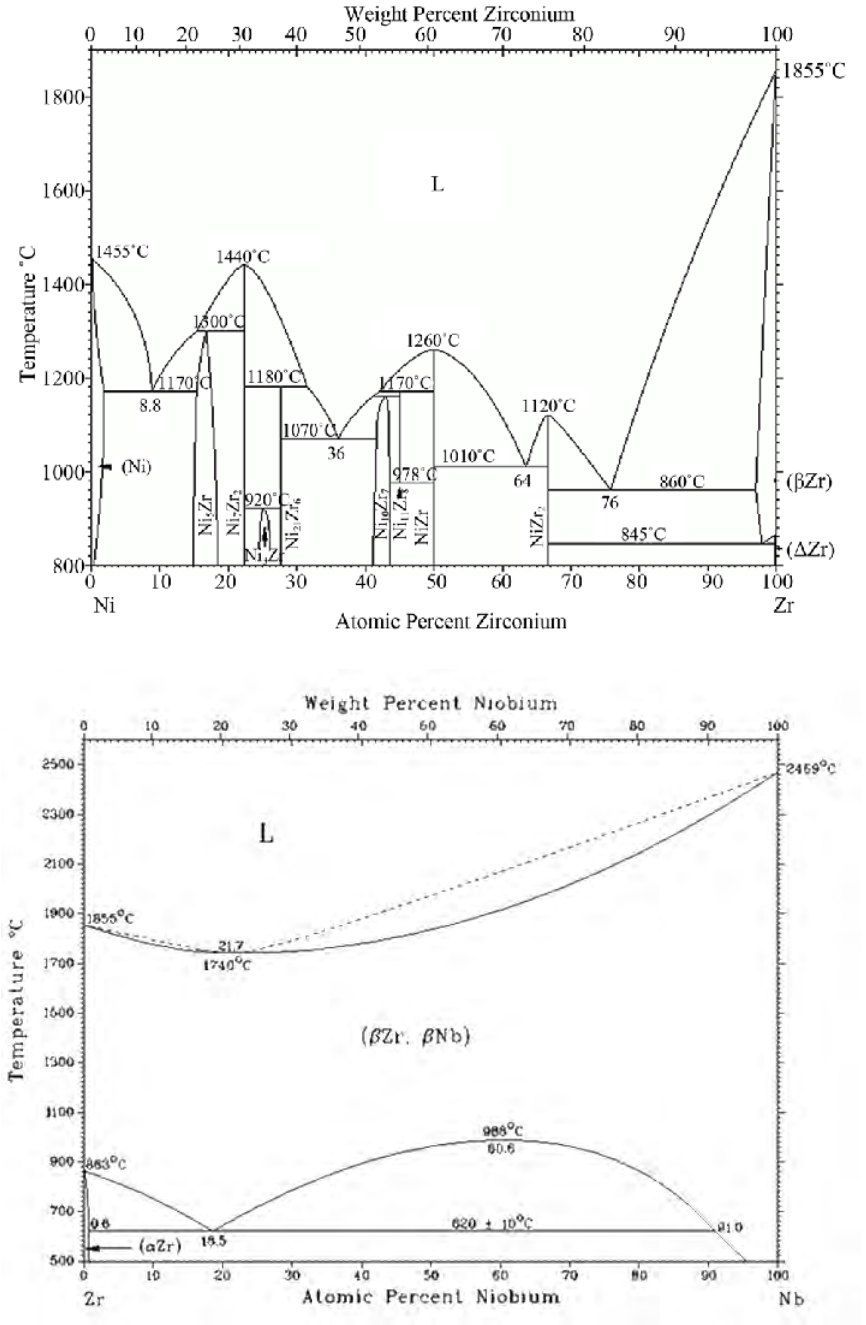

Figure 2-2. Zr-Fe [47], Zr-Cr [48], Zr-Ni [49], and Zr-Nb [50] binary phase diagrams.

2.2. Oxidation of the Zr-based alloys

In this section the general oxidation process, the kinetics of oxidation and the microstructure formed during the oxidation will be reviewed. The oxidation of different alloys and SPPs will be also shortly presented.

2.2.1. General description of the oxidation

The oxidation of Zr occurs at the metal-oxide interface by the migration of the oxidising species through the already formed oxide layer to the metal by grain boundary diffusion [51], [52]. The oxidation reaction of Zr in water can be summarized as:

$$Zr + 2H_2O \rightarrow ZrO_2 + 2H_2 \qquad (2\text{-}1)$$

The following steps are suggested as a possible way to describe the process [53]. Oxygen ions form due to the dissociation of the water molecules as in Eq. (2-2). This O^{2-} is adsorbed on the surface of the oxide layer (Eq. (2-2)). This step is followed by the adsorption of the O^{2-} by a charged oxygen vacancy ($V_{\ddot{O}}$) (Eq. (2-3) showing the half-cell reaction and it is to be considered together with Eq. (2-5) showing the other half of the reaction in which the vacancy formation occurs) [53]:

$$2H_2O \xrightarrow{dissociation} 4H^+ + 2O^{2-}_{adsorbed} \qquad (2\text{-}2)$$

$$O^{2-}_{adsorbed} + V_{\ddot{O}} \xrightarrow{absorption} O^{2-}_{absorbed} \qquad (2\text{-}3)$$

In the next step the O^{2-} diffuses through the oxide layer through different defects such as grain boundaries, dislocations, vacancies and interstitials. The rate limiting step is the diffusion of the oxygen anions [54].

Once the oxygen anion reaches the metal-oxide interface it reacts with Zr producing ZrO_2 and electrons [53]. This step can be divided into two parts as it is shown by Eq. (2-4) and (2-5) [53]:

$$Zr \xrightarrow{oxidation} Zr^{4+} + 4e^{-} \qquad (2\text{-}4)$$

$$Zr^{4+} + 2O^{2-} \rightarrow ZrO_2 + V_{\ddot{O}} \qquad (2\text{-}5)$$

An oxygen vacancy concentration gradient between the surface and the metal-oxide interface is developed due to the vacancy formation at the metal-oxide interface and the vacancies are occupied at the surface by O^{2-}. This gradient is the driving force of the oxidation process [54], [21].

The formed electrons migrate to the outer surface via a few electron conductive sites of the oxide and help to reduce the formed H^{+} cations at the cathodic site [53]:

$$4H^{+} + 4e^{-} \xrightarrow{reduction} 2H_2 \qquad (2\text{-}6)$$

However, not all hydrogen cations recombine with the electrons and rather migrate through the oxide layer to the underlying metal where they react with Zr and precipitate as Zr-hydrides once their solid solubility limit is exceeded. This is the basic process of the H-uptake which will be further discussed in Section 2.3.

The Ellingham diagram of the Zr-O system (Figure 2-3) shows that oxidation of Zr has a high negative free energy therefore it is favourable for Zr to oxidise [55]. The diagram also shows that Zr-O solid solutions are energetically even more favourable, and this indicates that some oxygen will be dissolved in the metal. The amount of dissolved oxygen depends on the temperature and it decreases with decreasing temperatures. It is estimated to be less than 10% at 400 °C [12].

There are three different phases of ZrO_2. The monoclinic structure is stable up to 1170 °C followed by the tetragonal structure which is stable up to 2370 °C beyond which the cubic structure is the stable structure. The melting point of zirconia is 2715 °C under ambient pressure [56]. During oxidation at room temperature or under reactor service conditions the formed bulk oxide is mostly monoclinic ZrO_2 and a sub-stoichiometric gradient can be observed towards the metal where, depending on the type of alloy some amount of tetragonal oxide is found [12], [54]. It is claimed that the tetragonal phase is stabilized by the high compressive stress at the interface [57] or being energetically more favourable when the grain size is fine (below 30-40 nm) [58], [59]. It is generally accepted that presence of the stoichiometric gradient is the driving force of the transport of the oxygen anions through the oxide layer [12], [60]. The electrons and positively charged vacancies migrate to the opposite direction, i.e. towards the outer surface of the oxide [12], [20], [61]. The vacancy concentration at the interface depends on the oxygen partial pressure and temperature [62], however a vacancy concentration gradient is present with more vacancies at the interface. The rate of oxidation is controlled by the slower moving ion, i.e. either the oxygen anion or the electrons [54] and it is further discussed below.

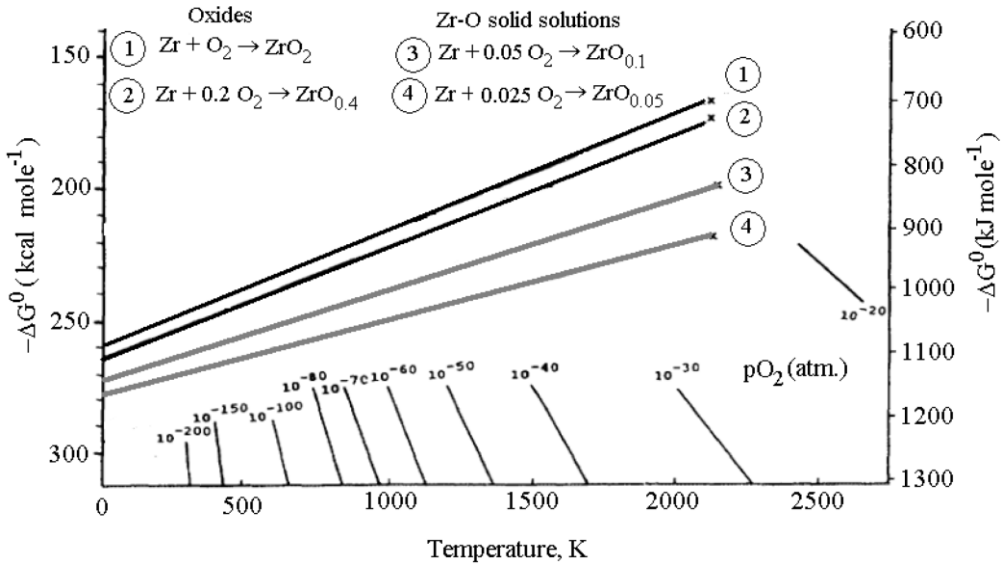

Figure 2-3 Ellingham diagram of Zr-O system [12], [54].

2.2.2. Oxidation kinetics

Wagner's theory describes the growth of an oxide if no space charges are present, i.e. local electro-neutrality is required [63]. The diffusion transport of the oxygen anions occur via charged vacancies. In this case the general oxidation kinetics can be described by the following generic equation for the weight gain of the alloy [59], [64]: $x = Kt^n$. Where x is the weight gain or oxide thickness, K and n are alloy dependent kinetics constants, and t is the time. In the case of the Wagner-theory only diffusional transport is rate-limiting and the ionic and electronic transport is coupled at all time. It is claimed that the transport of electrons is generally fast in the oxide and the rate limiting step of the oxidation is the diffusion rate of the oxygen anions [21]. If the oxygen anion diffusion is the rate limiting step, a parabolic weight gain with n=0.5 is the result [12], [20], [52], [61]. However, these requirements are not necessarily fulfilled during the oxidation of Zr alloys which also leads to the deviation of n constant from 0.5: in the case of Zr alloy oxidation n value differs between 0.2 and 0.6, i.e. sub-parabolic kinetics is

observed [65], [66], [67], [68]. Some explanations are proposed with the aim to understand the reason behind this deviation, e.g. grain boundary diffusion through oxide grains with changing size as the oxide grows [66]; compressive stress build-up in growing oxide [21], [64], [69]; occurrence of cracks, pores and other obstacles for oxygen migration [70], [71]. Other authors claim it is more probable that the driving force is caused by the effect of charges and electric fields [72], [73]; therefore electron transport would be the process which controls the oxidation kinetics. For example, the space charge model takes into account the modifications on the oxidation kinetics induced by the space charges at every location of the oxide layer, i.e. the effect of the electric fields [53], [72], [73], [74]. This model can give an estimation of the oxidation kinetics in the early stages of oxidation, however once the oxide is thick the local electroneutrality can be assumed in order to apply a less complex model (e.g. Wagner theory). The above mentioned model describe the so called pre-transition oxidation, i.e. the formation of a protective oxide. A correct description for the Zr alloy corrosion should explain the corrosion kinetics and the experimental results for the different claddings.

The corrosion process has two phases. In the beginning a protective layer is formed during the pre-transition phase which is followed by a transition (increase) in the rate of the oxidation which is called post-transition oxidation.

The pre-transition period follows a cubic or sub-parabolic kinetics while after the transition the corrosion can be described by a linear oxidation rate (n=1) or cyclic behaviour. In general, the transition occurs at around 2-3 μm of oxide thickness [54]. A general representation of the transition is in Figure 2-4 [12]. Depending on the type of alloy the kinetics and the transition can be different, see a few examples in Figure 2-5. The cause and the mechanism of the transition are not yet fully understood and is an active field of research [71], [75], [76], [77].

It is clear that the in depth behaviour of the Zr and its alloys in different environments including steam, oxygen, air and other gases would make the review much more comprehensive. However, for the sake of conciseness, these topics will not be treated in the thesis, and only reactor and autoclave environments simulating the reactor conditions to some extent, will be covered.

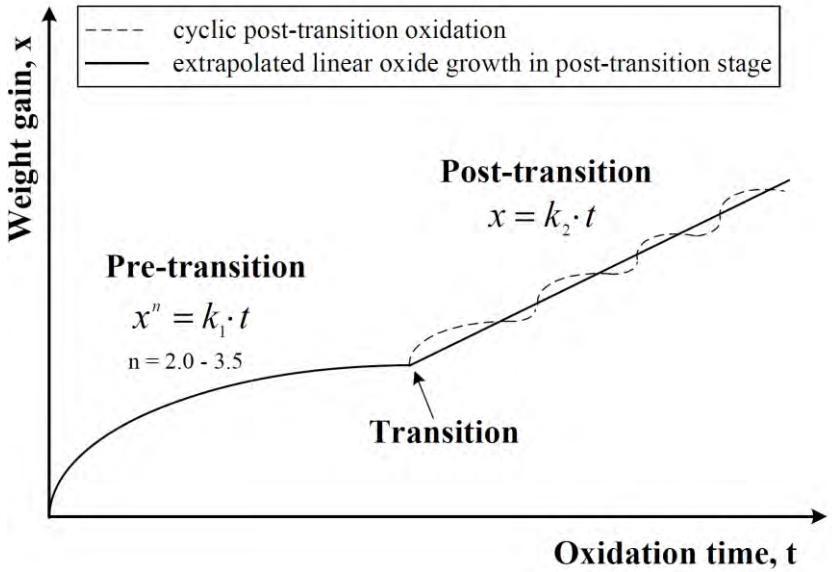

Figure 2-4. Schematic representation of the pre- and post-transition oxidation of Zr alloys in general at temperatures between 240-400 °C in oxygen-containing atmosphere [54], [78].

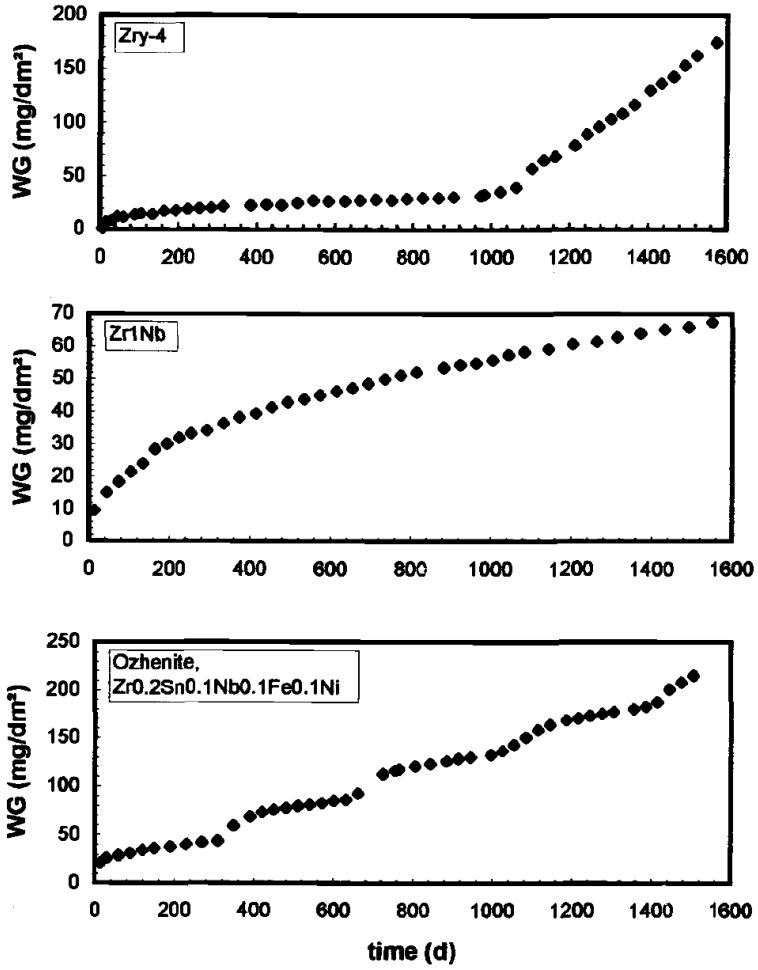

Figure 2-5. Typical graphs of weight gain (WG) – time (in days) for three different alloys in 350 °C 17-MPA water [79].

2.2.3. Microstructure of the formed oxide and the metal-oxide interface

The formed oxide at the related temperatures has a complex microstructure and it evolves with time. The formed oxide is mostly monoclinic [59] and contains tetragonal oxide in a small amount. The freshly formed oxide, i.e. at the metal-oxide interface contains a higher proportion of tetragonal phase. This phase is mostly stress stabilized [21], and it transforms to monoclinic structure as the oxide grows [59], [80].

The formed ZrO_2 shows a large volume expansion with a Pilling-Bedworth ratio of 1.56 (i.e. the volume of the oxide is 1.56 times larger than that of the metal) [12]. Because fresh oxide is formed at the oxide-metal interface [12], this expansion can result in the development of lateral compressive stresses. The stress which is built up in the growing oxide can break the oxide and produce cracks in the layer, particularly when growing on a convex substrate [21]. As a porous oxide layer is less protective than an oxide film without cracks, it is claimed that the pores could offer a shorter route for the oxidising species and hydrogen, or even for water to enter the material and reach the metal-oxide interface faster [81], [82], [83].

The oxide growth starts with the formation of small, equiaxed, randomly oriented grains at the metal-oxide interface [84]. Those grains grow into columnar shapes which are initially oriented in a certain way so that the stress accumulation is minimized. These orientations were reported as: $\bar{2}01$, $\bar{4}01$, and $\bar{6}01$ [85], [86]. The formed columnar grains are about 30-40 nm in diameter and 200 nm in length. Once this size is reached new grains will nucleate at the metal-oxide interface.

The solid solubility limit of O in Zr at PWR service temperature (360 °C) is around 28 at% (please refer to Figure 2-1) and this value could be expected at the metal-oxide interface. However, as the interface is moving during the oxidation, equilibrium may not always be established and metastable phases were observed at the metal-oxide interface such as amorphous [87] or omega phase [88], ZrO [89], Zr-30%O [90], Zr_3O [65] and a series of other different phases [91]. Other studies showed that all the above mentioned phases can occur at different times of oxidation [92], [93], [94]. In the metal part of the interface an oxygen saturated “suboxide” layer can be found. It was shown that during the transition the thickness of the above described layers decreases significantly most likely due to the lack of time for formation [59].

2.2.4. Oxidation of the Secondary Phase Particles

The $Zr(Fe, Cr)_2$ SPP has a Laves phase structure while $Zr_2(Fe, Ni)$ a body-centred tetragonal (BCT) structure [95]. Zircaloy-2 contains both types of SPPs, while Zircaloy-4 has only $Zr(Fe, Cr)_2$ type SPP. The oxidation of some type of SPPs (e.g. $Zr(Fe, Cr)_2$ and β-Nb and Zr-Nb-Fe) is delayed compared to the oxidation of the metal matrix [60], [90], [96], [97], [98], [99], [100], [101] [102], [103]. This means that these SPPs are metallic in the oxide layer close to the metal-oxide interface. At the later stages of oxidation the SPPs also oxidize leaving a fine-grained oxide behind them [103] with higher amount of tetragonal phase in the oxide matrix [97]. The reason behind the delayed oxidation could be that the alloying elements have intrinsically different oxidation behaviour, or it could be due to the different crystal structure of the SPPs [103]. Most likely the combination of the two is responsible [103]. In an in-situ study, Proff et al. [103] investigated binary alloys such as Zr1%Cr, Zr0.6%Nb, Zr1%Fe, and Zr1%Ni using ESEM and TEM. The temporal or sequential order of oxidation of the different phases are: $Zr_3Fe \approx Zr_2Ni \approx$ Zr-matrix > ZrNb > $ZrCr_2$. Figure 2-6 shows the free energy of oxidation for the different phases. It is emphasized that in the in-situ and other studies of Proff et al [103], [104], subsequently to the oxidation of Zr-1%Fe sample, Fe_2O_3 crystals were observed at the free surface of the oxide as it is shown in Figure 2-7 TEM image, marked by the arrowhead. Figure 2-7 provides the EDS analysis of the particle. The authors concluded that Fe diffuses from the SPPs to the free surface [103]. Similar protrusions were reported in the case of Ni after oxidation of Zr-1%Ni samples. However the other alloys did not show such behaviour [103]. Abolhassani et al reported that both Fe and Cr diffuses to the free surface on an in-situ oxidized Zircaloy-4 [105]. Figure 2-8 from their study demonstrated that Cr was observed on the top of the Fe layer on the surface of the oxide. In [104] the authors report that the Fe-protrusions are unlikely to be a contamination from the autoclave.

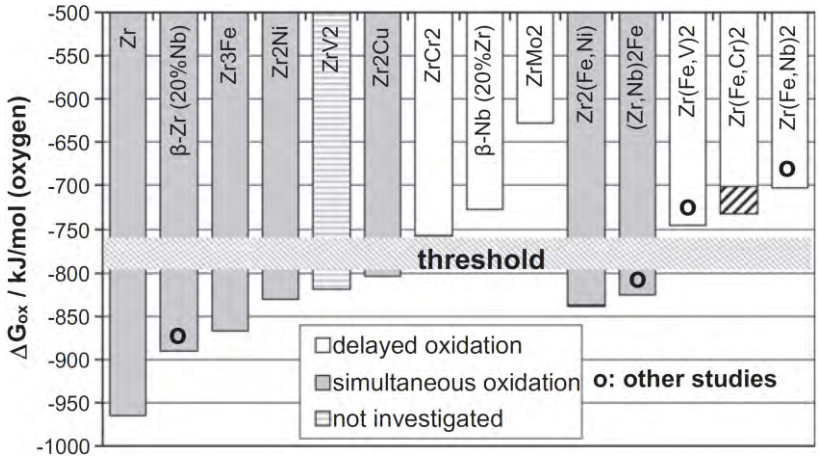

Figure 2-6. The free energy of oxidation for Zr and the different SPPs [101].

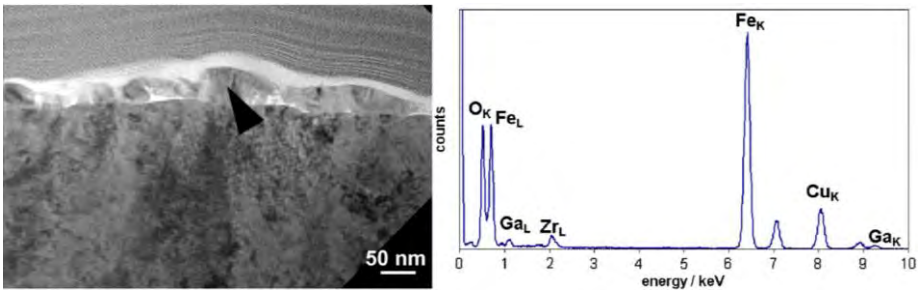

Figure 2-7 BF TEM micrograph of the oxide surface, arrowhead marks the Fe-oxide crystals formed on the oxide surface. EDS spectrum of Fe-crystal marked by the arrowhead [103].

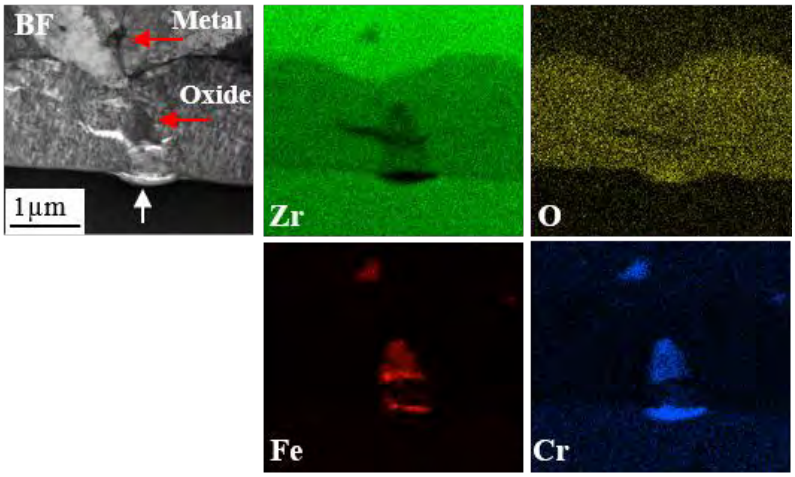

Figure 2-8 BF TEM micrograph and EDS elemental maps at the same region [105]. Red arrows: SPP in metal and in oxide. White arrow: protrusion of Fe and Cr crystal on the free surface of the oxide.

It is worth mentioning that precipitate-free Zr-Sn-(Fe, Cr) alloys which are melted from pure Zr and pure alloying elements show poor oxidation properties. However, once they are galvanically coupled with a noble intermetallic compound of $Zr(Fe_{0.66}Cr_{0.33})_2$ the oxidation resistance increases significantly [19]. This shows that the SPPs provide anodic protection increasing the oxidation resistance [19]. The mechanism behind this phenomenon is not yet fully clarified. It is possible that the chemistry of the oxide grain boundaries (GBs) formed on the alloy and on pure Zr are different [106], which could lead to the improved oxidation resistance [16].

2.3. Hydrogen uptake of the Zr-based alloys

During the corrosion process hydrogen is formed at the cathodic site as described before. This hydrogen can either recombine with the electrons which formed at the metal-oxide interface (anodic reaction) and migrated to the water-oxide interface or they can penetrate through the oxide layer, reach the metal-oxide interface and eventually enter the metal. This process is called H-uptake. The hydrogen pickup fraction (HPUF) can be described as the ratio between the amount of hydrogen which is absorbed by the metal and the hydrogen which was formed during the corrosion process [12], [107], i.e.: $f_H = \frac{H_{absorbed}}{H_{generated}}$ [107].

The HPUF is strongly dependent on the alloy composition and the environment (e.g. water, steam, different gases). As an example Hillner et al. [108] measured the HPUF of Zircaloy-2 in different environments above 330 °C and reported 2-7% HPUF in oxygenated water, 15-24% in degassed water, and 30-52% in hydrogenated water. It was reported that Ni addition to the cladding has a significant effect on the HPUF in the case of Zircaloy-2 [109], [110].

Zr has a high affinity for hydrogen and the oxide layer provides protection against rapid H-uptake. The Zr-H phase diagram is shown in Figure 2-9. The terminal solid solubility limit of H dissolution (TSSD) and precipitation (TSSP) is shown for pure Zr and Zircaloy-2 (see Figure 2-10) [111]. The reason behind the difference between the values of TSSD and TSSP is an active field of research [111], [112], [113], [114], and it associated with an additional energy that is needed upon hydride nucleation: during the cooling process the formation of hydrides requires reversible work on the matrix. When a hydride nucleates the H concentration is increased compared to the equilibrium solvus. When the hydride reaches a critical size, both elastic and plastic work is done. On the other hand, during heating, the contribution from plastic work is negligible. For more details please refer to references of [111], [112], [113], [114]. The TSSD is around 47 ppm in Zr and 60 ppm in Zircaloy-2 at 300 °C, while at 350 °C it is 90 and 111 ppm, respectively for Zr and Zircaloy-2 [111]. The excess hydrogen precipitates in a form of zirconium-hydrides [24].

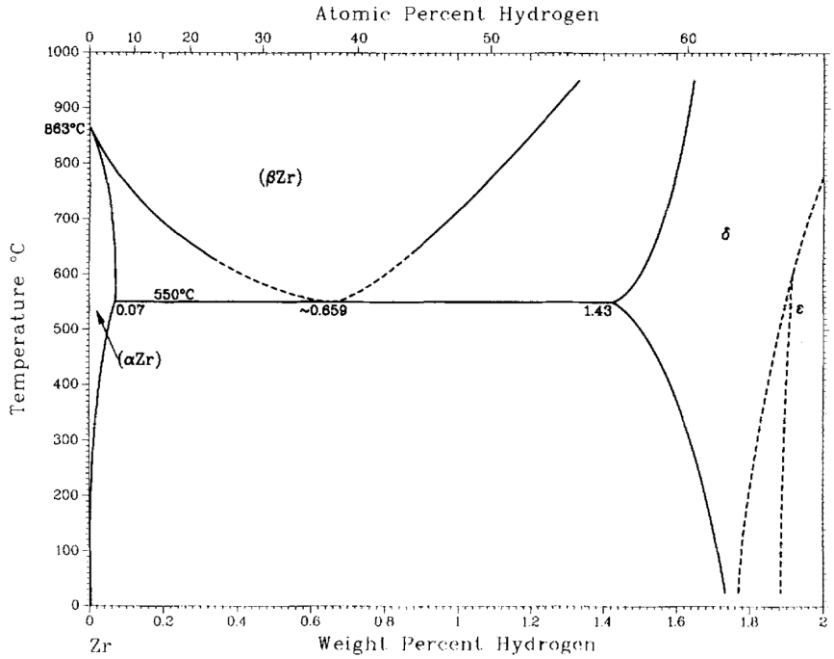

Figure 2-9. Zr-H binary phase diagram [115].

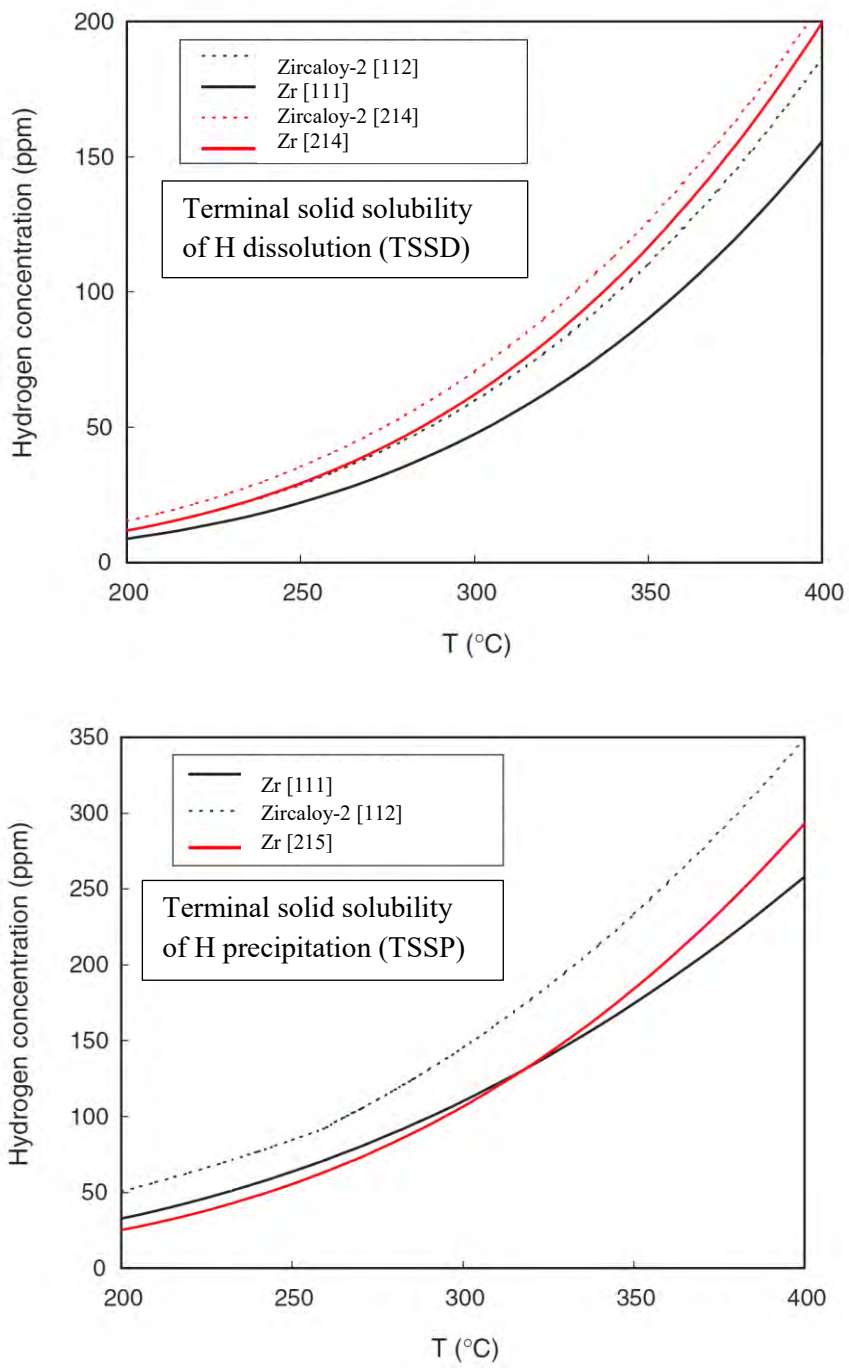

Figure 2-10. The TSSD and TSSP of H in Zr and in Zircaloy-2 modified figure of Une et al. [111].

These hydrides deteriorate the mechanical properties of the cladding by increasing the brittleness of the material [24]. There are three phases of zirconium-hydrides: δ, ε and γ, the first two are stable [23]. δ hydride assumes the fluorite structure in which Zr atoms are arranged in a face centred cubic (FCC) structure while the H atoms occupy eight of the tetrahedral sites in a random manner. The maximum occupancy of the sites by the H atoms is 83% giving the formula of $ZrH_{1.66}$. At room temperature this changes to $ZrH_{1.59}$ as the H atoms occupy only 6 sites. ε hydrides (ZrH_2) have face centred tetragonal (FCT) structure with Zr in tetrahedrally co-ordinated positions and H atoms fully occupying the tetrahedral sites. γ hydride is metastable and has a face centred tetragonal (FCT) lattice; in this system the half of the tetrahedral sites are occupied. The debate is currently open regarding the stability, the transformation temperature and the formation mechanism of the γ and ε systems, despite the extensive studies in the literature on this topic: [116], [115], [117], [118], [119], [120], [121], [122], [123].

The formation of brittle Zr-hydrides is one of the major life-limiting factors of the cladding [124], [125]. One of the main aims of the cladding producers is to limit the HPU of the material. Therefore, the HPU is one of the crucial phenomena that needs further understanding in order to decrease waste production and further increase the safety of the reactors. The driving force and the exact mechanism of the HPU is still to be better understood and is under intense research. It is worth mentioning that several international research groups and programs were formed with this aim, such as the MUZIC collaboration, SHIZAM programme, and NFIR hydrogen collaborations. Many publications are available from these collaborations: [83], [126], [127], [128], [129], [130], [131], [132] and many more.

2.4. Current knowledge regarding the mechanisms of oxidation and hydrogen uptake

2.4.1. The transition in the oxidation kinetics

The mechanism of the oxidation transition being a complex topic, it is extensively studied. Different alloys show different oxide transition thicknesses and this oxide thickness is characteristic for the given alloy [102]. The correct explanation of the oxidation transition should clarify why does the loss of protectiveness occur suddenly and it should also reveal the reason behind the characteristic transition thicknesses of different alloys. There are some hypotheses that aim to reveal the main controlling processes behind the oxidation transition, reported for example in references [17], [57], [59], [77], [133], [134], and [135].

One of these hypotheses [57], [133] claims that the different rates of stress accumulation in the different alloys are responsible for the transition and the variations in the transition oxide thicknesses. The different alloying elements could cause a slight change in the lateral strain during the oxidation; therefore the different in-plane stresses would cause the cracking of the oxide layer. This could lead to variations in the temporal occurrence of cracking in the different alloys. Therefore, the transition thicknesses would also vary depending on when the stress reaches a critical level in the oxide. The measurement of the stresses in the growing oxide is a difficult, however many authors have reported their results using different techniques and environments [86], [80], [133], [136], [137]. Roy et al. presented two methods for the measurement of the stresses generated during the oxidation process of Zircaloy-2 in dry oxygen at 500 °C [136]: they found fast increase of the average stress in the early stages of oxidation and maximum average stress (about 1.6 GPa) was found at an oxide thickness corresponding to the transition. The authors suggest that the stress is the highest in the inner oxide therefore it

gives the highest contribution to the measured stresses, while the outer oxide has negligible contribution. Other authors also reported values between 1 and 3 GPa of in-plain stresses during oxide growth [86].

Another hypothesis is based on the level of porosity in the oxide and claims that when the porosity reaches a critical density, the pores interconnect with each other and a continuous path would form through which the water can reach the metal-oxide interface leading to a sudden increment of the oxidation rate [77], [134], [135]. The difference in the transition thicknesses in the alloys would be caused by the variations in the accumulation of porosity. There are measurements which show some evidences regarding the interlinkage of the pores [77] and an increased density of pores just before the transition [134]. This hypothesis does not give an explanation regarding the decreased stresses at transition [59]. Therefore, it seems possible that the combination of the two hypotheses could explain the transition better rather than using them separately [59], [68].

It is also claimed that the undulation of the metal-oxide interface could play a crucial role in the oxidation resistance affecting the stress level and direction in the oxide close to the interface [138]. The amplitude and width of such undulations will change as a function of material, but from the observed data, they will vary usually in the range of 100 nm to micrometre in amplitude on the two sides of the metal-oxide interface. This undulation will only refer to what occurs around the metal-oxide interface. It was shown that the undulation has an effect on the stress distribution in the oxide [69], [138], [139]. Changes in the compressive and tensile stresses were revealed in an undulated interface by finite element modelling [138]. The undulation value in the work of Parise et al. was introduced to the model based on SEM micrographs of Zircaloy-4 oxidized in water at 340 °C, 15 MPa [138]. Three oxide thickness

values were studied: 0.5, 1, and 1.5 μm with an undulation amplitude of 0.1 μm. For the 1 μm oxide thickness further undulation amplitudes were modelled, namely 0.05, 0.1, and 0.2 μm [138]. The effect of undulation compared to the flat interface was clearly observable in the results, as a few examples: modified hoop stresses at the interface, increased compressive stresses in the oxide, arisen tensile stress in the metal, occurrence of radial stresses. A schematic drawing of the results is presented in Figure 2-11 from [138].

It is also claimed that the differences in the stresses have an influence on the diffusion coefficient of oxygen [69]. Correlation between the sites of circumferential cracks and the undulation of the metal-oxide interface was found by Bossis et al. [71] and this phenomenon was connected to the oxidation transition by Schefold et al. [140].

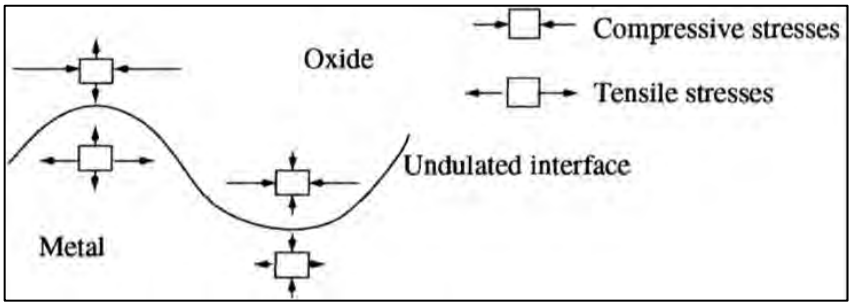

Figure 2-11 Schematic drawing of the stressed around an undulated interface [138].

2.4.2. Possible factors influencing the hydrogen uptake

Currently a few main processes and phenomena are identified and claimed to play decisive role in the HPU properties of the material [17]. The detailed description of these is presented in this section.

2.4.2.1. Hydrogen diffusion through pores and other flaws of the barrier oxide

The diffusion profile of hydrogen in the oxides formed on different Zr alloys are reported [141], [142], [143], [144]. Most of them used deuterium (D) by ion beam implantation. Based on the subsequent depth profiles before and after treatments at different temperatures and times the dispersion of the D peak was analysed and the diffusion coefficient was calculated. It was concluded that the diffusion of deuterium is via interconnected pores at the GBs of the oxide layer [145].

The same is concluded in the case of Zr-2.5Nb: the proton discharge and HPU sites are the cracks and pores in the oxide close to the metal-oxide interface [81], [82], [144]. Cox and Wong [81] found that the cracks and pores were the cathodic sites and they offer a fast route for hydrogen. Ramasubramanian et al [82] showed on pressure tubes that the water and the electrolyte species almost reached the metal-oxide interface. They have used depth profiling on these tubes after they were used in CANDU type reactor. They concluded that the migration of hydrogen atoms, protons and hydroxyls through the barrier layer is the main process which determines the HPU. They proposed two different options being the driving force for HPU: i) Due to the high electronic resistance of the oxide a potential gradient develops via the barrier layer, and ii) If there is metallic connection through the barrier layer then the driving force is the metal's high affinity for hydrogen. Furthermore a model for the hydrogen ingress through the bulk oxide was proposed in this paper. A schematic drawing explaining the model is shown in Figure 2-12. Based on their study on isotope incorporation and exchange experiments this model is the following: the hydrogen isotopes in Zr-2.5Nb alloy both in reactor and in autoclave would be found as hydroxyls and hydrogen-bonded water on the surfaces of oxide crystallites. The transport of hydrogen through the bulk oxide would happen through these "hydrated

pathways" on the surfaces of the oxide crystallites. The hydrogen ingress into the metal is therefore a localized electrochemical phenomenon. The sites where hydrogen can enter the metal are the end of these pathways. The entry for hydrogen is limited by a thin electrical barrier layer as it has a positive space charge due to the ionized anion vacancies [82].

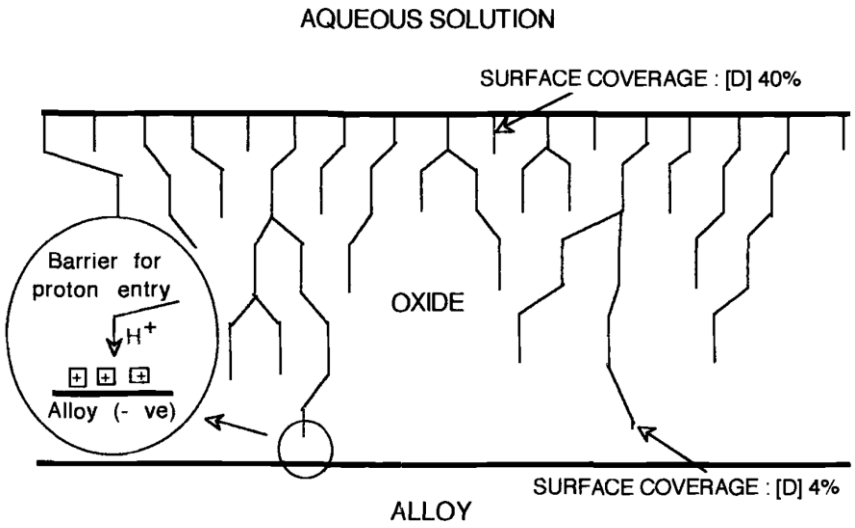

Figure 2-12. The schematic presentation of the proposed model for hydrogen diffusion through the bulk oxide in Zr-2.5Nb [82].

Li et al. [83] provided the distribution of deuterium in the oxide by 3D NanoSIMS in Zircaloy-4 oxidized in 360 °C 18 MPa pure heavy water for different time periods. The authors concluded that deuterium can be found in high concentration in the outer oxide near the water-oxide interface and there is a gradual decrease in the deuterium concentration towards the inner oxide. The study showed that in the oxide close to the metal-oxide interface deuterium is trapped in small cracks and pores serving as an evidence that these pores serve as easy paths for hydrogen towards the metal (Figure 2-13).

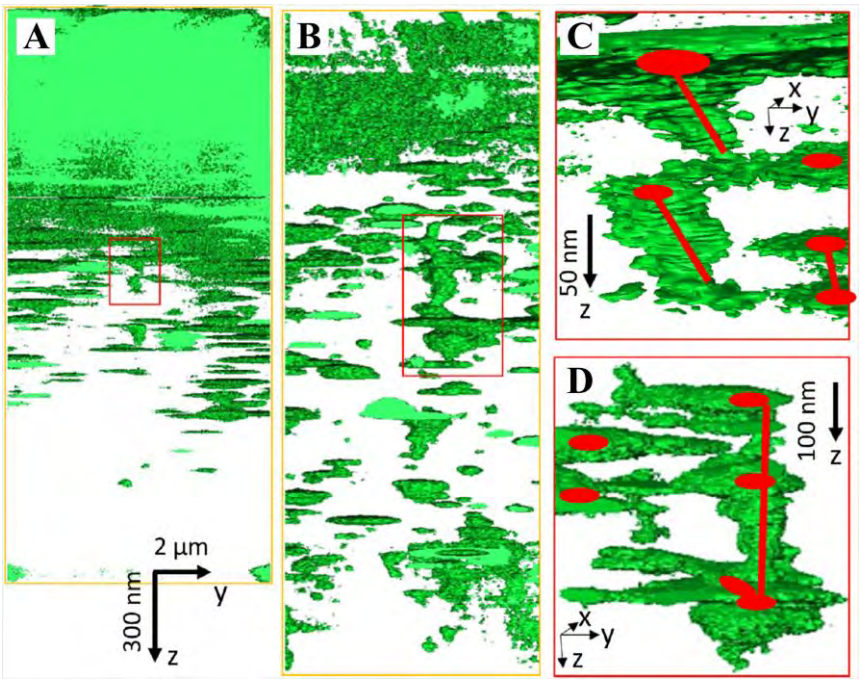

Figure 2-13 3D distribution of deuterium in oxidized Zircaloy-4 by NanoSIMS by Li et al. [83]. (A) and (B): samples oxidized for 61 days (pre-transition stage) and 106 days (around the oxidation transition), respectively. (C) and (D): magnified images of the red frames on (A) and (B). The green volume is the measured data while the red dots on (C) and (D) are suggestion of the real distribution estimated by the authors and the red lines are the possible paths for deuterium transport.

2.4.2.2. The composition of the outermost layer of the oxide influencing the H_2 formation

It is claimed that the proton reduction reaction can be enhanced by the effect of Nb_2O_5 or SnO_2 at the surface of the oxide, i.e. at the oxide-water interface [22]. This could lead to an increased H_2 formation in this region lowering the amount of protons which could diffuse through the oxide [22]. Therefore the HPU is decreased. The explanation is that there is an overlap between the SnO_2 or the Nb_2O_5 conduction band edge and the proton reduction energy level (Figure 2-14) which is a requirement for the red-ox reaction to occur at the oxide surface [22]. Therefore, Ramasubramanian et al. concluded that if oxidized Sn or Nb is present the reduction of protons is a favourable reaction [22].

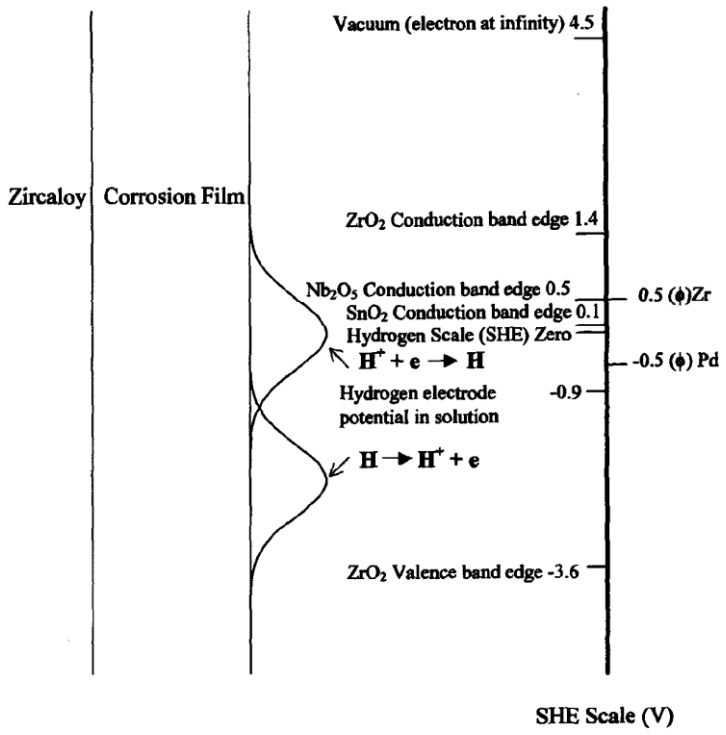

Figure 2-14 Schematic drawing of the conduction band edges for n-type oxides, ZrO_2, SnO_2, and Nb_2O_5 relative to the standard hydrogen electrode (SHE) potential in water (lithiated – pH 8, 315 °C) [22]. The Gaussian distributions show the probability of the energy levels for the red-ox reaction.

2.4.2.3. Hydrogen pickup influenced by the electrical conductivity of the oxide layer

Couet et al. [107] studied the relation between the HPUF and the oxidation kinetics of different Zr-based alloys (e.g., Zry-4, ZIRLO, Zr-2.5Nb, model alloys) using Vacuum Hot Extraction and Cold Neutron Prompt Gamma Activation Analysis. The alloys were exposed to pure water at 360 °C and 18.7 MPa pressure. The weight gain and the hydrogen content of the samples were measured periodically and from these data the pickup fraction was calculated. It was shown that the HPUF varies significantly with the time of exposure and with the alloys. The study concludes that the need to balance charge is the possible cause of the variation in the HPUF. In the dissertation of the same author [53] it is concluded that the driving force for the

HPU is the electrochemical potential gradient across the oxide layer. This potential gradient is mainly influenced by the electrical conductivity of the oxide which would mean that if the conductivity of the oxide layer is low, a higher potential would build up [53]. This would decrease the activation energy of the proton absorption at the cathodic site resulting in a higher HPU [53].

An inverse relationship was shown between the oxidation kinetics and the HPU showing that the oxide transport properties could play an important role in that case if the rate limiting step of the HPU is the transport of the charged species. As the alloying elements - both if they are present in dissolved state or in SPPs – would change the transport properties of the oxide, and this could give an explanation for the different HPU of the different alloys [53], [107].

The relationship between the electrical resistance of the oxide and the HPU is described in many publications, for example [22], [146], [147]. Baur et al. [146] studied Zircaloy-4 samples with different SPP size and Fe content and Zr-2.5Nb samples in 350 °C pressurized water with and without cathodic polarization. The corrosion, the rest potential, the current density, and the HPU were measured. The electrical resistance of the oxide increased in the pre-transition and dropped at transition and increased again after transition. A correlation was observed between the changes in the electrical resistance of the oxide barrier layer and the HPUF. The following was concluded: i) samples with larger SPP size and Fe content showed lower resistance and HPU than samples with smaller SPP size and Fe content; ii) Zr-2.5Nb sample showed the lowest resistance of the oxide barrier layer and the lowest HPUF and lowest sensitivity for the cathodic polarization; iii) in order to enhance the corrosion after transition more than -0.3V of potential difference over the barrier layer is necessary. This could mean that the increased corrosion of Zircaloy-4 with small SPPs is caused by the absence of a contribution from the SPPs to the

electrical conductivity of the barrier layer. The final conclusion was that the HPU is governed by the potential gradient over the oxide layer.

In Figure 2-15 a schematic drawing of the correlation between the electrical resistance of the barrier layer and the HPUF is presented [17].

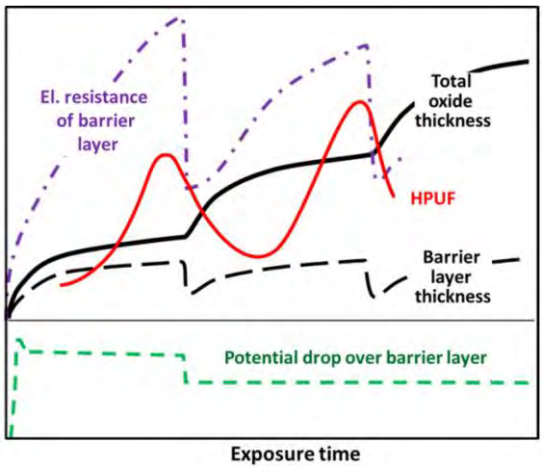

Figure 2-15. Schematic presentation of the correlation between the electrical resistance of the oxide layer and the HPUF [17].

2.4.2.4. Hydrogen uptake influence by the metallic SPPs in the barrier oxide layer

The role of the SPPs in the HPU is studied by many authors and it is claimed that those SPPs which remain metallic in the barrier oxide layer act as local fast routes H diffusion increasing the HPU [71], [110], [146], [148], [149].

A study of Bossis et al. [71] demonstrated a correlation between the sites of the SPPs and both the location of H in the oxide and the hydrides in the metal underneath the SPPs. They used Zircaloy-4 samples oxidized in 400 °C heavy water for 48 hours. The SIMS cross-section together with the schematic representation of their data is shown in Figure 2-16.

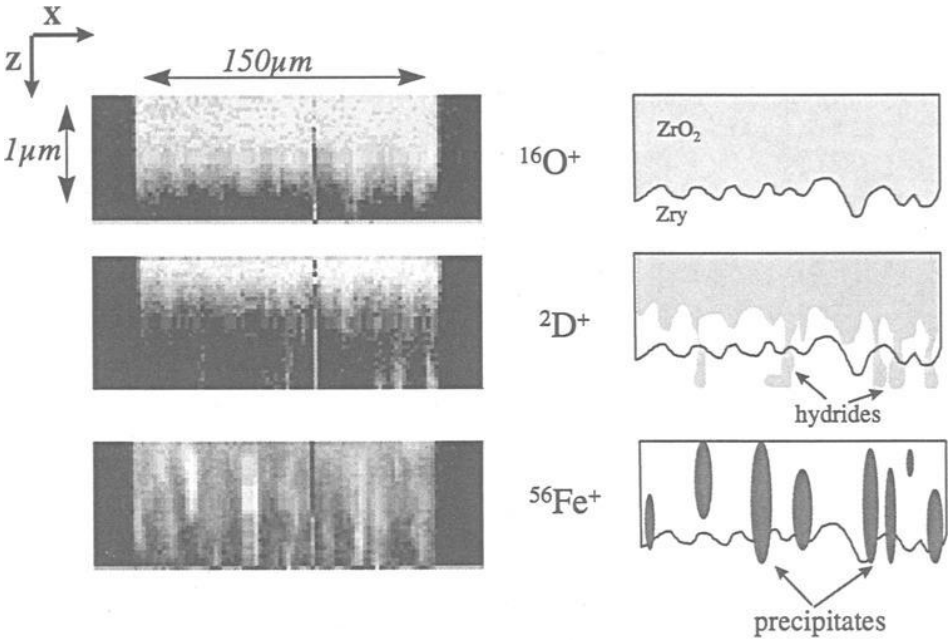

Figure 2-16 SIMS cross-sectional images of oxygen, deuterium and Fe in the oxide of Zircaloy-4 and schematic representation of the data [71].

Hatano et al. [148] and Baur et al. [146] both concluded that the size of the SPPs has a significant influence on the HPU of Zircaloy-2 and -4 oxidized in 350 °C and 450 °C in 100 bar pressure steam (pre-transition region was studied) [148] and in 350 °C water (long-term oxidation) [146]. Samples with larger SPPs showed higher HPU. Hatano et al. [148] explained this phenomenon that bigger SPPs remain metallic for longer period of time and act as expressway for H transport.

Although the results show correlation between the SPPs and the HPU, only assumptions exist as explanations. The proposed explanations are connected to i) the ability of the SPPs to absorb higher amount of H [148], ii) the assumption that H may have a higher diffusivity through the SPPs [148], [149], and iii) that metallic SPPs could be the sites of proton discharge and they could act as windows for the produced H to enter the metal [17], [149].

2.4.2.5. Hydrogen uptake influenced by the presence of Ni and Fe at the barrier oxide grain boundaries

In a review paper of Garzarolli et al. [109] the authors concluded that Ni could play an important role in the increased HPU when it is in a metallic form being in an SPP or dissolved in the oxide. It is possible that after dissolution of Fe and Ni from the SPPs in the oxide layer they may segregate at GBs throughout the barrier oxide even in a metallic form. A drastic increase in HPU would be the result, as these GBs could serve as "freeway" for H transport [109]. An Atom Probe Tomography (APT) study by Sundell et al. [150] experimentally demonstrated Fe segregation in the oxide GBs of Zircaloy-2. Furthermore, they showed that the same GBs are enriched of hydrogen, concluding that they enhance HPU by acting as pathways. It is suggested that hydroxyls and H-bonded water is present in the oxide GBs [82], [109].

In a study of Kuri et al. [131] XANES showed a homogeneous distribution of Ni^{2+} in the oxide layer of a medium burnup Zircaloy-2 cladding. DFT calculations demonstrated that Ni^{2+} is charge compensated by an oxygen vacancy (V_O). The compounds of Ni^{2+}-V_O could offer nucleation sites for hydride-ion (H^-) storage in rows of oxygen vacancies that would eventually short-circuit the barrier layer causing an "avalanche" of hydrogen into the metal. The authors show that the Ni^{2+}-H^- compound could also act as nucleation sites for a build-up of porosity in the oxide.

2.4.2.6. Dissolved alloying elements in the oxide layer altering the diffusion rate of hydrogen species

Many studies have concluded that an important HPU controlling parameter could be the classical diffusion of protons through the oxide matrix influenced by the dissolved alloying elements [110], [141], [151], [152].

Kakiuchi et al. [151] investigated the pre-transition region of Zircaloy-2 and HIFI alloy (high, 0.4 wt% Fe). They used 350 °C and 400 °C steam with 200 ppb O_2 and measured the potential and the HPU. They observed much lower HPUF in the HIFI samples. They concluded that the amount of proton that migrates through the oxide is dependent on the potential gradient through the oxide. With the decrease of the potential gradient the HPUF also decreased. The authors suggested that with additional Fe, the dissolved Fe^{3+} concentration in the ZrO_2 increases causing a higher electron concentration at the barrier layer which reduces the potential gradient.

Une et al. [141] studied three different alloys (Zircaloy-2 samples with 0.18 wt% and with 0.26 wt% (called GNF-Ziron), and a VB sample with the composition of Zr-0.5%Sn-0.5%Fe-1%Cr) in 400 °C steam and in 290 °C 1M LiOH. The measurements showed the same results: increasing Fe content decreased the HPUF of the Zr-based alloys. However, the explanation here was somewhat different: higher amount of dissolved Fe^{3+} in the oxide could decrease not only the potential gradient but the mobility of the interstitial protons therefore decreased HPU. The assumption is that the substitutionally dissolved Fe^{3+} could enhance the formation of defect clusters containing oxygen vacancies and other defects and the concentration of these increases with increased Fe content; while the concentration of electrons decreases [141].

Furthermore, the presence of these defect clusters would supress the mobility of protons through the oxide [141]. Therefore, the controlling parameter for the HPU is the diffusivity of protons in the oxide lattice [141].

The diffusivity of hydrogen and its species is believed to be affected by other phenomena as well, such as high stresses in the oxide and the fraction of tetragonal ZrO_2 (in which the diffusivity is lower). The delayed oxidation of the SPPs in the barrier oxide layer could introduce higher compressive stresses in the oxide which would in turn stabilize the tetragonal

oxide phase. Therefore, SPPs in the barrier layer could decrease the H-uptake of the material by reducing the mobility of the hydrogen. It is important to note that this is contradictory with the other studies, e.g. those presented in Section 2.4.2.4.

In another study of Une et al. [152] the relationship between the H absorption and diffusivity in the oxides were studied on the same alloys as in [141] and on Zr-2.5Nb [152].

The authors suggested that the dissolved Nb^{3+} in the oxide also helps the formation of oxygen vacancies and trapping hydrogen. The higher valence state Nb^{5+} would be dissolved only at the surface region of the oxide. In this case the formation of electronic defects would be energetically favourable and this would increase the electron and decrease the oxygen vacancy concentration [152]. The first could enhance the proton reduction at the surface and reduce the amount of proton entering the material and the HPU [152].

Takahashi et al. [110] studied the effect of the type of SPP on the HPUF in water at 280 °C. The HPUF was measured as 16.1% for Zircaloy-2 containing both Zr_2(Fe, Ni) and Zr(Fe, $Cr)_2$ SPPs; 3.5% for Zircaloy-4 with Zr(Fe, $Cr)_2$ SPPs; and 99.5% for Zr-1.5Sn-0.3Ni having Zr_2(Fe, Ni) SPPs. The Fe/Cr ratio was smaller for Zr(Fe, $Cr)_2$ SPPs that are incorporated in the oxide layer than that in the metal, i.e. during the oxidation of the SPP the alloying elements (especially Fe) diffuse out of the SPPs. The Fe/Cr ratio in the SPPs decreased within the oxide with the prolonged oxidation [110]. Based on molecular dynamics simulations the authors estimated the diffusion coefficient of H^+, H, and H_2 in ZrO_2 with the following results [110]:

1. H^+ has the highest diffusion coefficient both in pure ZrO_2 or if the oxide contains Fe, Cr, or Ni (Figure 2-17).
2. The oxide layer which contains Ni has a significantly higher diffusion rate of hydrogen compared to the oxide containing Fe or Cr (Figure 2-17).

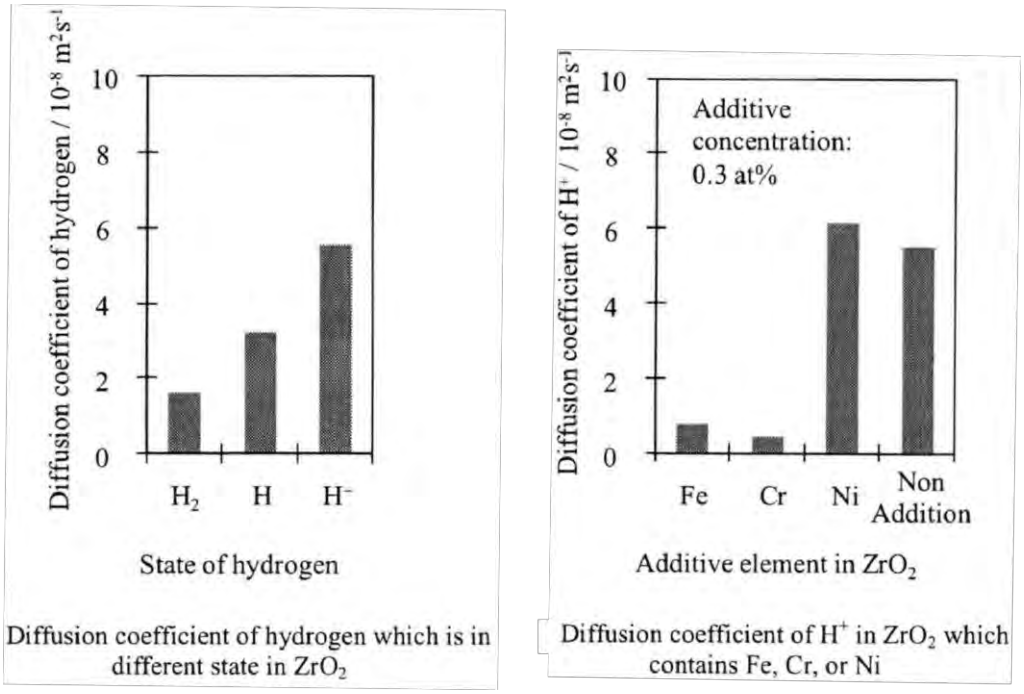

Figure 2-17 Calculated diffusion coefficient of H_2, H, and H^+ in ZrO_2. H+ diffusion coefficinet in ZrO_2 containing Fe, Cr, Ni, or no addition [110].

In a recent study on oxidized Zircaloy-4 (627 °C, 17 hours) it was claimed that dissolved Fe has a significant effect on the formation of defects in the oxide and the clustering of these defects depending on the chemical state of the dissolved Fe [153]. The defect structure was calculated by density functional theory (DFT) while X-ray Absorption Near Edge Structure (XANES) was used for the experimental measurements. XANES revealed the oxidation state of the dissolved Fe in the different parts of the oxide. In the case of a tetragonal oxide, which is more common at the metal-oxide interface it is in state 2+ and oxygen vacancies are bounded with one or two iron substitutional species [153]. A higher Fe concentration could stabilize the vacancies which would result in a reduced mobility of the vacancies. If the main route for oxygen is hopping via vacancies [154], this could lead to a reduced oxidation. In monoclinic ZrO_2 the dissolved Fe was found predominantly as a 3+ state. The calculation showed that this

Fe is defect charge compensated by electrons, and it was also shown that this leads to an increased hole concentration in the oxide. The increased hole concentration results in a build-up of positive charge in the oxide which could prevent the flow of H^+, i.e. reducing the HPU [153]. This suggests that dissolved iron at the outer part of the oxide could reduce the HPU of the material.

2.5. The impact of irradiation on the oxidation and hydrogen uptake – Studies on irradiated and high burnup materials

In the previous sections, autoclave studies without irradiation were presented. The studies on in-reactor irradiated claddings revealed that many aspects of the behaviour are different from the autoclave tests of the same material. The out-of-pile tests do not give an accurate prediction of the material's behaviour in-reactor, therefore studies of in-pile claddings are essential to better understand the properties of the claddings during service.

A short review is given on the differences between in-reactor and autoclave. Then the differences in corrosion and HPU in BWR and PWR is described, followed by the alloy-specific differences in the two reactor types separately. Finally, the current understanding of the reasons behind these differences and behind certain changes during in-reactor service is provided.

2.5.1. Differences between out-of-pile and in-reactor corrosion behavior

The oxide thickness produced in autoclave at the service temperature and in reactor on the same alloy is significantly different. The formed oxide is thicker in BWR and PWR, even in the early

stages of irradiation. A schematic example for PWR is presented in Figure 2-18. It is important to note that the degree of the increased corrosion is alloy-dependent.

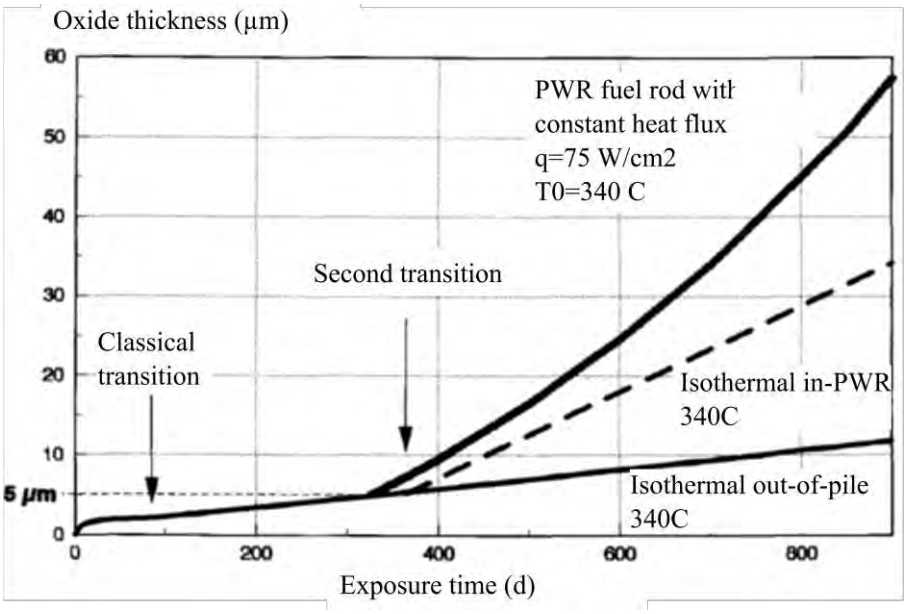

Figure 2-18 Schematic figure for comparison of the oxide thickness of PWR fuel rods with out-of-pile measurements. The Figure is from reference [155]. The drawing is based on in-reactor and out-of-pile measurements ([156], [157]).

The HPUF of a given alloy is sensitive to the environment, therefore it is difficult to directly compare the in-reactor and autoclave studies. However the general trends can be compared. The autoclave tests assume that the HPUF remains constant for oxides thicker than a certain value (7 µm in [60]). Below this limit some variations were observed [60]. An example is shown in Figure 2-19 for the autoclave measurements on different alloys from [60]. This aspect is different in the reactor: a schematic comparison of the in-pile and autoclave (both in oxygenated and hydrogenated environments) trends of Zircaloy-2 and 4 is presented in Figure 2-20 from reference [109] which collected data from [108], [158], [159].

These observations indicate that the irradiation and environment change the material's behaviour. The next section presents some of the parameters influencing the in-reactor performance of a cladding.

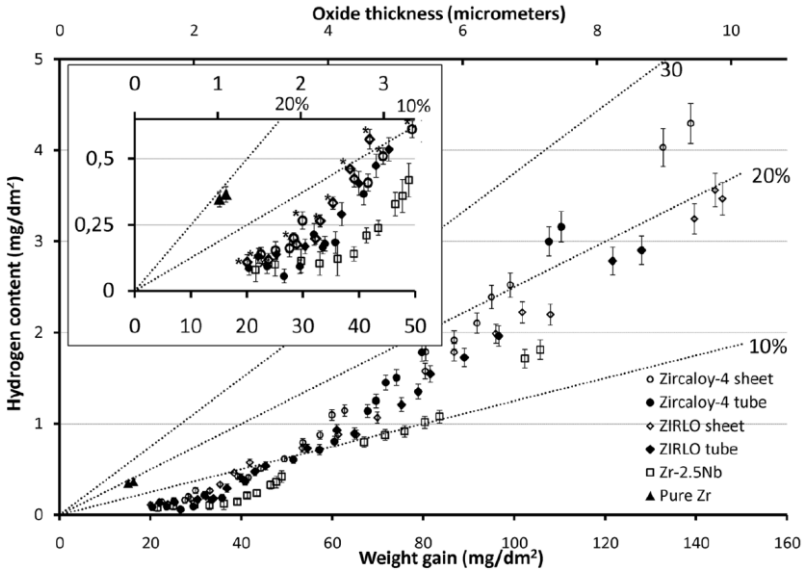

Figure 2-19 Hydrogen content as a function of oxide weight gain in different alloys in autoclave. Dotted lines show the HPUF [60].

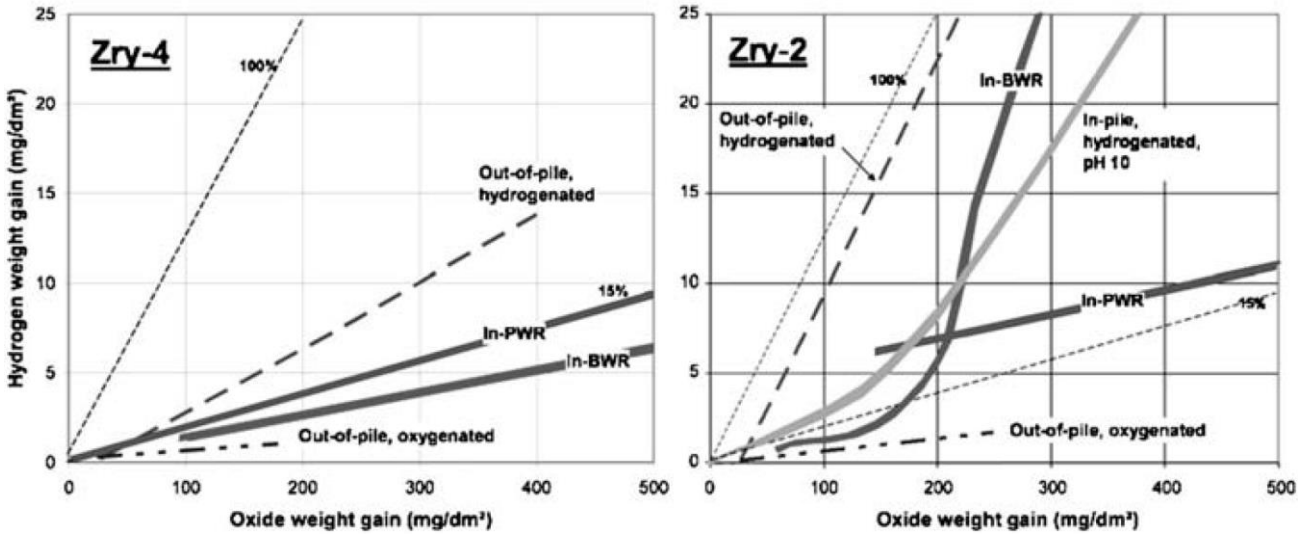

Figure 2-20 Time averaged HPUF of Zry-2 and Zry-4 in different environments from reference [109] which has collected data from [108], [158], [159].

2.5.2. Influencing parameters on the in-reactor behaviour

Besides the composition, the microstructure, and the SPP size distribution of the alloy, the service time of the cladding, the irradiation scheme and type of reactor are also to be considered as behaviour influencing parameters. The water chemistry is another factor that will influence the oxidation and HPU.

2.5.2.1. Type of alloy

The in-reactor performance is highly alloy specific. Also, the same alloy family shows different performance with a slight change in the composition and/or the heat treatment.

Figure 2-21 shows the oxide thickness along the elevation of different Zircaloy-4 type rods. In the Part (A) of that Figure the role of Sn is demonstrated: the purple line shows the conventional Zry-4 cladding containing 1.5 wt% Sn, blue line indicates the same composition with different heat treatment, orange line corresponds to 1.3 wt% Sn content. The red line shows a different alloy (ZIRLO with 1%Sn and 1%Nb). On Part (B) the role of Fe is stressed: the alloy with higher Fe content (purple) shows better oxidation properties. Figure 2-21 indicates that the behaviour of a certain type of cladding is not uniform along the length of the rod. This occurs due to the environmental differences, such as the temperature of the coolant at the different regions as well as the presence of the spacers at certain locations.

Considerable modifications in behaviour occur for completely different alloy types. In Figure 2-21-(A) the oxidation properties of ZIRLO (1 wt% Sn, 1% Nb, 0.1 wt% Fe) is better compared to the Zircaloy-4 type materials. Figure 2-22 shows the trends of the oxide thicknesses formed on different Zircaloy and Zr-Nb claddings. Studies of the PWR materials indicate that Nb-containing claddings display enhanced performance compared to the Zircaloy-4 type claddings.

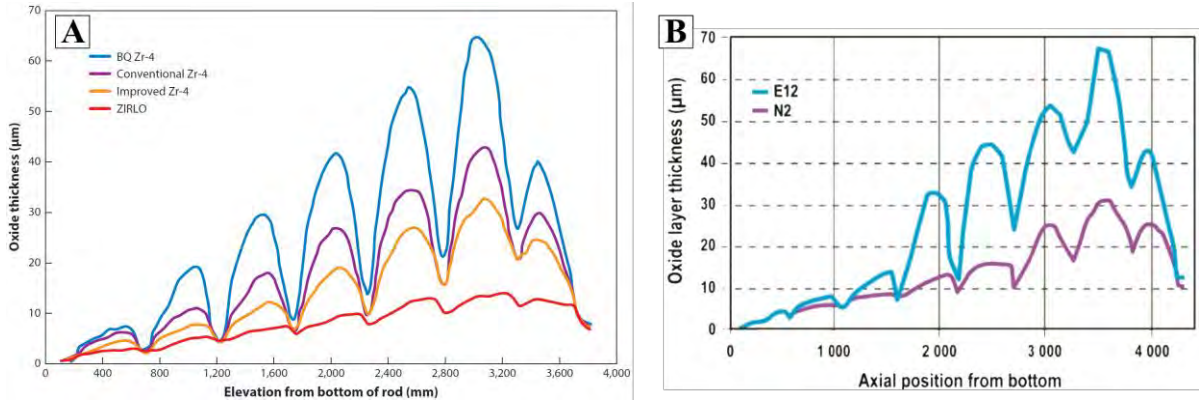

Figure 2-21 Zircaloy-4 rods with slight differences in composition or in heat treatment. (A): different Sn content and/or heat treatment from [59] who adapted data from [160]; (B): role of different Fe content [161]. For details please refer to the text.

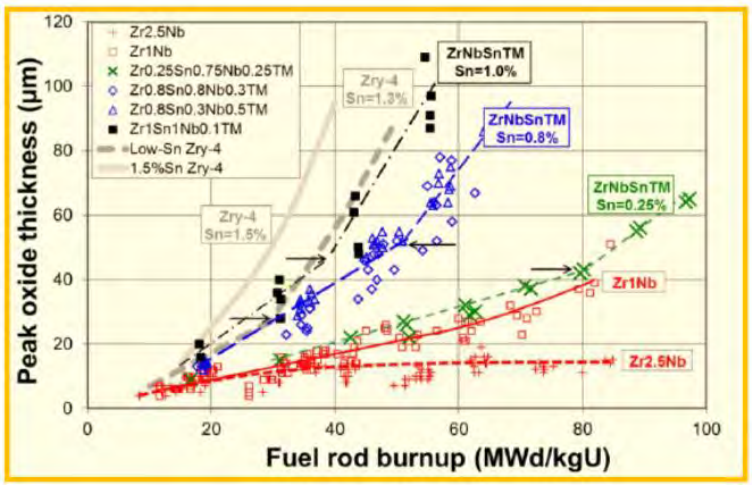

Figure 2-22 Corrosion behaviour of various claddings irradiated in PWR. Image is from [17] which used references [162], [163].

2.5.2.2. Size of the SPPs

Garzarolli et al. [109] reported a clear correlation between the SPP size and the oxidation of the cladding based on several studies from different authors [164], [165], [166]: significantly larger oxide weight gain occurred with small SPPs at higher fluences (Table 2-2 and Figure 2-23). Figure 2-23 shows the oxide thicknesses of irradiated claddings with different SPP sizes. LK2 has the smallest, LK3 has the largest SPPs while LK2+ is in between the other two. The hydrogen content was also reported in the same reference, shown in Figure 2-24:.claddings with smaller SPPs showed higher H content. Based on three Zircaloy-2 samples having same composition but different SPP sizes irradiated above 43 MWd/kgU, Tägtström et al. also reported a strong correlation between the increased HPU and oxidation rate with decreased initial SPP size up to medium burnup [167].

This indicates that the irradiation induced dissolution of the SPPs with different sizes has a significant influence on the alloy's performance.

Table 2-2 Weight gain and HPUF data for irradiated different claddings with various SPP sizes and under different fluences. A burnup of about 40 MWd/kgU corresponds to a fluence of 8.5×10^{21}. The table is from [109] who collected data from [168].

Specimen	*A*-Parameter(h)	Fluence(n/cm^2), $E > 1$ MeV	Average SPP Size(nm)	Weight Gain(mg/dm^2)	HPUF(%)
3R	1.45×10^{-19}	0	42		
2R	7.40×10^{-20}	0	32		
1R	3.46×10^{-21}	0	25		
3R	1.45×10^{-19}	2.5×10^{21}		40	2
2R	7.40×10^{-20}	2.5×10^{21}		53	3
1R	3.46×10^{-21}	2.5×10^{21}		45	2
3R	1.45×10^{-19}	8.5×10^{21}		112	26
2R	7.40×10^{-20}	8.5×10^{21}		204	35
1R	3.46×10^{-21}	8.5×10^{21}		294	25

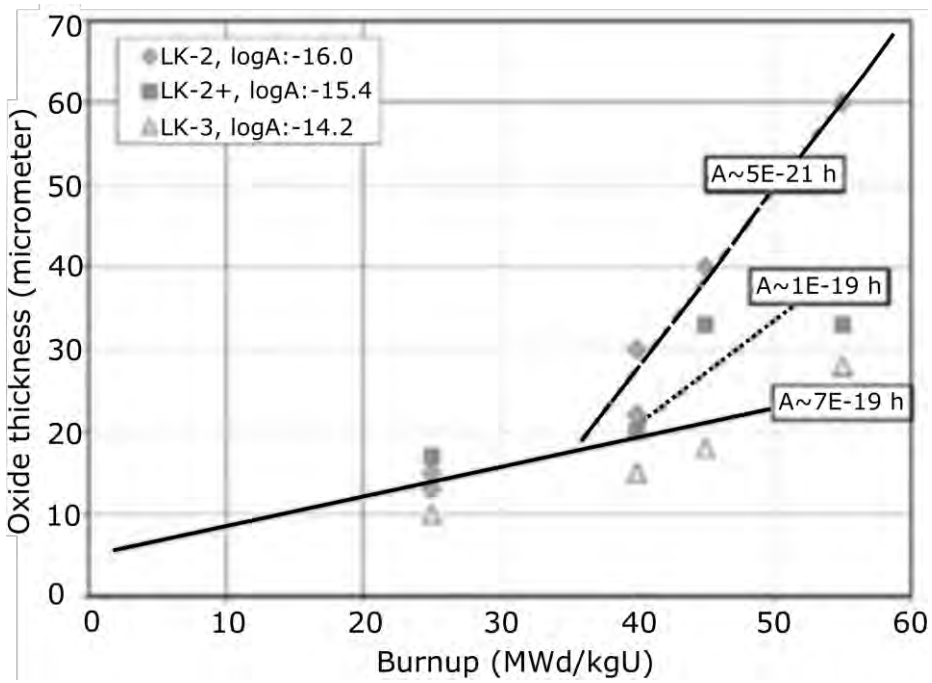

Figure 2-23 Oxide layer thickness of BWR claddings with different SPP sizes which is increasing in the following order: LK2, LK2+, LK3 [109] who collected data from [164], [165], [166].

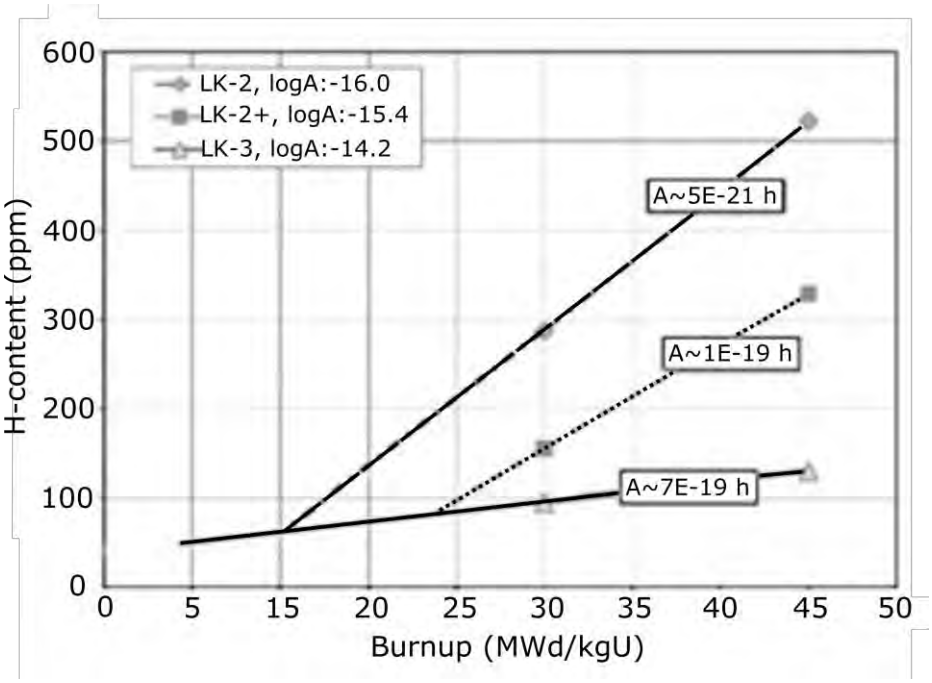

Figure 2-24 H-content of BWR claddings with different SPP sizes which is increasing in the following order: LK2, LK2+, LK3 [109] who collected data from [164], [165], [166].

2.5.2.3. Length of the service time - Burnup

Some alloys show modified behaviour at high burnups, i.e. the late life performance is significantly different from the medium or low burnup regions. The oxidation and the HPU properties can change during the service of the cladding. Previously, Figure 2-22 already indicated that for some alloys (e.g. Zircaloy-4) corrosion increases at high burnups while this is not the case for the Zr-Nb claddings.

Previously it was under debate whether the HPUF remains constant with time for the same alloy in reactor. Detailed characterization, by Abolhassani et al., of a Zircaloy-2 type claddings irradiated in the same reactor for different service times revealed that HPUF can vary with the service time (shown in Figure 2-25) [13]. In order to better understand the late life characteristics of a cladding, the Zircaloy-2 type LK3/L (1.34 wt% Sn, 0.18 wt% Fe, 0.11 wt% Cr, 0.05 wt% Ni) was kept in the reactor for 9 years (or 9 cycles), i.e. for 2 extra years above the designed service time. Dashed lines in the Figure show the calculated HPUF, results show that it is not constant for neither of the claddings. This result indicates that it is difficult to predict the value of the HPUF for a given alloy and only by measurement, it is possible to provide this value.

It is worth noting at this point that this experiment was carried out at PSI previously and it gave the basis of the current PhD thesis to characterize the highly irradiated material.

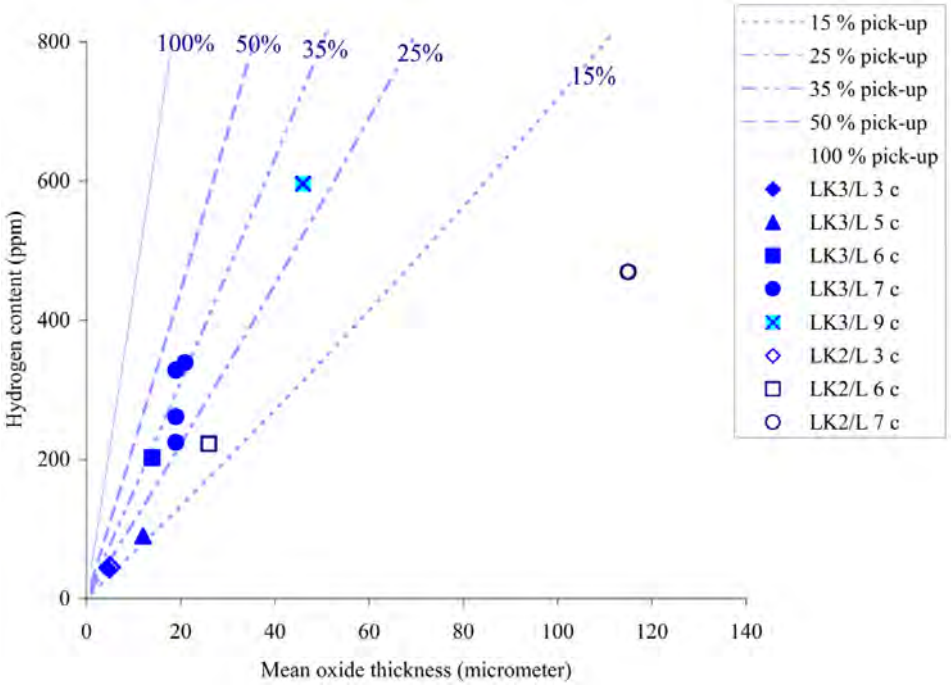

Figure 2-25 Mean oxide thickness and total H-content of LK3/L and LK2/L type Zircaloy-2 claddings irradiated in the same reactor. Dashed lines show the HPUF values. From [13].

2.5.3. Current understanding of the changed cladding behaviour in-reactor

The different parameters responsible for material degradation are described separately however they could occur at the same time during the service. In the present study, only in-reactor materials are examined, therefore the studies on proton and ion irradiation are not reported. Producing data on used claddings is difficult and time-consuming, therefore such data is much scarcer. Especially for the extreme high burnup region, the amount of available samples is quite limited.

First the in-reactor evolution of the SPPs and its effect on the oxidation and HPU is described. This is followed by the microstructural aspects, e.g. the changes in the oxide structure. The present knowledge on the role of the hydride phases is shortly covered.

2.5.3.1. Dissolution and evolution of the SPPs

In the studies of Abolhassani et al [29] and Valizadeh et al [14] the SPP evolution is analysed by TEM in Zircaloy-2 type irradiated claddings. In the following, the results on the LK3/L cladding will be presented.

The list of samples and the SPP analysis by TEM is in Table 2-3 [14]. The results for the 3 cycle sample are in reference [29]. The size distribution of the SPPs after the different stages of irradiation is shown in Figure 2-26: in Part (A) the archive material and after 3 cycles, in Part (B) the 5, 6, 7, and 9 cycle samples. The main conclusion is that the SPP number density decreases significantly with irradiation already after 3 cycles and practically complete dissolution of the SPPs occur at the higher burnup levels. Abolhassani et al concluded that the stability of the SPP can vary with its composition: the lower the Fe:Cr ratio the less stable the precipitate is [29]. This ratio decreases significantly already after 3 cycles (Table 2-4).

The mechanism of the SPP dissolution is discussed in [14]: the Fe-Cr precipitates show amorphization during their dissolution. They show a “duplex structure”: the core of the SPP is crystalline and the periphery is amorphous. This amorphous layer progresses towards the inner core until the SPP is fully amorphized, i.e. at higher cycles and when the Fe:Cr ratio is under around 0.2. This phenomenon is linked to the Fe depletion of the SPP and the depletion may be the cause of the amorphization. The Fe-Ni type SPPs do not show amorphization during dissolution. The study discusses the possible effects of the SPP dissolution (i.e. increased HPU and rod growth) and it correlates the results with the acceleration of corrosion and HPUF of the cladding under service. The study mentions that there seems to be a direct correlation between the Fe depletion of the Fe-Ni type SPPs and the accelerated HPU.

Table 2-3 List of LK3/L samples and the results of their SPP analysis from [14] where s is the standard deviation of the measured population and s_{mean} is the standard deviation of the mean SPP diameter. Sample names are as follows: AEB069-E4 is 5 cycle; AEB068-E4 is 6 cycle; AEB071-E4 is 7 cycle; and AGB108-G6 is 9 cycle LK3/L cladding segments.

Rod ID	Fast Neutron Fluence at Specimen Elevation [10^{21} n/cm^2]	Position of the Specimen Elevation [mm]	Number of Cycles	SPP Diameter				SPP Density [10^{19} m^{-3}]	Number of SPPs	Analysed Volume [10^{-18} m^{-3}]
				Mean [nm]	Median [nm]	s [nm]	s_{mean} [nm]			
Unirradiated	0		0	42	30	32	3.0	6.4	111	1.7
AEB069-E4	10.7	2700	5	59	49	40	4.2	2.2	92	4.2
AEB068-E4	11.6	2700	6	60	52	26	2.6	1.5	100	6.9
AEB071-E4	11.8	2100	7	53	48	28	3.6	1.5	60	3.7
AGB108-G6	17.9	2100	9	80	75	34	5.0	1.0	47	4.9

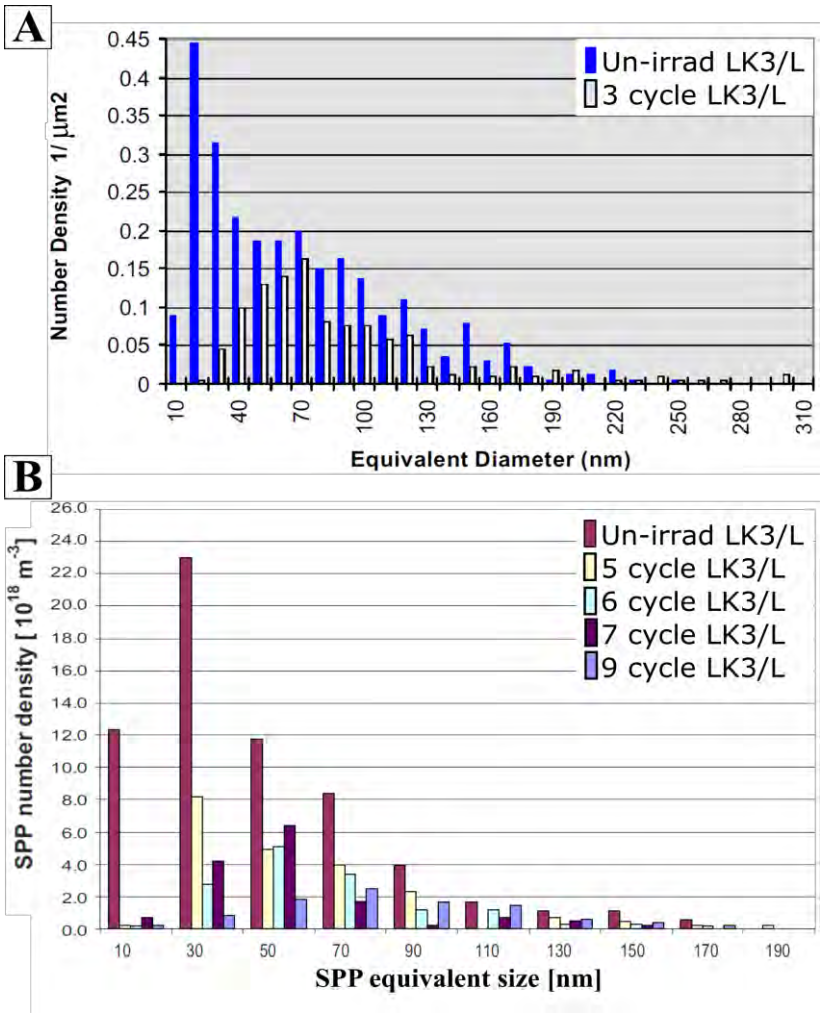

Figure 2-26 The SPP size distribution in LK3/L type claddings. Part (A): un-irradiated sample and after 3 cycles [29]; Part (B): un-irradiated sample and after 5, 6, 7, and 9 cycles [14].

Table 2-4 Oxide thickness, HPU, element ratios of SPPs and other parameters given after different cycles [14].

Rod Identity	Number of Cycles	Rod Growth [mm]	Oxide Thickness [μm]	Rod Av. Metal H2 (ppm)	Hydrogen Pickup Fraction (%)	Fast Fluence [10^{21} n\cm^2]	Average Fe\Ni			Avareage Fe\Cr			Number of Analysed Particles (EDX)
Uniradiated	0					0	max 2.1 min 1.6	1.9	0.8	max 1.1 min 0.7			39
AEB070-E4	3	10.5	5 ± 2	44 ± 2	12.8	5.9	max 1.3 min 0.9	1.5	0.2	max 0.4 min 0.1			15
AEB069-E4	5	12.7	12 ± 2	75 ± 22	12.7	8.7	max 4 min 0.8	1.5	0.2	max 0.4 min 0.1			42
AEB068-E4	6	16.6	15 ± 3	205 ± 4	23.2	9.5	max 4 min 0.8	1.5	0.1	max 0.3 min 0.1			45
AEB071-E4	7	15.34	26 ± 4	327 ± 19	25.6	9.7	max 4 min 0.8	1.6	0.1	max 0.4 min 0.1			40
AGB108-G6	9	28.5	45 ± 7	664 ± 94	30.0	17.9	max 2 min 0.5	1	0.2	max 0.5 min 0.1			33

2.5.3.2. Structural aspects of the oxide layer

The morphology and the composition of the metal-oxide interface of an irradiated Zircaloy-4, low-tin Zircaloy-4 and Zr-2.5Nb samples were compared using TEM [169], [170], SIMS, and EPMA [13].

SIMS results clearly reveal the transition region between the metal and the oxide. As it can be seen from Figure 2-27 the concentration profile of oxygen and other elements from stoichiometric oxide to the bulk metal is different, and the material with an improved oxidation resistance has a larger transition distance [13]. The mass measured as ZrO originates from ionized ZrO_2. The transition thickness was 2 μm for Zircaloy-4 and 2.5-3 μm in Zr-2.5Nb (shown in Figure 2-27). The longer oxygen diffusion path in Zr-2.5Nb was claimed to contribute to the lower HPU and the lower (around 5 times lower) corrosion rate of this cladding.

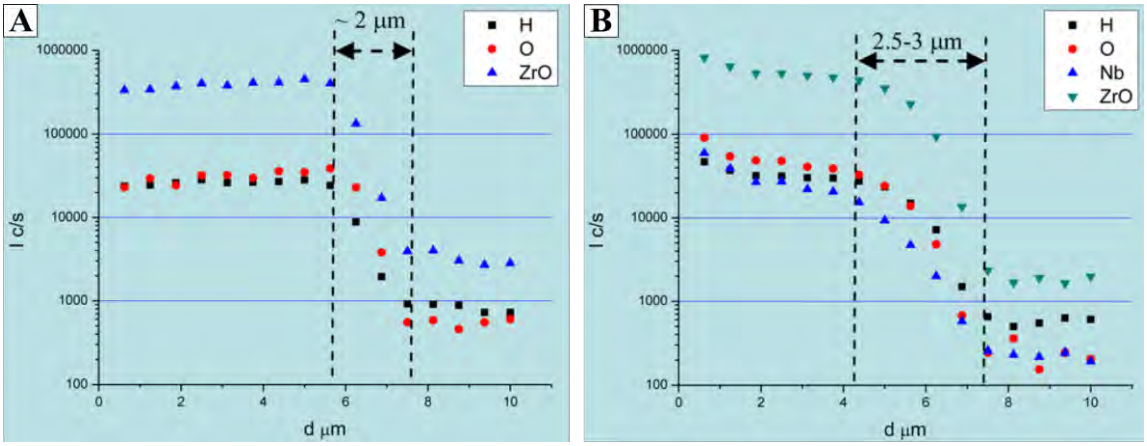

Figure 2-27 SIMS result at the metal-oxide interface of a 4 cycle Zircaloy-4 (A) and a 3 cycle Zr-2.5Nb (B) sample showing the average transition area between the dashed lines [13].

Furthermore the morphology of the metal-oxide interface of the Nb-containing material shows a jigsaw-like structure while the low-tin Zircaloy-4 has a rather straight interface. A jigsaw shaped metal-oxide interface is correlated to a better stress distribution at the interface [13], [169]. It is suggested that metallic Nb in the oxide improves the mechanical properties of the oxide at the interface and that these phases help to stop crack propagation in the oxide [169]. Furthermore, the oxide of the Zr-Nb material showed higher level of sub-stoichiometry at the interface which is clearly associated with the better corrosion resistance [13], [169].

The claddings studied by Abolhassani et al. are the samples that are provided for the PWR sample matrix of this current thesis for further examination.

The role of oxide grain size is another factor that needs to be discussed. If O is diffusing through the grain boundaries, the oxide grain size should play a role on the rate of corrosion. The grain structure and orientations were examined by Garner et al. on two BWR claddings [171]. The orientation maps of the un-irradiated, a 3 cycle LK3 and a 6 cycle LK2 Zircaloy-2 in TEM are shown in Figure 2-28. The LK3 sample has 4 µm oxide thickness, while LK2 has 108 µm.

Columnar oxide grain structure was found before irradiation (grain length: 200-300 nm, width: around 50 nm). The 3 cycle Zircaloy-2 cladding shows larger amount of equiaxed grains with 100-200 nm and a much finer grain structure is revealed for the 6 cycle Zircaloy-2 sample (50-100 nm). The authors note that due to the difference in the cladding grade types, the modification of the grain structure cannot be solely attributed to the service time in the reactor but the differences in the SPP size could also play a role [171]. The authors conclude that the results indicate some modifications in the process of oxide growth and nucleation in BWR. The finer grain structure could result in increased porosity which in turn could increase the oxidation.

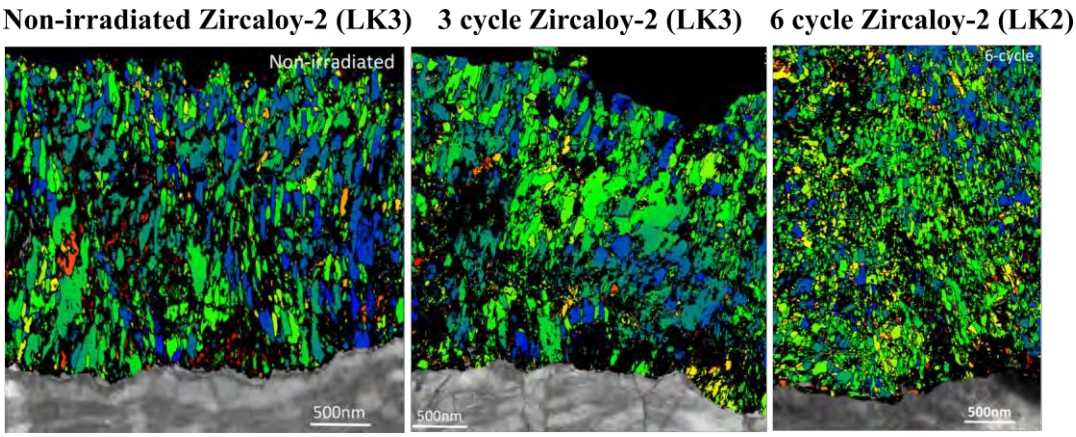

Figure 2-28 Automated crystal orientation maps of un-irradiated and irradiated Zircaloy-2 (LK3 and LK2) samples. The axial section of the samples is shown. From [171].

Bossis et al. studied the corrosion of PWR irradiated materials, such as low-tin Zircaloy-4 and M5 [172]; Zircaloy-4 and Zr-1Nb-O claddings [173] with many different microscopy methods (e.g. SEM. XRD, TEM). Among other factors, the micro-crack formation and its possible causes were described.

They concluded that low-tin Zircaloy-4 oxide shows a modification in the cracking behaviour with time while in the case of M5 there is no sign of change in the corrosion mechanism. It

shows periodic sublayers with the same thickness. A modified crack distribution occurs in the oxides formed at high burnups (59-70 GWd/t) on Zircaloy-4: the outer 20-30 μm of the oxide shows periodic circumferential crack distribution but the rest of the oxide has less noticeable periodicity with smaller cracks. The authors suggest that this phenomenon is linked to the accelerated corrosion of this cladding at higher burnups. Others also observed connection between the crack distribution and the corrosion kinetics: [71], [76], [174], however these are autoclave studies. Bossis et al. discuss other factors that could be responsible for the accelerated corrosion (i.e. the presence of preferential sites for crack formation; Sn content) [172]. Furthermore, the authors claim that the significant difference in the behaviour of M5 and Zircaloy could be caused by the difference in their site of proton reduction: close to the metal-oxide interface for Zircaloy-4 (i.e. metallic SPPs) and at the oxide-water interface for M5 (Nb^{5+} in the outer oxide) [172].

2.5.3.3. The effect of the hydride phases

The influence of the hydride precipitation on the accelerated corrosion of Zircaloy-4 is also discussed in reference [172]. At the interface a hydride rim is present with high concentration of hydrogen. Other studies found a connection between the presence of a massive hydride rim and the modifications in corrosion kinetics in autoclave [15], [175], [176], [177]; and only limited information is available for in-reactor influence [178]. It is revealed that high concentration of hydrogen at the interface region results in a finer crack distribution and more crack-free veins in the oxide [172]. It is concluded that the accelerated corrosion could be the result of the presence of the hydride phases [172]. Only the studies of [15] and [178] discuss the possible mechanisms that how could the hydrides influence the cracking of the oxide. It is claimed that the hydride phases oxidize faster [179], and this is one possible factor leading to an overall acceleration of corrosion [178]. It is also possible that the tetragonal to monoclinic

transformation of the oxide would be assisted by the hydride precipitates [178], as the part of the tensile stress, which is induced in the metal substrate due to the volume expansion of a forming oxide, would be relieved by the formation of hydrides [175] due to the volume expansion of the metal when a hydride forms. This, in turn would relax the compressive stress on the oxide layer. As the tetragonal oxide is stabilized by the stress in the oxide at the metal-oxide interface [180], the reduction in this stress would lead to the enhanced transformation of the tetragonal phase to monoclinic phase, or even to the formation of monoclinic phase only [178]. Due to the volume expansion during the tetragonal to monoclinic transformation pores in the oxide could be generated. This could lead to the loss of protective layer and therefore could increase the corrosion [178]. The authors claim that the accelerated corrosion that was observed in the Ziraloy-2 alloy would increase towards higher burnups. The explanation could be the following: it is expected that the amount of hydride precipitates at the metal-oxide interface would increase t with longer service time. This would lead to more sites at the metal-oxide interface where the stress relaxation of the oxide can occur (i.e. the authors claim that the amount of hydride phases at the interface is proportional to the stress relaxation of the oxide) [178].

2.5.4. Short summary on the impact of irradiation and the objective of this study

Despite the increasing amount of information on irradiated claddings, the main factors that influence the HPU and oxidation in-reactor are still to be further explored. For example there is very limited data available on extreme high burnups materials where these processes may be very much enhanced.

On the accelerated corrosion of some of the PWR type claddings only few papers were found. No literature was found on high burnup BWR cladding studying the increased oxidation and the impact of oxide microstructure, and searching for the effect of hydrides at the high burnup region.

There is a lack of information on the comparison of medium and high burnup samples both from BWR and PWR in order to search for generalities between the two types of claddings and their behaviour. Also, in general, when the cracks and hydrides of the irradiated materials are characterized the used microscopy techniques observe only the surface of the sample and provide two-dimensional information. There is a possibility to use methods providing information in three-dimension where the different objects and phases of the cladding could be characterized in space and more detailed information can be extracted, such as the spatial relationship between the different objects.

The main focus of the current thesis is on the detailed characterization of a 9 cycle BWR cladding (i.e. extreme high burnup) by means of different analytical techniques. This work aims to contribute to the further understanding those processes that occur at extreme high level of burnup. Subsequently the work is supported with the characterization of other, lower burnup samples from BWR and the comparison to different types of claddings from PWR. Results are presented in the thesis with the aim to search for some generalities in the hydrogen uptake behaviour between the different cladding materials.

It must be mentioned that despite the fact that many studies have led to conclusions in form of hypothesis, the actual causes behind many observation is still to be determined. The aim of this thesis is to perform in-depth chemical and structural analysis of the specific claddings and attempt to explain the observed phenomena.

3. MATERIALS AND CHARACTERIZATION METHODS

In this chapter the materials investigated and the methods used for characterization are presented.

3.1. Materials

The materials used in this study have been selected with the aim of comparing the cladding behaviour (i.e. HPU and oxidation properties) in different conditions such as:

i. The same alloy in the same reactor environment with different cycles[2] (i.e. service time in the reactor): 3, 6, 7 and 9 cycle Zircaloy-2 from BWR.

ii. Different alloy composition in the same reactor environment with similar service time: 3 cycle Zr-2.5Nb and 4 cycle Zircaloy-4 from PWR.

iii. Different reactor environments with slightly different alloy composition with similar service time (e.g. 3 cycle Zircaloy-2 in BWR and 4 cycle Zircaloy-4 in PWR). It is expected doing so, to separate the reactor- and material-specific behaviours from those that are general processes.

The Zircaloy-2 samples are from the same cladding grade (LK3/L), from the same reactor and the elevations of the segments is also very similar. Therefore, it is possible to describe the behaviour of the LK3/L cladding grade at mid-span elevation in the BWR condition. However,

[2]Each cycle is 11 months, in the reactors studied in this project and the reactor being down for service for approximately one month per year.

the statements and conclusions based on the LK3/L samples would not be necessarily valid for other materials with different compositions and different reactors.

Therefore, in order to have a complete overview and understanding; other Zr-based alloys, from PWR, have been also characterized and the results have been compared with each other.

The aim is to see whether the different phenomena are present in all the alloys and are general or the observed behaviour is rather specific to the given alloy and condition.

Two types of PWR alloys, namely Zircaloy-4 and Zr-2.5Nb, from the same reactor have been also investigated. The details about each of the cladding and their compositions of the materials is given in the following sections.

3.1.1. Zircaloy-2 - Grade of LK3/L

Zircaloy-2 samples with LK3/L grade have been studied. The cladding material is designed by Westinghouse Electric and the designation "/L" indicates that the fuel cladding has an inner liner to enhance the Pellet-Cladding Interaction (PCI) resistance [181]. All samples have experienced the same reactor environment, namely they have served in the Swiss KKL (Kernkraftwerk Leibstadt) [182], which is a BWR type reactor.

The composition of the LK3/L material and heat treatment parameter is provided in Table 3-1.The exact steps of the heat treatment process are usually not open to the public, instead a parameter is provided to specify the treatment. This parameter is the cumulative annealing parameter and it is described as $A = \sum t_i e^{\frac{-Q}{RT_i}}$ [30], [31], where i is the i^{th} heat treatment (after the last β-quench) at T_i (K) temperature for t_i (h) time, R is the gas constant and Q is the activation energy for precipitate growth [31], here equal to 63 000 cal/mol [32], [29].

Samples served 3, 6, 7 and 9 cycles in the reactor have been studied in order to have an

overview of the microstructural and chemical changes of the material at different stages of the residence time. The weight gain and HPU data for several claddings with different residence times have been already measured by Abolhassani et al. [13] and are given in Table 3-2. The un-irradiated material has been investigated as well in order to observe the initial status of the material before irradiation. In Table 3-3 the elevation of the investigated claddings are summarized.

Table 3-1. The composition of the LK3/L fuel rod with Zr as balance [13].

LK3/L composition	Sn	Fe	Cr	Ni	Fe+Cr+Ni	O (ppm)	Si (ppm)	log A
wt%	1.34	0.18	0.11	0.05	0.34	1320	70	-14.2
at%	1.02	0.29	0.19	0.077	0.557			

Table 3-2. Measured data showing the oxide thicknesses and hydrogen content of the LK3/L cladding after different service times [13].

Number of cycles	Peak burnup (MWd/kgU)	Segment elevation for oxide thickness measurement (mm)	Mean oxide thickness (μm)	Segment elevation for H_2 measurement (mm)	Total hydrogen content (ppm)
3	44.6	2005	4.4 (±0.7)	2002	44
5	59.6	2005	12	2002	90
6	66.9	2005	14	2002	202
7	67.4	1998	19 (±1.4)	2004	261
7	67.6	1995	21 (±0.9)	2000	339
7	73.3	1998	19 (±2.3)	2004	328
7	73.0	1998	19 (±2.3)	1995	224
9	89	2039.5	46 (±2.5)	2045	595

Table 3-3. Parameters of the different LK3/L materials investigated in this study.

*** TEM sample only.**

Residence time (cycle)	Segment elevation (mm)
3	2011
6	2014.5-2019
7*	1928
9	2039

3.1.1.1. 3 cycle LK3/L sample

This material has been selected in order to investigate the cladding at a medium burnup. During the study the 9 cycle cladding material has been characterized first and based on the results the 3 cycle sample has been selected as a proper candidate for answering the questions that arose. For this reason the microstructure, the chemistry, and the morphology of the oxide, the metal, and the metal-oxide interface of the two materials have been compared. EPMA, TEM and 3D reconstruction have been carried out on this sample.

3.1.1.2. 6 and 7 cycle LK3/L samples

Two samples after high burnup stage have been studied. A 6 and a 7 cycle sample have been selected for EPMA and TEM measurements, respectively. It is worth mentioning that usually the cladding is removed from the reactor after 6-7 cycles.

3.1.1.3. 9 cycle LK3/L material

In order to examine an extremely high burnup cladding material a 9 cycle sample has been selected for a full characterization (i.e. EPMA, TEM, and 3D reconstruction). This fuel rod has a special irradiation scheme: it has been irradiated for 6 cycles, after which it has been stored in the pool side for one cycle, and subsequently irradiated for 3 further cycles (see Figure 3-1)

[33]. This is an important aspect to be taken into account when evaluation the data of this cladding. It must be mentioned that rods with such long residence times are produced very rarely to examine the material behaviour in extreme conditions [33]. Therefore, the full characterization (i.e. EPMA, 3D reconstructions, TEM studies) of this material was one of the main aims of the study and there will be a more detailed description on the 9 cycle sample compared to the other cycles.

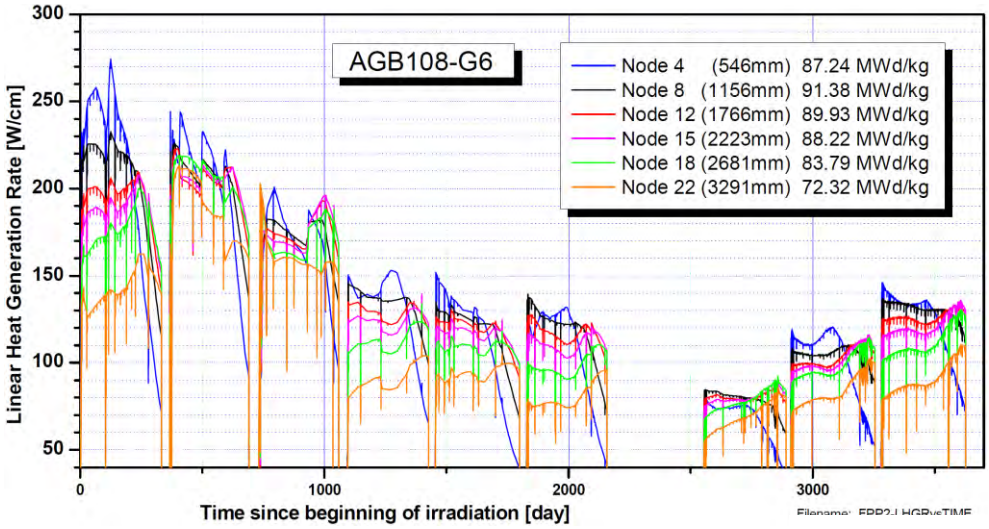

Figure 3-1 Typical power history of the 9 cycle LK3/L cladding showing six different elevations (here called nodes) [33]. The local burnup is provided in the inset for each elevations.

3.1.2. Low-tin Zircaloy-4

Table 3-4 shows the composition of the low-tin Zircaloy-4 material designed by Framatome GmbH. Compared to the LK3/L Zircaloy-2 material, this cladding contains less Sn, slightly more Fe and Cr and does not contain any Ni. This material is used in PWRs.

Table 3-4. Composition of the low-tin Zircaloy-4 fuel rod with Zr as balance [13]. HT: heat treatment; SRA: stress relieve annealed.

Composition	Sn	Fe	Cr	C (ppm)	O (ppm)	H (ppm)	HT	SPP mean size (nm)
wt%	1.20	0.22	0.107	140	1730	8	504°C SRA	190
at%	0.914	0.356	0.186					

3.1.2.1. 4 cycle low-tin Zircaloy-4 material

A cladding segment has been investigated after 4 cycles of service time of the cladding in the PWR type KKG "Kernkraftwerk Gösgen" reactor. Further parameters regarding this sample and the oxide thickness and HPUF can be found in Table 3-5 and in Table 3-6 respectively. The H content and oxide thickness vary along the rod elevation due to the gradient of the coolant temperature from the bottom of the rod (lowest T) to the top (highest T). Interestingly in the case of this rod the hydrogen content increases with oxide thickness and the HPUF shows little variation for the segments studied, which are not in the spacer. Electron Probe Micro-Analysis (EPMA) and 3D FIB tomography have been carried out on this sample.

Table 3-5. Parameters for the 4 cycle low-tin Zircaloy-4 segment [13].

Residence time (cycle)	Segment elevation (mm)	Rod maximum oxide thickness (µm)	Burnup (MWd/kgU)
4	1468	59	51.1

Table 3-6. Oxide thickness and H content data for the 4 cycle low-tin Zircaloy-4 rod [13].

Rod elevation (mm)	Oxide thickness (µm)	Hydrogen content (ppm)	HPUF (%)
353	7.5	52.2 ± 5	~15
1561	25	209 ± 19	~19
2525	44	367 ± 31	~19
3120	56	460 ± 44	~18

3.1.3. Zr-2.5Nb

Table 3-7 shows the composition of the Zr-2.5Nb cladding produced by Framatome GmbH. The rod is from the same reactor as the low-tin Zircaloy-4, namely from KKG and the parameters regarding its burnup, oxide thickness and H content are presented in Table 3-8.

Table 3-7. The composition of the Zr-2.5Nb. HT: heat treatment; PRX: partially recrystallized condition [13].

Composition	Nb	Fe	Si (ppm)	C (ppm)	O (ppm)	H (ppm)	HT
wt%	2.5	0.07	60	180	1170	10	500°C PRX
at%	2.438	0.114					

3.1.3.1. 3 cycle Zr-2.5Nb sample

The studied cladding segment is from a rod which served 3 cycles in KKG. The parameters of this segment are presented in Table 3-8. EPMA and 3D reconstruction have been carried out on this sample.

Table 3-8. Parameters of the analysed segment and for the full Zr-2.5Nb rod [13]. *From one data point.

Residence time (cycle)	Segment elevation (mm)	Burnup (MWd/kgU)	Rod max oxide thickness (μm)	Rod available data for H content (ppm)
3	869	41.4	16	70*

3.2.Characterization Methods

3.2.1. Scanning Electron Microscopy and Focused Ion Beam tomography

For this study a Zeiss NVision 40 dual-beam FIB/SEM system with a field emission gun (FEG) has been used in Paul Scherrer Institute for imaging, TEM sample preparation and also for focused ion beam (FIB) tomography. This FIB system uses Ga^+ source and can be operated from 5 keV to 30 keV, and from pA to nA range, respectively. A high current ion beam is typically used to cut and mill the sample while a low range of FIB current is used to polish the sample or deposit different materials (e.g. Pt, C). Alternating FIB cutting and SEM imaging enables the acquisition of a stack of images from a volume of material. These images can be used to reconstruct the 3D microstructure of the material, using adapted software. This is the principle of the FIB tomography.

During the study ImageJ 1.50 and Avizo 9.2.0 were used to reconstruct the 3D microstructure. In the following subsections a more detailed description about both the experimental and the computational procedure will be given.

3.2.1.1. Experimental procedure of the FIB tomography

The slice-and-view process starts with the selection of the area (or more correctly the volume) of interest on the sample. After this step, Pt is deposited on the site of interest in order to avoid any damage that could be caused by the ion beam. Briefly, the types of damage due to Ga ion are i) ion implantation which modifies the chemistry of the region and ii) to some extent the irradiation damage at the surface and the surfaces such as amorphization. The role of contamination from the atmosphere of the FIB chamber and in particular artefacts induced by

the FIB sample preparation, including hydrides observed at the surface of the sample, have been studied recently [183]. In order to avoid any artefacts in this study, care has been taken to observe hydrides in the SEM prior to cutting and to keep the conditions similar, to be able to compare results with one another. In the next step, the surrounding area is removed and the so called trenches are created around the volume of interest, by gradually reducing the milling current towards the volume of interest. Table 3-9 shows the currents which have been applied before and during the slice-and-view process. Once the selected cube is ready to be studied, the serial sectioning can start. This step is also destructive for the cube of interest: using the FIB consecutive slices are removed from the sample and each slice is followed by the acquisition of an image by SEM on the surface of the freshly cut cross-section (shown in Figure 3-2). Many detectors (e.g. SE, BSE, EDS) can be used depending on the objective of the measurement. In this study either SE or BSE images have been acquired.

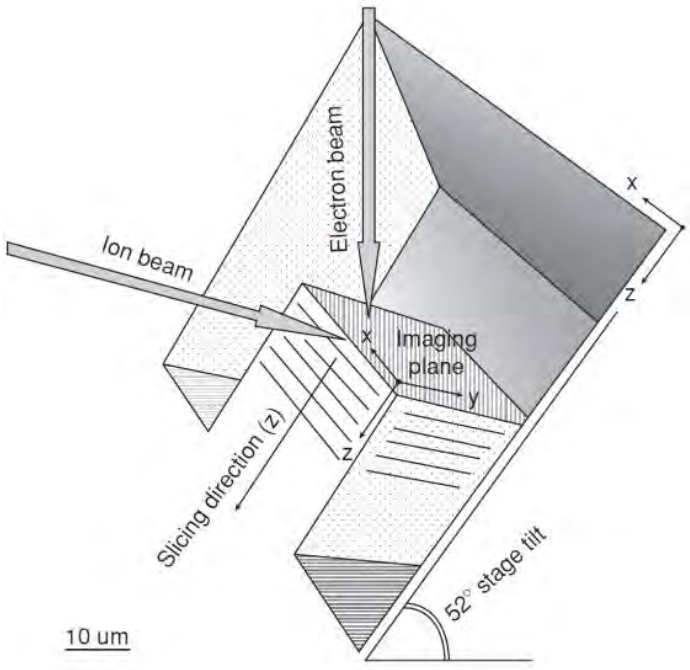

Figure 3-2. Illustration of the slice-and-view method [184].

Table 3-9. The sequential milling currents applied during the rough mill and slice-and-view. A 30 kV FIB gun voltage was applied throughout the process.

Distance from the edge of the deposited area (μm)	Applied milling current
4	13 nA
3	6.5 nA
1.5	3 nA
0.5	1.5 nA
0	700 pA
During slice-and-view	300 pA

3.2.1.2. Computational process of the FIB tomography

In order to reveal the 3D microstructure of the different sites of the samples, in the case of the 3 and 9 cycle LK3/L materials ImageJ 1.50 image processing software and its plugin TrakEM2 have been used on the acquired image stack. In the case of the 6 cycle LK3/L, the low-tin Zircaloy-4, and the Zr-2.5Nb materials Avizo 9.2.0 programme has been used. Furthermore, in order to be statistically more meaningful, two of the samples have been re-examined and the slice-and-view on a new area of the sample and subsequent 3D reconstructions have been repeated. These results were also reconstructed using Avizo 9.2.0 programme. For the sake of continuity and validity of comparison, one set of data was checked with both software and the differences were minimal.

The computational process starts with the alignment of the images. It is necessary due to any image shift, or if the sample was drifting during the slice-and-view process. Either automatic or manual alignment of the images can be applied. In both of the cases there are more alignment options (e.g. automatic: using a gravity centre, automatic optimization of a quality function, edge detection based alignment; manual: translation of the slices manually, or defining

landmarks on the images). In general, the automatic alignment options did not give the expected result for the images obtained from the cladding samples. Therefore, during this study, mainly manual or semi-automatic (landmarks) alignment has been used. When it was possible, first the automatic image alignment was applied and further fine alignment was carried out manually.

The segmentation and labelling of the images (i.e. identifying and separating the different objects – for example the cracks in the oxide from the oxide matrix – in the images) is the next step of the reconstruction. There are some options for automatic segmentation but for this the objects of the images and the brightness-contrast difference between different objects have to be easily distinguishable. Segmentation has been carried out manually in those cases where ImageJ was applied. In those reconstructions where Avizo was used, either manual or automatic segmentation was employed depending on the contrast-brightness differences of the objects. However even in those cases where automatic procedure was possible, a following manual interaction was needed in order to correct the wrongly segmented group of pixels. As an example, during the slicing of the oxide, most of the times the "curtaining effect" is visible below the cracks (see Figure 3-3). These wavy traces, having a pixel value very close to cracks' pixel value, they will be automatically selected together with the cracks. This can be corrected manually. Figure 3-3 shows the labelling of an SEM image at the metal-oxide interface in the case of the 3 cycle material: the objects with green colour are labelled as cracks and the transparent pink colour is associated with the oxide matrix.

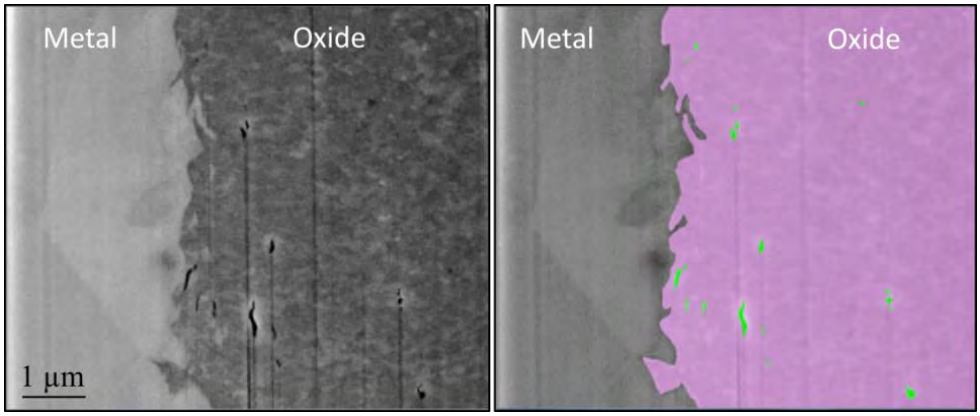

Figure 3-3. An example for the acquired SE images (left) and the segmentation and labelling of the image (right). On the segmented image, cracks are labelled as green, while the oxide matrix is shown as transparent pink.

After every object is correctly labelled on all the collected images, in the last step the visualization of the 3D volume is done by generating meshes automatically. It is possible to measure the volumes of different objects. However, it must be mentioned that several factors could cause some errors in the determination of these calculated or allocated volumes. Some of these are listed as follows:

(1) error of the estimation of the slice thickness cut by FIB,

(2) error due to the destructive nature of the method (i.e. fine features or objects present between the two consecutive layers are removed and not accounted for, fine changes in the shape of the objects),

(3) limitation due to the resolution of the SEM images,

(4) error during segmentation of the images (e.g. overestimation or underestimation of the contours of an object),

(5) possible modification of microstructure by ion beam.

3.2.2. Electron Probe Micro-Analysis

Electron Probe Micro-Analysis (EPMA) provides quantitative and qualitative measurement of the chemical composition on microscopic scale. Focused electron beam is applied for the imaging and for the interaction with the sample and Wavelength Dispersive Spectroscopy (WDS) is used for the accurate chemical analysis of the characteristic X-rays. The EPMA system takes the advantage of analysing crystals which preferentially diffract a chosen wavelength from the X-ray signal coming from the sample towards the detector (proportional counter). The basic principle of the EPMA is shown in Figure 3-4. The advantage of this technique compared to those which utilize Energy Dispersive Spectroscopy (EDS) is that the resolution of the WDS is significantly higher therefore overlap of the peaks can be avoided, and even trace elements can be measured. However, this process is slower than EDS, as here only one wavelength (i.e. energy) can be detected at any single time.

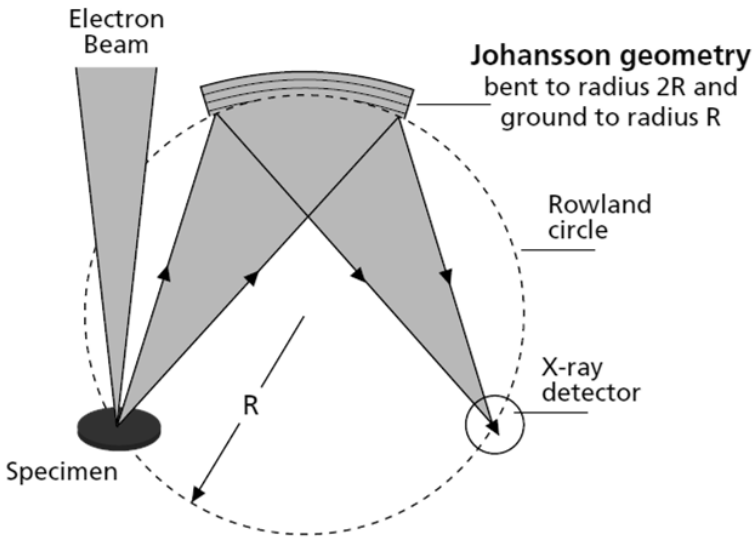

Figure 3-4. Schematic drawing showing the basic principles and the geometry used in the EPMA [185].

A JEOL JXA-8500F EPMA with a FEG has been used in this work. All measurements on Zircaloy type samples were obtained using the K_α signal of O, Cr, Ni, Fe, and L_α signal of Zr and Sn and in the case of the Zr-2.5Nb sample L_α of Nb. Table 3-10 shows the detailed parameters of the crystals used for the detection of different elements. The following parameters were used during the different type of EPMA analyses:

- Point measurements for local information (e.g. SPP or hydride concentration; or concentration changes across the metal-oxide interface) have been carried out using the smallest beam size at 15 kV acceleration voltage and at 240-260 nA probe current (about 100 nm beam diameter). Quantitative point analyses were performed in the metal and in the oxide (precision of the analysis is given in Table-AII 1 in Appendix II).
- A larger, 2 μm beam diameter (selected from the software settings) has been used for the rest of the point measurements when an average concentration information was satisfactory (e.g. long line scans in the bulk metal). Here as well, 15 kV accelerating voltage and 240-260 nA beam current was applied.
- The spot size at 15 kV accelerator voltage and beam current of 240-260 nA was selected during all elemental maps. The spatial resolution of the elemental maps is 200-300 nm.

The beam diameter at different conditions as well as the elemental map resolution is estimated based on the machine specifications given by the producer and on the data available in the literature (e.g. [186]). The maps are only qualitative analysis to represent the distribution information about each element in the material. Therefore, it is worth mentioning that different maps cannot be compared on a quantitative basis. All point analyses are quantitative and the results are normalized.

Table 3-10. The crystals used for element detection during EPMA measurements and their parameters. The k-value is the reflective index of the given crystal.

Crystal	Name	Formula	Orientation	2d (Å)	k	Approx. range (Å)	Measured elements
LIF	Lithium fluoride		200	4.0267	0.000058	0.8-3.0	Zr, Sn
PET	Pentaerythritol	$C(CH_2OH)_4$	002	8.75	0.000144	2.2-7.1	Cr, Fe, Ni, Nb
PC1 or LD1		W-Si		60	0.010000	25-80	O

3.2.3. Transmission Electron Microscopy

Throughout the study two different types of TEMs have been used: a JEOL JEM 2010 for imaging and crystallography study and an FEI TALOS F200X for EDS measurements using its so called "ChemiSTEM". The measurements on the first microscope have been carried out at PSI and the latter one was used at the University of Birmingham and at ETH Zürich. All the TEM experiments were performed with the acceleration voltage of 200 kV. The JEOL JEM 2010 is equipped with a LaB_6 cathode and an INCA EDS system of Oxford Instruments. The FEI TALOS F200X TEM is equipped with a brighter X-FEG gun and with 4 EDS detectors in order to achieve high speed chemical measurements (e.g. element maps and line scans).

3.2.3.1. Sample preparation procedure for TEM studies

The TEM measurements require a thin foil sample with a thickness between 50-100 nm. For this study samples approximately 100 nm thick have been prepared by the ZEISS NVision 40 system. After choosing the area of interest (AOI), the selected region was covered (or both Pt and C) with 1-2 μm thick Pt layer deposition and – depending on the size which is required for the study – the area selected for Pt deposition was around 10x3 μm^2, the deposition was

performed with 5 pA/μm^2 FIB current. The surrounding area from the three sides of the AOI has been removed using the FIB with decreasing currents (same as presented in Table 3-9). The depth of the cut also depends on the type of sample observed and can be in the range of 5 to 10 μm. The next step is to cut the bottom of the ~3-4 μm thick lamella free. For this the sample has to be tilted by around -10° and an L-shaped cut using 1.5 nA FIB current has to be carried out. Subsequently the lamella is transferred to a TEM sample grid using the Kleindiek micromanipulator: after the needle is almost touching or touching the free side of the lamella, Pt is deposited on the touching area on both the sample and the needle. Once the sample and the needle are stably attached to each other, the other side of the lamella is also cut so that the lamella is free. Then the bulk sample is displaced and the TEM grid is brought under the micromanipulator needle, the micromanipulator is moved close to one of the fingers of the grid and touches it with the free side of the lamella. This side is attached to the finger of the grid in the next step by Pt deposition. Finally, the Pt weld between the needle and the lamella is cut by the FIB. The successful transfer is followed by further thinning of the lamella from the initial thickness of 3-4 μm to 1.5 μm using the range of the middle level FIB currents (see in Table 3-11). Between the thickness of 1.5 μm and 100 nm (i.e. to the final size) a range of the low currents are used (Table 3-11). In the final step the lamella is polished by a gentle beam with low acceleration voltage and low currents. All milling sequences always have to be repeated on both sides of the lamella. After this sample preparation, the TEM examination of the lamella is possible if the quality of the lamella is good.

Table 3-11. The currents used during the TEM sample preparation. *Short milling, about 30-40 s on each sides. **About 100-120 s on each sides. * With low magnification (1000-2000 x), full image, fast scanning about 120-180 s on each sides.**

Distance from the edge of the deposited area (μm)	Used milling current and accelerator voltage
Step 1 – Rough cuts (All with 30kV)	
7	27 nA
3	13 nA
1.5	6 nA
1-0.5	3 nA
Step 2 – Fine cuts (All with 30kV)	
0 (On the thick lamella)	700 pA
	300 pA
	150 pA
	80 pA
	40 pA
Step 3 – Final polishing and cleaning	
0 (On the thin lamella)	300 pA – 10 kV*
	20 pA – 5 kV**
	60 pA – 2 kV***

4. LK3/L TYPE ZIRCALOY-2 – PART 1: MICROSTRUCTURAL CHANGES IN THE OXIDE AND THE METAL

4.1. Introduction

The LK3/L Zircaloy-2 sample was characterized in details, therefore the microstructural and compositional results are presented in two chapters. However, the two parts are complementary to each other and should be considered together.

The normal service time of a cladding in KKL is about 6-7 cycles. The 9 cycle cladding serves for scientific purposes as it represents the conditions after extremely high burnup. Such high burnup rod is commonly not available; for this reason the literature and knowledge about it is valuable. It is expected that the typical late-life phenomena and changes (in composition and microstructure) occur in an emphasized way in this cladding. The data related to this material can be expected to help to evaluate the mechanisms involved to reach such extreme conditions. Therefore, this sample was fully characterized and these measurements were the starting points of this study. Other samples with lower burnups have been chosen specifically in order to answer some questions which have come about after the evaluation of the 9 cycle sample, and for comparison. These materials have not been studied to the same extent, only the examinations that would bring new insights for the understanding were carried out. The results are presented in the order of increasing burnup, i.e. the sample before irradiation is given first, followed by the 3 cycle, the 6 cycle, and the 9 cycle sample.

This chapter reports the manner of sample selection based on the subdivision of the 9 cycle sample's oxide layer in the first part. The selected materials are discussed subsequently, their overall structure is always shown first (by TEM), followed by the 3D FIB reconstruction of

their oxide and metal-oxide interface. The changes in the morphology of the metal-oxide interface is briefly described. The last part deals with the evolution of the hydrides in the metal, and considers their influence on the microstructure and protectiveness of the forming oxide.

4.2. Microstructure of the un-irradiated material

The un-irradiated material was already studied at the Paul Scherrer Institute in order to describe its general characteristics, such as grain size and texture. The average grain size is lower than 3 µm. The grains are oriented and the c-axis of the HCP lattice is parallel to the radial axis of the tube. JEOL JEM 2010 has been used for observation in this study and a micrograph is shown in Figure 4-1 and the SPPs are visible. The two types of SPPs have been identified using ChemiSTEM maps which is presented in Chapter 5, there the composition of the SPPs are further discussed. Based on the ChemiSTEM maps the mean diameter of the $Zr(Fe, Cr)_2$ SPPs was measured as 48 nm based on 58 particles. The $Zr_2(Fe, Ni)$ are rather elongated and the average diameter is 95 nm in the shorter and 135 nm in the longer dimension based on 12 measured SPPs. Abolhassani et al. [29] and Valizadeh et al. [14] provided the SPP size distribution with high statistics on the same (presented in Chapter 2 (Figure 2-26)). The authors reported 6.4×10^{19} m^{-3} SPP density and 42 nm average SPP size with median of 30 nm [14].

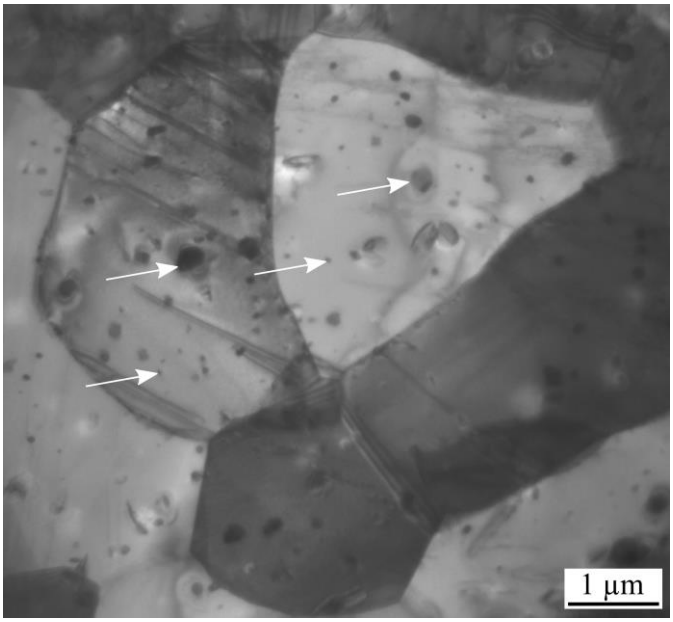

Figure 4-1 TEM micrograph of the un-irradiated LK3/L sample (by JEOL JEM 2010). Some of the SPPs are marked by arrows.

4.3.Microstructural evolution of the oxide and the metal-oxide interface

In order to observe the oxide layer evolution of the material in an efficient way, the selection of the claddings to be studied is a crucial step. The method of selection and the reasons for choosing a certain cycle cladding is described in the following.

The study started on the 9 cycle sample. Its oxide shows the full oxidation history of the cladding, therefore it was used when selecting the sample matrix for the thesis. The oxide thicknesses after specific residence times (after 3, 5, 6, and 7 cycles) are known from [13]. Based on these values the 9 cycle cladding's oxide was separated into sub-layers, each of them showing the formation of the oxide after 3, 5, 6, 7 and 9 cycles. For this, we assumed that the rate of oxide growth during these earlier stages of the 9 cycle cladding's life was similar to the individually measured values. In other words, the oxide was used as a "fossil" that preserves

the microstructure of the previously formed layers. The validity of this assumption was also tested during the study.

In this way, it is possible to investigate specific areas of interest separately; considering some important factors such as:

i. the microstructure of the given layer (e.g. high amount or no observable cracks);

ii. the change in the oxidation kinetics just before or after the formation of the specified layer;

iii. the changes in the HPU before or after the given cycle.

The microstructural changes are analysed to understand the modifications brought with the number of cycles. In the following the subdivision of the 9 cycle sample's oxide layer is described and the selection of other cycles which are considered as highly interesting based on at least one of the above mentioned points.

4.3.1. Subdivision of the oxide layer of the 9 cycle cladding

The available values for HPU and oxide thickness as a function of cycles of the LK3/L rods were taken from a previous publication [13] and are shown in Table 4-1. These thicknesses were measured and marked on the 9 cycle oxide. It is clear that the latest formed oxide that formed in the last cycle is the innermost oxide at the metal-oxide interface while the outermost oxide formed in the beginning of the service. Figure 4-2 shows the outer part of the 9 cycle cladding, consisting of the crud, oxide and metal parts, and the result of the oxide subdivision.

Table 4-1. Measured data for LK3/L claddings with different cycles [13].

Number of cycles	Peak burnup (MWd/kgU)	Segment elevation for oxide thickness measurement (mm)	Mean oxide thickness (μm)	Segment elevation for H_2 measurement (mm)	Total hydrogen content (ppm)
3	44.6	2005	4.4 (±0.7)	2002	44
5	59.6	2005	12	2002	90
6	66.9	2005	14	2002	202
7	67.4	1998	19 (±1.4)	2004	261
7	67.6	1995	21 (±0.9)	2000	339
7	73.3	1998	19 (±2.3)	2004	328
7	73.0	1998	19 (±2.3)	1995	224
9	89	2039.5	46 (±2.5)	2045	595

The following is observed after subdivision.

- The oxide part which formed in the first 3 cycles seems to have no cracks.
- A large circumferential crack along the entire circumference of the segment is observable in the oxide which formed between the 3rd and 5th cycles. The time of formation of this crack is not necessarily this period. Between these cycles the oxide layer has grown an additional 7.6 μm and it is 2.7 times thicker than after 3 cycles. The H content increased by an additional 46 ppm (a factor of 2.3).
- Between the 5th and the 6th cycles the oxide growth was slower and the oxide microstructure does not show extreme cracking. The average oxide thickness increased only by 2 μm, from 12 to 14 μm. However, the H content doubled as the material picked up an extra 110 ppm H.
- Between the 6th and 7th cycles the oxide became around 1.5 times thicker growing an additional 5-7 μm. In the case of the 7 cycle sample three data points are given from similar elevations, therefore more statistics is available and certain scatter is observed. The HPU was 1.1-1.7 times higher (additional 22 and 137 ppm H).

- In the last two years of the service, i.e. between the 7th and the 9th cycles the oxide growth is significantly increased (from 19-21 µm to 46-47 µm) and the H content is 1.8-2.7 times higher. A large, continuous circumferential crack is present in this region of the oxide (Figure 4-2). If this crack formed during the service, its time of formation is most likely between the 8th and the 9th cycles or during the 9th cycle.

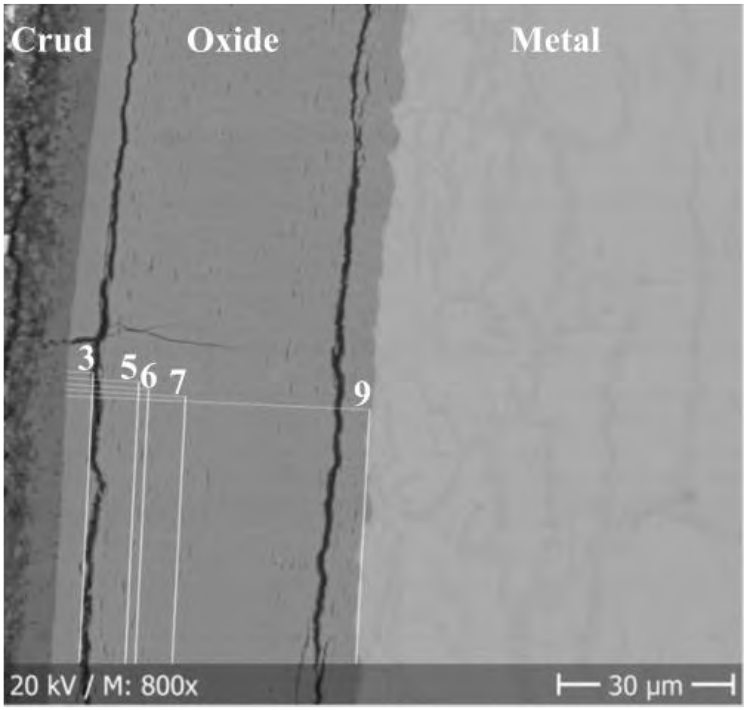

Figure 4-2. BSE micrograph of the oxide of the 9 cycle LK3/L sample representing the subdivisions of the oxide layer. Straight lines indicate the estimated oxide thicknesses expected to have grown during the given cycle; please refer to the text for the explanation.

Figure 4-3 shows the increment in the additional H content and oxide thickness in yearly average. For the 7 cycle cladding the average of the four data points (Table 4-1) are given. From 5 to 6 cycles the yearly average of HPU increases significantly while the oxide growth slows down. The HPUF is not constant during the service (Figure 4-4): it is around 15-20% in the 3 and 5 cycles, 35% in the 6 cycle samples while it varies for the 7 cycle segments between 25-40% (the average is shown in the graph) and it was around 30% after 9 cycles.

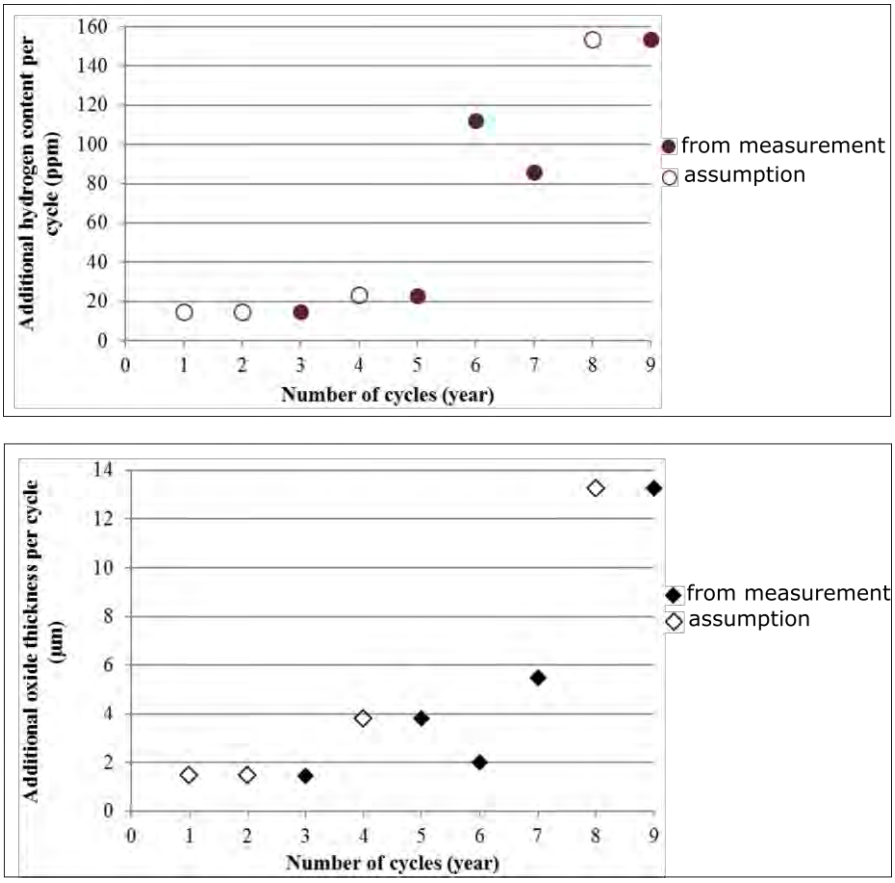

Figure 4-3 Graphs for the average yearly increase of hydrogen content and oxide thickness of the LK3/L claddings between the indicated cycles. The empty markers indicate average values based on assumption and they are not from measurements.

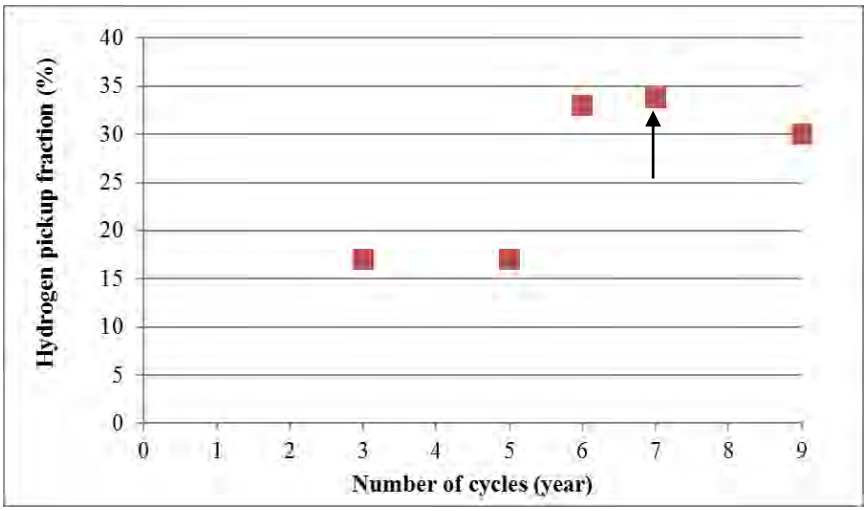

Figure 4-4 The hydrogen pickup fraction values in the different cycles of the LK3/L cladding segments from similar elevations (~2000 mm). The average of 3 samples is shown in the case of the 7 cycle sample (indicated by arrow).

The 3 cycle sample has been selected for more detailed investigation due to the following reasons:

- Protective oxide layer is expected against rapid oxidation and HPU. It gives a good comparison with the less protective oxides which formed at higher burnups.
- It helps to validate our assumption that the microstructure of an already formed oxide is preserved with further service (i.e. the oxide acts as a “fossil”) if we compare it with the outermost layer of the 9 cycle oxide.

For the higher burnup region the 6 cycle sample is a good candidate due to the following reasons:

- It seems to be more protective against rapid oxidation but less protective against HPU compared to the previous cycles.
- It is close to the normal length of the lifetime of the cladding in the reactor.
- Regarding the service time and burnup this cladding is in between the 3 and 9 cycle samples therefore it is the ideal sample for comparison with a relatively low and an extremely high burnup cladding.

Finally, the 9 cycle oxide is presenting the extreme high burnup state of the cladding with increased HPU and oxidation, therefore it is highly interesting.

The next section deals with the microstructural evolution of the LK3/L cladding based on the selected samples.

4.3.2. Characterization of the crack microstructure after 3, 6 and 9 cycles by TEM and FIB tomography

4.3.2.1. 3 cycle LK3/L sample

The microstructure of the 3 cycle sample by TEM

A TEM micrograph of the 3 cycle oxide is shown in Figure 4-5. The oxide contains a mixture of equiaxed and columnar grains with a grain size between 20-65 nm (average of 41 nm based on 12 grains) in the first case and 35-40 nm width and 80-170 nm length in the latter case (from 4 measurements). In Figure 4-6 the metal-oxide interface is also shown, the GBs and small hydride precipitates are visible. Figure 4-7 shows the metal-oxide interface at higher magnification. It is worth noting that the presence of the hydride precipitates were confirmed by observing their diffraction pattern when JEOL JEM 2010 was used. During the measurements using FEI TALOS F200X, although the electron diffraction of these precipitates were not available, the nature of such precipitates have been several times confirmed by means of electron diffraction in TEM. The formation of columnar oxide grains is captured as well as small hydride in the metal about 200 nm from the interface.

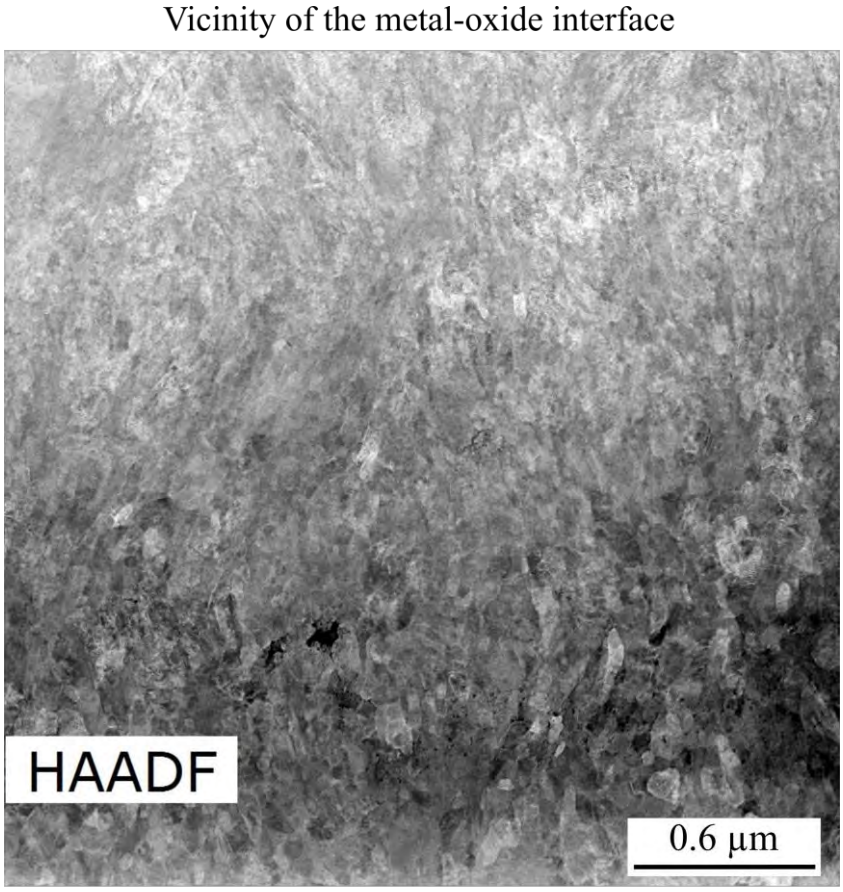

Figure 4-5 TEM micrograph on the oxide of the 3 cycle LK3/L sample. The upper part is showing the oxide in the vicinity of the metal-oxide interface, the bottom part is the outermost oxide.

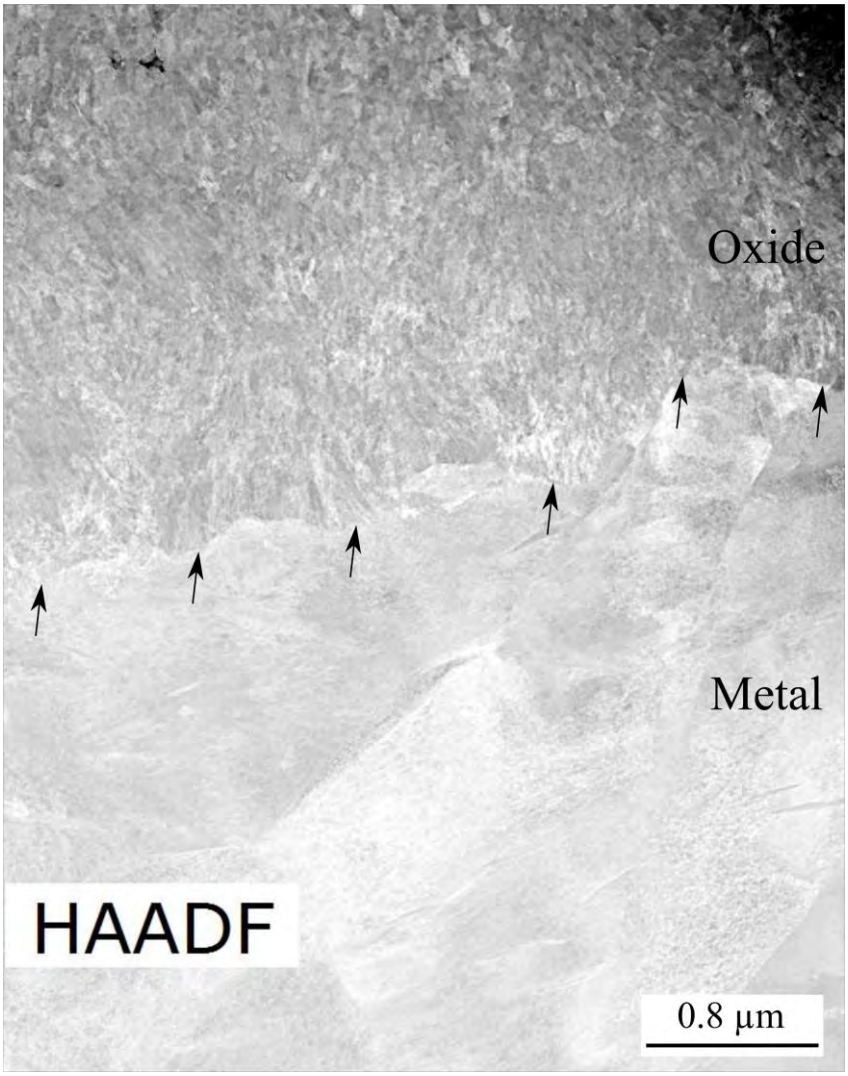

Figure 4-6 Low magnification TEM micrograph on the metal and oxide of the 3 cycle LK3/L sample.

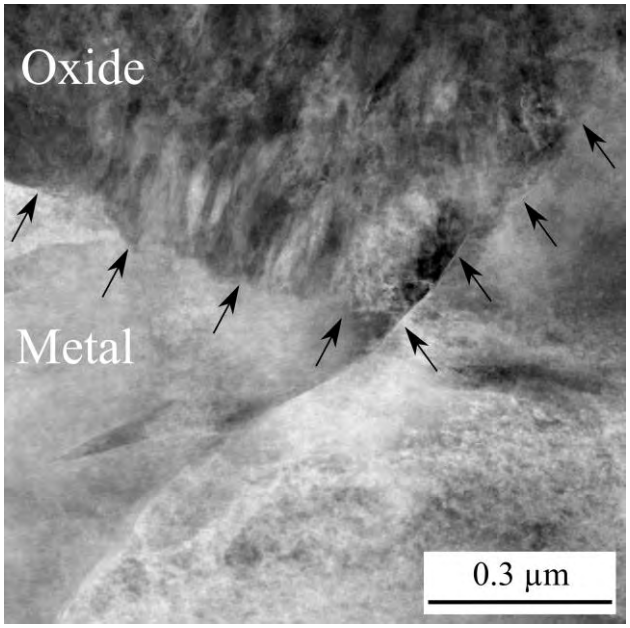

Figure 4-7 TEM micrograph of the 3 cycle LK3/L at the metal-oxide interface. The metal-oxide interface is indicated by the arrows.

FIB tomography on the 3 cycle sample

SE images of the 3 cycle cladding's outer part is presented in Figure 4-8. In Part (A) the axial direction of the tube is normal to the image. Part (B) shows the cross-sectional cut of this, i.e. the image is taken parallel to the tangential axis. The oxide layer is thin and in the metal few, small size hydrides are formed, close to the metal-oxide interface. The 3D reconstruction of the oxide is shown in Figure 4-9 [3]. The coordinates are defined as follows: X axis is parallel to the tube radial direction, while Y is parallel to the tube axial direction and the direction of the incident ion beam. Therefore, X-Y surface corresponds to the cross-section of the sample (i.e. where the images were taken). Axis Z gives the direction of slicing and is parallel to the tangential direction of the tube. In total 113 SE images were acquired using 10 kV accelerating

[3] Please note that the oxide – when displayed in the 3D reconstructions – is presented with a transparent color (transparent pink) throughout the thesis, therefore the objects inside the oxide are visible in the full volume.

voltage. The average slice thickness is 28.5 nm. The reconstructed oxide volume is 65.39 (± ~10) μm^3 from which 0.13 (± ~0.02) μm^3 belongs to the cracks, i.e. the crack volume fraction is 0.19%. For the detailed description of the estimation of the error, please refer to Section 8.1.1.1 (Error estimation of the FIB tomography results). The volume fraction is calculated as: $V_{crack}/V_{total} \times 100$; where V_{crack} is the volume of cracks and V_{total} is the total reconstructed volume. A second reconstruction has been produced at the same region for higher statistics. It shows higher crack volume fraction, namely 0.76%. This is due to the high statistical variation of brittle failure in the ceramic materials. In this second region the cracks are bigger in size compared to the first region. Here, fine radial cracks are also revealed (example SE micrograph in Figure 4-10). Although the crack volume fraction varies from region to region, these results show that only few cracks can be found in the oxide layer after the first 3 years and that fine radial cracks occurred at certain regions of the oxide. The low level of porosity of this oxide is one of the factors that provides good protection against further oxidation and HPU of the 3 cycle cladding.

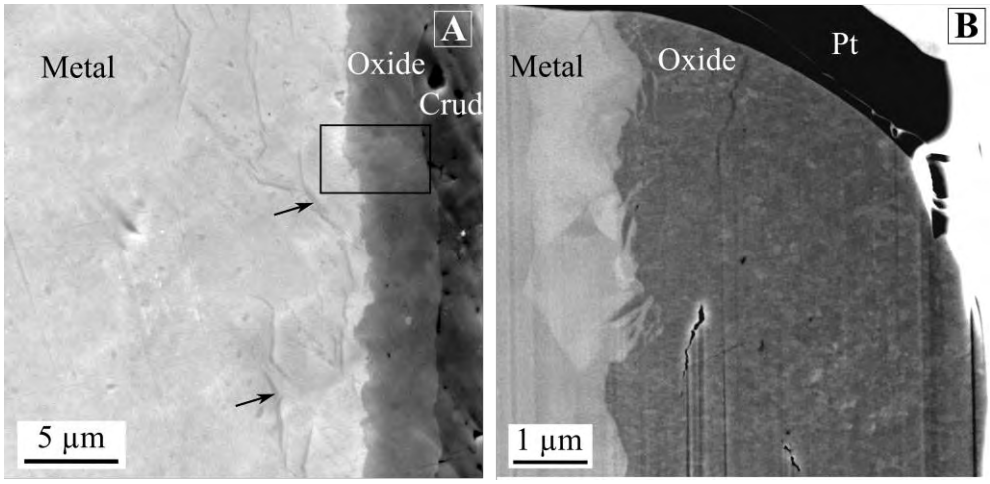

Figure 4-8. SE images of the outer part of the 3 cycle LK3/L cladding. (A): Top view. Arrows indicate hydrides in the metal. The black square merely indicates a similar area where the 3D cuts were made; it does not represent the exact position of the cuts. (B): The FIB cross-section of the sample, i.e. one of the slices used for the 3D reconstruction.

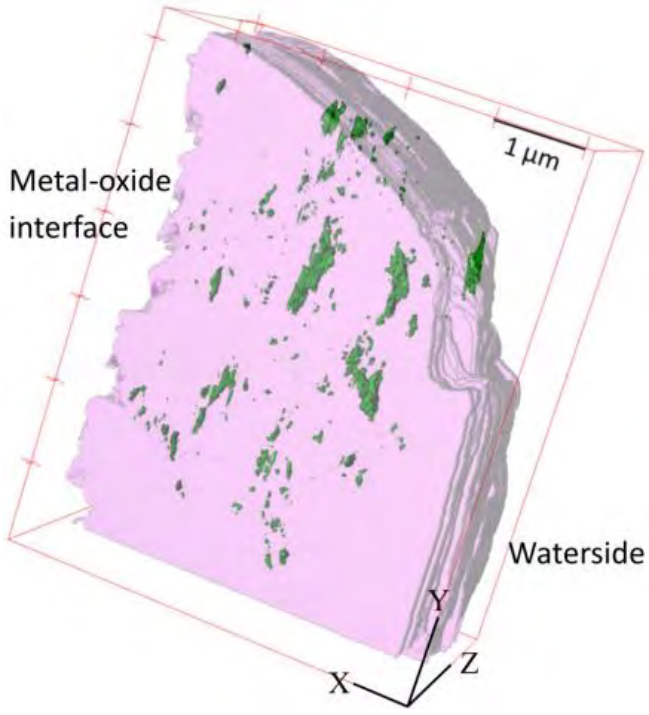

Figure 4-9. 3D reconstruction (by ImageJ) of the oxide of the 3 cycle LK3/L sample. Green objects: cracks, transparent pink object: oxide matrix. Dimensions of the "bounding box": X=4.97 µm, Y=6.30 µm, Z=3.2 µm.

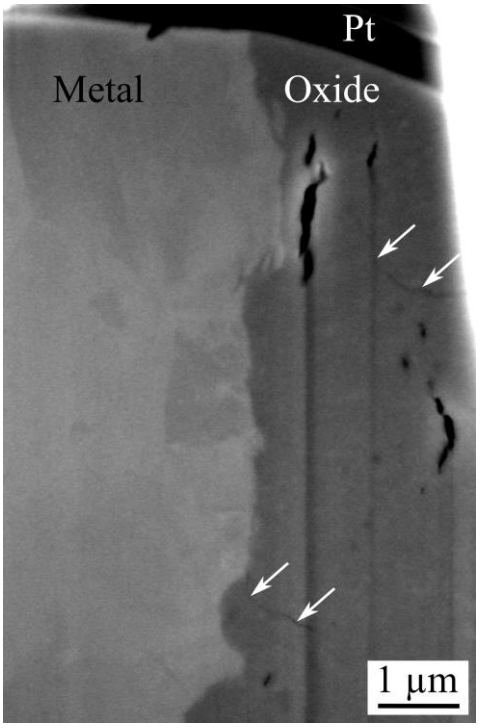

Figure 4-10 SE image of the 3 cycle LK3/L metal-oxide interface. Arrows mark the fine radial cracks in the oxide.

4.3.2.2. 6 cycle LK3/L sample

The microstructure of the 6 cycle sample by TEM

The TEM analysis of the 6 cycle sample was not performed, however TEM observations on the 7 cycle sample are reported in Chapter 5 – Section 5.2.2.3.

FIB tomography on the 6 cycle sample

The outermost part of the sample is presented in Figure 4-11-(A). In Part (A) the normal vector of the image's surface is parallel to the axial axis of the cladding. In Part (B) the surface's normal vector is parallel to the tangential axis. Between 5 and 6 cycles around 2 µm of oxide was formed. In both images the red dashed line is separating the oxide which has formed during the 6th cycle. The 3D visualization of the volumes is shown in Figure 4-12. As before, the X axis is parallel to the tube radial direction, while Y is parallel to the tube axial direction and axis Z gives the direction of slicing and is parallel to the tangential direction of the tube. In total 58 images have been taken along 1.3 µm of the oxide (z direction). The reconstruction contains two image stacks that are combined together: the two stacks are continuation of each other and only the step size is different between them. This is because the step sizes needed to be changed during the milling process during the slice-and view of this volume. In the beginning of the slicing, along the first 0.81 µm the step size was 32.4 nm (25 images) while along the next 0.52 µm the slice thickness was 15.8 nm (33 images). The motivation behind the change in the step size was to increase the resolution of the reconstruction to the highest possible without a very high increment of the time of the slice-and-view measurement. The total volume size of this reconstruction is smaller than that of the others in this study due to the significant charging of the oxide that began after the first 58 images, it was not possible to obtain a micrograph with a contrast that is optimal for imaging the metal and the oxide simultaneously. It is worth

mentioning that a 0.5 μm region of the oxide close to the interface did not show charging (see in Figure-AI 1 in Appendix I).

The reconstructed oxide is thicker than 2 μm in the X direction but only a 2 μm thick layer has been taken into account as this is what formed during the 6th cycle[4]. The crack volume fraction in the two volumes from the two image stacks are 2.41% and 3.21%, separately. This indicates that the level of error caused by the different step sizes should not be significant and it seems to have a slight influence on the result. The slightly higher crack volume fraction in the reconstruction with the smaller step size could be caused by an actual difference or the by the better resolution for the small cracks. The crack volume fraction of the total reconstructed volume is 2.73%. It is reasonable to consider the two volumes as one dataset, as they are exactly from the same site of the oxide and they are the continuation of each other. The crack volume fraction is 2.30% in the oxide close the metal-oxide interface (up to a distance of 1 μm). The hydrides in the metal are also shown in the 3D visualization, their volume fraction is 8.53%. More details on the hydrides can be found in the section 4.4.

[4] The result for the full reconstruction with the thicker oxide (i.e. including the 5th cycle oxide) is shortly reviewed in the Discussion of this chapter.

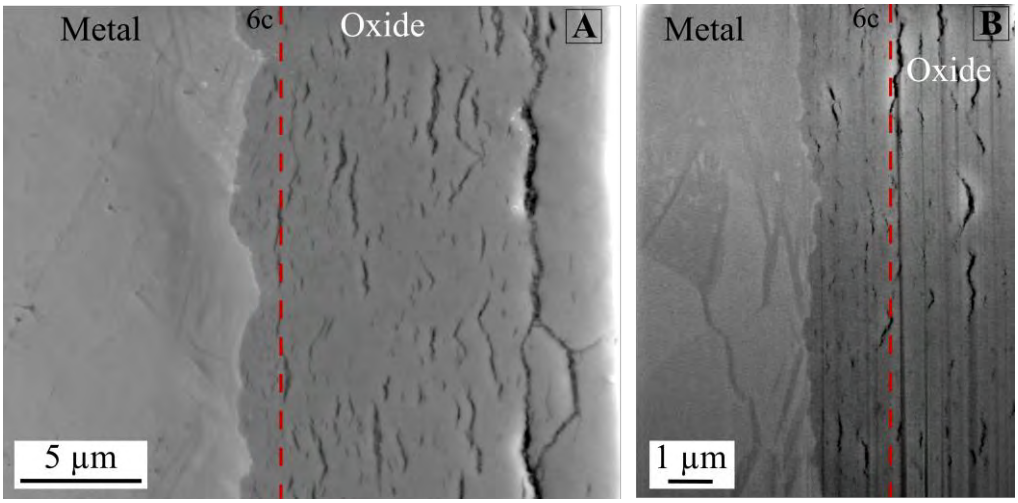

Figure 4-11 SE micrographs of the 6 cycle LK3/L sample. (A): outermost area of the cladding (B): metal-oxide interface. The red dashed line indicates the oxide formed during the last cycle in reactor, based on results of destructive test provided in Table 4-1.

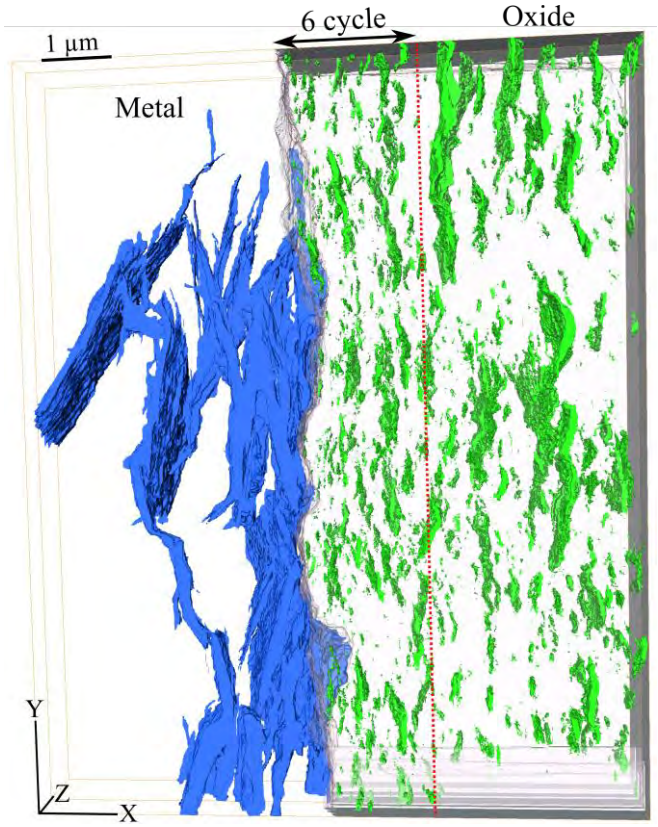

Figure 4-12 3D reconstruction of the innermost oxide including the metal-oxide interface on the 6 cycle LK3/L sample (by Avizo). Hydrides in the metal: blue objects; cracks in the oxide: green objects. The lastly formed 2 µm of the oxide is formed in the 6th cycle and it is separated by the red line. "Bounding box" size: X=8.692 µm, Y= 10.750 µm, Z1= 1.3 µm.

4.3.2.3. 9 cycle LK3/L sample

The microstructure of the 9 cycle sample by TEM

This sample has a 46 μm thick oxide layer. The outer oxide and inner oxide regions were examined separately, both by TEM and 3D FIB.

Microstructure of the outermost oxide

Figure 4-13 shows a high-angle annular dark-field (HAADF) TEM image of the outer region of the 9 cycle sample's oxide, i.e. from 2 to 7 μm away from the crud-oxide interface. This oxide formed within the first 3-4 cycles, and before the end of the 5th cycle of service. A mixture of equiaxed and columnar grains are present. The equiaxed grain size is in between 30-69 nm with an average of 47 nm (13 measured grains). The columnar grains have an average width of 36 nm (values are in between 23 and 62 nm) and average length of 155 nm (values between 112 and 194 nm), obtained from 9 measured grains. The oxide does not contain many cracks and it is mostly dense especially in the outermost 1 μm. However an interconnected pore system is visible on figure; marked by dashed arrows and shown in Figure 4-14.

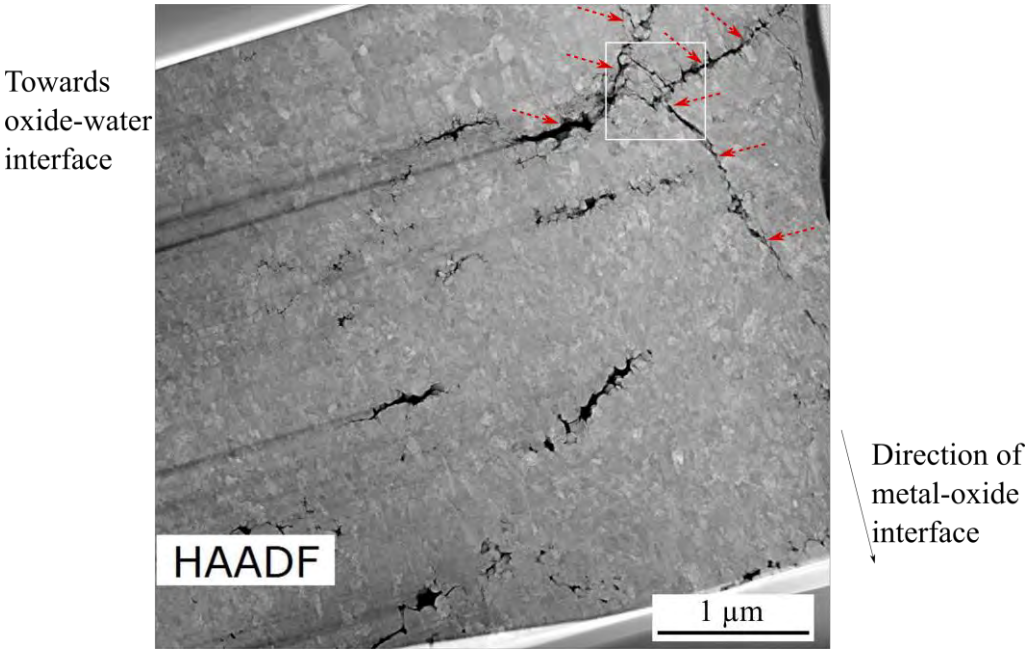

Figure 4-13 TEM micrograph on the outer oxide region of the 9 cycle LK3/L sample. Interconnected pore system is marked by the red dashed arrows. The area marked by the white square is shown in Figure 4-14.

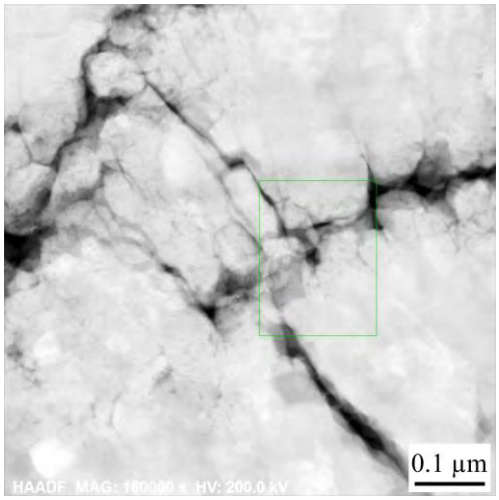

Figure 4-14 TEM micrograph on the outermost oxide of the 9 cycle LK3/L sample showing interconnected pore network built up by both radial and circumferential cracks and pores.

Microstructure of oxide and metal at the metal-oxide interface

A TEM micrograph of the metal-oxide interface of the 9 cycle sample is shown in Figure 4-15. Significant increase both in the size and the amount of cracks is observable compared to the outermost oxide. Columnar and equiaxed oxide grains are present as it is shown in a bright field (BF) (Figure 4-16) and a dark field (DF) micrograph (Figure 4-17) showing two different regions of the oxide. The diameter of the equiaxed grains is in the range of 11-36 nm (average of 21 nm from 11 measurements). The columnar grains are around 100-200 nm in length (4 measurements).

The TEM lamella that was prepared in the metal close to the metal-oxide interface is shown in Figure 4-18. Larger and significantly higher amount of hydrides can be observed in the metal of this sample compared to the 3 cycle sample and to a certain extent to the material with 6 cycles. It must be noted that the chemical analysis of all the samples are reported in Chapter 5.

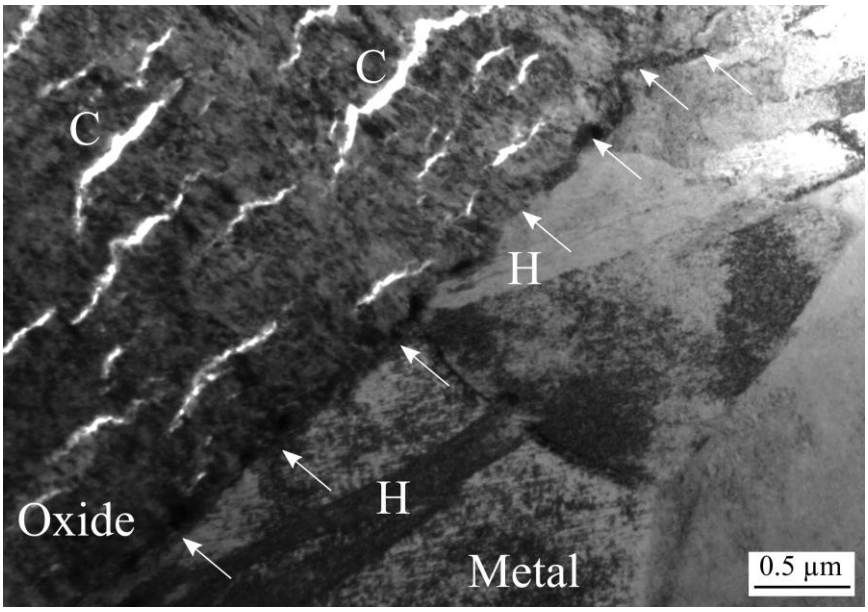

Figure 4-15 TEM micrograph on the metal-oxide interface of the 9 cycle LK3/L sample. Arrows indicate the metal-oxide interface. Cracks are indicated by "C", hydrides by "H".

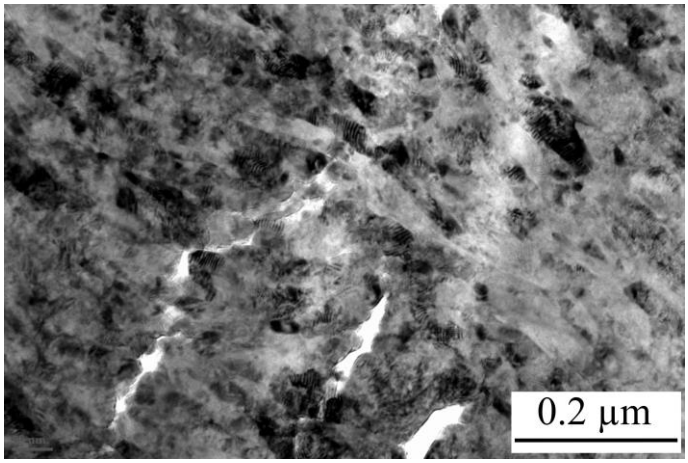

Figure 4-16 TEM BF micrograph of the inner oxide of the 9 cycle LK3/L sample.

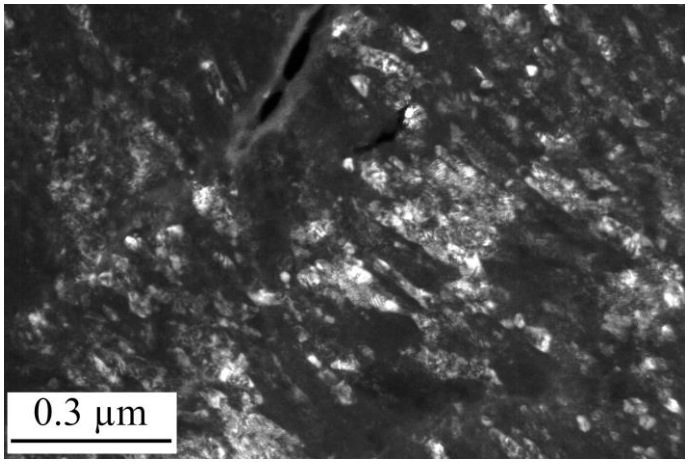

Figure 4-17 TEM DF micrograph of the inner oxide of the 9 cycle LK3/L sample.

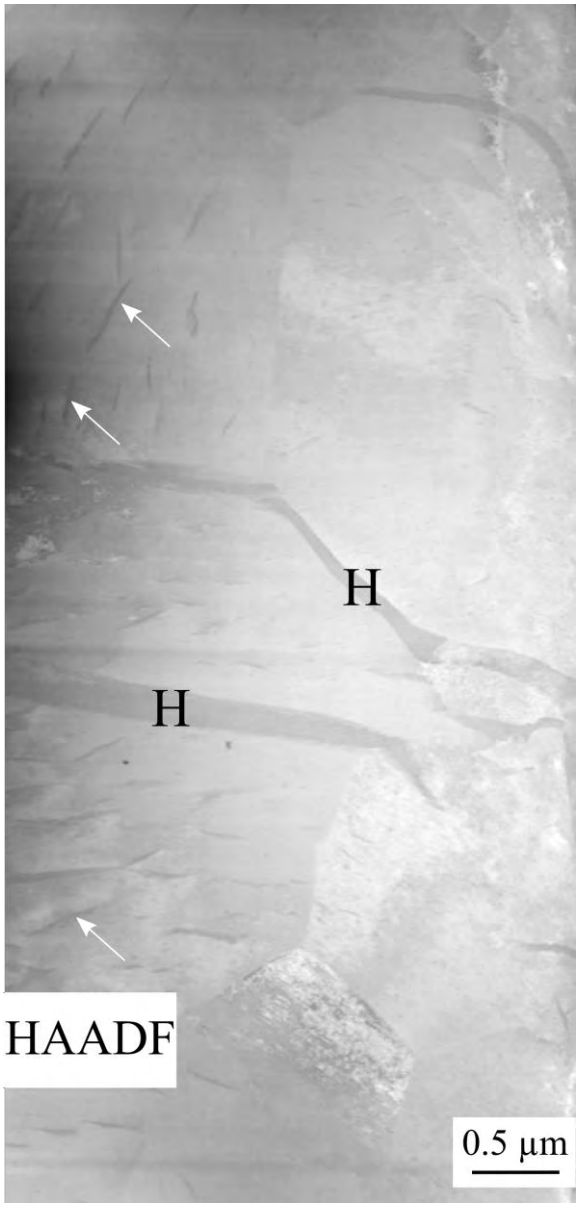

Figure 4-18 HAADF micrograph on the metal of the 9 cycle LK3/L sample close to the metal-oxide interface. Small and large hydrides are marked by the arrows and "H".

FIB tomography on the 9 cycle sample

Two regions have been selected for the 3D reconstruction that are shown in Figure 4-19. Figure 4-19-(A): the tube axial is normal to the image plane. Figure 4-19-(B) and (C) are the cross-sectional cuts on the positions that is marked by the black squares, the tube tangential is normal to the image plane.

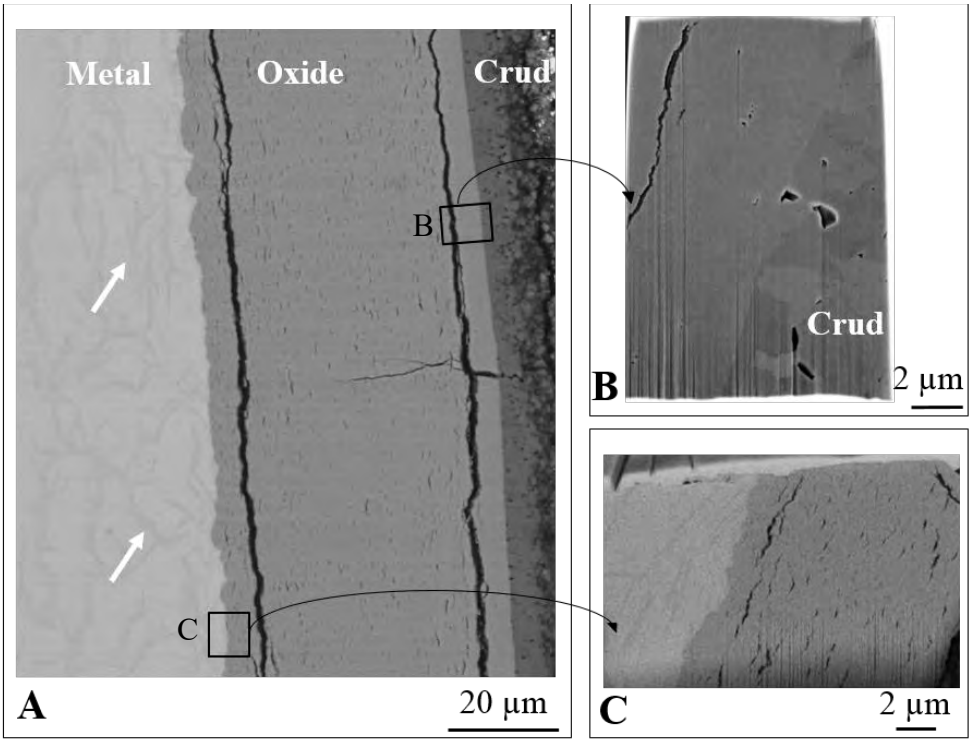

Figure 4-19. SEM images of (A): the outer part of the 9 cycle LK3/L cladding (BSE) (white arrows indicate the hydrides). The squares indicate the areas selected for reconstruction and one example is shown for both regions: (B): outer part of the oxide (SE) and (C): at the metal-oxide interface (BSE).

Outermost oxide

The outermost part of the oxide was formed during the first few years of the service. This region has been reconstructed and presented in Figure 4-20.

Part (A) shows the oxide that were formed during the first 3 cycles. The difference between Part (A) and B in only the length in the X direction: Part (B) shows a thicker oxide and includes the large circumferential crack that occurred at the position of the oxide that was formed between 3 and 5 cycles. It is important that the time and cause of the formation of this crack is not known and it was not necessarily formed between the 3rd and 5th cycles. The coordinates are defined in the same way as before, please refer to the previous description for details (page 94). For the reconstruction 341 SE images were acquired using the accelerating voltage of 5 kV with an average step size of 12±5 nm, i.e. cracks are visualized in 4.2±0.8 µm depth (Z direction). The average length of the reconstructed volume in the Y direction is 9.1 µm, while in the X direction it is 4.7 µm for Part (A) and 5.7 µm in Part (B). The reconstructed oxide and crack volumes are: 185 (± ~28) µm^3 and 0.15 (± ~0.02) µm^3 respectively in Part (A), and 216 (± ~32) µm^3 and 2.8 (± ~0.42) µm^3 in Part (B). For the detailed description of the estimation of the error, please refer to Section 8.1.1.1 (Error estimation of the FIB tomography results). The crack volume fraction is 0.08% in Part (A) and 1.28% in Part (B) where the large crack is responsible for higher percentage of micro-cracks. The oxide that formed in the first 3 cycles is dense; only a few micro-cracks are observed, similar to the oxide layer of the original 3 cycle sample. This indicates that the oxide can indeed be used as a “fossil” and it preserves its microstructure even with further service.

However, it is expected that the oxide fails under different environmental conditions (stresses, expansion or contraction, etc.) and induces large cracks in the structure at a later stage. Therefore, these large circumferential cracks could be exceptions to the above statement. One

of the large cracks occurred at the distance of more than 4.4 µm from the outer surface of the oxide (Figure 4-20B), therefore it is sure that it was not formed during the first 3 cycles, however we cannot conclude anything else about its time of formation.

Due to the preserved microstructure of this oxide, Part (A) of Figure 4-20 is directly comparable to the 3 cycle oxide in Figure 4-9. The crack volume fraction of this outer oxide is even lower than in oxide of the 3 cycle sample with a similar order of magnitude. Variations could be caused by the slight changes in composition and by the fact that the crack formation in ceramics has a certain inherent variability. Moreover, the slice thicknesses for the two reconstruction were not the same. It is clear that, in general, it is not possible to obtain identical numbers within the different measurements, even for the same number of cycles.

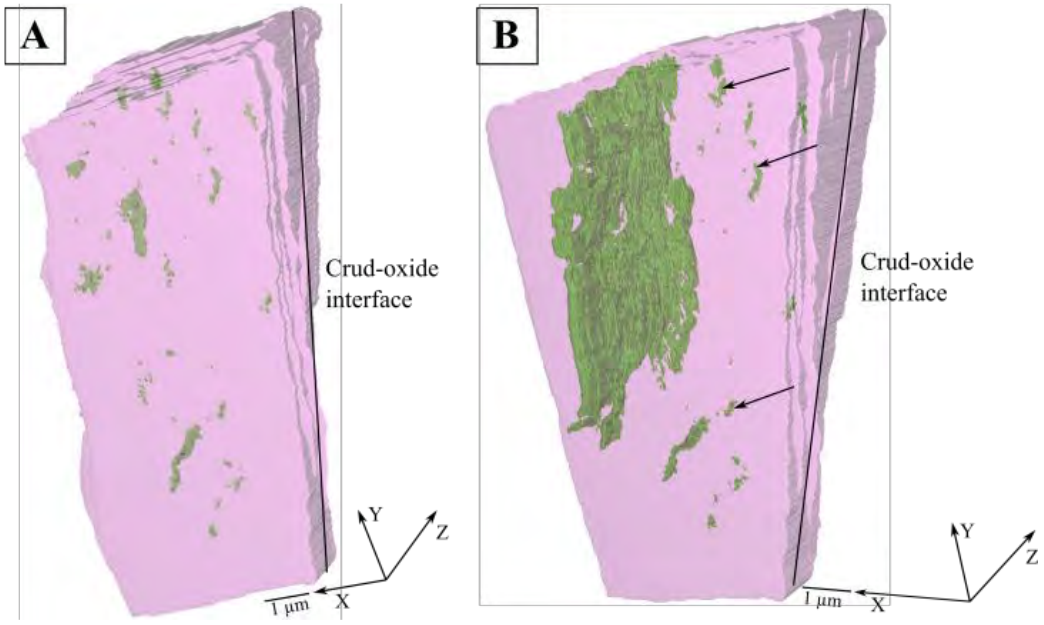

Figure 4-20. 3D reconstruction (by ImageJ) of the outermost oxide (transparent pink) and the containing cracks (green) of the 9 cycle LK3/L sample. (A): Oxide formed in the first 3 cycles. (B): Same as in (A) including the large crack occurred after the 3rd cycle. Arrows indicate fine cracks formed during the first 3 cycles. Largest dimensions – (A): X=5.04 µm, Y= 10.90 µm, Z=4.2 µm; (B): X=7.10 µm, Y, Z as in Part (A).

Inner oxide

The fabricated cube at the metal-oxide interface prior to the FIB study is shown in Figure 4-21. In total 152 BSE images were collected along 3.71±0.04 μm depth in Z direction (i.e. average step size of 24.4 nm). The reconstructed oxide is about 200 (± ~30) μm^3 and contains 9.76 (± ~ 1.5) μm^3 of cracks. For the detailed description of the estimation of the error, please refer to Section 8.1.1.1 (Error estimation of the FIB tomography results). The reconstructed crack network is shown in Figure 4-22. The X, Y, Z system is defined the same way as before. This oxide was formed during the end of the service. The crack system is built up mainly from circumferential cracks; however one radial crack is observed and indicated by an arrow. The crack volume fraction in the inner part of the oxide is 4.9%, which is around 61 times higher than that in the outermost layer. Another 3D FIB measurement was prepared in order to increase the statistics of the results. A higher, 8.1% of crack volume fraction was measured. This is the result of the natural variations of the oxide cracking. Furthermore, SE images have been collected that has slightly increased the resolution of the micrographs.

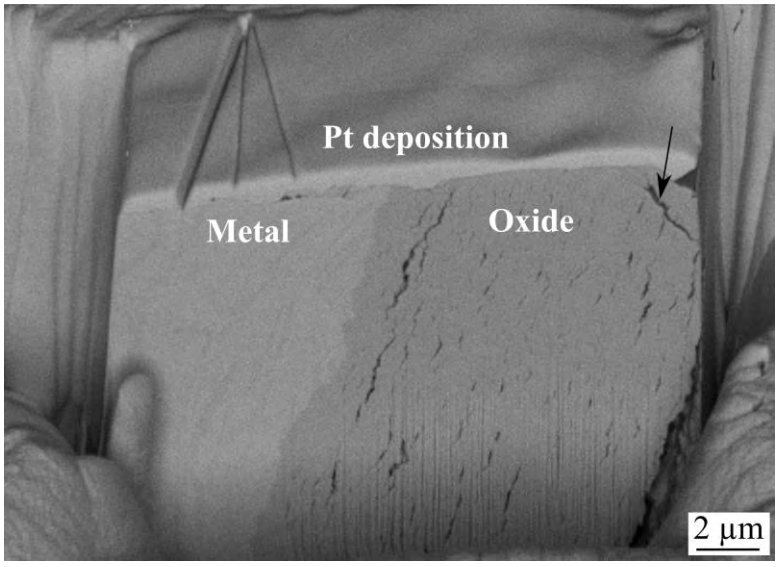

Figure 4-21 BSE image of the fabricated cube used for the reconstruction of the cracks in the oxide and the hydrides in the metal, 9 cycle LK3/L sample. Arrow marks a radial crack.

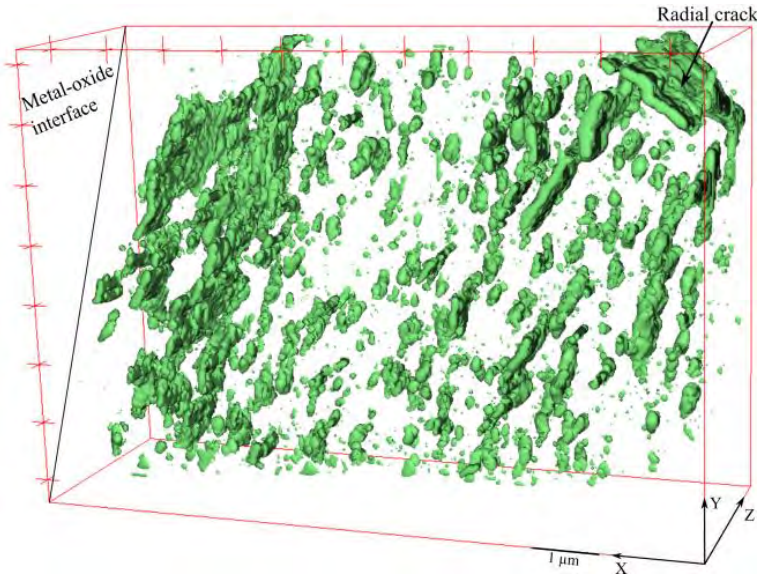

Figure 4-22 3D reconstruction (by ImageJ) of crack system in the oxide that formed towards the end of the service of the 9 cycle LK3/L cladding. The red frame is provided merely to perceive the spatial position of the objects and its volume is not equal to the volume that has been reconstructed. Dimensions of the "bounding box": X=10.32 µm, Y= 7.15 µm, Z= 3.71 µm.

Metal-oxide interface

The reconstruction of the metal-oxide interface is shown in Figure 4-23. The hydrides in the metal are presented here but their relevance is discussed in the following section. In total 196 SE images along 3.92 ± 0.04 µm depth were collected (i.e. step size of 20 nm). Table 4-2 summarizes the data obtained from this region. This oxide was formed in the end of the 9th cycle. The volume fraction of the cracks of the oxide is 5.4%. The previously mentioned second reconstruction of the innermost oxide includes the metal-oxide interface as well, and up to the distance of 1 µm from the interface it shows 8.3% crack volume fraction. The two results show that there is a variation in the crack volume fractions from one site to another. This is a typical property of the ceramic type materials. These results clearly demonstrate that the oxide that formed in the end of the 9th cycle shows the highest crack volume fraction compared to other studied regions on this sample or on the other LK3/L samples.

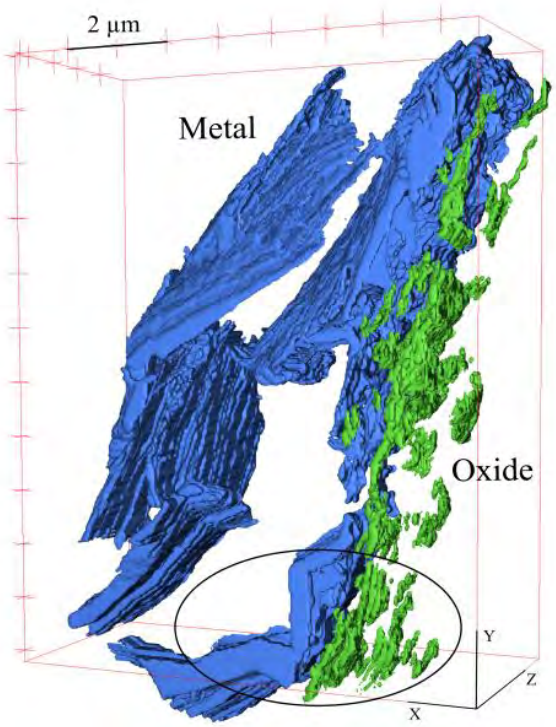

Figure 4-23. 3D reconstruction (by ImageJ) of the hydride precipitates (blue) in the metal and the cracks (green) in the oxide at the metal-oxide interface of the 9 cycle LK3/L sample. The red "bounding box" is provided merely to perceive the spatial position of the objects and its volume is not equal to the volume that has been reconstructed. Largest dimension: X=8.64 µm, Y= 12.58 µm, Z=3.92 µm. The circled regions represents an area where the hydride phases that are close to the metal-oxide interface are followed by a group of cracks in the oxide side.

Table 4-2. The volume of hydrides and cracks, extracted from the 3D the reconstruction by ImageJ of the 9 cycle LK3/L cladding. The total volume used for the reconstruction, i.e. the total volumes of the used metal and the oxide part are given as well. For the detailed description of the estimation of the error, please refer to Section 8.1.1.1 (Error estimation of the FIB tomography results).

Phase	Object	Colour of the object	Volume of the reconstructed object (µm^3)	Total volume of the phases (µm^3)
Metal	Hydrides	Blue	33.2 (± ~5)	193.2 (± ~29)
Oxide	Cracks	Green	1.7 (± ~0.2)	31.7 (± ~ 5)

4.3.3. Morphology of the metal-oxide interface of the 3, 6 and 9 cycle materials

Several studies showed that the undulation of the interface has an effect on the stress distribution in the oxide [139], [69], [138]. Changes in the compressive and tensile stresses were revealed in an undulated interface by 2D finite element modelling [138]. It was claimed that the differences in the stresses have an influence on the diffusion coefficient of oxygen [69] and that the morphology of the metal-oxide interface could affect the oxidation and the HPU of the materials [169]. It was concluded that an irregular profile of the metal-oxide interface could provide a better corrosion resistance than a profile with regular (i.e. well-defined, flat) shape [169].

In Figure 4-24 the profiles of the metal-oxide interface of the 3, 6, and the 9 cycle cladding segments are shown. The morphology of the interface is irregular in the case of the 3 cycle sample (Figure 4-24-(A)). In Figure 4-24-(B) and (C) the 6 and 9 cycle samples are shown, respectively. The morphology of their interface does not show a large difference and are both exempt of the large undulation or uneven wavy interface, i.e. the interface shows a smoother shape at higher cycles. This strengthens the statements that the undulation of the interface can be correlated to the protectiveness of the oxide, as in this study as well, the lower the protectiveness of the oxide, the less undulated the interface is.

It is worth noting that the 3 cycle sample's oxide showed a mild charging during the slice-and-view that did not disturb the image acquisition significantly. Whereas, in the 6 cycle sample the charging phenomenon became significant during the measurement, except for a region within 1 μm distance from the interface. The 9 cycle sample's oxide behaved similar to the 6 cycle sample, although the measurements were undisturbed for a much longer time. Here as well, the oxide at the metal-oxide interface (within about 1 μm) behaved differently indicating no

charging. Example images are shown in Figure-AI 1 in Appendix I. The conductivity measurement of these oxides is included in a currently ongoing PhD project as the continuation of the present PhD in the Nuclear Fuels group at the Paul Scherrer Institute and results are expected in the near future.

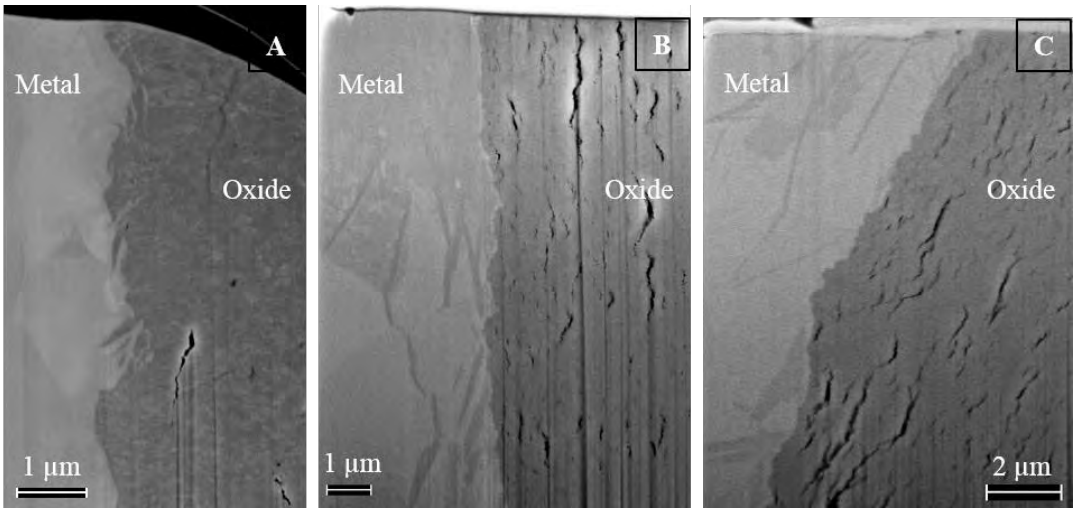

Figure 4-24. SE images of the metal-oxide interface of the 3 cycle (A), 6 cycle (B) and the 9 cycle (C) LK3/L cladding segments.

4.4. Microstructural evolution of the metal

The microstructure of the metal changes as well during the service of the cladding, one important change being due to the hydrogen content which increases with time leading to the formation of hydride phases above the solubility limit. Here, their overall distribution in the metal is shown after different cycles. As the HPU and oxidation occur at the metal-oxide interface, the relevance of the hydrides at this region of the metal is discussed, based on the 3D FIB measurements. As the microstructure of the metal (i.e. hydrides) evolves with time, the fresh oxide forms on a gradually changing alloy. Logically, this should induce some changes

in the microstructure of the newly forming oxide layer. This section captures the role of hydrides in this process.

4.4.1. Evolution of the hydride phases from medium to extreme high burnups

The hydride phases in the metal are characterized using SEM images and by FIB tomography after each selected cycles. The distribution of the hydrides along the radial direction of the cladding is briefly described. The hydrides at the metal-oxide interface are shown by 3D reconstruction in order to see their shape in volume and to reveal whether they are interconnected.

4.4.1.1. Hydrides after 3 cycles

In the 3 cycle LK3/L Zircaloy-2 the H content is very low, 44 ppm (Table 4-1). The solid solubility limit of H in Zircaloy-2 at 300 °C temperature is around 60 ppm [111]. This means that no or not relevant amount of precipitated hydride is expected at this stage of the service. Even at room temperature we did not observe hydrides at the metal-oxide interface during the slice-and-view method. Therefore, no 3D reconstruction of hydrides is presented for the 3 cycle sample.

A BSE image is shown on the full thickness of the cladding in Figure 4-25 (A). Some hydride phases are revealed and they are segmented by Avizo software, shown in Figure 4-25 (B), in order to quantify their spatial distribution in the radial direction. Part (C) shows the area fraction at the different selected areas. As an example selected area 0-10 gives the hydride area fraction in the metal in the region between 0 and 10 μm from the interface. The area fraction is very low even close to the metal-oxide interface, just above 1%. However, it is assumed that during the

service H was mostly in a dissolved form. Therefore, it is proposed that the influence of the hydrogen content on the oxide microstructure is negligible during the first 3 cycles.

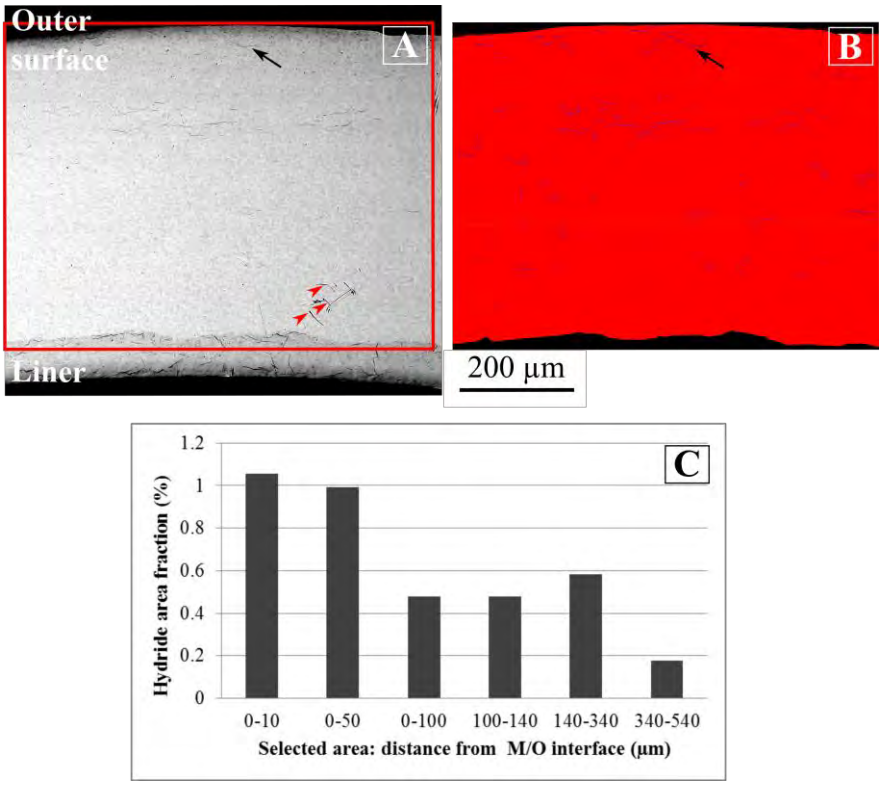

Figure 4-25 (A): BSE image of the full cladding thickness of the 3 cycle LK3/L sample. The red square shows the area used for quantification. A hydride is marked by the black arrow. Red arrowheads mark scratches due to sample preparation. (B): Image from segmentation module from Avizo to quantify hydride surface area. The metal matrix is red and the hydrides are in blue. (C): Graph showing the hydride area fraction of different selected areas. The liner was not taken into account.

4.4.1.2. Hydrides after 6 cycles

The hydrogen content after 6 cycles is 202 ppm which is above the solid solubility limit of H in Zircaloy-2 at service temperature. Therefore we assume that hydride phases were present during service. At room temperature we expect to observe more hydrides compared to the amount in the reactor. The additionally precipitated hydrogen is estimated to be around 60 ppm which is relatively low but certainly adds an error to the amount of hydrides observed compared

to the reactor temperature. Figure 4-26-(A) and (B) show the BSE and segmented image and Part (C) shows the quantification for the hydride distribution Inhomogeneous hydride distribution is observed in the radial direction. Accumulation of hydrides is observed close to the metal-oxide interface. It is worth mentioning that this technique gives only two-dimensional information.

The metal-oxide interface is in the main focus as the oxide forms here. The 3D characterisation of the hydride phases at the interface provides detailed volumetric information from this region of interest. The 3D visualization of the hydrides after 6 cycles is shown in Figure 4-12. The volume fraction of the hydrides is 8.53%. However when selecting the volume only at the distance of up to 1 μm away from the metal-oxide interface the volume fraction is much higher, namely 21.1%. The hydride phases are large and they are mostly interconnected in the reconstructed volume.

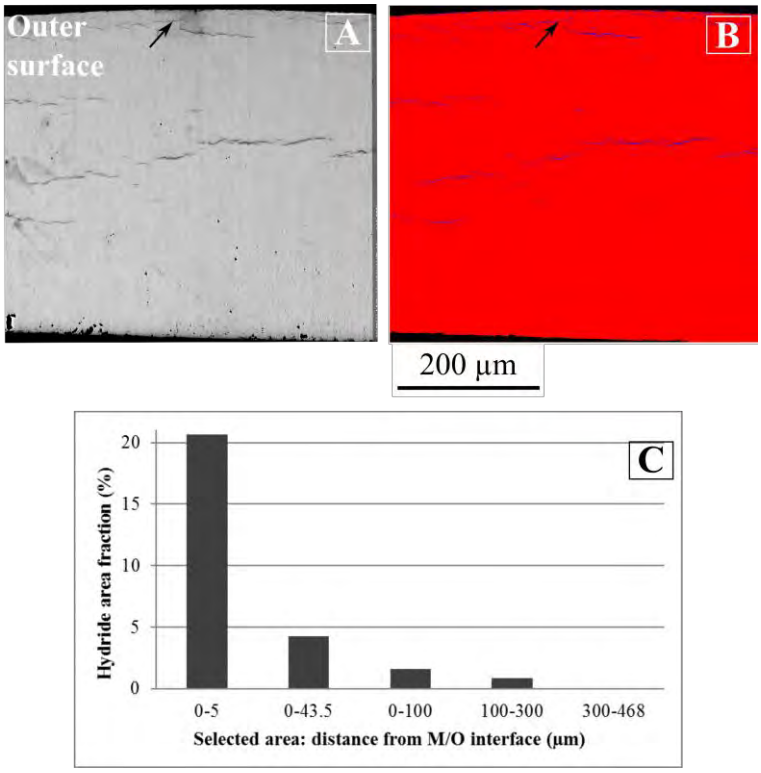

Figure 4-26 (A): BSE image of the full cladding thickness on the 6 cycle LK3/L sample. Hydride is marked by the black arrow. (B): Image from segmentation module from Avizo to quantify hydride surface area. The metal matrix is red and the hydrides are in blue. (C): Graph showing the hydride area fraction in different selected areas.

Table 4-3 The volume of hydrides and metal of the 6 cycle LK3/L sample, extracted from the 3D reconstruction by Avizo. For the detailed description of the estimation of the error, please refer to Section 8.1.1.1 (Error estimation of the FIB tomography results).

Phase	Object	Colour of the object	Volume of the reconstructed object (µm^3)	Total volume of the phase (µm^3)
Metal	Hydrides	Blue	4.96 (± ~0.7)	53.2 (± ~8)

4.4.1.3. Hydrides after 9 cycles

After 9 cycles the H content of the sample is 595 ppm which is far beyond the solubility limit of H in Zircaloy-2 even at service temperature. The hydrides observed in this sample have formed during the long term service life of the cladding and were indeed present at service

temperature. The additional precipitation of hydrogen at room temperature is negligible in the case of this material.

An example of a low magnification BSE image is shown in Figure 4-27 together with the labelled image where red is the metal matrix while hydrides are in blue. The quantification of the hydride area fraction at the surface of this segment is presented (Part (C)). The cladding shows an increasing area fraction of hydrides towards the metal-oxide interface.

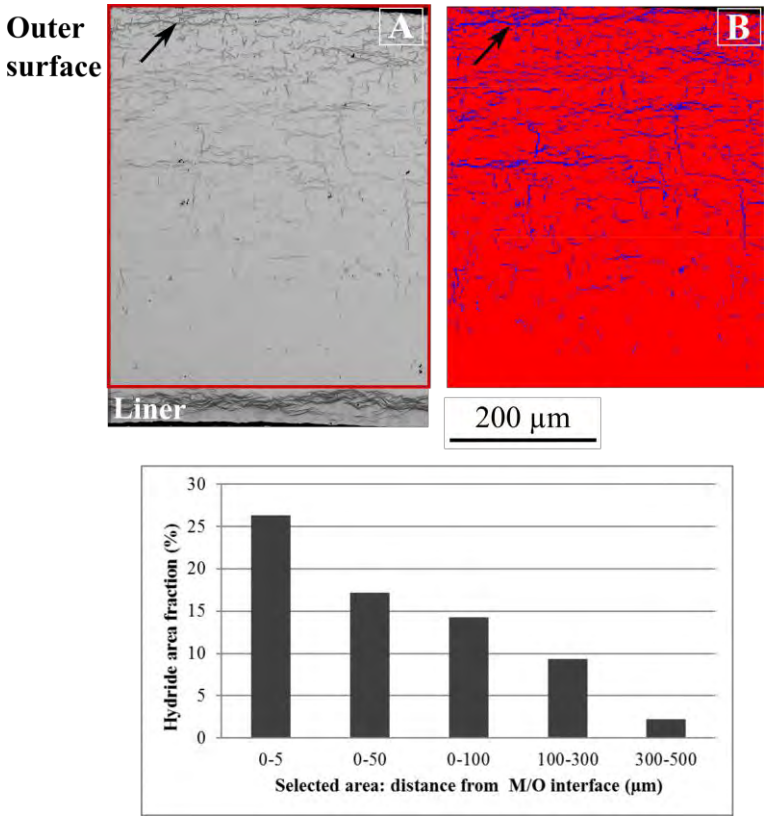

Figure 4-27 (A): BSE image of the full cladding thickness of the 9 cycle LK3/L sample. The red square shows the area used for quantification. A hydride is marked by the black arrow. (B): Image from segmentation module from Avizo to quantify hydride surface area. The liner is not taken into account. (C): Graph showing the hydride area fraction in different selected areas.

The 3D reconstruction of the hydrides at the metal-oxide interface of the 9 cycle sample is shown in Figure 4-23. It shows that hydrides are spatially extended planes with relatively large

surfaces. It could indicate that the supply of hydrogen contributes to the precipitation of hydrides in the vicinity of the existing precipitates, or to allow the growth of existing hydride creating larger hydride precipitates. The hydride volume fraction in the entire volume is 17.2%. In order to characterize the volume very close to the interface, the volume was measured also up to 1 µm distance from the oxide and the hydride volume fraction is 26.3%. An example of labelled hydrides and cracks is shown in Figure 4-28. Hydrides which are large platelet-like precipitates are sometimes extended in more than one grain and are in most places interconnected. It is observed that in the case of those hydrides which touch the interface they are followed by groups of cracks in the oxide such as it is shown in the circled area on the figure. This phenomenon was observed also in the TEM sample at the metal-oxide interface and it is shown in Figure 4-29. In the dark field (DF) image the hydride extended to the interface is visible and the group of cracks in the oxide can be seen in the bright field (BF) micrograph.

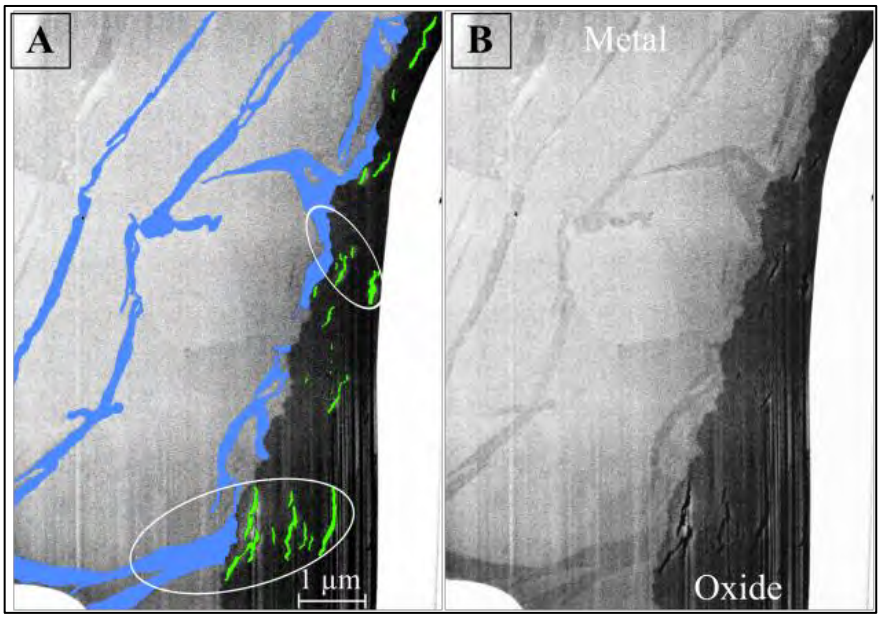

Figure 4-28 One of the SE images used for 3D reconstruction of the hydrides in the metal and the cracks in the oxide at the metal-oxide interface, of the 9 cycle LK3/L sample. (A): Labelled image. Hydrides are in blue and cracks are in green. Circled areas show that the hydrides touching the interface are followed by a group of cracks in the adjacent oxide. (B): Original image.

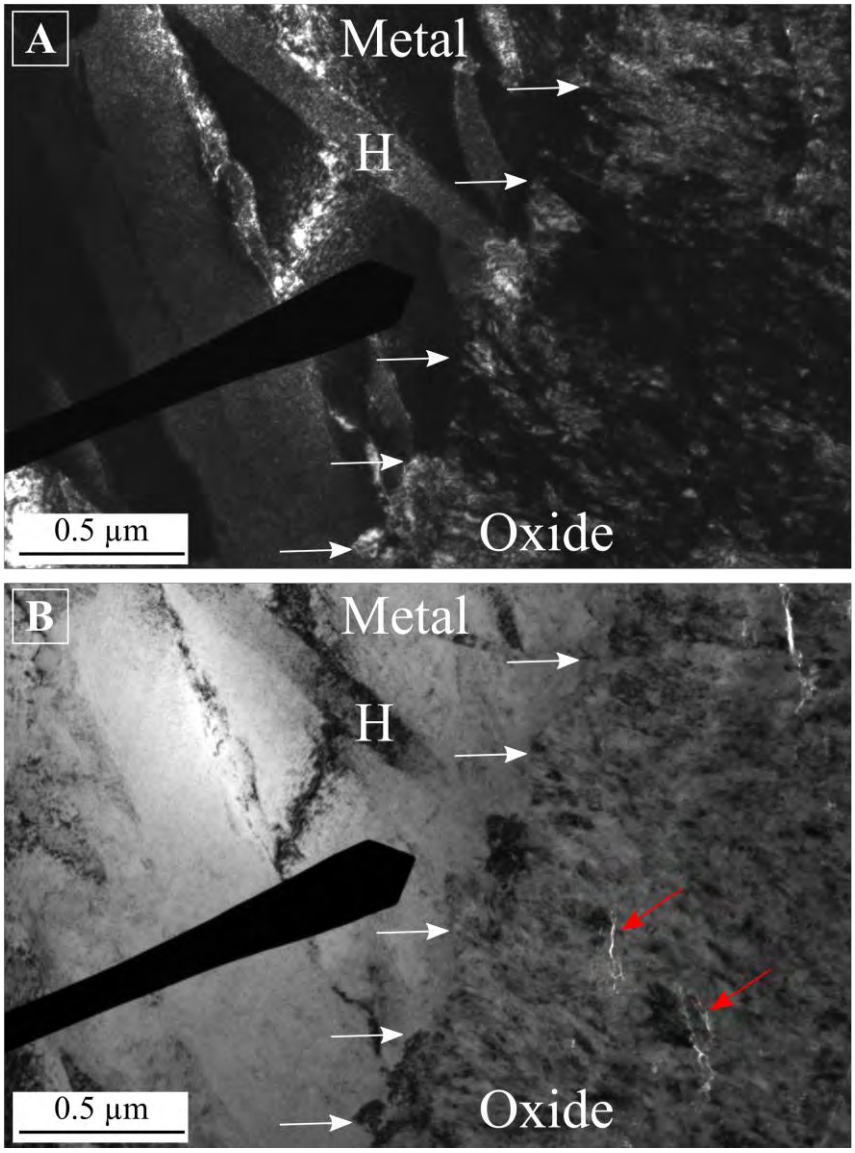

Figure 4-29 DF (A) and BF (A) TEM micrographs of the metal-oxide interface of the 9 cycle LK3/L sample revealing a hydride phase (marked as H) touching the interface (marked by white arrows) and followed by a group of cracks in the oxide side red arrows).

4.5. Discussion of the microstructural evolution of the oxide and the metal and its impact on the hydrogen uptake

In this chapter the microstructure of the metal-oxide interface and waterside oxide of LK3/L Zircaloy-2 claddings after 3, 6 and 9 cycles were reported. The crack microstructure of the oxide in all the three cases was studied creating their 3D reconstruction by FIB tomography. In the case of the high and extreme high burnup samples, i.e. 6 and 9 cycle claddings, the hydrides in the metal at the metal-oxide interface was visualized. Due to the absence of hydride phases in the 3 cycle sample the metal part was not visualized.

Discussion about the 3D reconstruction technique: knowing that the technique has some advantages but also some limitations; we will discuss this aspect in the final Discussion of the thesis. The discussion of the topic is considered knowing the limitations of this methodology.

The 3D reconstruction of the oxides of the 3, 6 and 9 cycle cladding materials showed how the microstructure evolved during the service. The crack volume fraction in the different parts of the oxides has been quantified. In order to compare the microstructural changes of the cladding, the innermost oxide has been separated into two parts: oxide at the metal-oxide interface and the inner oxide. The “inner oxide” is the region up to about 4, 2, and 10 µm from the metal-oxide interface in the case of the 3, 6, and 9 cycle samples. For the "interface oxide" the oxide is up to 1 µm away from the interface. Figure 4-30 shows how the crack volume fraction in the different parts of the oxide changes with the time spent in reactor. It is clear that the crack volume fraction increases with the number of cycles in both regions of the oxide.

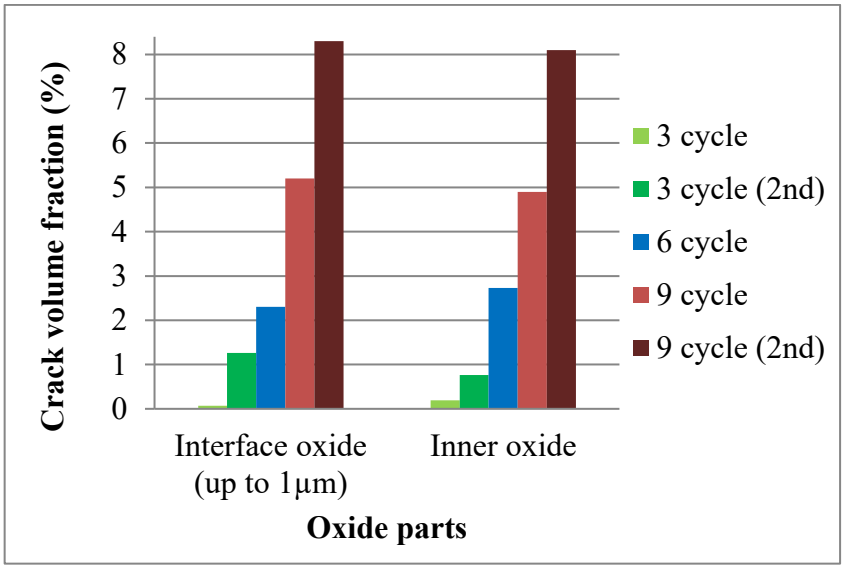

Figure 4-30 The measured crack volume fraction in the full inner oxide (i.e. including the interface oxide) and in the interface oxide for the 3, 6, and 9 cycle samples. The second reconstructions are marked by "2nd".

The oxide was dense in the first three years of the service containing little amount of cracks and micro-pores. This is in agreement with the behaviour of the cladding, i.e. low oxidation and low HPU, in the early cycles (Table 4-1). The outermost part of the 9 cycle cladding's oxide showed similarly low crack volume fraction. In the case of the 6 cycle material FIB tomography was not applied at the outermost oxide, due to the limited time of the study, however the SEM images confirm that its outermost oxide is mainly crack-free. These observations indicate that an already formed oxide layer preserves its microstructure with further service. The large circumferential cracks could be exceptions to this statement.

It appeared that the protectiveness of the oxide layer in the LK3/L Zircaloy-2 is decreasing with time as the crack volume fraction increases with the number of cycles. The material shows a significant increase of H ingress at 6 cycle while the oxidation is slow. In the 6 cycle cladding segment cracks are observed with much higher volume fraction than in the 3 cycle material. The reconstructed oxide includes the part which was formed in the end of the 5th cycle of the

service. The crack volume fraction is 4.35% in this region. A high, 5.30% was measured in the region which is corresponding to the "interface oxide" of the 5 cycle oxide. This is more than two times higher than the interface region of the oxide that formed in the 6th cycle. The crack size are also larger in this 5 cycle region of the 6 cycle sample. This indicates that either a more porous oxide formed before the 6th cycle or indicates to possibility that more than 2 µm oxide layer was formed in this segment between the 5th and 6th cycles Although, during the evaluation exactly 2 µm was taken into consideration as 6 cycle oxide, it is indeed possible that a thicker oxide was formed on this cladding. The oxide thicknesses that are taken from a previous publication [13] in Table 4-1 are not strict and absolute values, and some variation is always occurring from one individual cladding to another. If more, e.g. 3 µm thick oxide was developed during the 6th year then a higher crack volume fraction is to be considered. This could better explain the observed phenomenon, i.e. increased HPUF in the 6th cycle. Importantly, in order to make a statement regarding the 5 cycle oxide the original sample should be investigated.

The microstructure of the oxide in the 9th cycle shows a large number of small cracks in the vicinity of the metal-oxide interface. This implies that the oxide is less protective than in the beginning of the service, and it could have a higher permeability to the oxidizing species. The outer, inner and innermost oxide have been measured in the 9 cycle sample and an increasing crack volume fraction is observed in this order with more than 60 times higher crack volume fraction at the interface region.

The metal-oxide interface of the 9 cycle material showed that the crack volume fraction in the oxide is much higher after the long-term service. The H content is also high. It is concluded that the fine cracks offer faster routes for the hydrogen ingress into the metal and therefore a large number of coarse hydrides are formed in the metal phase.

It is worth noting that increasing crack volume fraction with increasing oxide thickness was shown in recent studies on autoclaved ZIRLO, a widely used commercial PWR material [187], and in Zircaloy-2 [188] by TEM. Tejland et al. reported that the sample having similar composition as the sample presented in the current study showed 0.4%, 1.7% and 2.8% crack volume fraction at 1 μm, 2 μm, and 9 μm oxide thicknesses, respectively. It is difficult to make a direct comparison between materials oxidised in reactor and in autoclave [188]. However, the trend of increasing volume fraction of cracks is present in both cases. In [188] a correlation between the SPP size distribution and the number of cracks in the oxide was shown concluding that SPPs are one of the important factors in the crack formation.

Nevertheless, as mentioned in the conclusion of that paper, "other mechanisms are also present" for crack initiation and growth. In the case of extreme high burnup material, taking into consideration that the SPPs are mainly dissolved, other mechanisms come into action and cause further cracks. In this respect, the distribution and role of hydrides comes into consideration and will be discussed in the following.

The images collected during the slice-and-view process at the metal-oxide interface of the 9 cycle material and its 3D visualization showed that the occurrence of the cracks could be related to the sites of the hydrides at the metal-oxide interface. Figure 4-31 presents a site at the metal-oxide interface where a crack and a hydride are connected to each other at the interface. The hydrides are presented in blue and the cracks in green. It is possible to extend a line into the oxide part from those hydrides which are touching the metal-oxide interface. Doing so, it is clear that a group of cracks can be correlated to these hydrides in the adjacent part of the oxide (shown by a circle in Figure 4-23 and Figure 4-28). As the microstructure of the metal is changed, the oxidation will occur both in the metal matrix and on the hydrides, which have different properties. Therefore, the oxidation of hydrides affects the microstructural properties

of the oxide. In other words, the microstructural changes in the metal at the metal-oxide interface could affect the microstructure of the oxide.

In order to correlate the occurrence of hydrides to the crack formation the crack volume fraction after 3, 6, and 9 cycles is plotted as the function of the hydride volume fractions and it is shown in Figure 4-32; where the hydride volume fraction for the 3 cycle cladding is taken into account as practically 0%. Both parameters are taken at the metal-oxide interface, i.e. up to 1 μm away from it. A strong correlation is observed; however it must be noted that more than three points would be needed in order to prove a statistically strong correlation between two phenomena. A calculation has been carried out as well in order to quantify the amount of "void" created merely by the volume expansion differences between the oxidizing metal matrix and hydrides. The used equations are presented in the Appendix I.

In the case of the 9 cycle material more than half of the formed cracks could be correlated to the hydride oxidation. The correlation between the cracks and the hydrides together with the fact that hydrides are large precipitates after 6 and 9 cycles can be a clear explanation of the increased number of pores and cracks in the vicinity of the metal-oxide interface in the 6 and 9 cycle samples. In other words the oxidation of the hydrides is one of the causes of increasing crack formation in the oxide layer at higher burnups.

Furthermore, it can be claimed that the large stresses induced due to the inhomogeneous distribution of hydrides in the metal, could be responsible to a certain extent for a part of the remaining pore and crack volume. The stress distribution in the oxide has not been the topic of the thesis. The internal stresses of this oxide material have been studied by micro-XRD [189].

Another aspect which is to be taken into account at higher burnups is the hydride formation in the metal matrix. The effect of the formed hydrides on the microstructural changes of the material is described in this chapter while in the following chapter (Chapter 5) the caused compositional changes will be described. After reaching the solid solubility limit of H in the metal all the excess hydrogen above this limit will be in a precipitated hydride phase. Due to the fact that all measurements were carried out at room temperature an overestimation of the size and volume of the hydride phases is unavoidable, compared to that present at service temperature. H content was measured as 44 ppm in the 3 cycle samples, therefore hydride precipitates are not expected at this stage of the service. The H content was measured to be 202 ppm in the 6 cycle sample and 595 ppm in the 9 cycle sample. These values are highly above the solubility limit of H in Zr or Zircaloy-2 even at the service temperature. This suggests that most of the H was present as precipitated hydride phases even during the service, in particular for the 9 cycle sample. Memory-effect of Zr-hydrides was demonstrated by heating-cooling cycles, and it was shown that the hydride locations prior to heating strongly influence the subsequent hydride nucleation and growth after cooling [190]. Therefore, we assume that those hydride precipitates which were investigated during this study (both in TEM and SEM) have been at the same site during the service and that they show their characteristics as it has occurred during service.

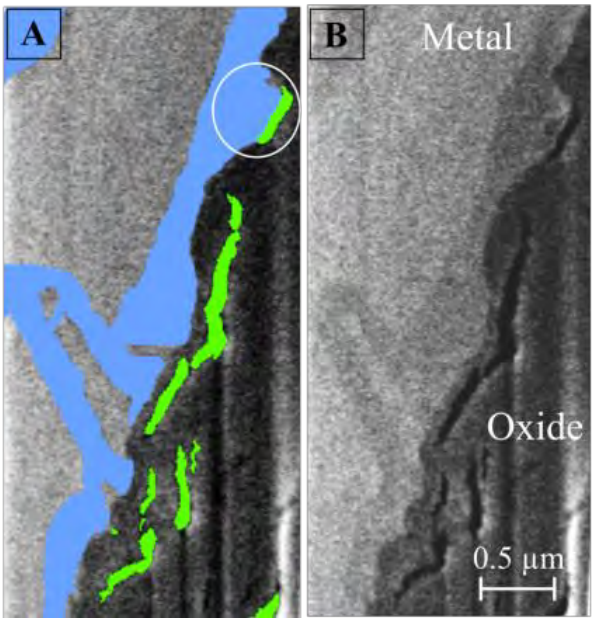

Figure 4-31 (A): Segmented and (B): original SE image of a connected hydride (blue) and crack (green) at the metal-oxide interface (in the circle).

It is worth noting that in the case of the 9 cycle material, the power history was not typical for late life of cladding. The power history is provided in Chapter 3 and in reference [33] in more details. Also, this cladding had been taken out from the reactor for investigation after 6 cycles. The cooling of the rod could have an influence on the microstructure, for example it could be postulated that large circumferential cracks in the oxide are due to this cooling, however, this is not certain. It is unlikely that these large cracks have been formed directly due to the hydride oxidation. The observations indicate that hydrides create small micro-cracks when they oxidize. However, the possibility remains open that due to the increased micro-crack formation, some sites of the oxide will be particularly weak with low resistance against crack propagation. Therefore an opening of such large crack in the oxide under stress could be indirectly induced by the hydride oxidation.

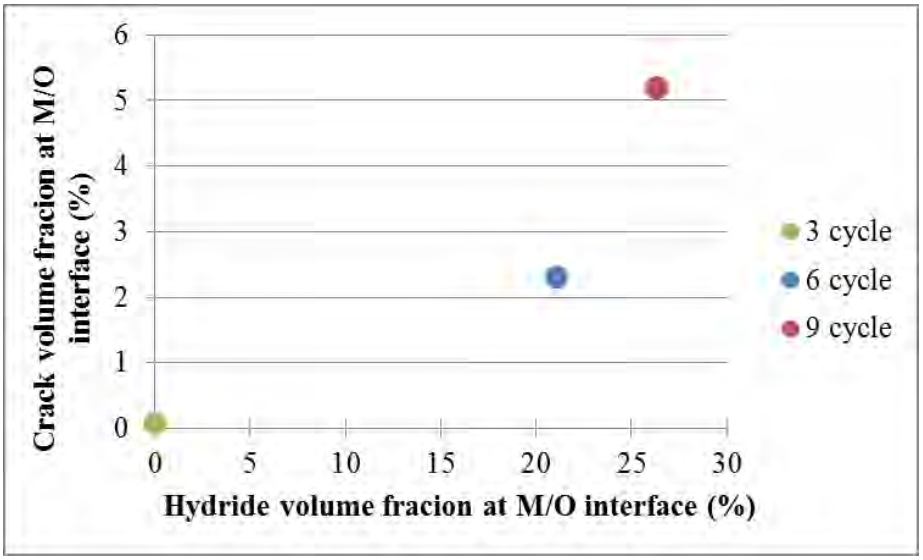

Figure 4-32 The crack volume fraction in the oxide versus the hydride volume fraction in the metal after the investigated service times.

The undulation of the interface was also observed. The acquired images at the metal-oxide interface of the three claddings show that the morphology of the interface is different after low and high burnups: in the case of the 3 cycle sample the interface is irregular while after 6 and 9 years it becomes more regular. Besides the microstructure of the metal and the oxide, the morphology of their interface changes as well during the service. As it has been described in the literature review (Chapter 2) a more undulated interface could result in a better stress distribution and a higher resistance against cracking in the interface region of the oxide. This could affect the oxidation behaviour and H-uptake of the material.

It is to be mentioned that multiple transitions are observed during autoclave oxidation and it is probable that the same type of transition can occur for in-reactor oxidation as well. During the autoclave tests regular sampling for the determination of the oxidation process and the oxide thickness as a function of oxidation time is performed. It is therefore, possible to correlate the oxide transition points to the tetragonal to monoclinic transformation and to determine the stress that is involved in the transformation. In the same manner, a relationship could be established

between the number of transitions and the number of cycles that the material spent in the reactor. This would help to understand how the transition of the oxide influenced the cracking of the oxide in the reactor and as a consequence, the HPU. Although this could be an important factor in the better understanding of the increased HPU at late life, the samples studied in this thesis are very scarce to perform such correlation, and no such data is available to correspond the cycles to the number of transitions of the oxide.

4.5.1. Summary

As a summary of the above described discussion, a schematic drawing is presented in Figure 4-33. In Part (A) the metal-oxide interface is shown at the early stages of oxidation. Low amount of pores without interconnection are present in the oxide.

Figure 4-33-(B) shows the metal-oxide interface and the outer oxide at the late stages of oxidation. Change in the amount of pores and the appearance of interconnected micro-cracks describe the oxide at this stage of the service. One of the causes of the increased crack production is the oxidation of large hydrides in the metal. When more and more interconnected micro-cracks occur they offer fast route for the ingress of H and oxidizing species. This causes increased H-uptake at late life service of the LK3/L cladding.

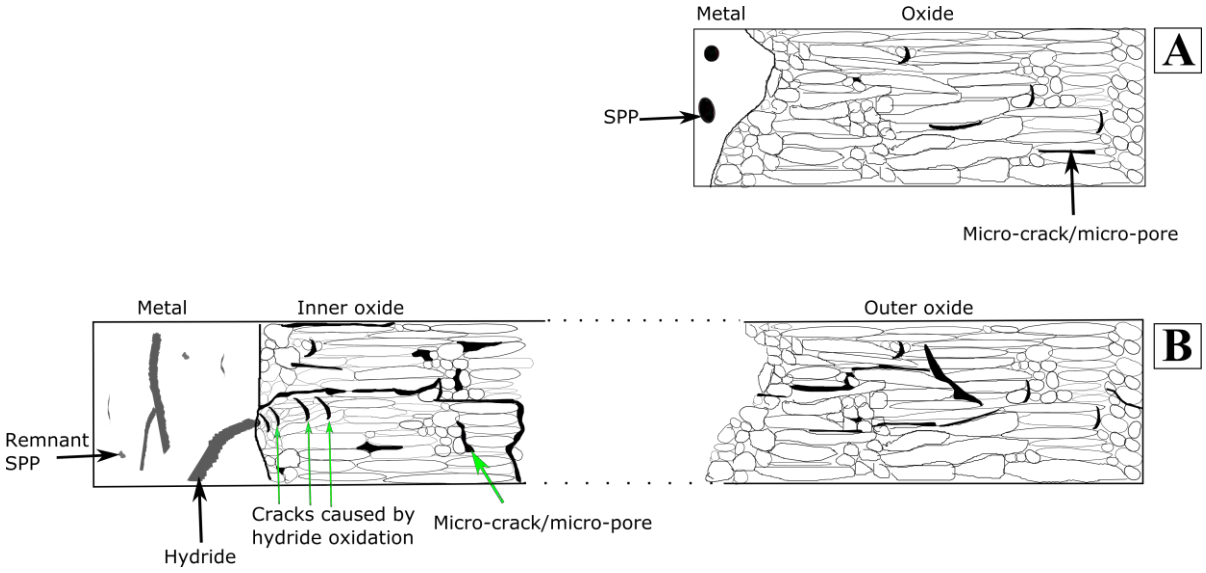

Figure 4-33 Schematic drawing of the oxide and metal-oxide interface at different stages of service. (A): Early stages of oxidation, i.e. corresponding to the 3 cycle sample. Small amount of micro-pores. (B): During late life service (e.g. 9 cycle sample) the oxide shows interconnected pores, cracks are produced by hydride oxidation near the interface. Dotted region represents a long distance between the inner and outer oxide which is not presented in details in the figure.

4.6. Conclusions

In this chapter the microstructural characterization of the LK3/L Zircaloy-2 BWR cladding has been provided in details. The main objective of this chapter is to correlate the microstructural changes to the change of oxidation and HPU behaviour of the cladding from medium level up to high and extremely high levels of burnups.

The microstructural evolution of the oxide and metal parts on three irradiated materials with medium and high burnups are observed by TEM, SEM and FIB tomography. From the comparison of the data obtained from these cladding materials and also using some previous observations (i.e. H-content and oxide thickness data) the following can be concluded:

- The 3D FIB reconstruction of the oxide microstructure reveals the presence of an impervious oxide layer in the early stages of oxidation, in particular up to the third cycle. The volume fraction of cracks in this oxide is negligible.
- The outermost oxide of the 6 and 9 cycle samples (i.e. the region which was formed in the first 3 cycles of the service) also contains low amounts of crack. FIB tomography gave the same order of magnitude in the 9 cycle sample's outer oxide as that of the 3 cycle oxide. This means that an oxide layer that already formed will not change significantly with further service in the reactor. The large, continuous circumferential cracks however could be exceptions, as they have formed most probably by the stress relaxation of the oxide at a certain point of time which is most probably not the time of formation of the given oxide layer.
- The crack volume fraction of the inner oxide, i.e. the freshly formed oxide increases with the service time. In other words the oxide formed in the 9^{th} cycle shows the highest number of cracks per unit volume while the oxide formed in the 6^{th} cycle shows an intermediate value between the 3 and 9 cycle samples. Enormous change is observed in the oxide microstructure and morphology between the 3 and 9 cycle cladding at the interface.
- In the 9 cycle sample the crack concentration shows tendency to increase towards the interface where the oxide looks practically porous.
- After 6 and 9 years the metal contains large hydrides. The occurrence of cracks in the 9 cycle oxide can be related to the location of the hydrides in the metal which reach the interface. Along the extension of these hydrides, cracks are revealed in the oxide. At those sites at the interface where no hydride reaches the interface, the oxide generally contains no cracks. This shows that the oxidation of the hydrides could induce or

promote the crack formation in the oxide. This could be one of the reasons for the increased crack volume fraction. Therefore, the protectiveness of the oxide is reduced which, in turn, could cause an increase in the oxidation rate and the H-uptake of the material.

- The in-depth study of the fine micro-cracks in an oxide are possible by means of 3D-FIB tomography. This powerful technique allows the investigation of the oxidation phenomenon and gives reliable quantification about the size of the different objects.

- Results on the LK3/L Zircaloy-2 show that the presence of hydrides induces higher volume fractions of micro-cracks in the oxide at extreme high burnups, which in turn reduces the overall protectiveness of the oxide to oxidation and HPU. However, it is important to indicate that the material is still resistant to rapid oxidation even after 9 cycles, though it shows a higher oxidation and hydrogen pickup rate.

Some of the parameters leading to a change of oxidation and hydrogen uptake have been demonstrated, with the morphology and the micro-crack distribution of the oxide in the main focus of this chapter. As it has been already noted in the literature review other studies have shown that several other parameters such as stoichiometry, space charges and conductivity, composition and other factors come into consideration, see for example [13], [191], [109], [170], [151]. From these factors, the compositional and microstructural changes are in the scope of this thesis; and some of other properties (e.g. conductivity of oxides of the different samples) are being investigated in the scope of other PhD work in the continuation of this project, in the Nuclear Fuels group.

5. LK3/L TYPE ZIRCALOY-2 – PART 2: CHEMICAL CHANGES

5.1. Introduction

The results of the chemical analysis of the LK3/L type Zircaloy-2 samples provide the compositional evolution of the cladding, and are presented in this chapter. The characterization of the samples from μm to nm range is provided by two techniques:

(1) EPMA is used for overall information regarding the element distribution in large-scale by qualitative maps. The local chemical composition is measured by quantitative point analysis.

(2) TEM and ChemiSTEM provide high spatial resolution for the composition at nanometric scale.

EPMA data is presented first, followed by the TEM results. The description of the results starts with the un-irradiated material, followed by the 3 cycle, the 6 cycle (for EPMA only), the 7 cycle (for ChemiSTEM only), and the 9 cycle sample.

5.2. Chemical changes in the material

The behaviour of Zr-based cladding is controlled by many parameters. One of the most important ones is the chemical factor, i.e. the added alloying elements (type and amount), and the distribution and size of SPPs. The exact chemical composition of the alloy together with its specific heat treatment provides the starting material as cladding. However once the service starts in the reactor the material begins to change immediately. Therefore, the chemical state of the cladding is not fixed; it is a dynamically and continuously changing parameter. The overall

and local chemical measurements at different stages of irradiation help to better understand the compositional evolution of the cladding and how the different alloying elements are distributed. The final aim is to determine how these changes influence the oxidation and the HPU properties of the alloy.

5.2.1. Analysis of the samples by EPMA – Dissolution of SPPs and the behaviour of dissolved alloying elements

Initially, the alloying elements which have low solid solubility limit in the Zr matrix (Fe, Ni, and Cr) are in the form of SPPs while Sn is homogeneously distributed in the matrix. As soon as the cladding is placed in the reactor's high temperature water, the irradiation together with the oxidation and the HPU changes the cladding's microstructure and the composition. As mentioned before, due to neutron irradiation, SPPs start to dissolve and defects form in the Zr lattice. This could affect the oxidation and HPU properties. The oxide forms at the metal-oxide interface [12], [52] and the metal which transforms into oxide is not the same after many years in the reactor compared to the beginning of the service (or to any other irradiation stage) [29], [14]. In fact, the material is continuously changing, both in terms of composition and microstructure [14], [29], [178], [172]. The dissolved alloying elements can affect the oxidation and HPU properties of the material (described in Chapter 2 – Section 2.4.2). Therefore studying the distribution of the dissolved elements could improve the understanding of the changes in the oxidation and HPU properties during service.

In the following the dissolution of the SPPs and subsequent distribution of the dissolved elements after different residence times is described. Quantitative point analysis and qualitative elemental maps are presented. A colour scale is provided for the maps, which indicates only the

relative concentration levels for the given element. The colour scale indicates increasing concentration towards white. The concentration levels (i.e. the exact concentration values corresponding to a given colour in the colour code) are different for each map, and not comparable to each other. When it is presented, oxygen map is shown in grey scale coding. It is worth noting that some small concentration changes in the EPMA maps may be more visible on the online version of the thesis.

For most of the EPMA point line-scans (a point line scan is a series of quantitative point analyses which are carried out along a straight line, so that although they are similar to a line scan, they are individually quantitative and are separated by a fixed distance) for all types of materials the ratios of the alloying elements to Zr are shown or also shown together with the raw dataset (as an example, refer to Figure 5-2 (B) and (C)). This ratio has an importance when the composition is compared in the different phases, for example in oxide and in the metal or in the hydrides. When comparing different phases of the sample the ratio will indicate the actual concentration value of the alloying elements with respect to the concentration of Zr in the given point and this helps to avoid a misleading impression which only occurs when the raw result are used for the comparison of the alloying elements in these different phases. As an example of this issue, Figure 5-1 is presented, where Part (A) shows the collected raw data on the metal-oxide interface of the 9 cycle sample, while in (B) the ratios to Zr are shown. When only the metal composition is discussed there would be no need for using the ratio of the elements to Zr. However, in order to make the comparison in the future easier, the ratio is also given for the metal measurements.

In general the point line-scans measured the composition along an extended length of the sample, e.g. from the metal till the outermost oxide. However due to the obvious compositional

differences of some regions even in the same phase, the long point line-scans have been subdivided into smaller ranges and data points acquired within have been used for characterizing only the selected region of the material.

In many cases only the matrix composition is studied, and the values of the SPPs are not taken into account. For this the point line-scans are plotted first and the prominently high concentration data points are taken out as SPPs. For an automatically analysis of the results by mathematical methods would need to establish an average concentration corresponding to the matrix and then removing all data which deviate from this average value. As in that case, the SPPs had to be included from the beginning and it could cause an error, it was decided to perform a manual selection of SPP values to exclude them from the calculations. It is possible to estimate the range of values corresponding to the matrix concentration, by simple visual inspection. In this manner, 80-90% of the points selected will belong to the matrix. It must be emphasized that this is an estimation for the matrix value and it could be slightly different depending on the observer. When presenting the average matrix compositions, the number of data points extracted from a given point line-scan varies due to the number of SPPs taken out for the different alloying elements (as an example, Cr could be removed from the Cr data set, but not Ni, Sn and even Fe which has dissolved from the SPP).

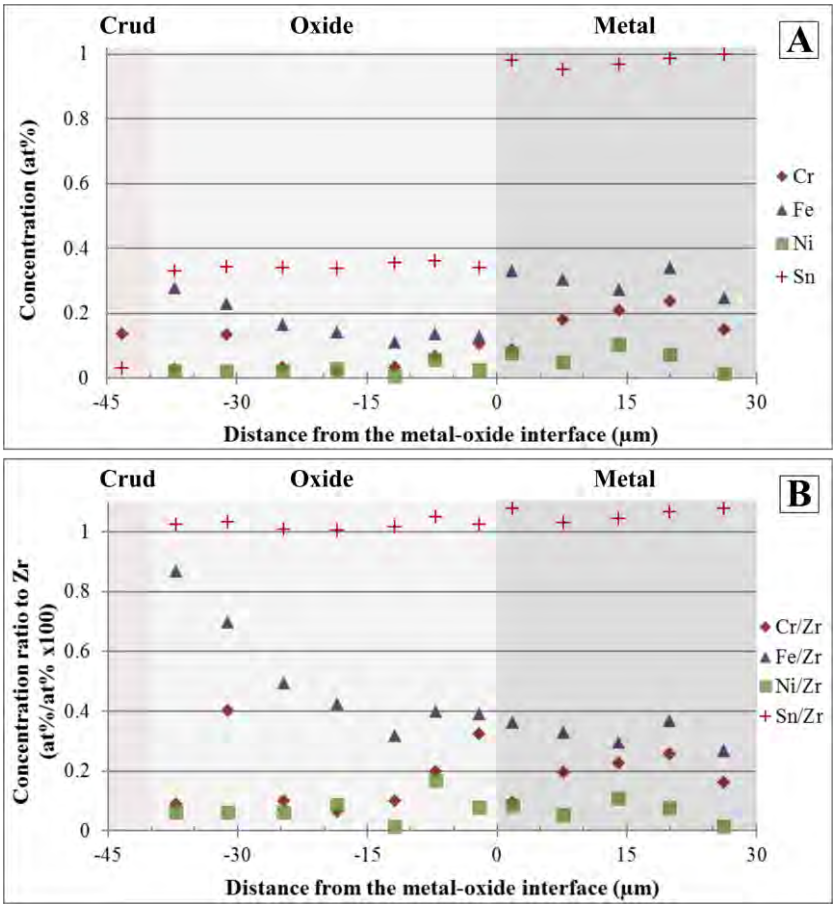

Figure 5-1 An example image of an EPMA line-scan on the 9 cycle LK3/L sample, through the metal-oxide interface showing the raw data points (A) and the element ratios to the Zr matrix (B). The issue of the sudden change in composition due to the difference in phases is visible on (A).

5.2.1.1. The chemical composition of the un-irradiated material

The un-irradiated cladding of this Zircaloy-2 grade has been studied before and the microstructure is available, as well as the compositions of the two families of SPPs [29], [14]. In this study the extra information is from the GB segregation, in order to observe the initial state of the material, i.e. before irradiation, and only ChemiSTEM measurements are available on the archive material (refer to section 5.2.2.).

5.2.1.2. The chemical composition after 3 cycles

Chemical analysis of the metal after 3 cycles

A long EPMA point line-scan on the metal part of the 3 cycle LK3/L sample is shown in Figure 5-2.

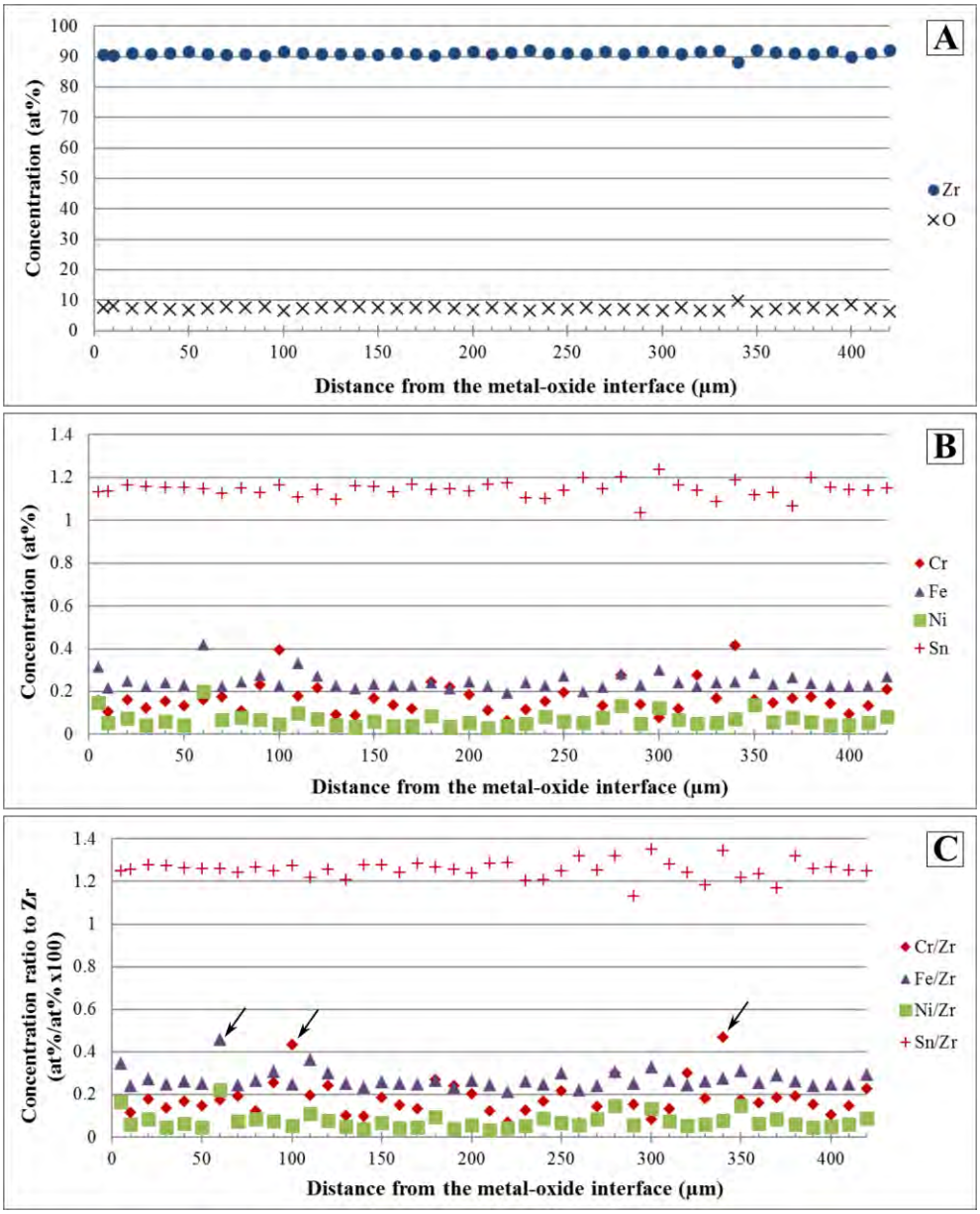

Figure 5-2 EPMA point line-scan (acquisition parameters: 15 kV, 240-260 nA, 2 µm beam diameter) in the outer 480 µm of the metal part of the 3 cycle sample. A: Zr and O; B: Element concentrations in at%; C: Element concentration ratios to Zr. Arrows indicate some precipitates.

Part (A) of Figure 5-2 shows the Zr and O signals. Part (B) and (C) show the alloying element distribution. Here the vertical scale is much finer therefore the fluctuations in the element concentrations are well-observable.

The Fe content in the matrix changes between 0.19 at% and 0.25 at%; the Ni content is between 0.028 and 0.082 at%. The value of the Cr concentration varies between 0.061 and 0.19 at%. Signals coming from both types of SPPs are detected. Although the EPMA is not usually used to determine the maximum concentration of alloying elements in the SPPs due to the large interaction volumes compared to the average size of SPPs, the maximum concentrations determined by direct point analysis on the SPPs are reported and it is as follows: 1.68 at% Cr and 0.36 at% Fe for a $Zr(Fe, Cr)_2$ and 2.11 at% Ni and 2.86 at% Fe for $Zr_2(Fe, Ni)$. In order to be able to locate the SPPs previous maps are used.

Cr signal shows the largest scatter due to the slow dissolution of Cr from the SPPs resulting in a higher number of $Zr(Fe, Cr)_2$ in the material. Therefore during the point line-scan the beam can hit either a Cr containing SPP or low-Cr concentration site in the matrix. Not all of these SPPs contain Fe which is already dissolved from most of the $Zr(Fe, Cr)_2$ particles as it can be observed on the maps (Figure 5-3). Therefore the signal of Fe does not have the same scatter as Cr. One reason for this difference in the behaviour between Cr and other alloying elements could be the different diffusion coefficients of these species in the Zr [192]. No specific behaviour of the alloying elements is observed in terms of the bulk metal except for the metal close to the metal-oxide interface. Sn is relatively homogeneously distributed in the material, its variation is due to the SPPs which contain less Sn than the metal matrix.

The maps in Figure 5-3 show the metal 5 μm away from the interface. The number of the Cr containing SPPs is the highest and most of them do not contain detectable amounts of Fe. In the maps of Cr, Fe, and Ni, a lower concentration region can be observed around most of the

SPPs. An example is shown for Ni in the inset of the Figure: the green area around the red spot is what is referred to as lower concentration region. These regions can come from two sources simultaneously: i) the known fact that SPPs dissolve is one of the causes; and ii) the resolution limit of EPMA can also contribute to the appearance of these low concentration regions.

The average alloying element concentration of the metal matrix (not including the SPPs) is given in Table 5-1 together with the metal at the metal-oxide interface, i.e. within 1.5 µm from the metal-oxide interface. For the calculation of the average value in the bulk metal 7 point line-scans were used, including 73-109 data points in total; depending on the alloying element. In order to calculate the average metal composition at the Metal-oxide interface 6 point line-scans were used extracting a total of 9-11 points out of all of them.

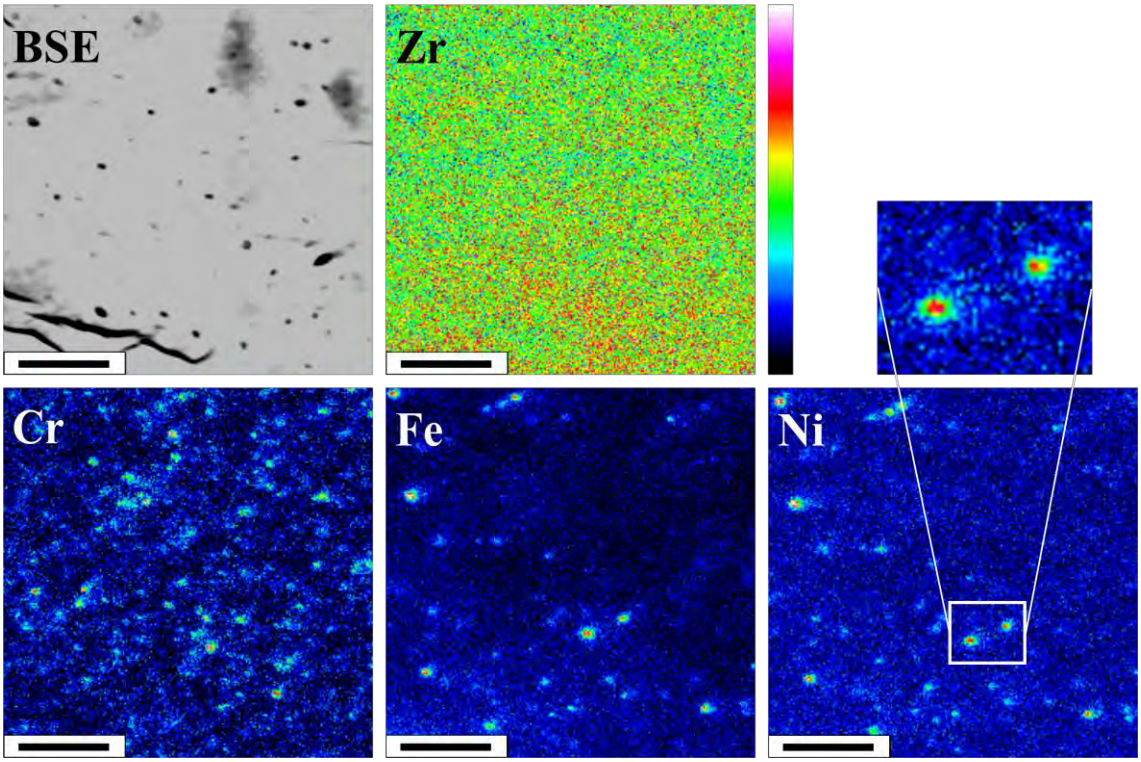

Figure 5-3 BSE micrograph and elemental maps (acquisition parameters: 15 kV, 240-260 nA, spot size) on the metal 5 µm away from the metal-oxide interface of the 3 cycle LK3/L sample. The inset shows the enlarged area of two SPPs; lower concentration regions (green regions) around the core of the SPPs (in red) are observable. The scale bar is 5 µm.

In Figure 5-4 the average composition of these two regions are plotted in order to better visualize the differences. The metal at the metal-oxide interface is slightly enriched by Fe and Ni. The difference is systematic and the individual point line-scans show this slight increment towards the interface. One example for a map and a line scan through this region is presented in Figure 5-5 and Figure 5-6. The Fe map confirms this observation. In the case of Ni however this average change of 0.02 at% does not show itself significantly. This could be due to the fact that the intensity range of the maps is aligned in such a way so that the minimum and maximum measured concentrations on a given area of measurement are fixed on the colour scale, i.e. the areas with the lowest concentration of a given element (e.g. in the matrix) are black while the areas with the highest concentrations appear as white (e.g. Fe and Ni in the crud) on the map. As the crud is also included the concentration values are stretched in a large range of concentration values therefore such a slight change could be no more visible.

The Fe, Cr, and Ni concentrations in the metal matrix are unexpectedly high while the SPPs measured show low concentrations. This can be explained by the nature of the EPMA measurements and the size of SPPs in the material, in other words the large interaction volume together with the high number of small SPPs. As there are still many SPPs after 3 cycles it is very probable that even when the aim is to measure only the matrix, some interaction occurs with an underlying SPPs due to the large interaction volume. In turn, when the SPPs are measured by point analysis directly on them, the beam interacts with the surrounding metal matrix as well. This induces a certain error for the measurements. The trends presented regarding the element distribution are important and give precious information about the chemical evolution.

Table 5-1 Average element concentrations in the bulk metal and at approximately 1.5 µm from the metal-oxide interface of the 3 cycle sample. Only the metal matrix is taken into account (SPPs excluded).

Phase	O (at%)	Zr (at%)	Sn (at%)	Cr (at%)	Fe (at%)	Ni (at%)
Bulk metal	7.91	90.49	1.14	0.12	0.22	0.056
Metal close to the metal-oxide interface	9.02	89.40	1.10	0.12	0.27	0.077

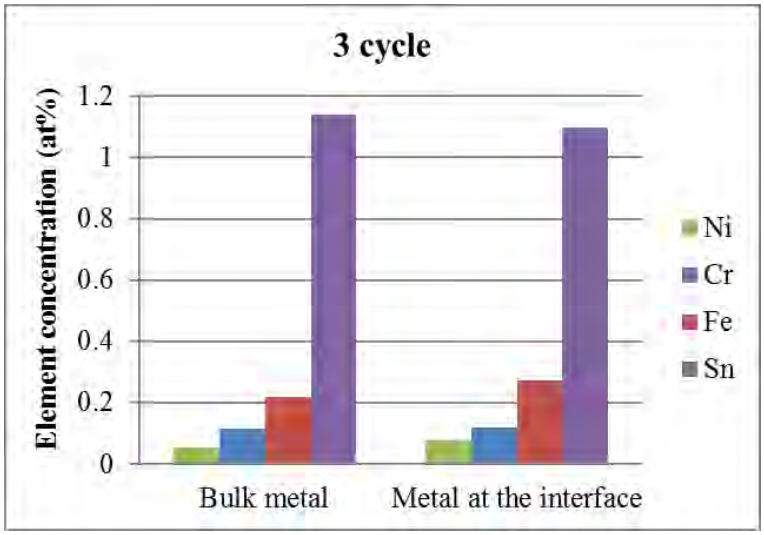

Figure 5-4 The average element concentrations at the different regions of the metal matrix of the 3 cycle LK3/L sample measured by EPMA.

Chemical analysis of the oxide and the metal-oxide interface after 3 cycle

Figure 5-5 presents the BSE micrograph, the EPMA maps on the full oxide together with the outermost part of the metal. The dissolution of the SPPs both in the metal and the oxide is detected. Based on this and many other maps, the number of SPPs in the oxide is significantly lower than that in the metal. This can be explained by the higher diffusion coefficient of the elements in the oxide together with the fact that the SPPs dissolve in the oxide even when no irradiation is present [105], [103]. In un-irradiated and in-situ oxidized Zircaloy-4, Fe and Cr were shown to diffuse to the outermost surface of the oxide once the SPP is incorporated into

the oxide [105]. We could assume that similar phenomenon is valid in this material. As the oxide layer is very thin at this stage there is a short diffusion path for the alloying elements.

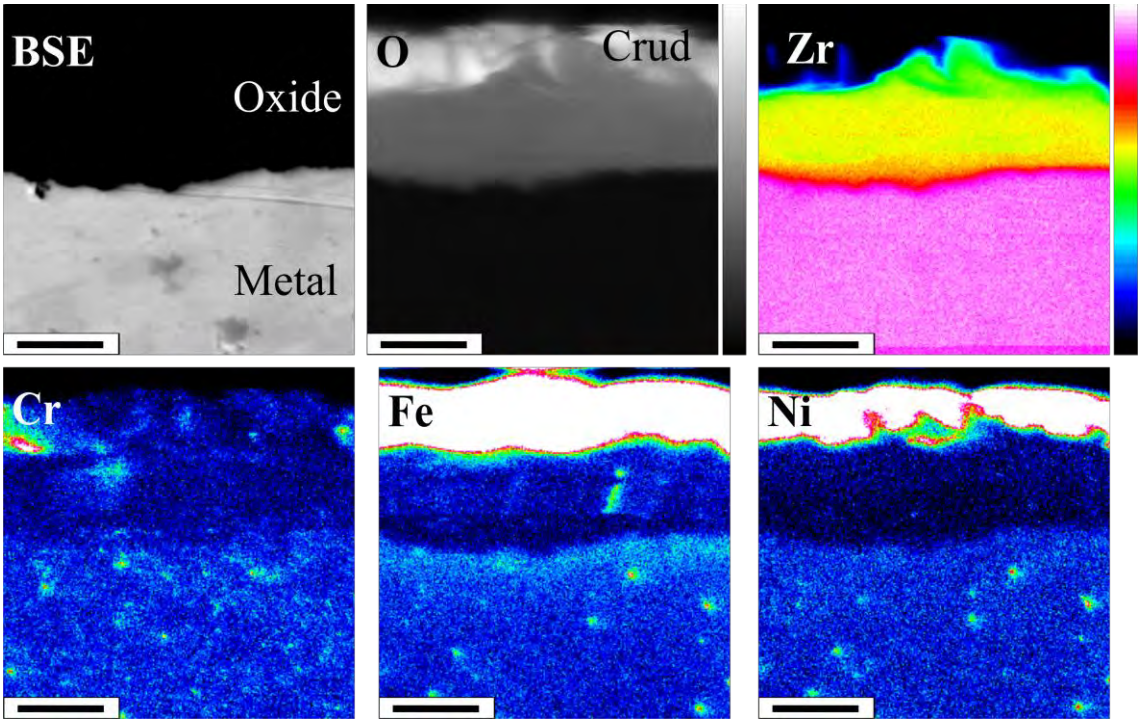

Figure 5-5 BSE micrograph showing the metal part only and EPMA elemental maps (acquisition parameters: 15 kV, 240-260 nA, spot size) of the outer region of the 3 cycle LK3/L sample. The scale bar is 5 µm.

While the interface is enriched in Fe and Ni at the metal side, the oxide at the interface seems to be depleted of these alloying elements. The possibility of detecting an artefact due to sample preparation was tested and excluded during the study; refer to Appendix II for details. A quantitative point line-scan through the metal-oxide interface is shown in Figure 5-6. As the two phases are compared here, the element ratios to Zr is given.

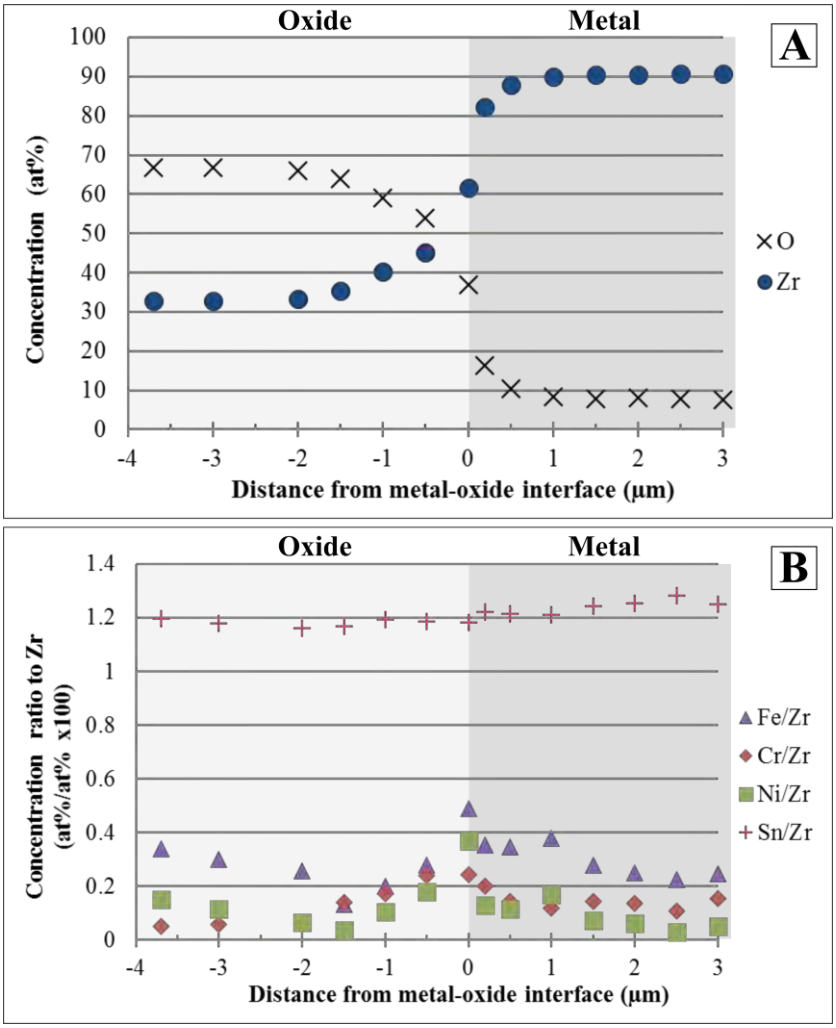

Figure 5-6 EPMA point line-scan through the metal-oxide interface of the 3 cycle sample (acquisition parameters: 15 kV, 240-260 nA, spot size). (A): Zr and O; (B): Element concentration ratios to Zr.

The full oxide scale is included in this scan. A step-like transition of the element concentrations through the interface and a valley of concentrations in the oxide is observed. Furthermore, a slight increment in the concentration of Fe and Ni towards the outermost part of the oxide is revealed. Cr does not show significant scatter in the oxide as the SPPs are mostly dissolved in the oxide. The element distribution shows a trend in the oxide, therefore it was necessary to separate the oxide layer into three parts and the average concentrations for these regions are given in Table 5-2. The different parts are as follows: the innermost 1.5 µm of the oxide is called “Inner oxide”; the “Outer oxide” is the outermost 1 µm or 2 µm (depending on the oxide

thickness which varies between 4 µm and 6 µm in this segment). The oxide layer in between these two regions is the "Intermediate oxide". These parameters were selected based on the maps and point line-scans. Concentration is given in at% instead of ratios to Zr as only the oxide is discussed and no comparison is given to another phase. For the values with ratios to Zr please refer to the Discussion section of this chapter. In the case of the inner oxide: 7 point line-scans and 10-12 data points were used. For the intermediate oxide: 7 point line-scans and in total 12 data points while in the outermost oxide: 7 data points are collected from 5 point line-scans. In Figure 5-7 the data is plotted for better comparison. An increasing average Fe and Ni concentration can be observed towards the outermost oxide. The inner oxide seems to contain slightly higher amount of Cr. The tin ratio to Zr shows that its concentration does not change. In the case of Fe, the explanation of this phenomenon could be the intrinsic behaviour of Fe to dissolve from the SPPs as soon as it is incorporated in the oxide and diffuse to the outer surface.

Table 5-2 Average concentrations of the different regions of the oxide matrix of the 3 cycle LK3/L sample. Inner oxide: up to 1.5 µm from metal-oxide interface; Intermediate oxide: 2-3 µm from metal-oxide interface; Outermost oxide: 4-6 µm from metal-oxide interface depending on the thickness of the oxide.

Phase	O (at%)	Zr (at%)	Sn (at%)	Cr (at%)	Fe (at%)	Ni (at%)
Inner oxide	62.96	36.47	0.43	0.04	0.056	0.019
Intermediate oxide	66.22	33.24	0.40	0.028	0.077	0.027
Outermost oxide	66.23	33.22	0.40	0.024	0.094	0.040

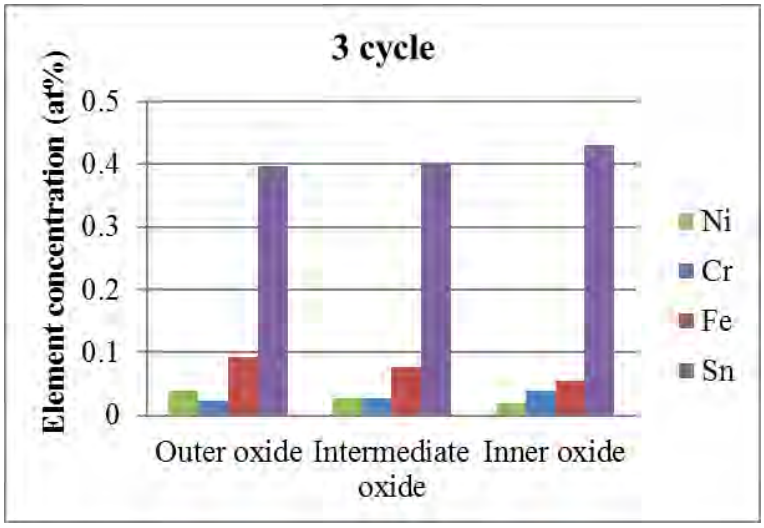

Figure 5-7 The average element concentrations at the different regions of the oxide of the 3 cycle LK3/L sample measured by EPMA.

5.2.1.3. The chemical composition after 6 cycles

The 6 cycle sample represents a high burnup and it is close to the average life-time of a cladding in KKL.

Chemical analysis of the metal after 6 cycles

A typical point line-scan for the large-scale composition of the bulk metal is given in Figure 5-8. The step size between each point is 10 µm and the outer 200 µm of the metal is presented. In Part (A) of the Figure the Zr and O signals are shown, while the alloying element distribution is presented in Part (B) and Part (C). This latter gives the element concentration ratios to Zr.

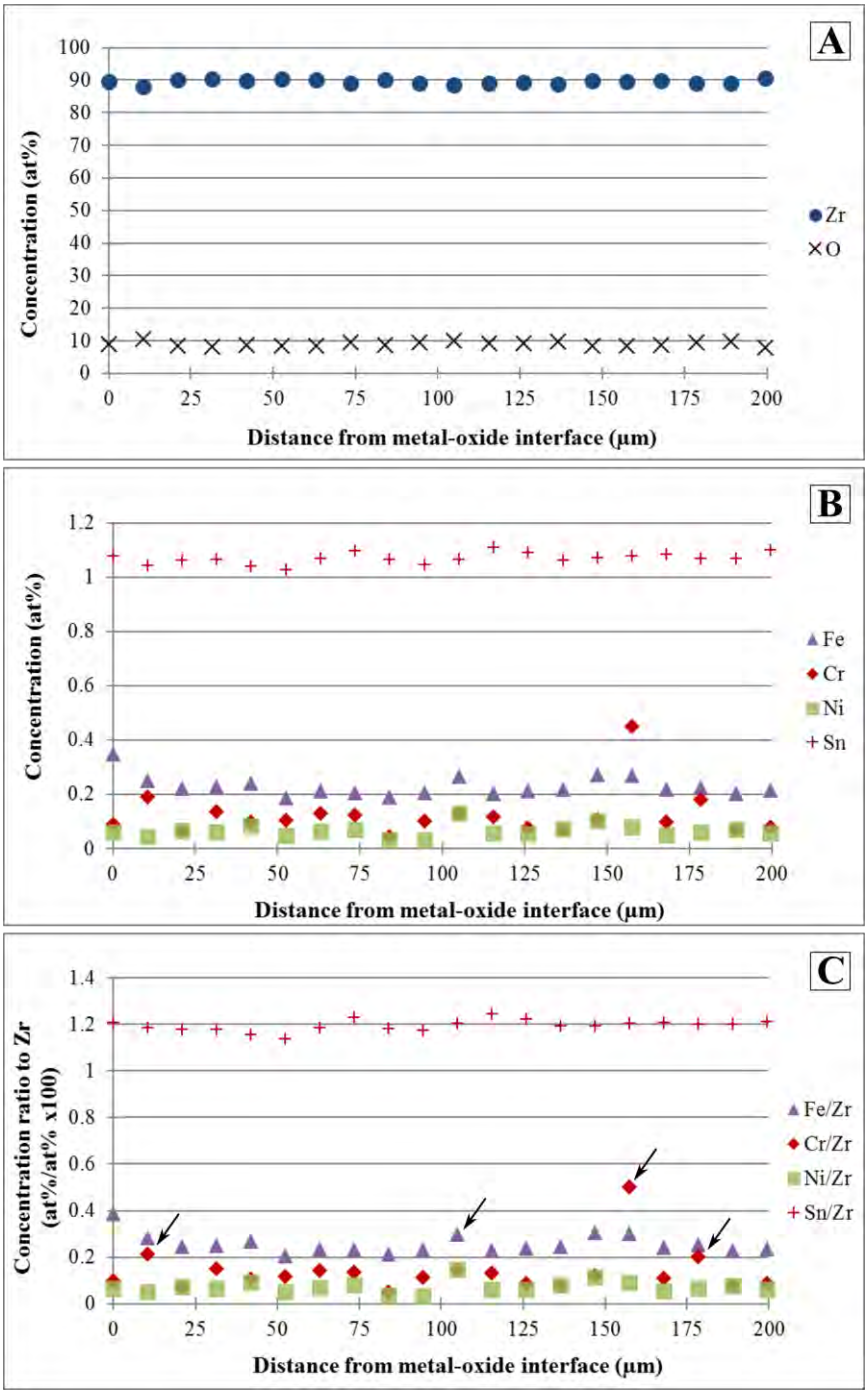

Figure 5-8 EPMA point line-scan (acquisition parameters: 15 kV, 240-260 nA, spot size) from the oxide to the outer 200 µm of the metal of the 6 cycle LK3/L sample. (A): Zr and O; (B): Element concentrations in at%; (C): Element concentration ratios to Zr. Arrows indicate some SPPs.

Using four point line-scans acquired on the metal, in the bulk metal matrix only (i.e. SPPs are excluded, as well as the region close to the metal-oxide interface): it is observed that the Fe content changes between 0.19 at% and 0.36 at%; the Ni content is between 0.03 and 0.084 at% while the amount of Cr varies between 0.045 and 0.18 at%. The maximum value for Fe is high due to the concentration increment towards the metal-oxide interface which, for some of the point line-scans, starts from 4-5 μm from the interface, i.e. it is taken as bulk metal.

When the bulk metal of the 6 cycle sample is compared to the same region (i.e. bulk metal) of the 3 cycle sample, 0.04 at% higher average Fe concentration is measured in the 6 cycle sample. The amount of Ni and Cr is in the similar range. Signals from both types of SPPs are observed after 6 cycles as well. However, the distribution of the elements is much smoother compared to what is observed after 3 cycles, which indicates that after 6 cycles the numbers of remnant SPPs are reduced in the LK3/L material, and thus the dissolution of SPPs has further continued.

Cr – being the slowest alloying element diffusing out from the SPP – shows large scatter and its remnant SPPs are still present.

The elemental maps in the metal 5 μm away from the metal-oxide interface are shown in Figure 5-9. The maps confirm all statements described above. A hydride is included in the map. The alloying elements show no special behaviour around the hydride. The number of SPPs is significantly lower than in the 3 cycle sample.

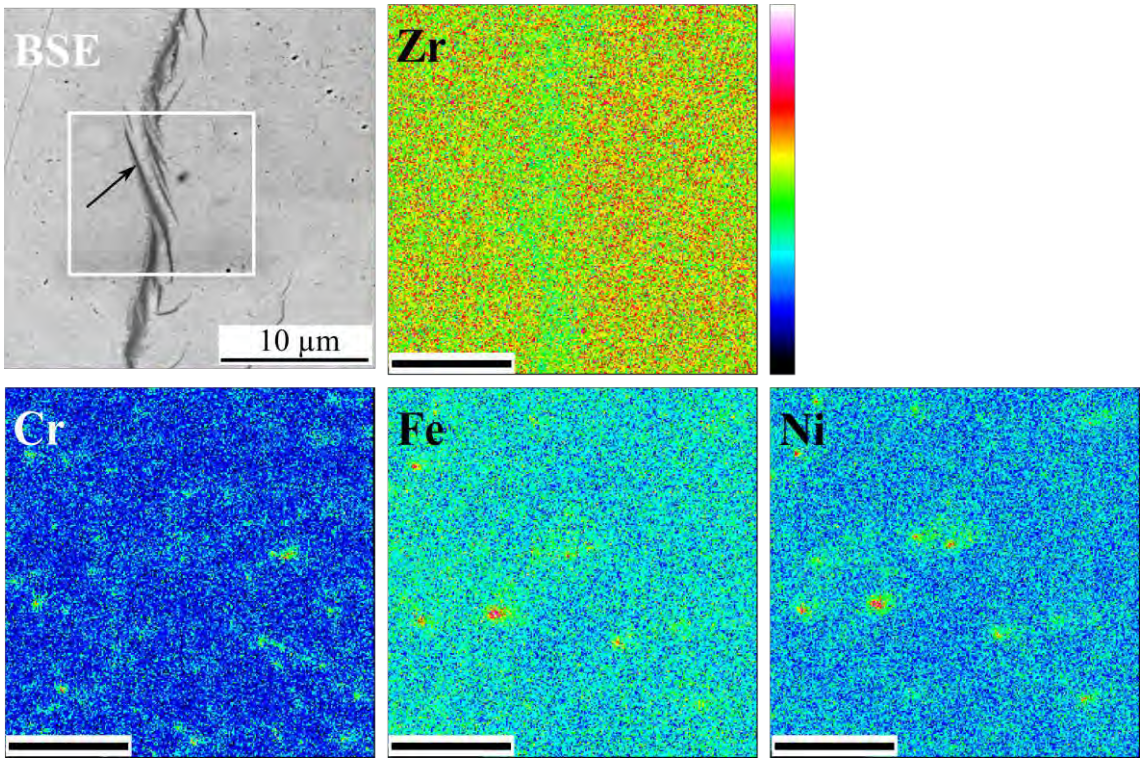

Figure 5-9 BSE micrograph and EPMA elemental maps of the 6 cycle sample in the metal side with a hydride included (acquisition parameters: 15 kV, 240-260 nA, spot size). The mapped region is around 5 µm away from the metal-oxide interface. The scale bar is 5 µm.

The average element concentration values that are extracted from the line-scans are provided in Figure 5-4 and Figure 5-10. Here as well, the metal is divided into two parts. The "metal close to the interface" is the first 1.5 µm of the metal from the metal-oxide interface. The average of three point line-scans (in total 7-8 points) is given. The "bulk metal" describes the rest of the metal. Average of 4 point line-scans (24-28 data points) is provided. SPPs are excluded. In the region of the Metal-oxide interface, Fe increased. The composition after different cycles is compared in the Discussion (section 5.3).

Table 5-3 Average concentrations of the metal matrix of the 6 cycle sample in the bulk: measured 10-200 µm from metal-oxide interface; and "close to the interface": up to 1.5 µm from the metal-oxide interface. The SPPs are excluded.

Phase	O (at%)	Zr (at%)	Sn (at%)	Cr (at%)	Fe (at%)	Ni (at%)
Bulk metal	8.94	89.53	1.07	0.11	0.26	0.060
Metal close to the metal-oxide interface	10.30	88.05	1.07	0.12	0.38	0.066

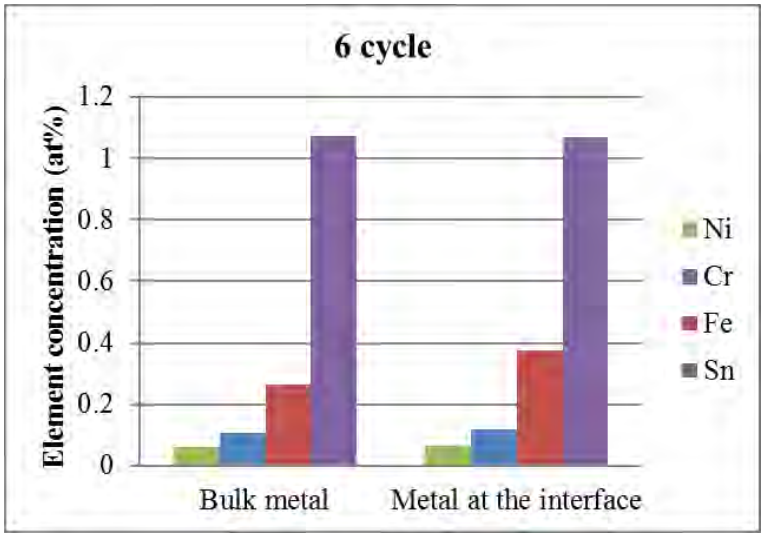

Figure 5-10 The average element concentrations at the different regions of the metal of the 6 cycle sample measured by EPMA. Bulk metal: measured 10-200 µm from metal-oxide interface; and "close to the interface": up to 1.5 µm from the metal-oxide interface.

Chemical analysis of the oxide and the metal-oxide interface after 6 cycles

In Figure 5-11 the quantitative point line-scan of the full oxide together with some part of the outer metal and the metal-oxide interface is shown. The step size of the scan is smaller through the interface in order to see the local changes. The maps are shown in Figure 5-12 for the same region. An increasing tendency in the Fe concentrations from the interface towards the outer oxide is revealed. Ni shows rather constant concentration throughout the oxide scale and higher concentration can be observed at the outer 2.5 µm of the oxide. This outer part of the oxide is

also enriched in Cr. Cr still shows the highest scatter in concentration suggesting the presence of SPP remnants however, based on the elemental maps, the number of these is much less. The maps with a higher magnification (Figure 5-14 and Figure 5-15) show that the shapes of these SPP remnants are not well-defined anymore.

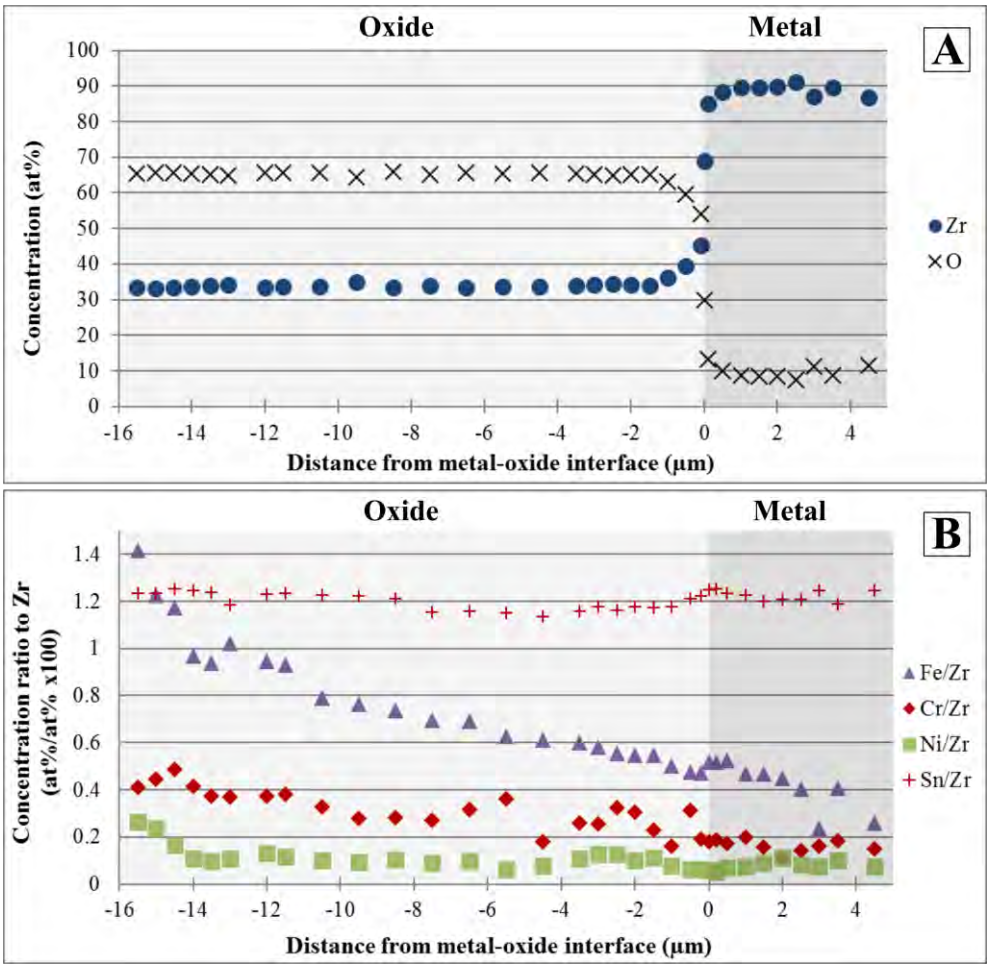

Figure 5-11 EPMA Point line-scan on the full oxide scale, through the metal-oxide interface and some part of the metal of the 6 cycle LK3/L sample (acquisition parameters: 15 kV, 240-260 nA, spot size). Smaller step size is used at the metal-oxide interface. (A): Zr and O distribution; (B): Alloying element concentration ratio to Zr.

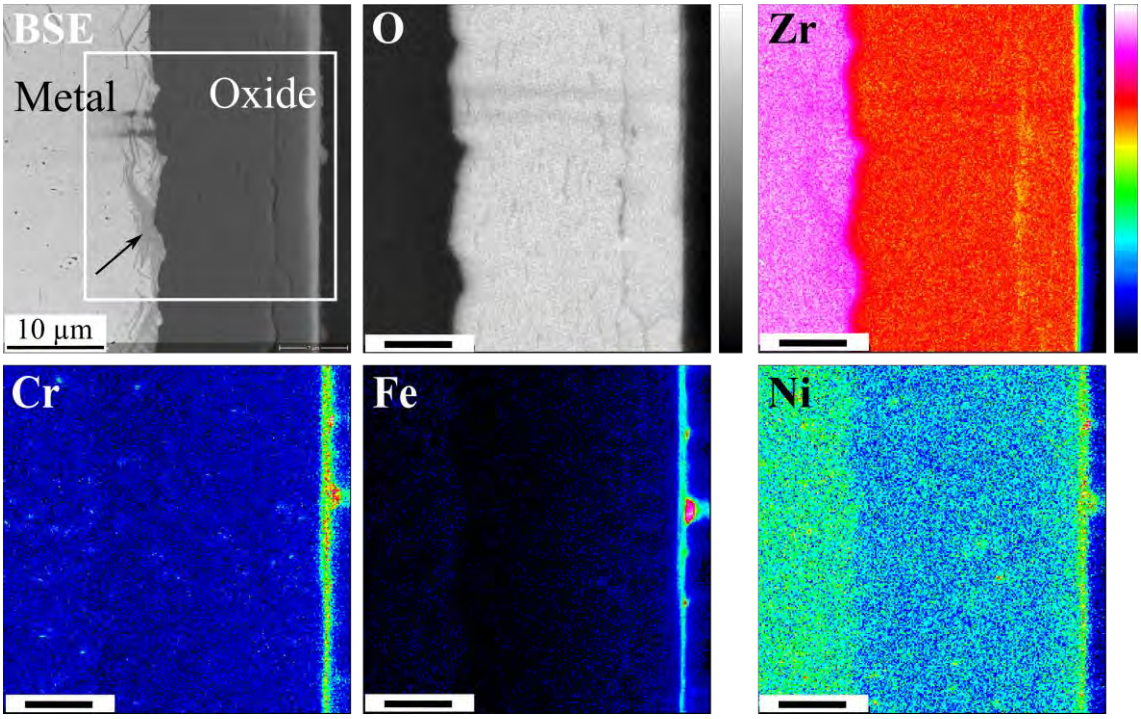

Figure 5-12 BSE image and EPMA maps on the full oxide scale and the outermost part of the metal on the 6 cycle LK3/L sample (acquisition parameters: 15 kV, 240-260 nA, spot size). The scale bar is 5 µm.

In order to reveal the behaviour of the different elements at the Metal-oxide interface, the point line-scan is enlarged only at that region and is shown in Figure 5-13. Fe shows a drop in the first 0.5 µm of the oxide close to the interface which is followed by a steady increment in its concentration.

The Fe map on this region (Figure 5-14) confirms this observation; Fe has decreased in the oxide close to the interface. Cr and Ni do not show the same step like change at the interface, their transition to the oxide is smooth, and the concentration of these elements is inherited from the metal without change.

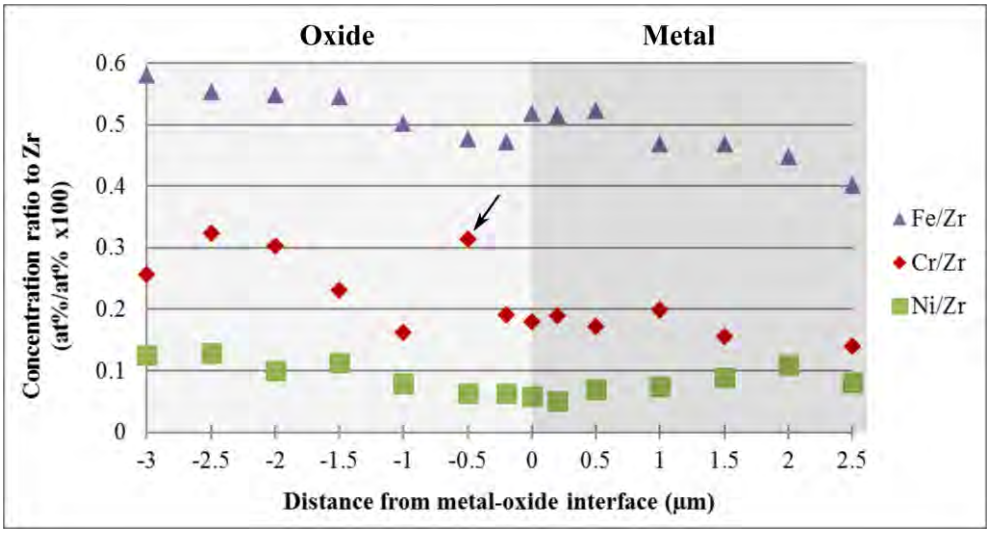

Figure 5-13 Point line scan through the metal-oxide interface of the 6 cycle LK3/L sample (acquisition parameters: 15 kV, 240-260 nA, spot size). Concentration ratio to Zr is given. The arrow indicates an SPP.

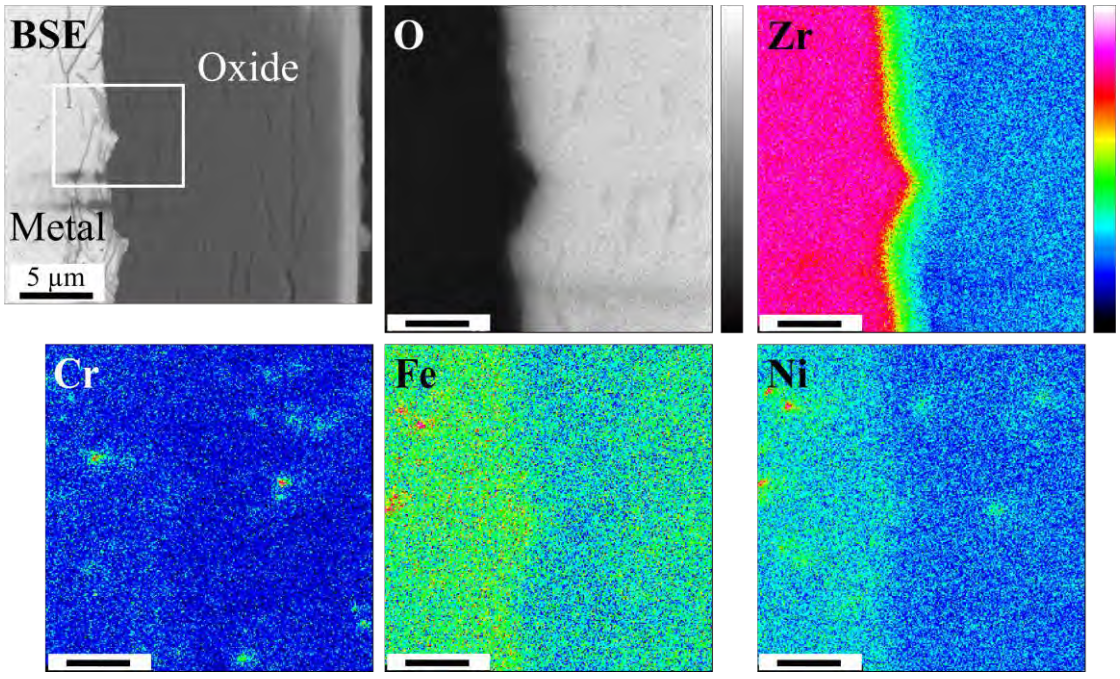

Figure 5-14 EPMA maps on the metal-oxide interface of the 6 cycle sample (acquisition parameters: 15 kV, 240-260 nA, spot size). The scale bar is 2 µm.

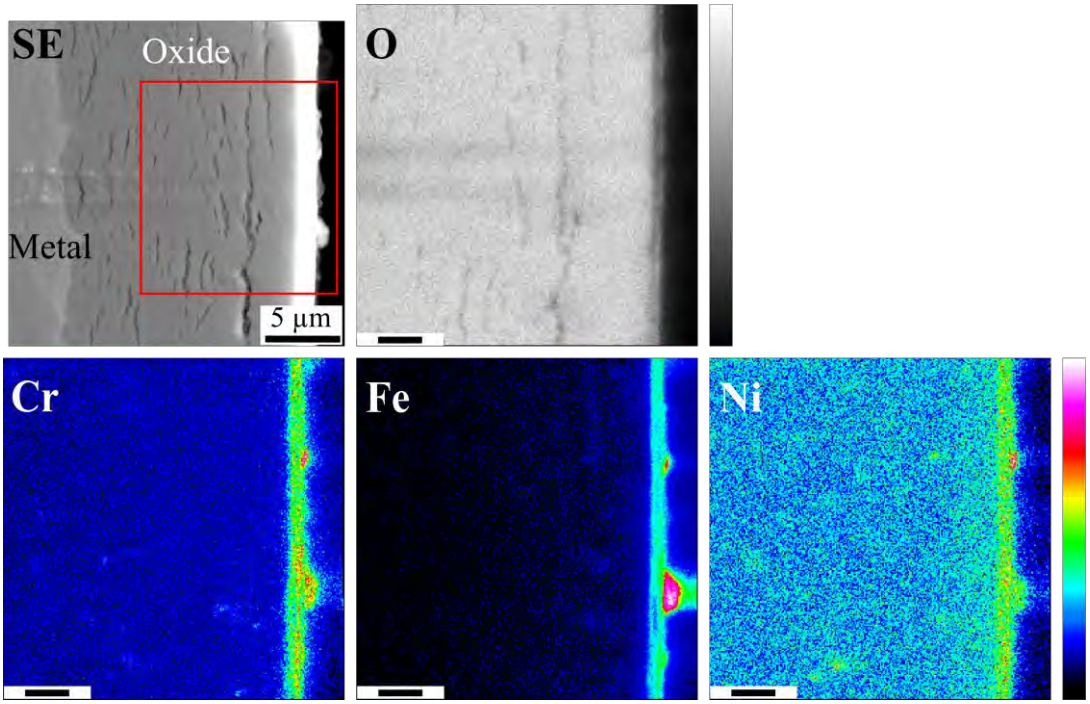

Figure 5-15 EPMA maps on the outer part of the oxide layer of the 6 cycle sample (acquisition parameters: 15 kV, 240-260 nA, spot size). The scale bar is 2 µm.

The oxide shows different characteristics in terms of composition in the different regions. Therefore in order to give an average composition which describes the oxide properly, the average concentration values are given according to these regions. The "inner oxide" is the innermost 1.5 µm; "outer oxide": the outer 2-3 µm of the oxide depending on the local oxide thickness of the sample; "intermediate oxide" represents the region in between the inner and outer oxide. The data is presented in Table 5-4 and in Figure 5-16. 3 point line-scans with 7-8 data points gave the average for the Inner oxide, same number of scans with 23-26 points are collected for the intermediate oxide and 2 scans with 7-9 points for the outer oxide. The SPP remnants are excluded. With the exception of Sn which has a slightly higher concentration at the inner oxide, all the other elements have an increasing concentration towards the outer oxide.

Table 5-4 Average concentrations of the different parts of the oxide matrix of the 6 cycle LK3/L sample by EPMA point analysis. "Inner oxide": innermost 1.5 µm; "outer oxide": the outer 2-3 µm; "intermediate oxide": region in between the inner and outer oxide.

Phase	O (at%)	Zr (at%)	Sn (at%)	Cr (at%)	Fe (at%)	Ni (at%)
Inner oxide	61.35	37.93	0.46	0.07	0.16	0.031
Intermediate oxide	65.75	33.48	0.40	0.10	0.24	0.034
Outermost oxide	65.70	33.31	0.41	0.14	0.38	0.056

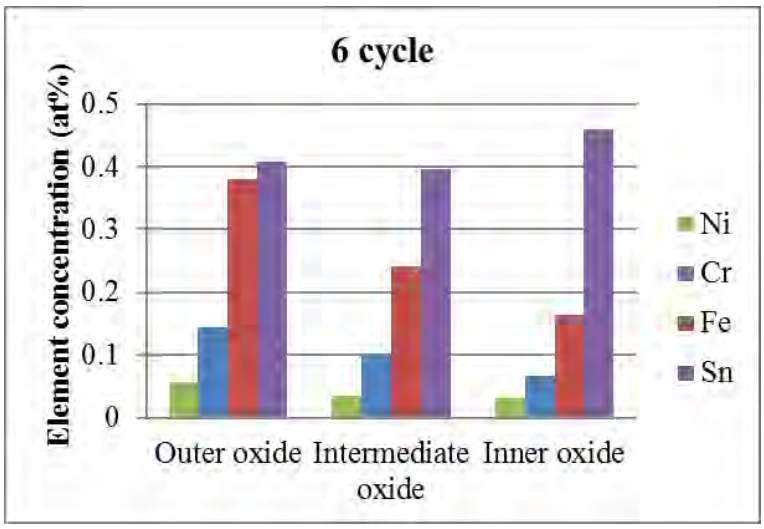

Figure 5-16. The average element concentrations at the different regions of the oxide of the 6 cycle LK3/L sample. For the definition of the different parts please refer to the text.

5.2.1.4. The chemical composition after 9 cycles

In the case of the 9 cycle material a complete fuelled segment was studied by EPMA and measurements were performed around the segment in every 45°. For the definition of the orientations on the segment, a zero sign was used. The orientations are defined as it is shown in Figure 5-17. At each orientation, a set of elemental maps were obtained in the metal, at the metal-oxide interface and in the oxide. Therefore, larger amount of data is collected than for the other cycles. Only the most important results are presented due to the length limitations of the thesis.

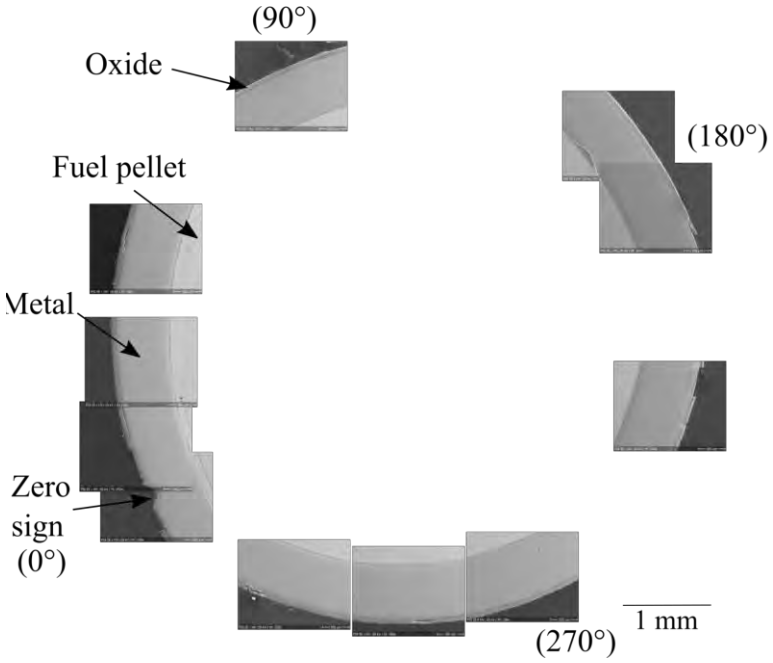

Figure 5-17 Collection of SE images showing some parts of the full segment of the 9 cycle LK/L sample, and its orientations.

Chemical analysis of the metal after 9 cycles

Figure 5-18 represents an EPMA point line-scan along the whole metal cladding. In Part (A), Zr and O are shown and their distribution is relatively homogenous with a slight change close to the metal-oxide interface and the metal-inner liner interface. Figure 5-18-(B) shows the distribution of the alloying elements with a much finer vertical scale. Using this and other point line-scans on the base metal, the concentration ranges of the elements (excluding SPP remnants) are as follows. The Fe content changes between 0.16 and 0.32 at%. The Ni content varies between 0.013 and 0.08 at%. The minimum values could be influenced (lowered) by the hydrides. This is further discussed below. The value of the Cr concentration has a scatter between 0.03 and 0.20 at%. Cr shows higher concentration fluctuation in this sample as well, due to its SPP remnants.

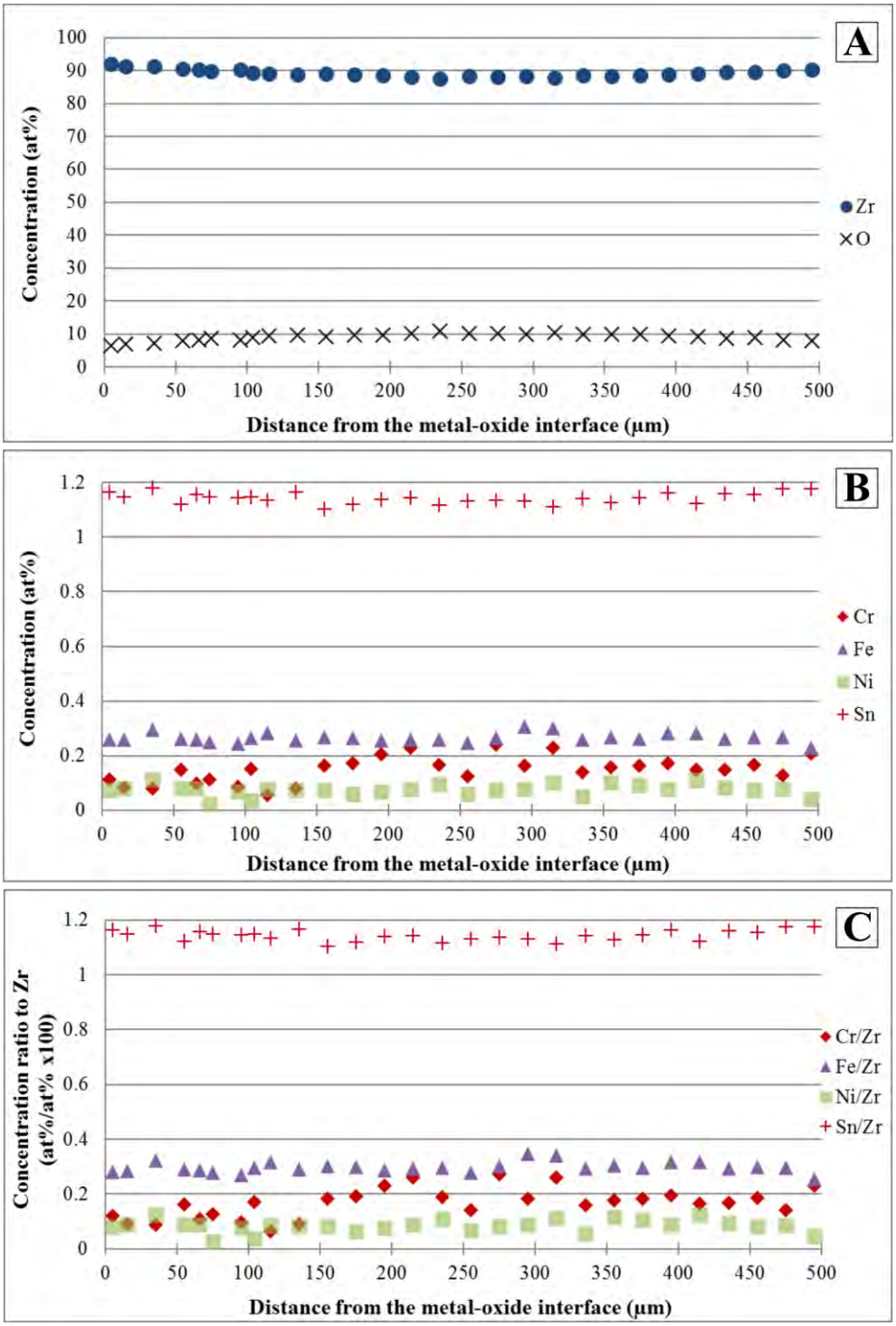

Figure 5-18. EPMA point line-scan across the base metal at 40° of the 9 cycle LK3/L sample (acquisition parameters: 15 kV, 240-260 nA, 2 µm beam diameter). (A): Concentration of Zr and O. (B): Concentration of Cr, Fe, Ni, and Sn. (C): Element concentration ratio to Zr.

Figure 5-19 shows the average element concentration in the metal at different orientations of the cladding. Each data point represents an average of 10-25 measurements. The SPPs are excluded. All alloying elements show fairly homogenous distribution around the circumference. Due to the asymmetry of the burnup, it was expected to observe a certain variation of element distribution, in particular a smaller dissolution of alloying elements in the lower burnup side. Although a slight drop of Cr concentration in the matrix is observed around 180° (which is close to the lower burnup side), no considerable variation could be observed.

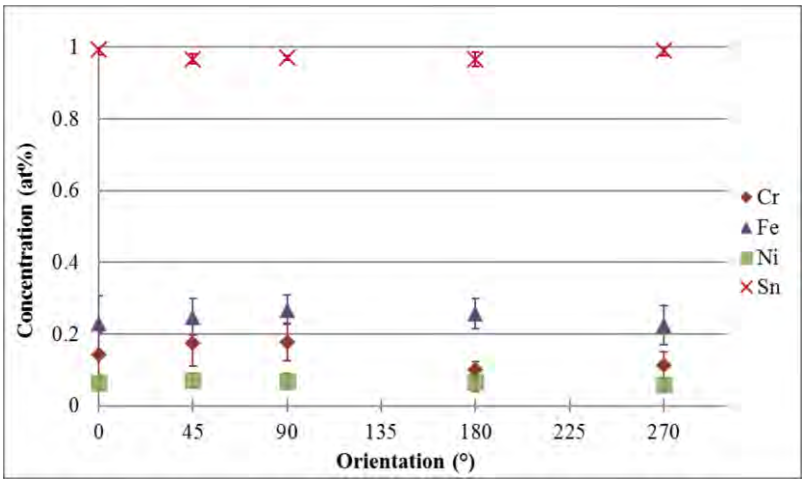

Figure 5-19. Average element concentration by EPMA point analysis of the metal part at different orientations of the 9 cycle LK3/L sample. All data was collected at a distance of up to 20 µm from the metal-oxide interface. The data shows only the matrix, the SPP remnants are excluded, while the hydrides were not distinguished and removed.

One example of the elemental maps obtained is shown in Figure 5-20. Only few Zr_2(Fe, Ni) remnant SPPs are present and Zr(Fe, Cr)$_2$ SPP remnants are mostly depleted of Fe. The highest measured element concentration for the SPPs were determined by point analysis directly on the SPPs which were located based on the elemental maps. It is 1.58 at% Cr and 0.33 at% Fe for a Zr(Fe, Cr)$_2$ and 0.12 at% Ni and 0.35 at% Fe for Zr_2(Fe, Ni). The element distribution in the

metal matrix is homogeneous except in the areas of the hydrides which show Fe and Ni depletion compared to the surrounding matrix.

Figure 5-21 shows the measured Fe/Zr and Ni/Zr ratios in the matrix (average of 3-21 measurements) and in the hydrides (averaged over 3-6 point measurements) at five different orientations of the segment. The concentration of these two elements in the hydrides is lower by a factor of 1.5-2.4. Cr and Sn do not show detectable difference in the hydrides by EPMA point measurements, therefore, their ratios are not provided.

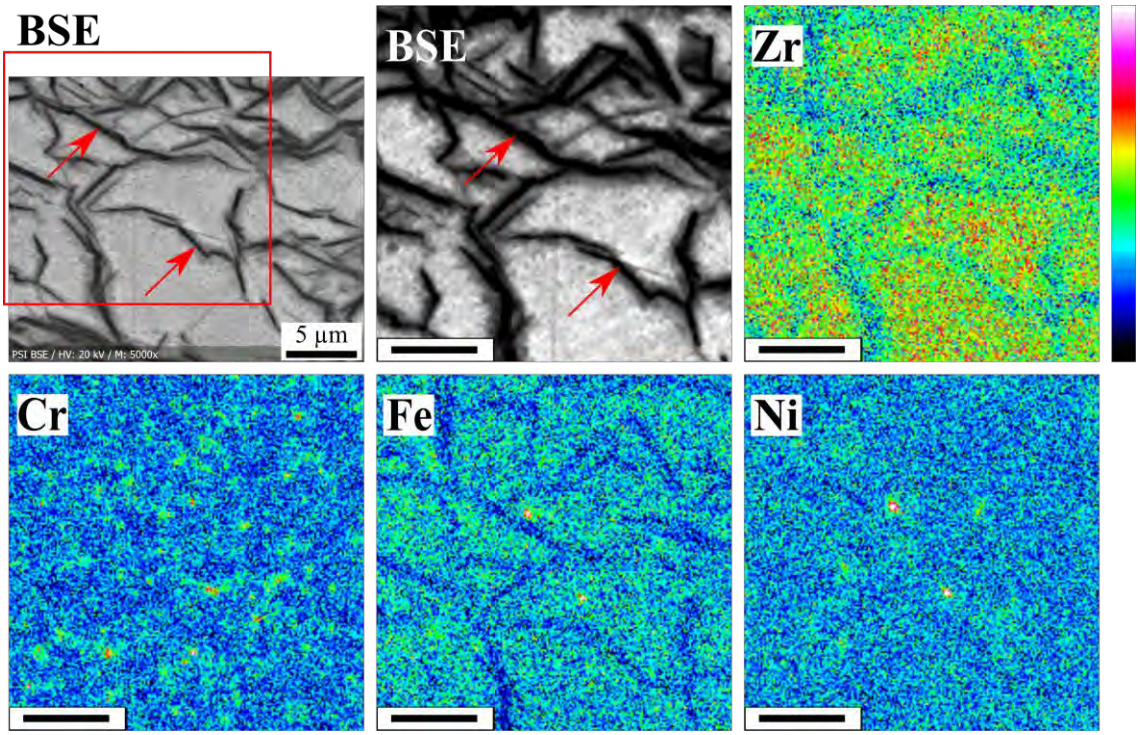

Figure 5-20. BSE image and elemental maps of Zr, Cr, Fe, and Ni in the metal matrix 30 µm from the metal-oxide interface at 0°, of the 9 cycle LK3/L sample. The frame shows the mapped area and the arrows point to the hydrides. The scale bar is 5 µm.

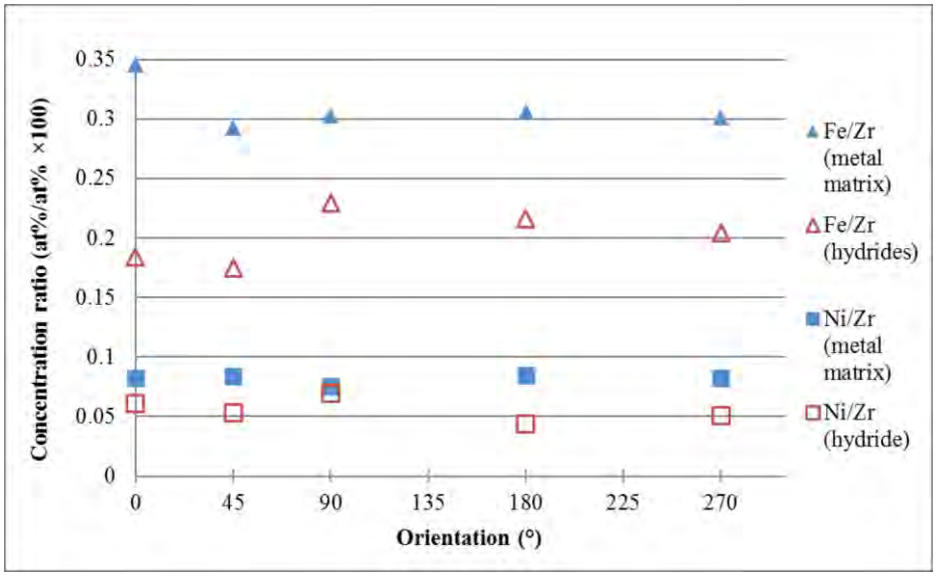

Figure 5-21. Average ratios of Fe/Zr and Ni/Zr of the 9 cycle LK3/L sample in the hydrides and in the surrounding metal matrix up to 20 µm from the metal-oxide interface, obtained by EPMA point analysis (acquisition parameters: 15 kV, 240-260 nA, spot size).

Although, the bulk and the interface metal show similar composition, for the better comparison with the other materials, these regions are given separately. The average data is presented in Table 5-5 and in Figure 5-22. 11 point line-scans with 138-166 data points in total were collected for the bulk region while 5 scans and 15-16 points for the interface region. As before, the interface region is defined as the distance up to 1.5 µm from the metal-oxide interface.

Table 5-5. Average concentrations of the metal matrix of the 9 cycle sample obtained by EMPA point analysis, in the bulk metal: 2-520 µm from metal-oxide interface; and close to the interface: up to 1.5 µm distance from the interface. The SPPs are excluded.

Phase	O (at%)	Zr (at%)	Sn (at%)	Cr (at%)	Fe (at%)	Ni (at%)
Bulk metal	9.34	89.16	1.03	0.12	0.25	0.06
Metal close to the Metal-oxide interface	12.16	86.39	1.03	0.11	0.25	0.06

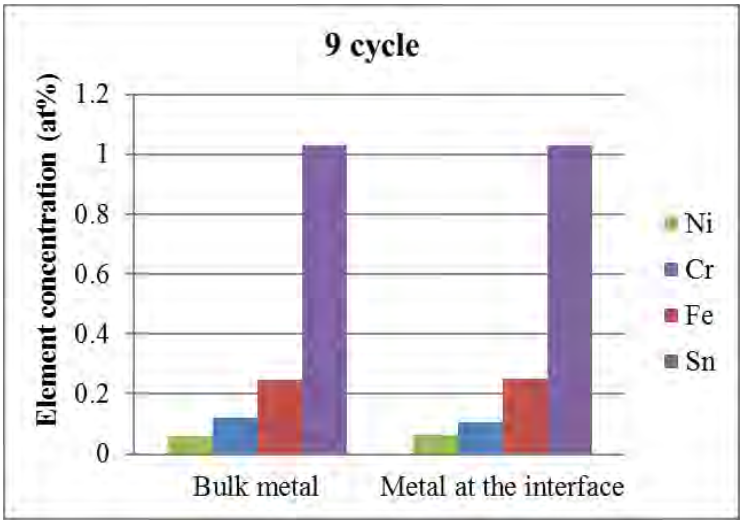

Figure 5-22. The average element concentrations at the different regions of the metal of the 9 cycle LK3/L sample measured by EPMA.

Chemical analysis of the oxide and the metal-oxide interface after 9 cycles

Figure 5-23 shows a quantitative point line-scan between the crud-oxide and the oxide-metal interface. The step size is relatively large providing an overview of element distribution. In Part (A), the Zr and O signals are plotted. The Ni and Fe content can also be observed in the crud. In Part (B) the ratios of the alloying elements to Zr are shown. Fe shows an increasing concentration towards the outer oxide. The points indicated by arrows in Figure 5-23-(B) show an increased ratio of Cr or Fe which are most probably SPP remnants.

Figure 5-24 presents two sets of point line-scans with smaller step size, one at the close environment of the metal-oxide interface (A shows at% and B shows the ratios to Zr) and another at the outer side of the cladding (C: in at% and D: ratios). Increased concentration of Ni is revealed as well at the outer region of the oxide. A point line-scan with high resolution through the metal-oxide interface is presented in Figure 5-25. The oxide region close to the interface seems to be slightly depleted by the alloying elements compared to the rest of the oxide scale.

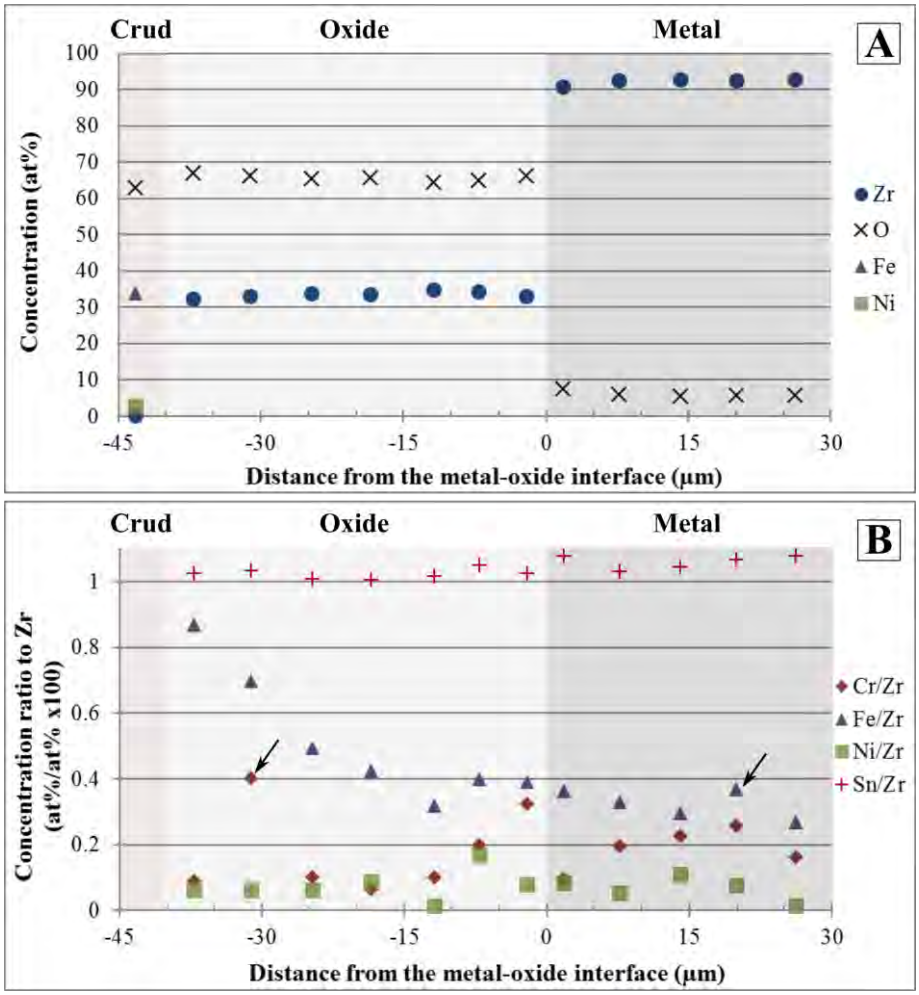

Figure 5-23. EPMA quantitative point line-scan between the crud-oxide and the oxide-metal interface at 120°, of the 9 cycle LK3/L sample (acquisition parameters: 15 kV, 240-260 nA, spot size). (A): Zr and O. Ni and Fe are higher in the crud than in other regions, therefore these elements are plotted in A. (B): Element concentration ratios to Zr. Arrows indicate the possible remnants of SPPs.

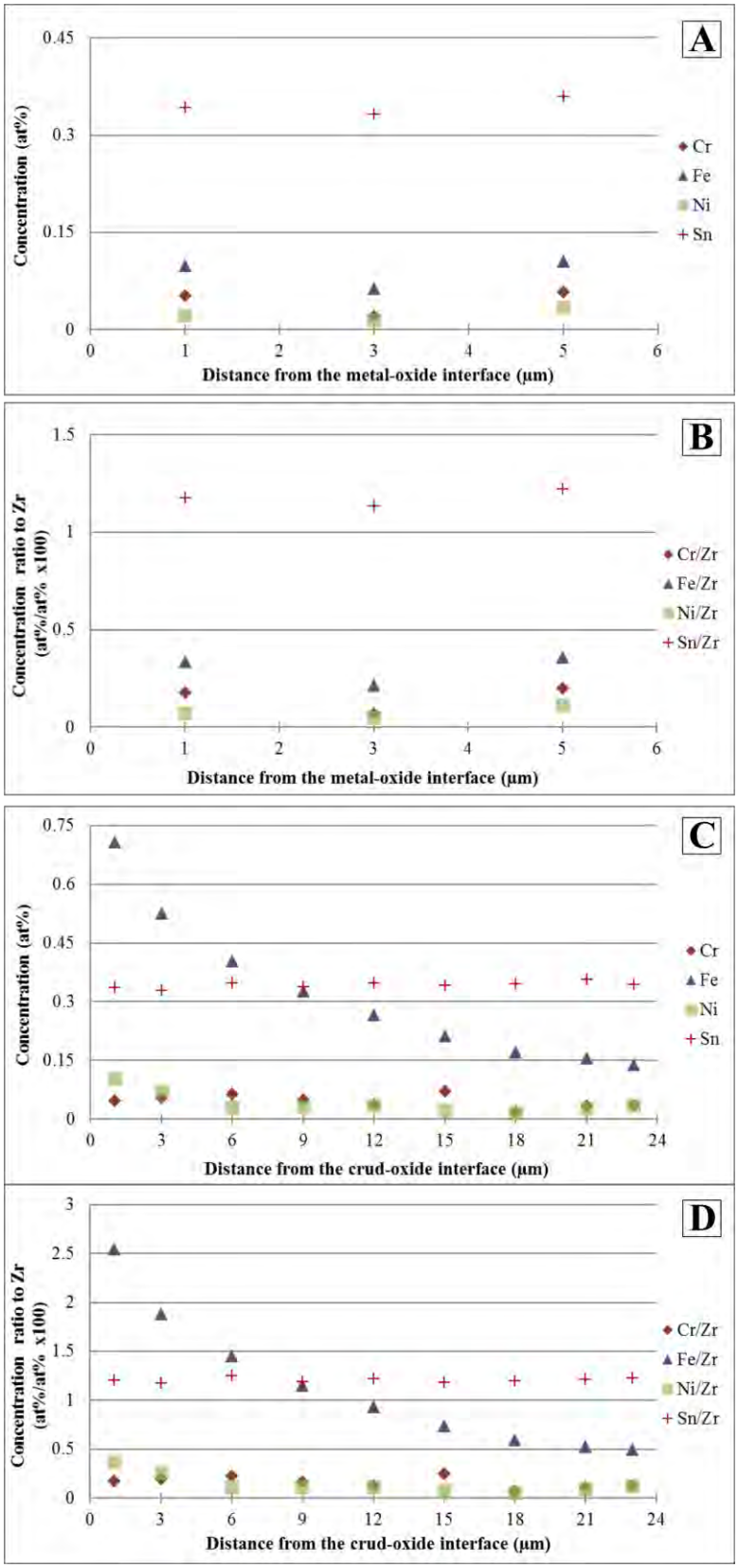

Figure 5-24. EPMA quantitative point line-scans of the oxide of the 9 cycle LK3/L sample at 270° orientation (15 kV, 240-260 nA, spot size). Alloying element concentrations and ratios close to the metal-oxide interface (A, B); and at the outer region of the oxide (C, D).

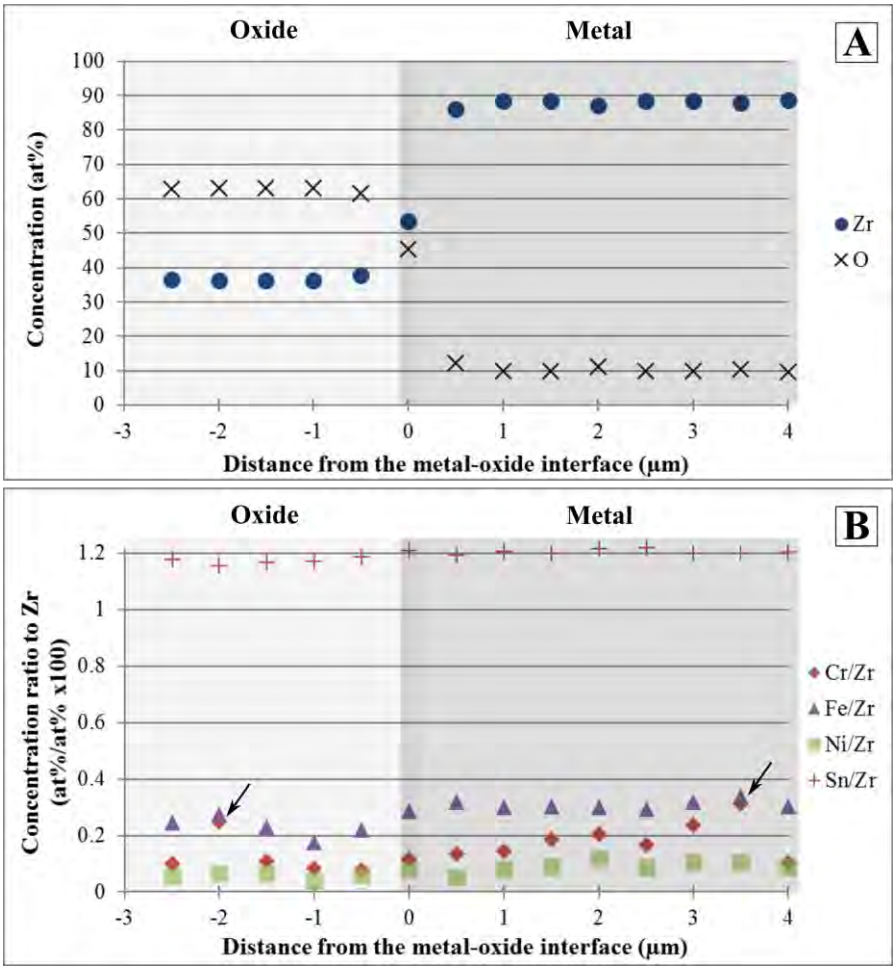

Figure 5-25. EPMA Point line scan through the metal-oxide interface of the 9 cycle LK3/L sample on a half segment (i.e. orientation is not known) (acquisition parameters: 15 kV, 240-260 nA, spot size). (A): Zr and O concentrations. (B): element concentration ratios to Zr.

The elemental maps acquired from the outer and the intermediate regions of the oxide are shown in Figure 5-26 and Figure 5-27, respectively. The increasing concentration of Fe towards the outermost oxide is observable. In the oxide, as in the metal, most of the SPPs are already dissolved, but some remnants of $Zr(Fe, Cr)_2$ SPPs still can be observed, therefore, the distribution of Cr is much more inhomogeneous. Similar clusters of Fe and Ni are very rare in the oxide. Figure 5-26 shows the Fe enrichment at some sites of the oxide layer. The superposition of the Fe and O maps shows that the intense Fe signal is superimposed on the

long crack in the oxide. The crud and the crud-oxide interface are enriched in Fe and to a lower extent in Ni. In Figure 5-27 some slight segregation of Sn is also observable. Maps at the metal-oxide interface are shown in Figure 5-28. The Fe depletion at the interface oxide was not clearly observable in this or other maps. Due to the fact that it is clearly observable in the point line-scans, it is expected to be a narrow, not very well-defined region in the oxide.

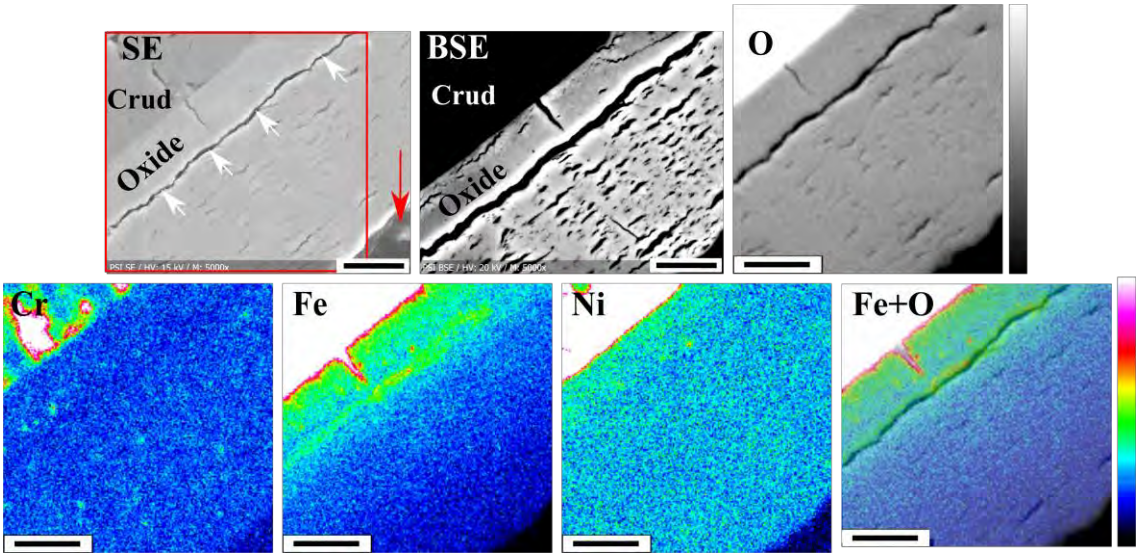

Figure 5-26. SE, BSE images and elemental maps of the 9 cycle LK3/L sample, at the crud-oxide interface at 270°. A superposition of Fe with O maps also provided. The red frame indicates the mapped area and a crack (due to sample preparation – it contains resin) in the oxide is marked by the arrow. The scale bar is 5 µm.

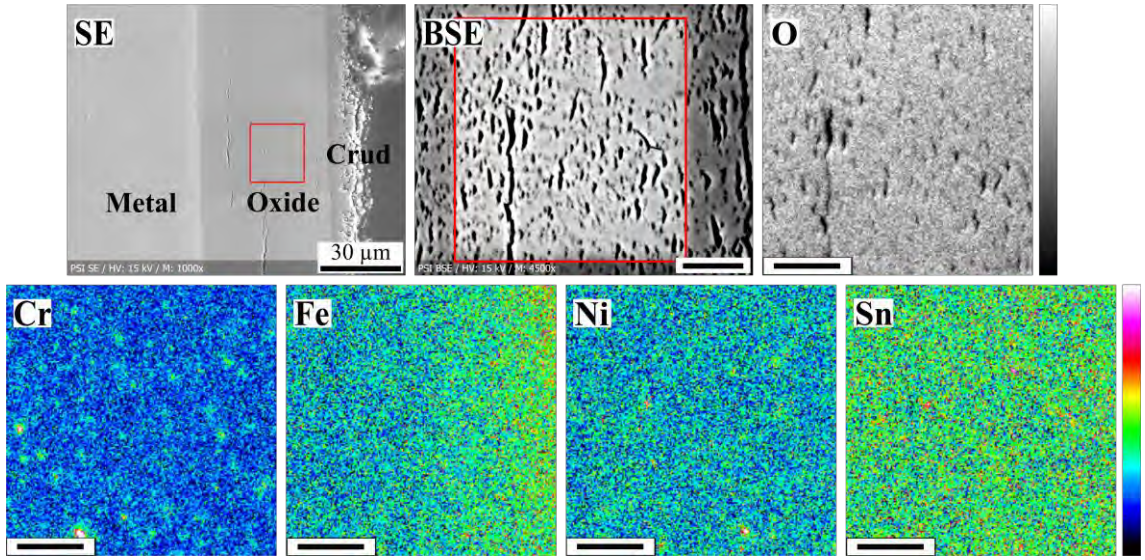

Figure 5-27. SE, BSE images and elemental maps of the 9 cycle LK3/L sample in the oxide at 45°. The frame on the SE image and the BSE image show the mapped area. The scale bar is 5 µm.

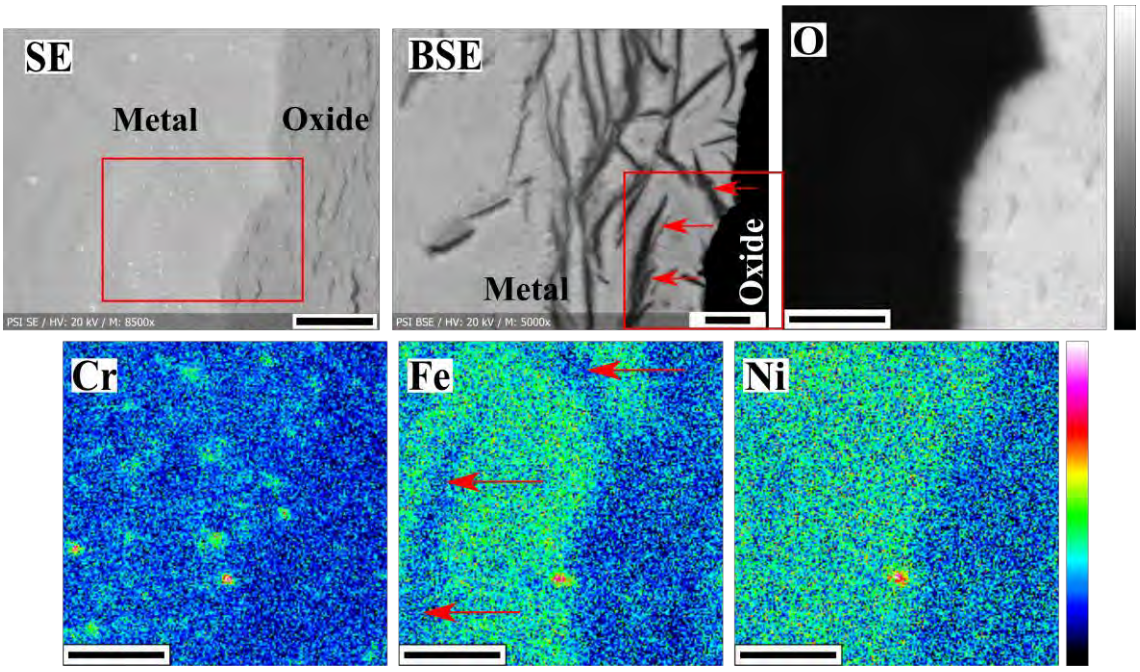

Figure 5-28. SE, BSE images and elemental maps of the 9 cycle LK3/L sample at the metal-oxide interface at 200°. The red frame shows the mapped area. The scale bar is 3 µm.

The average values of three parts of the oxide are given separately, in Table 5-6. The “inner oxide” is up to a distance of 1.5 μm from the interface; the “outer oxide: is the outermost 4 μm (this region is enriched in Fe and Ni). The region in between these two sites is referred as “intermediate oxide”. The data is provided from all measured orientations together, as no considerable difference in concentrations is observed in different orientations. The SPP remnants are excluded. Between 12 and 15 point measurements in total from 9 different point line-scans gives the average concentration of the inner oxide. The intermediate oxide composition is calculated from 7 point line-scans containing 85-98 data points in total. 12-13 point from 9 point line-scans are used for the outer oxide. In the case of Sn less data points were considered because for some of the point line-scans the Sn value was fixed in order to decrease the time of the measurement. The fixed values are not included in the average calculation therefore 15, 67, and 3 points were considered for Sn in the inner, intermediate, and outermost oxide, respectively. The inner part of the oxide shows the lowest concentration for each alloying element, except for Sn which is slightly higher at this part of the oxide. The Fe concentration increases significantly, while concentration of Ni and Cr increase moderately towards the outermost oxide.

Table 5-6. Average concentrations of the different parts of the oxide matrix of the 9 cycle LK3/L sample from EMPA point analysis. For the definition of the different parts please refer to the text.

Phase	O (at%)	Zr (at%)	Sn (at%)	Cr (at%)	Fe (at%)	Ni (at%)
Inner oxide	62.39	37.01	0.44	0.036	0.09	0.028
Intermediate oxide	64.12	35.26	0.42	0.045	0.13	0.031
Outermost oxide	65.40	33.50	0.39	0.061	0.58	0.087

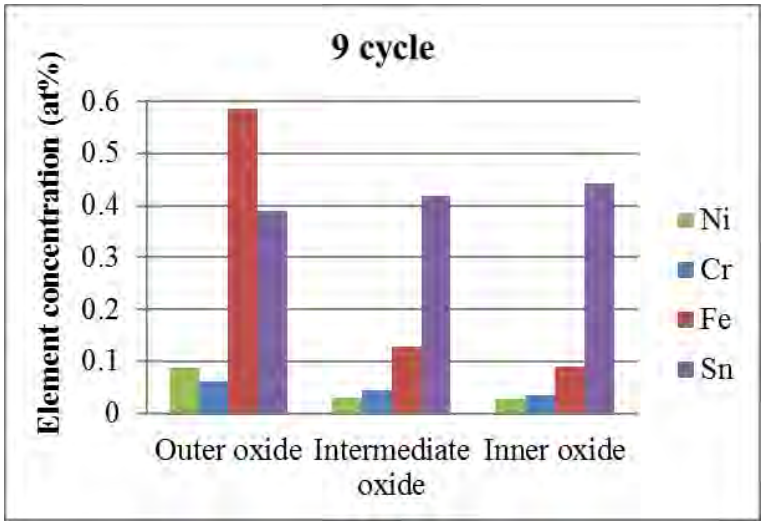

Figure 5-29. The average element concentrations at the different regions of the oxide of the 9 cycle LK3/L sample. For the definition of the different parts please refer to the text.

5.2.2. Analysis of the samples by ChemiSTEM – Local changes of composition

In this section the effect of irradiation on the element re-distribution (e.g. in GBs and in the metal and oxide matrices) at the nanometric scale is followed up. The un-irradiated, and the 3, 7, and 9 cycle cladding samples examined by ChemiSTEM are reported. The observed differences between the materials with different service times are correlated to the change of oxidation and HPU at high and extreme high burnups.

The SPPs are present in the alloy to enhance the oxidation resistance [19]. Under irradiation they dissolve gradually and their solubility limit in the metal matrix is very low [40]. The behaviour and redistribution of the dissolved elements in the metal matrix could influence the subsequent oxidation and HPU properties of the cladding.

5.2.2.1. Un-irradiated LK3/L

An electro-polished un-irradiated material from the same batch as the irradiated LK3/L samples was studied. This sample accurately represents the initial conditions of the material and provides a good basis for comparison.

The two types of SPPs, namely $Zr(Fe, Cr)_2$ and $Zr_2(Fe, Ni)$ precipitates, are revealed and are shown on the overview maps in Figure 5-30.

The average composition of the metal matrix and the highest measured composition for the two types of SPPs are shown in Table 5-7. The high O signal possibly originates from the natural oxide film that has formed on the thin foil. These SPP concentration values do not represent the highest compositions expected (i.e. the atomic concentrations for each species of the SPPs). In Figure 5-31 the GB segregation of Fe and Ni prior to irradiation is shown. No Cr or Sn segregation was observed in any of the measured GBs.

The GB segregation have been determined based on the elemental maps by a point line-scan across the segregation and not by direct point analysis. Therefore it is rather qualitative and the ratio is given between the segregation and the matrix. In the case of Fe, 5.5 times and for Ni, 4.6 times higher concentrations were measured in the GB.

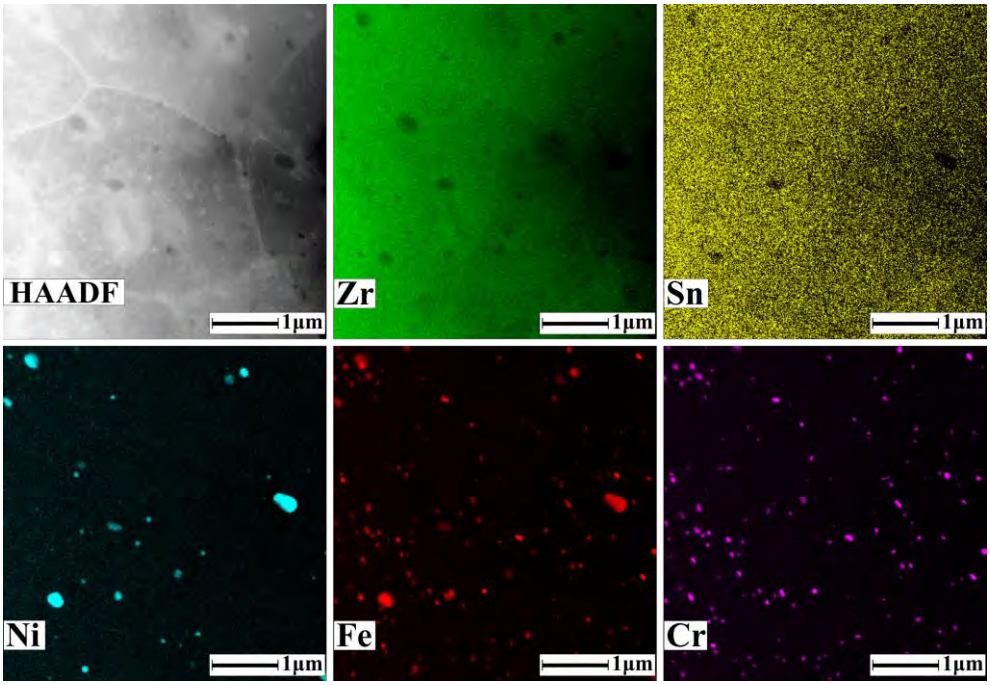

Figure 5-30 HAADF images and ChemiSTEM maps obtained from the un-irradiated LK3/L sample. $Zr(Fe, Cr)_2$ and $Zr_2(Fe, Ni)$ SPPs are revealed.

Table 5-7 The measured average metal matrix composition from 3 points in the un-irradiated LK3/L. Composition of the SPPs: the highest measured concentration is given. These SPP concentration values do not represent the highest compositions expected.

Phase	O (at%)	Zr (at%)	Sn (at%)	Cr (at%)	Fe (at%)	Ni (at%)
Metal matrix	18.51	80.42	0.95	0.008	0.10	0.007
$Zr_2(Fe, Ni)$	5.86	72.89	0.28	0.11	12.44	8.42
$Zr(Fe, Cr)_2$	7.90	64.74	0.52	13.01	13.66	0.17

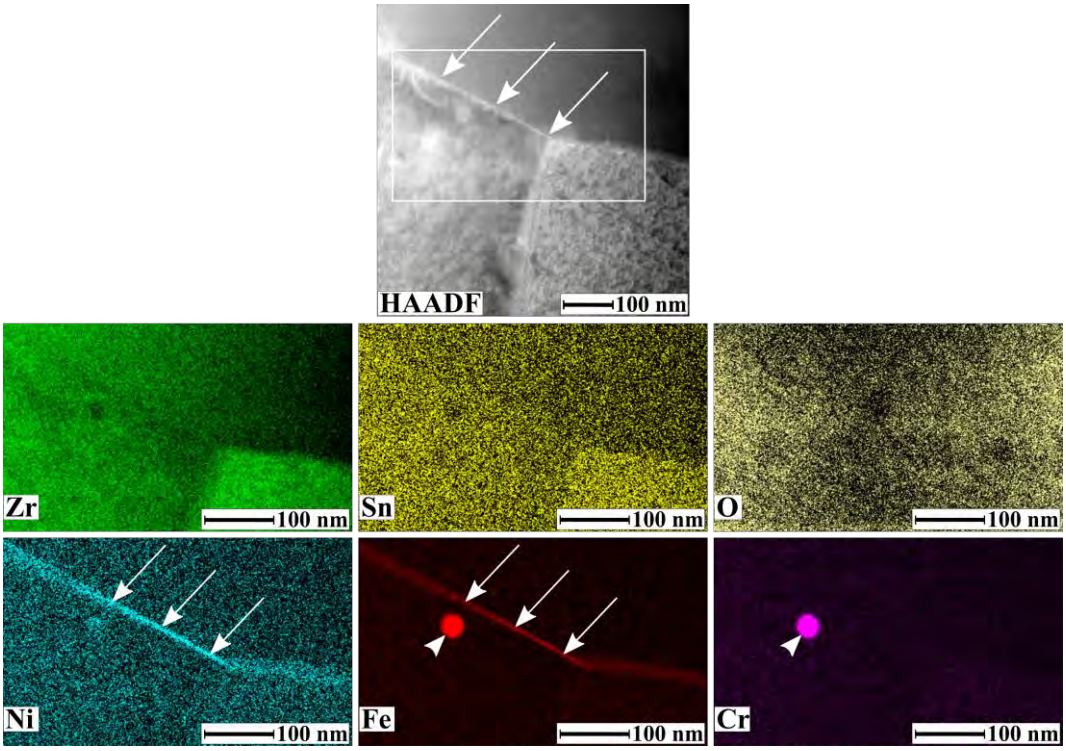

Figure 5-31 HAADF image and ChemiSTEM elemental maps obtained from the un-irradiated LK3/L sample. The mapped area is marked by the white rectangle. GB segregation of Ni and Fe is visible and marked by arrows. A Zr(Fe, Cr)$_2$ SPP is marked by the arrowhead. Some amount of Ni can be observed as well in the SPP.

5.2.2.2. 3 cycle LK3/L

After 3 cycles in reactor the SPPs have dissolved to a certain extent. The segregation of Fe and Ni at the metal GBs are observed and presented in Figure 5-32. The metal matrix composition together with the values obtained from the point measurements on the different SPPs is presented in Table 5-8. The measured maximum concentration values for Fe and Ni at the GB are about 3.6 and 3 times higher than in the matrix, respectively.

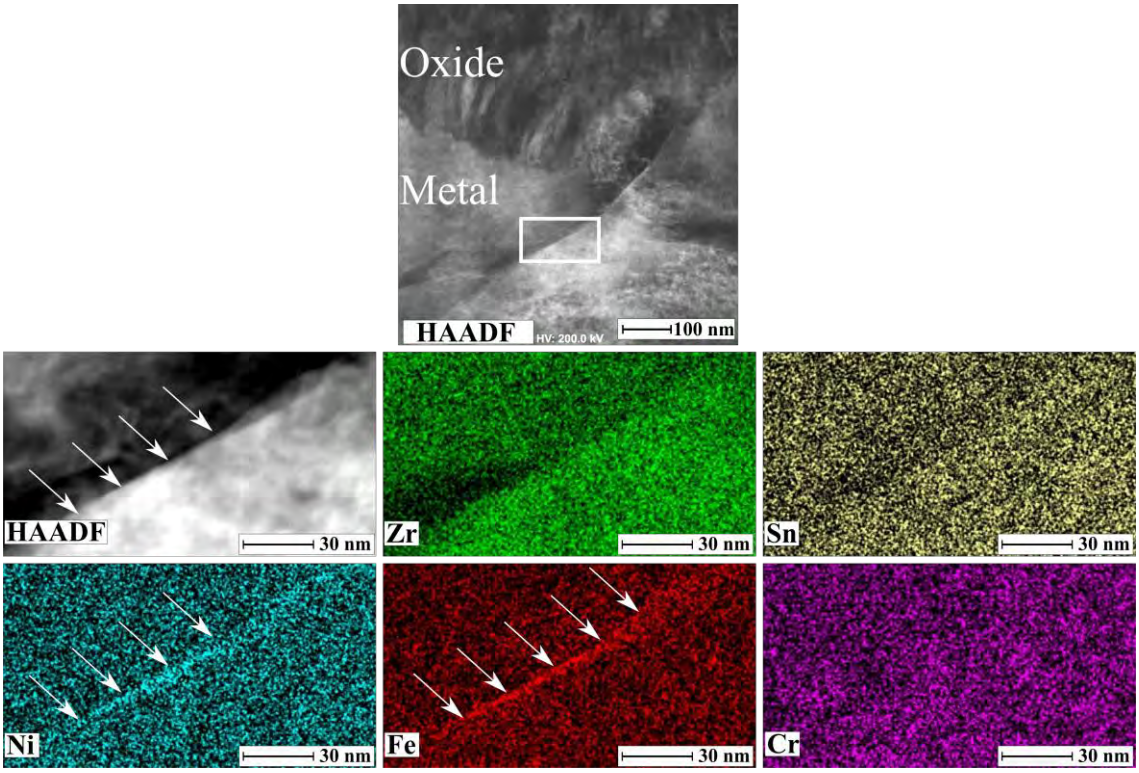

Figure 5-32 HAADF image and ChemiSTEM maps of a metal GB close to the metal-oxide interface in the 3 cycle LK3/L sample. The mapped area is marked by the white rectangle. GB segregation of Ni and Fe is visible and marked by arrows.

Figure 5-33 shows a dissolving SPP which has been incorporated into the oxide on the last oxide formed, i.e. at the metal-oxide interface. On the ChemiSTEM maps, Fe and Ni segregation is observable, most likely in the oxide GBs. The concentrations of the different phases and the maximum measured SPP values are presented in Table 5-8. The O concentration in the oxide indicates a low value therefore sub-stoichiometric oxide is assumed. The O value could be slightly higher if a higher lamella thickness is considered but even then it is around 60 at%. This issue is further discussed in the Discussion of this chapter. For more quantitative data regarding the O value in the bulk oxide please refer to the EPMA results in Section 5.2.1.2. As the lamella was prepared at the metal-oxide interface high Fe concentration is measured in the metal matrix due to the Fe-enrichment of this region which was already presented by EPMA (Table 5-1). The value observed here represents the interface metal and does not represent the

Fe concentration in the bulk matrix; for the bulk concentration of Fe please refer to Table 5-1. Much higher (about 2.5 times) Fe concentration is measured by ChemiSTEM than by EPMA. This can be explained by the fact that the interaction volume of the sample and the beam is much larger in EPMA than in ChemiSTEM. As the Fe-enriched region is rather narrow, EPMA could give a rather mixed signal partially coming from the area designated as "bulk metal" region as well while in ChemiSTEM only this so called "metal at interface" region is measured locally.

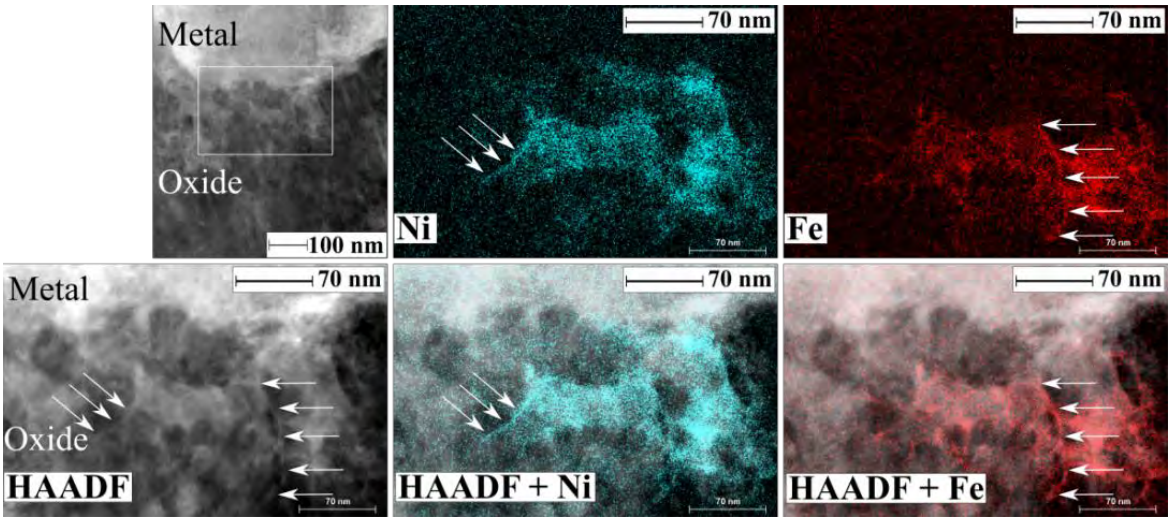

Figure 5-33 HAADF image and ChemiSTEM maps on the oxide close to the metal-oxide interface of the 3 cycle LK3/L sample. The mapped area is marked by the white rectangle. Arrows indicate fine lines of Fe and Ni.

Table 5-8 Results of point analysis by ChemiSTEM. The average metal and oxide matrix composition from 3 points measured at the metal-oxide interface of the 3 cycle LK3/L cladding. Composition of the SPPs in both phases is given for the highest measured concentration.

Phase	O (at%)	Zr (at%)	Sn (at%)	Cr (at%)	Fe (at%)	Ni (at%)
Metal matrix*	15.62	82.52	1.07	0.04	0.67	0.068
Fe-Ni SPP in metal**	14.46	80.92	0.90	0.086	2.18	1.45
Fe-Cr SPP in metal	14.98	80.14	1.06	2.82	0.82	0.17
Oxide matrix*	49.24	49.70	0.74	0.015	0.24	0.06
Fe-Ni(-Cr) SPP in oxide	45.40	45.52	0.32	1.41	4.59	2.75
Fe-Cr SPP in oxide	43.89	43.38	0.71	10.20	1.46	0.35

*For the O and Zr content of the bulk metal and bulk oxide matrix please refer to the EPMA result.
**Measurement based on spectra collected during mapping, i.e. providing only semi-quantitative data.

5.2.2.3. 7 cycle LK3/L

In the absence of a 6 cycle metal-oxide interface TEM lamella, due to time limitation, a 7 cycle TEM lamella available was selected for this study. Figure 5-34 shows that the GB segregation of Fe and Ni is present at high burnups as well. Although Sn has a relatively high solid solubility limit and its segregation in the metal is not expected, Sn segregation occurs at the GBs of the 7 cycle sample. The highest measured Fe, Ni, and Sn concentration at the GB are 3.6, 2.3, and 2.2 times higher than their concentration in the metal matrix, respectively. No such phenomenon has been observed in the case of Cr. In the metal part both type of SPPs could be observed. The number of remnant SPPs in the oxide is very low and they contain mostly Cr. The compositions of the metal and oxide matrices and the containing SPPs are shown in Table 5-9. Due to the lack of SPPs, the statistics are low in the oxide. An example for the SPP remnants in the metal and the oxide is shown in Figure 5-35 and Figure 5-36, respectively.

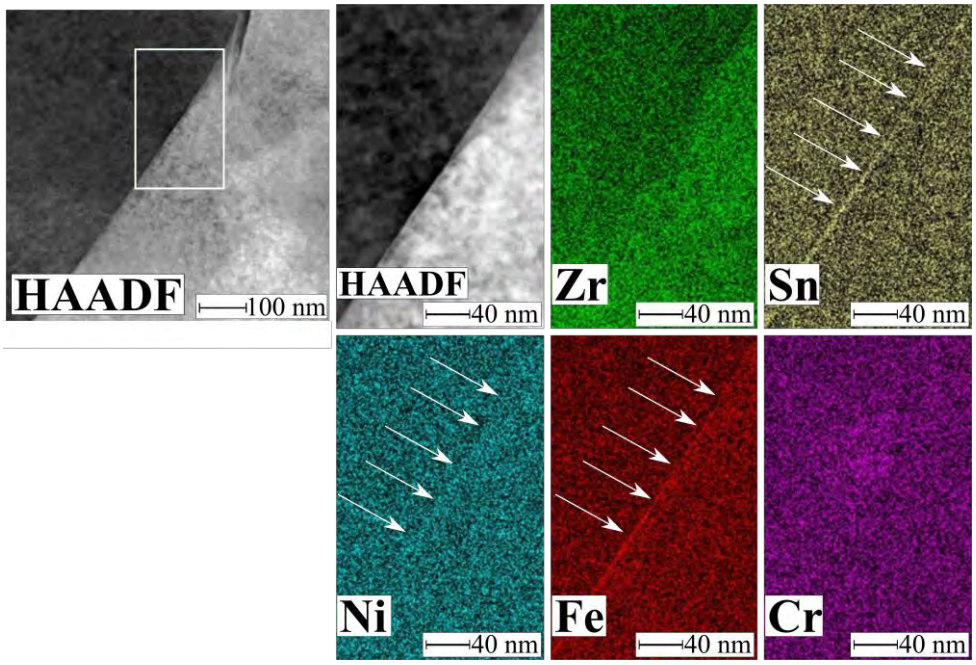

Figure 5-34 HAADF micrograph and ChemiSTEM maps of the metal of the 7 cycle LK3/L sample. The arrows show the GB segregation of the elements.

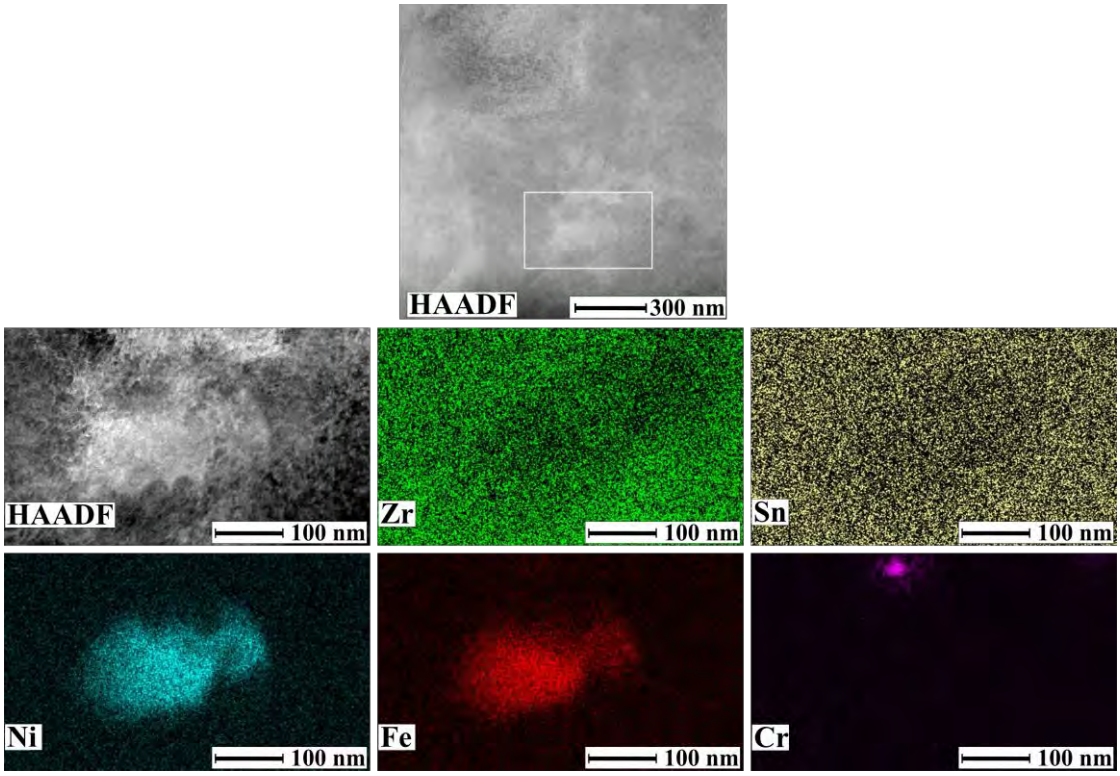

Figure 5-35 HAADF micrograph and ChemiSTEM maps in the metal part of the 7 cycle LK3/L sample. A remnant of a Zr_2(Fe, Ni) SPP and a small Cr-containing particle is revealed.

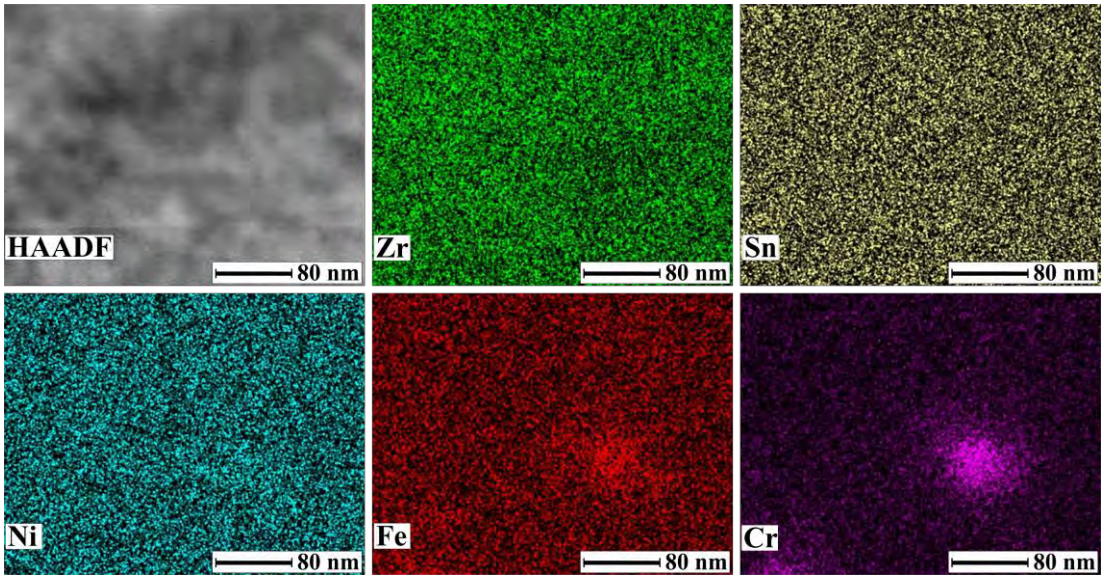

Figure 5-36 HAADF micrograph and ChemiSTEM maps in the oxide of the 7 cycle LK3/L sample. A remnant of a $Zr(Fe, Cr)_2$ SPP is revealed.

Table 5-9 Results of point analysis by ChemiSTEM of the 7 cycle LK3/L cladding. The average metal and oxide matrix composition from 3 and 9 points measured, respectively. Composition of the SPPs in both phases: the highest measured concentration is given.

Phase	O (at%)	Zr (at%)	Sn (at%)	Cr (at%)	Fe (at%)	Ni (at%)
Metal matrix*	15.91	82.42	1.17	0.036	0.37	0.095
Fe-Ni SPP in metal	4.88	84.72	0.89	0.07	4.83	4.61
Fe-Cr SPP in metal	15.01	75.20	0.90	7.78	0.79	0.33
Oxide matrix*	64.90	34.18	0.63	0.039	0.21	0.034
Fe-Ni SPP in oxide	not available					
Fe-Cr SPP in oxide**	57.02	36.38	0.78	3.85	1.27	0.39

* For the O and Zr content of the bulk metal and oxide matrix please refer to the EPMA result.
**Measurement based on spectra collected during mapping, i.e. providing only semi-quantitative data.

5.2.2.4. 9 cycle LK3/L

The ChemiSTEM results on the 9 cycle sample revealed Fe and Ni segregation at the GBs. The observations confirm that Sn segregates as well at the metal GBs at extreme high burnups (Figure 5-37). Based on the Cr map in Figure 5-37 Cr shows traces of segregation at a limited region of the same GB where Fe and Ni segregation is observed. The highest measured concentrations at the GB for Fe is 6.7, for Ni, 3.6, for Sn, 2.5, and Cr, 4.3 times higher than in the metal matrix.

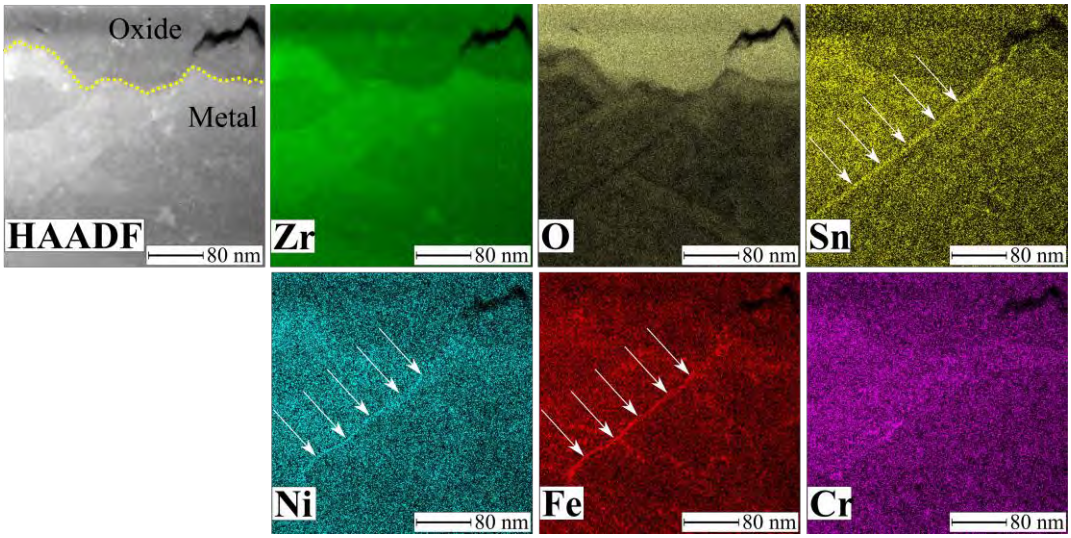

Figure 5-37 HAADF micrograph and ChemiSTEM maps at the metal-oxide interface of the 9 cycle LK3/L sample. Dashed line on HAADF micrograph represents the metal-oxide interface. The arrows mark the GB segregation.

Table 5-10 summarizes the average matrix compositions and the highest measured SPP remnant concentrations. The metal matrix composition was measured by point analysis collected 2.5-7 µm from the interface. For the oxide matrix direct point analysis is available only from the TEM lamella which was prepared at the outer region of the oxide (within 2-7 µm from the crud-oxide interface) and presented in Table 5-10. Based on a QMap, a point line-scan through the metal-oxide interface (see Figure-AII 3 in Appendix II) revealed that the oxide is stoichiometric both

away from the interface and in the vicinity of the interface. A very thin (~5-10 nm) transition layer is observed, i.e. the O signal drops suddenly at the interface. An SPP remnant in the oxide close to the metal-oxide interface is shown in Figure 5-38. The maps show that Fe and Ni segregate in the oxide in the shape of fine lines away from the core of the SPP, presumably in an oxide GB, or the interface of the original SPP.

Table 5-10 The average metal and oxide matrix composition from 3 and 4 point measurements respectively, in the 9 cycle LK3/L cladding. Composition of the SPPs in both phases: the highest measured concentration is given.

Phase	O (at%)	Zr (at%)	Sn (at%)	Cr (at%)	Fe (at%)	Ni (at%)
Metal matrix*	24.41	74.12	1.01	0.03	0.36	0.07
Fe-Ni SPP in metal*,**	23.85	64.52	0.09	0.66	3.14	5.72
Fe-Cr SPP in metal*	14.74	74.94	0.76	8.65	0.84	0.07
Oxide matrix***	66.89	32.60	0.28	0.04	0.17	0.03
Fe-Ni SPP in oxide***	65.48	26.81	0.05	0.31	3.29	4.06
Fe-Cr SPP in oxide***	57.33	23.60	0.08	17.47	1.45	0.08

For the O and Zr content of the bulk metal and oxide matrix please refer to the EPMA result. *Data collected 2.5-7 µm away from the interface. **Measurements are based on spectra collected during mapping, i.e. providing only semi-quantitative data. ***Measured on the lamella which was prepared at the outer part of the oxide (within 2-7 µm from the crud-oxide interface).

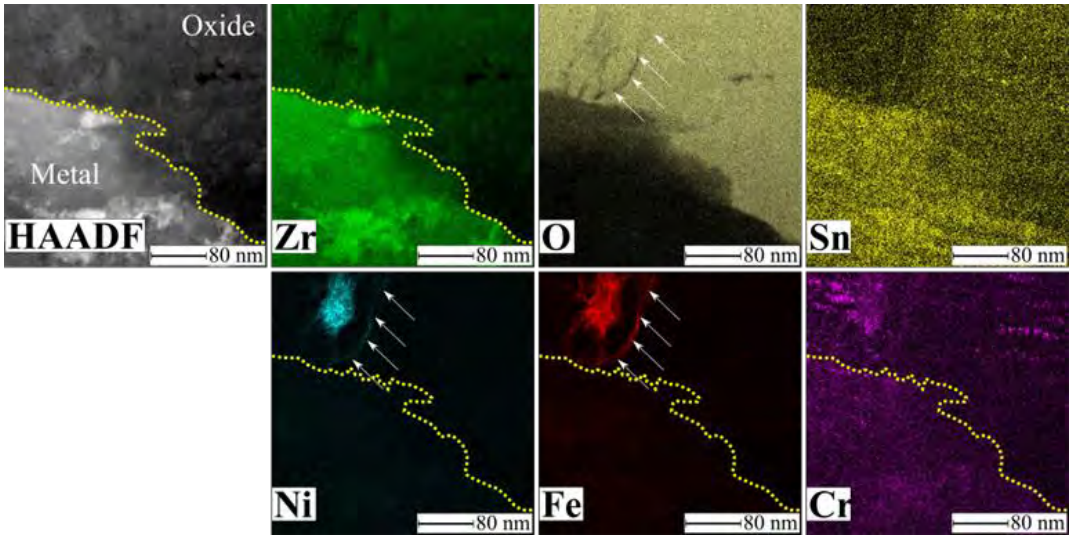

Figure 5-38 HAADF micrograph and ChemiSTEM maps at the metal-oxide interface of the 9 cycle LK3/L sample. A remnant of a Zr_2(Fe, Ni) SPP is revealed. Arrows show Fe and Ni in a shape of a fine line in the oxide. Dashed line represents the metal-oxide interface.

5.2.3. The effect of hydrides on the chemical composition at high burnup

The effect of the hydride on the microstructure is presented in Chapter 4 while this section examine their impact on the chemical composition. The H content of the high and extreme high burnup samples are above the H solubility limit in Zircaloy-2. As the H content is very high in this cladding, we assume that most of the hydrides investigated have occurred during service.

In the case of the 9 cycle sample the EPMA results have shown Fe and Ni depletion of the hydrides (Figure 5-21).The hydride and metal matrix compositions were compared by direct point measurements in TEM as well. In the 7 cycle sample no systematic difference was observed. In the case of the 9 cycle sample systematic differences were revealed not only for Fe and Ni but in the Sn concentration as well: 1.1-1.7 times less Fe, 1.2-1.3 times less Ni and 1.1-2.6 times less Sn is measured in the hydrides than in the metal matrix. The ChemiSTEM maps on the hydrides confirm this observation, shown in Figure 5-39. In the case of Cr, despite a certain drop observed on the images, clear quantitative depletion was difficult to detect in the hydrides.

While EPMA did not show Sn depletion in the hydrides, slightly higher level of depletion of Fe and Ni has been observed by EPMA. This could be due to the better statistics, i.e. higher number of large hydrides available on the bulk sample while in TEM the amount of available hydride phases is very limited.

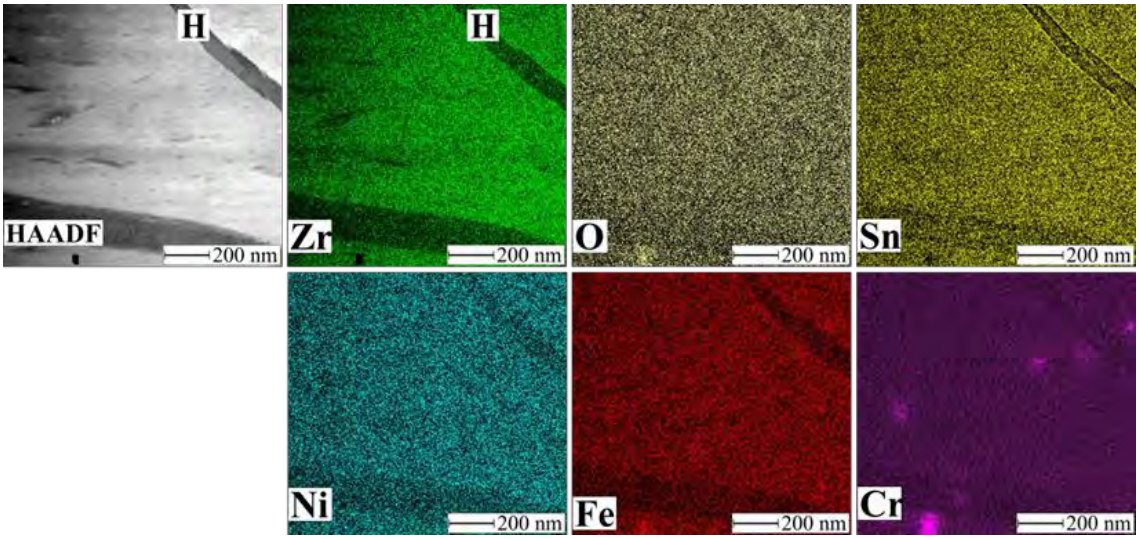

Figure 5-39 HAADF micrograph and ChemiSTEM maps on the hydrides in the metal of the 9 cycle LK3/L sample. One of the hydrides is marked by H.

5.3. Discussion on the chemical evolution of the metal and oxide matrices and its impact on the hydrogen uptake

A detailed chemical analysis of the LK3/L type Zircaloy-2 cladding has been presented in this chapter. The aim is to explore in depth the chemical changes occurring after different stages of irradiation in reactor. It is expected to find some correlation between these changes and the cladding's modified HPU and oxidation behavior at high burnups.

The limitations of the techniques used are discussed in the Discussion chapter of the thesis. The precision of the EPMA measurements are presented in Table-AII 1 in Appendix II.

In order to compare the obtained results by the two techniques, a short description Figure-AII 4, Figure-AII 5, Figure-AII 6 are presented in Appendix II.

The results of EPMA and TEM confirm some of the previous observations presented in the literature, such as the continuous dissolution of alloying element from the SPPs under irradiation, or the formation of hydrides as a function of time. However some of the observations are not reported in the literature and add new parameters to be considered as possible causes of the changes in the HPU or the oxidation. For instance the redistribution of the alloying elements due to the hydride formation and the fact that hydrides repel some of the elements is one of these findings.

It seems that there is no available data in the literature on the chemical composition of the hydrides in irradiated Zr-based cladding materials, and the question whether they contain any alloying elements is not yet answered by any quantitative measurement. The question could arise whether zirconium-hydrides do contain alloying elements or not. However, this question cannot be systematically answered, as binary intermetallics of Zr and Fe or Ni, do form hydrides as shown in [193] and [194]. In those studies, the formation of the Zr_2FeH_x systems by hydration of the Zr_2Fe compound even at low temperatures and low hydrogen pressures [193], and formation of the Zr_2NiH_x hydride systems have been shown [194]. Therefore, it is not evident and not necessarily expected that the hydrides would be depleted of certain alloying elements and this is shown for the first time in this study, to the best of our knowledge.

The observed phenomenon (i.e. hydrides being depleted of some of the elements) can affect the hydride formation after long-term irradiation where the matrix is rich in alloying elements by leading to the growth of the existing hydrides rather than nucleation and growth of smaller grains. This phenomenon could be at the origin of accumulation of hydrides at the outer wall of the cladding, and could add an extra parameter to the stresses developed in the material.

GB segregation is another phenomenon which was revealed in this study. Other authors studied the behaviour of the alloying elements as well, both with and without irradiation. As an example an APT study on un-irradiated Zr-based alloys showed GB segregation of some elements in the metal [93]. Ni and Fe segregation in un-irradiated Zircaloy-2 both at the metal and the oxide grain boundaries was observed in [106], while Sn segregation in the oxide [195]. Another APT study on the 9 cycle LK3/L material presented Sn and Fe clustering in the metal in ring-shaped features as well as Fe and Cr-rich nano-sized precipitates [126]. The authors suggest that precipitation of these elements occur at the site of dislocation loops or in their stress field [126]. In this thesis the evolution of the GB segregation has been revealed. Based on the example of irradiation-induced dissolution of the alloying elements from SPPs, it was expected that the GB segregation observed in the un-irradiated material may disappear with irradiation. However, the studies on the 3, 7 and 9 cycle samples reveal persistent presence of such segregation.

In the following, the effect of irradiation, a. on the metal and oxide matrix compositions, b. on the behaviour and distribution of different elements, and c. on the GB segregation are discussed.

The metal matrix is separated into two parts: the bulk metal and the metal close to the interface while the oxide layer is separated into three parts: the outer, the intermediate and the inner oxide. This separation is necessary due to the well-noticeable composition difference between these regions. Figure 5-40 shows the changes in concentration after 3, 6, and 9 cycle in these regions for each alloying elements separately. The metal and the oxide are shown together. This provides the evolution and behaviour of the different elements from low to high burnup region. As the two different phases are compared, the element ratio to Zr is given. For the concentrations in at% for the metal and oxide separately please refer to Figure-AII 7 and Figure-AII 8 in Appendix II.

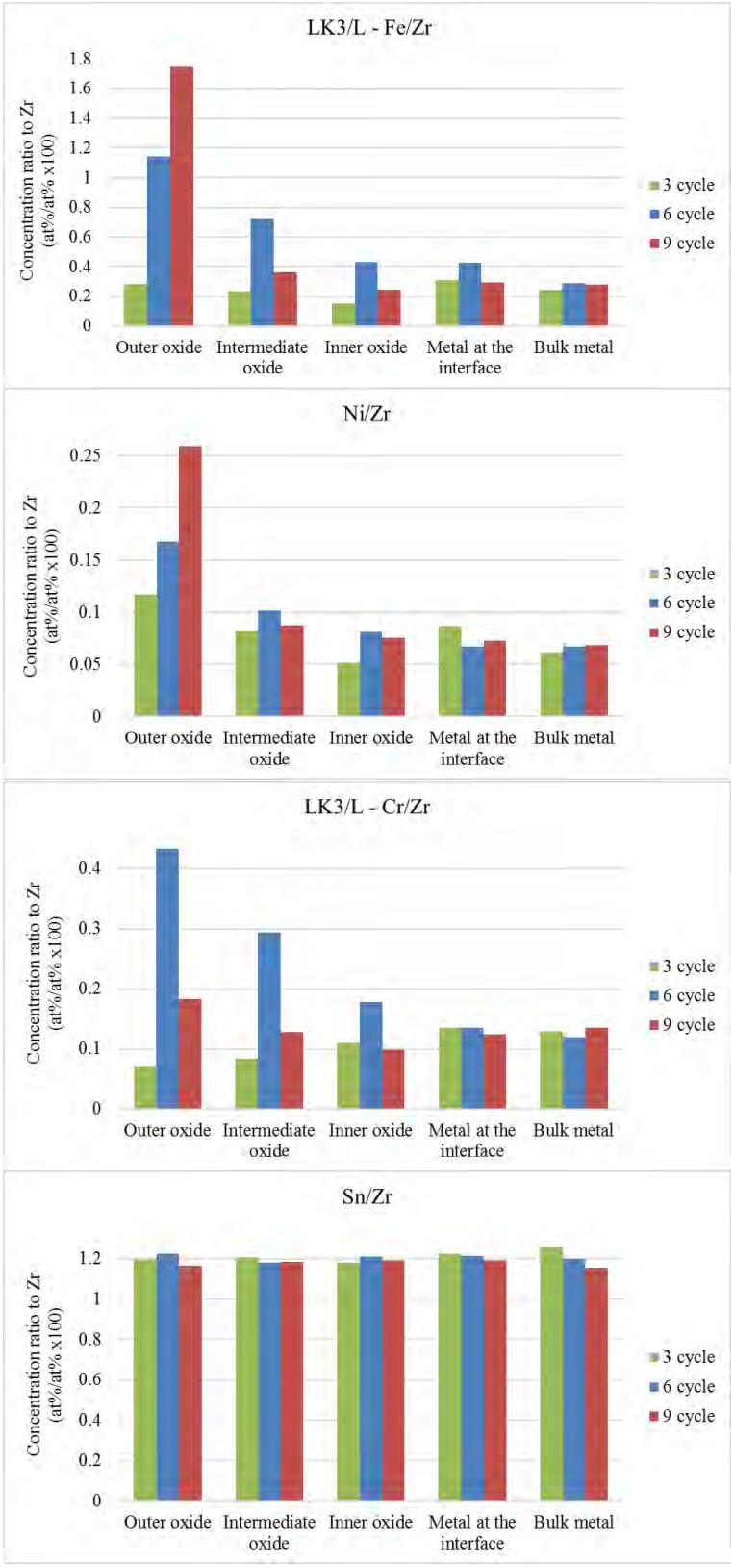

Figure 5-40. Comparative data for each alloying elements and each cycles showing the chemical evolution of the cladding in the metal and oxide matrices based on the EPMA point line-scans. SPPs are excluded.

Based on the results of Fe by EPMA in Figure 5-40 it is clear that at each region of the material there is an increase in the Fe concentration from 3 to 6 cycles. This can be explained with the SPP dissolution: as Fe is the fastest element which diffuses out from the SPPs an overall enrichment of the matrix is expected. However between the 6^{th} and the 9^{th} cycles sample the tendency is different. Although the bulk metal composition is similar in the 9 and the 6 cycle samples, in the other regions the 6 cycle sample shows higher Fe concentration. The explanation for the Fe "deficiency" in the 9 cycle sample can come from the fact that this sample has a significantly higher Fe content at the outermost oxide than in the other parts of the sample and also compared to this region in the other cycles. This indicates that once the material is saturated of the dissolved Fe there could be a driving force which leads the excess iron to the outer surface of the material. Another explanation could be that the original composition of the 6 cycle cladding was slightly different from the other claddings.

There is a tendency of drop in Fe concentration in the oxide side of the metal-oxide interface, compared to the metal side, for all claddings at different cycles. This drop is slight for the 6 and 9 cycle samples when the average is considered, however it is clearly observable in the individual point line-scans. If the mobility of Fe was similar in the oxide and the metal, as the oxide interface moves into the metal, it would be expected that the concentration of Fe on the two sides of the interface be the same, with respect to Zr. Therefore, it is unambiguously clear that the Fe has a higher mobility in the oxide and thus, should diffuse out.

Furthermore, it is systematically observed that the Fe content increases towards the outer oxide in all samples; and the level of enrichment in this region increases with the number of cycles. It could be the case that this is a general behaviour of Fe in zirconia, i.e. Fe seems to dissolve with a higher rate in the oxide and diffuse to the free surface. This phenomenon is observed

without irradiation as well [105], [103]. Although the crud has not been the topic of the thesis, both under and without irradiation, the migration of Fe to the free surface could influence the formation of crud, or in turn the crud could change the behaviour of Fe in the oxide. Considering the fact that in the above mentioned studies ([105], [103]) Fe accumulation was not observed at the outer oxide in those alloys which did not contain Fe, the possibility that the enrichment is due to contamination from the coolant could be rejected. The similar behaviour of the other elements further strengthen this statement. Despite the observations in autoclave that have provided unambiguously demonstrated Fe diffusion to the outer oxide surface and its accumulation there, in the case of in-reactor studies the water chemistry cannot be excluded. Therefore, this question remains open until further studies provide evidence that supports one or the other statement.

Ni increases slightly in the bulk metal towards the higher burnups. The Ni concentration reaches its maximum level in the intermediate oxide in the 6^{th} cycle. The inner oxide shows a higher percentage of Ni at high burnups (6 and 9 cycles) than after 3 cycles. This could modify the HPU behavior of the cladding based on the study of Kuri et al [131]. The authors claim that Ni, even in oxidized form in the vicinity of the metal-oxide interface, could increase the HPU. Ni concentration increases towards the outer oxide in all samples and the level of Ni-enrichment increases with increasing burnup. These observations indicate that Ni dissolves and a part of it accumulates at the outer oxide.

The formed hydrides which are large phases at high and extreme high burnups repel Fe and Ni from their volume; therefore further limit the capacity of the alloy to keep these elements in solid solution.

The observed segregation of Fe and Ni in the metal GBs after all cycles measured indicates that the GB segregation could be a path for the diffusion, i.e. the phenomenon could be considered rather as a “highway” for the alloying elements to diffuse out of the metal matrix, due to their low solid solubility limit. The alloying element concentration in the GBs compared to the metal matrix is given in Figure 5-41, after each cycles. However this data provides only the concentration ratio of matrix/GB, i.e. it shows that after each cycles how much the GB is enriched by the given element compared to the bulk composition. However, ChemiSTEM does provide only semi-quantitative data and very local information on the bulk matrix composition. Therefore, the compositional evolution of the GBs based on only the ChemiSTEM data cannot be provided. In order to estimate how the concentration of different elements evolved in the GBs, the quantitative data with high statistics obtained on the bulk matrix by EPMA analysis were used: The element ratios to Zr are taken into account for each elements and, for each cycles, multiplied with the concentration increments of the given element in the GB segregation (presented in Figure 5-42). In other words the calculation was done as follows:

$$(C_A^{Matrix}/C_{Zr}^{Matrix})_{EPMA} \times (C_A^{GB}/C_A^{Matrix})_{ChemiSTEM} \approx C_A^{GB}/\, C_{Zr}^{Matrix}$$

where C_A^{Matrix} is the concentration of element *A* (A=Fe, Ni, Cr, or Sn) in the matrix; C_{Zr}^{Matrix} is the concentration of Zr in the matrix; C_A^{GB} is the concentration of the element in the GB; EPMA and ChemiSTEM subscript expresses that from which measurement the data was used. In this way it is possible to give an estimation for the GB segregation evolution with cycles.

No EPMA measurement of the un-irradiated sample is available, therefore the data is based on the ChemiSTEM results. For the calculation of the GB segregation after 7 cycles the EPMA results on the 6 cycle sample was used. A trend of increasing element concentration in the GBs with the number of cycles emerged from this calculation (Figure 5-42). It must be noted that the statistics of the GB measurements are low. At extreme high burnup the GBs are enriched of

all four alloying elements but the Cr segregation was not observed along the whole GB only at certain limited locations.

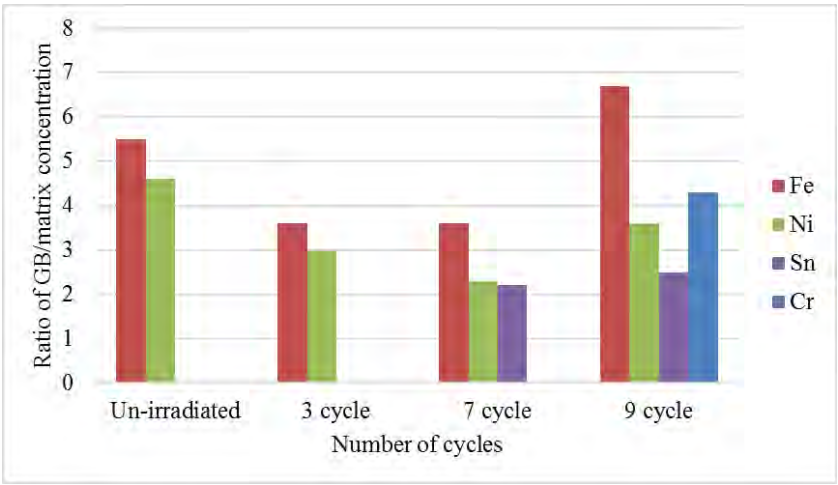

Figure 5-41 Amount of alloying elements at the GBs compared to the metal matrix after each measured cycles. Cr segregation after 9 cycles was observed only at limited sites of the GB.

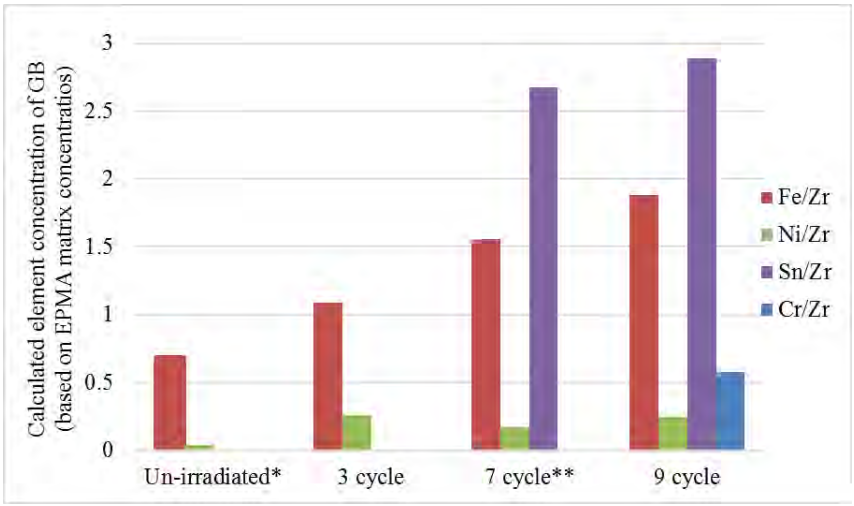

Figure 5-42 The evolution of GB segregation with the number of cycles calculated based on the metal compositions measured by EPMA and on Figure 5-41. The element ratios to Zr were used. The un-irradiated matrix composition is based on the ChemiSTEM results. The 6 cycle sample composition was used from EPMA to calculate the GB segregation of the 7 cycle sample. The composition of the "metal at the interface" region was used from the EPMA of the 3 and 6 cycle samples. 9 cycle EPMA data from the "bulk metal" region.

It was claimed that dissolution of certain alloying elements, such as Fe and Ni (and Nb in Zr-Nb alloys) in the oxide could change the diffusivity of H in the oxide layer by affecting the potential gradient through the oxide [151] or the mobility of interstitial protons [152], [141]. The role of Fe on the HPU was claimed to be dependent on its state: when in form of SPP Fe is claimed to increase the HPU [148]. Dissolved Fe^{3+} in the monoclinic and Fe^{2+} in the tetragonal oxide were associated with lower HPU [147], [153] and oxidation, respectively [153].

In un-irradiated and oxidized Zircaloy-4 the highest proportion of Fe^{3+} was measured near the oxide surface [153]. Although the oxidation state of the dissolved Fe has not been examined in this PhD work; a higher oxidation state could be expected in the outer region of the oxide. An Fe-rich outer oxide layer is observable in all irradiated samples. Although we could assume that a certain level of protection is provided by the chemical composition of the outermost oxide layer due to its Fe enrichment, we conclude that the level of protectiveness provided by this layer is negligible after a certain period of time. In other words, other processes that are coming to action at higher burnups could overcome on its effect and significantly reduce the relevance of this composition-based protection. For example, once there is an interconnected pore system which allows the water to flow inside the oxide, this protective behaviour would be lost.

As it was already described in the Chapter 2– Section 2.4.2.5, metallic Ni in the barrier oxide was claimed to have a negative effect on the HPU by offering a "window" for H-ingress to the metal [109], or in an oxidized form increasing the diffusion of H^+ through the oxide significantly [110] or offering nucleation sites for hydride-ion (H^-) storage at the oxide grain boundaries [131].

A higher fraction of Ni in the inner oxide layers was measured in the high burnup samples by EPMA. This could be a factor in the increased HPU of the sample at high burnups.

An unexpected behaviour is revealed in the case of Cr (Figure 5-41): although the Cr content does not change significantly in the metal at all stages of irradiation it shows a dominant maximum in the 6 cycle sample in all oxide regions. The causes of this significant change between 3 and 6 cycles and the decreased Cr content between the 6^{th} and the 9^{th} cycles need to be explored in future studies. One of the clarifications for this behaviour could be that dissolved Cr in the oxide rather goes out to the crud. It has been demonstrated in a previous in-situ measurement performed in the laboratory on oxidized Zircaloy-4 that when Fe and Cr dissolve from the SPPs and diffuses to the outer oxide Cr actually forms a layer on the top of the Fe accumulation [105]. The significant decrease of Cr content between 6 and 9 cycles could be explained by this process. Another possibility could be that the original composition of the 6 cycle cladding was slightly different from the other claddings with higher initial Cr and Fe content.

It must be mentioned that the pressure vessels and the tubing contain Cr, Fe, and Ni as alloying element and one can argue that this could be a possible source of these elements in the coolant. However, no data is available regarding the Cr water chemistry changes due to the mentioned phenomenon. Therefore we cannot reject the possibility that some of the observed Cr, Fe, and Ni could come from the coolant and further analysis (e.g. Cr water chemistry data) is needed in order to take a final conclusion on this point. It is worth noting that no Cr segregation has been observed in the metal GBs with the exception of a very limited region with accumulation of Cr with high concentration. Therefore it is logical to expect that Cr would not use the GBs of the metal as a route to access the outermost regions of the cladding. In fact, based on the observations regarding Cr and the fact that Cr is the slowest element which dissolved from the

SPPs it could be the case that once the Cr-containing SPPs are incorporated into the oxide layer there is a driving force to diffuse out to the water side surface.

Sn did not show significant changes during the service of the cladding (Figure 5-41). A trend of slight increment in Sn content is observable from medium to the higher burnups in the oxide close to the metal-oxide interface. At the same time, a trend of decreasing Sn content in the bulk metal and in the interface region of the metal is revealed. In the 9 cycle sample ChemiSTEM has shown some Sn segregation at the metal GBs and that the segregation continues to the oxide as well through the metal-oxide interface. It was claimed that Sn segregation in the oxide could enhance the tetragonal to monoclinic transformation of the oxide reducing its protectiveness [196]. Sn segregation is also observed at the boundary of a hydride precipitate and a metal grain (Figure 5-39).

EPMA point line-scans through the metal-oxide interface suggest a sub-stoichiometric oxide up to 2 μm from the metal-oxide interface after 3 cycles with 55-60 at% O (Figure 5-6). This region seems to decrease to 1.5 μm after 6 cycles with 55-63 at% O (Figure 5-11); and even further narrows to 0.5 μm after 9 cycles with higher, 62 at% O (Figure 5-25). It is important to notice that, although the WDS system has a higher sensitivity compared to EDS, EPMA also has lower sensitivity when measuring elements with low atomic number. Therefore, the values that are obtained for O needs to be handled with certain precaution, keeping the limitation of the EPMA technique in mind. However, the relative comparison of the oxygen concentration at different distances from the metal-oxide interface can be considered with confidence and allows to make a statement about the variation of O concentration.

The ChemiSTEM measurements confirm the presence of a sub-stoichiometric oxide of the 3 cycle sample. The measured O value in the oxide is quite low. The obtained O and Zr value has a dependency on the lamella thickness. Even when composition was re-calculated using a range of thicknesses, the O value remained low. A maximum of 60 at% O was reached when using 180 nm thickness which is certainly higher than the actual thickness of the lamella. Even though the O value could be slightly higher than measured and some uncertainty remains due to the lamella thickness, it is certain that the oxide is sub-stoichiometric after 3 cycles. Here as well, the limitations of the EDS technique regarding the measurement sensitivity of low atomic number elements has to be taken into account. However, the difference between two regions or two samples can be considered as confirmation of the above mentioned results. Work is in progress for the further evaluation of the oxide phase of the 3 cycle sample as a continuation of this PhD. The ChemiSTEM data confirmed the stoichiometry of the 9 cycle oxide also in the vicinity of the interface (please refer to Figure-AII 3 in Appendix II).

It has been demonstrated that a sub-stoichiometric oxide would result in a higher conductivity [197], therefore lower H-uptake [60]. Therefore, the change in this property can be one of the reasons for the decreased protectiveness against HPU at high burnups.

The EPMA results show an increasing O content in the metal in the region close to the interface. After 3 cycles the O/Zr ratio is 10.1 (Figure 5-2). The ratio is 11.7 after 6 cycles (Table 5-3) and 14.1 after 9 cycles (Table 5-5). Faster oxidation has been correlated to the higher dissolved O content in the metal at the interface [169], [170]. Therefore, this is also an indicator of the reduced protectiveness of the material towards higher burnups.

Furthermore, the undulation of the metal-oxide interface has an effect on the stress distribution in the oxide [139], [69], [138]. Changes in the compressive and tensile stresses were revealed in an undulated interface by modelling [138]. It was also claimed that the differences in the stresses have an influence on the diffusion coefficient of oxygen [69], [21]. Due to the appearance of the local stress at the metal-oxide interface the free energy of the vacancy formation and therefore the vacancy concentration will be changed [21].

To the best of our knowledge there is no study on the topic of how the changes in the stress distribution at the interface would influence the diffusion of other elements. However, based on the example of O, it is highly possible that other elements are also influenced by the stresses. In Chapter 4 it is demonstrated that the undulation indeed changes in the different samples with different service time spent in the reactor. It is important to note that the undulation of the interface in the different materials is not a site-specific property: based on the 2D images that are collected for the 3D visualization, as well as the general SEM inspection of the segments with an overview of the interface along the whole segment has shown the same undulation; no significant variation of the undulation was observed.

5.4. Conclusions

This chapter studied the compositional changes of LK3/L Zircaloy-2 claddings after 3, 6/7, and 9 cycles in a BWR and attempts to correlate these changes to the change of oxidation and HPU behaviour of the cladding at high burnups. The important findings of the chapter can be summarized as follows:

A. Metal:

- The composition of the metal part of the cladding has extremely changed with the increasing time of irradiation and especially after 9 cycles: the alloying elements present in the secondary phase particles have dissolved to a great extent. However it is important noticing that some remnant of SPPs – majority containing only Cr –still exist in the metal even after extremely long irradiation time which is beyond the design of the cladding.
- The bulk metal matrix (SPPs/remnants excluded) is enriched of the alloying elements after irradiation compared to the initial state of the matrix. However, the alloying element content of the matrix at high burnups, i.e. between the 6^{th} and 9^{th} cycles, does not differ to a great extent.
- The O content of the metal at the interface increases from medium to higher burnups. Such increment is correlated to higher corrosion rates.
- The hydrides are present in particular in the vicinity of the metal-oxide interface and they are depleted from Fe and Ni at high burnups. This implies that the hydrides repel alloying elements and this could lead to further enrichment of the matrix in these elements.
- GB segregation of Fe and Ni before and at all stages of irradiation have been revealed in the metal. GB segregation of Sn is present only in the high and extreme high burnup claddings (7 and 9 cycle). The element content of the GBs seems to increase with the number of cycles. These findings suggest that the GBs could be the diffusion routes for these elements.

B. Oxide:

- The oxide contains very few SPPs, regardless of the service time, as a faster dissolution of them occurs once they are incorporated in this phase. The oxide matrix is increasingly enriched of the alloying elements towards high burnups.
- All samples showed increasing Fe and Ni content towards the outermost region of the oxide. Furthermore, a trend of increasing Fe and Ni content of this region is revealed with the increasing number of cycles. In conclusion, the elements from the dissolved SPPs have a tendency to accumulate at the outer oxide or; in the case of Fe; other free surfaces, such as in the large cracks of this region. Based on the observations and the previous studies in the literature, dissolved Fe in the oxide could have a positive effect on the HPU. However, it seems to have a negligible effect in the high and extreme high burnups (i.e. 6 and 9 cycle) when other factors (e.g. interconnected pore system, etc.) might overcome this protectiveness. It is claimed that metallic Ni has the opposite effect on the HPU by increasing the H diffusion in the oxide. Therefore Ni may help to increase the H-pickup besides other processes at high burnups.
- The fact that Cr still remains as remnant SPPs in the material even after 9 cycles of irradiation indicates that Cr could be one of the reasons why the cladding did not undergo rapid corrosion under extreme conditions. The observed overall decrease in the Cr content in the material from 6 to 9 cycles remains to be explained. It is proposed that Cr could diffuse out to the crud or that the 6 cycle cladding had a slight difference in its original composition. However there is no evidence to support any of these statements.

The stoichiometry of the oxide changes with time and that reduced protectiveness (through reduced conductivity) is characteristic at high burnups. The correlation between the electronic resistance of the oxide and the HPU in other materials in autoclave was already

described in Chapter 2 – Section 2.4.2.3: in an oxide with lower conductivity a higher electrochemical potential gradient would build up across the oxide resulting in a decreased activation energy of the proton absorption at the cathodic site resulting in a higher HPU [53]. Despite the fact that the 9 cycle oxide is stoichiometric at the interface, a very thin sub-stoichiometric layer of oxide even in the 9 cycle cladding leads to an intermediate behaviour that is confirmed by a narrow layer that is more conductive than the rest of the oxide (provided in Figure-AI 1 in Appendix I). This confirms that the oxide formed after long term stay, i.e. at higher burnup shows a stoichiometric composition, knowing that such oxide will be less conductive, the charge compensation will be satisfied more by the H migration near the metal-oxide interface and thus the pick fraction will increase.

- All samples show some drop in the Fe and Ni content in the oxide side of the interface compared to the metal side when high resolution EPMA point line-scans were carried out. Furthermore, the 3 cycle cladding shows an accumulation of alloying elements at the metal-side of the interface, which has decreased after the 6^{th} cycle and which is not present in the 9 cycle sample. This could be the result of the change in the morphology of the metal-oxide interface. As it was discussed the undulated interface could change the diffusion properties of the elements through the metal-oxide interface compared to a less undulated or straight interface.
- Ni content increases with the number of cycles in the inner oxide region. Oxidized Ni close to the interface could increase the HPU.
- With a great coincidence, in the 3 and the 9 cycle samples, one Zr_2(Fe, Ni) SPP is observed by TEM in the vicinity of the interface in the oxide. Both precipitates show early stages of their oxidation. Alloying elements are observed in the surrounding of

these SPPs which seem to decorate possibly the oxide grain boundaries. These clusters are formed a few nm away from the core of the observed SPPs, therefore these segregations could also be simply the remnants of the boundary of the original SPP. If the first suggestion is true, i.e. these are GB segregations, that could indicate that these elements use GBs as paths for diffusion, at the early stage of incorporation into the oxide. Such a statement should be further confirmed by more studies.

- In the 9 cycle sample segregation of Sn is observed in the oxide close to the metal-oxide interface as a continuation of the metal GB segregation. Although the segregation of Sn is surprising due to its high solid solubility, such segregation in the oxide is claimed to degrade the oxidation properties by helping the tetragonal to monoclinic transformation [196]. Lower H diffusivity is reported in the tetragonal oxide. Therefore segregation of Sn at the GBs could increase the HPU at high burnups.

- The results show extreme change of composition of the alloy such as the dissolution of SPPs; the presence of large hydrides pushing away the dissolved elements; the change in the oxide's stoichiometry; combined with processes in the nanometre scale such as Sn segregation in the interface oxide are the factors which could be responsible for the reduction of the overall protectiveness against fast oxidation and increased HPU. On the other hand, it is important to emphasize that even though the cladding shows a higher oxidation and HPU rate at late-life, it is still resistant to deleterious HPU and oxidation and performs well even beyond the designed service time.

6. PWR MATERIALS – LOW-TIN ZIRCALOY-4 AND ZR-2.5NB

In the previous chapters the behaviour of the LK3/L type cladding that has served in a BWR reactor has been described. The variable parameter was the service time in the reactor which gave a good basis for following-up the changes in the chemical composition and the microstructure. In this manner the evolution of the material can be better understood. In this chapter two cladding materials that are designed for PWR environment and which have served in the same PWR reactor (KKG reactor) with different composition are presented and compared to each other. These claddings show different performance in the reactor. In general Zr-Nb claddings show lower hydrogen pickup and they are used extensively in PWRs. The description about the general behavior and differences between the two cladding alloys as well as the possible factors responsible for this difference is described in more details in the Literature Review. For the composition of the as-received samples and the measured oxide thickness and H content after service please refer to Chapter 3. As a reminder of the most important parameters:

The 4 cycle Zircaloy-4 has a burnup of 51.1 MWd/kgU. The alloy composition is: 0.91 at% Sn, 0.356 at% Fe and 0.186 at% Cr (calculated based on wt% data). The analysed segment is from the elevation of 1468 mm, the maximum oxide thickness of the rod is 59 µm. The H-content measured on the closest elevation (1561 mm) is 209 ppm.

The 3 cycle Zr-2.5Nb contains 2.438 at% Nb and 0.114 at% Fe (calculated based on wt% data). The segment is selected from the elevation of 869 mm, with 70 ppm H content, 41.4 MWd/kgU burnup. The maximum oxide thickness measured on the rod (not the segment) is 16 µm.

The aim of this chapter is to:

- Find additional parameters that could be responsible for their different performance.
- To provide data for the comparison between the BRW and PWR claddings (Chapter 7) in order to better understand the factor of different reactor environments and to differentiate between general and alloy-specific phenomena.

Therefore, the microstructure and the chemical composition of the different regions of the materials are presented in a similar manner as for the LK3/L Zircaloy-2 sample. The microstructure of the samples is studied using 3D reconstruction by FIB tomography and it is shown in the first part. EPMA maps and point line-scans will be presented in the second part of the chapter.

6.1. Microstructural changes in the PWR materials

The second part of the chapter presents the comparison of the oxide microstructure of the two samples having the crack system in the centre of the attention. The Nb-containing samples show better resistance to cracking. Cracks in the oxide have been claimed to be a possible short-cut for the faster diffusion of the different species through the oxide, helping the penetration of oxidizing species and hydrogen. The reason behind the better performance of the ZrNb and the absence of cracks in the oxide is a topic of research and some explanations have been already suggested such as the higher undulation and roughness of the metal-oxide interface in the case of the ZrNb resulting in a better stress distribution compared to a straighter interface. In the case of the Zircaloy-4 type sample the outer part of the metal with the hydride phases is also present. During the sectioning of the Zr-2.5Nb sample no hydride phase was observed therefore the metal is not reconstructed in more details.

In this current section FIB tomography is applied on the two irradiated samples with the aim to better understand the causes behind the formation of a higher quality oxide in the Zr-2.5Nb compared to that of the low-tin Zircaloy-4. The possible role of the Nb phases in the crack formation is described.

6.1.1. 4 cycle low-tin Zircaloy-4

6.1.1.1. Overview of the microstructure by SEM

A low and a higher magnification SE micrograph of the outer part of the sample are presented in Figure 6-1. The oxide thickness of the segment was measured as 25 µm (±1.5 µm). The oxide is very uniform in terms of thickness. The SEM micrographs show that the outermost ~2.5-3 µm part of the oxide is dense and it contains no or only small-sized micro-cracks. As an example for the overview of the hydride distribution in the sample a BSE micrograph is shown in Figure 6-2. At this magnification it can be observed that large hydride phases are present in the metal with the highest concentration close to the metal-oxide interface.

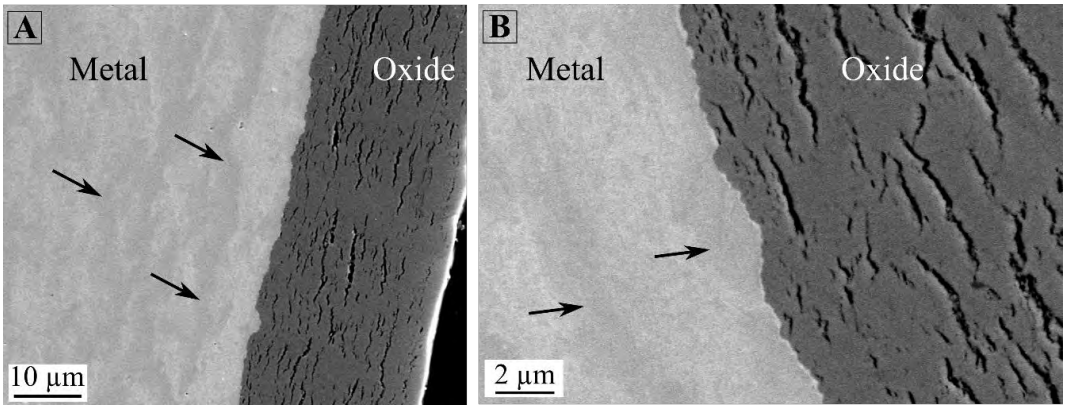

Figure 6-1 SE images of the outer part of the 4 cycle low-tin Zircaloy-4 cladding. (A): low magnification; (B): higher magnification of the metal-oxide interface. Arrows show some of the hydride phases.

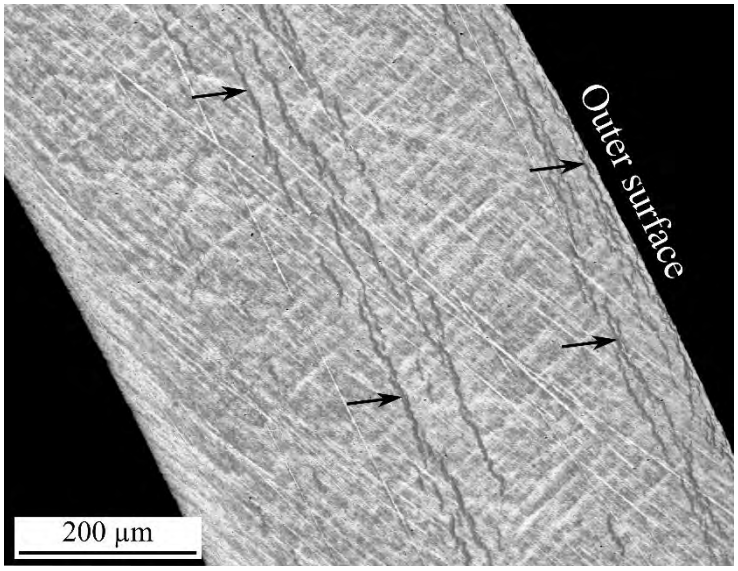

Figure 6-2 BSE micrograph on the metal part of the 4 cycle low-tin Zircaloy-4 cladding showing the hydride distribution. Arrows show some of the hydride phases.

6.1.1.2. Characterization of the oxide layer and the metal-oxide interface by FIB tomography

Two different sites of the oxide have been reconstructed and will be presented here: 1. the outer part of the oxide layer (around the first 7 µm of the oxide from the water-oxide interface); and 2. the metal-oxide interface including the hydrides in the metal as well.

An example SE image is shown for both the outer (Part (A)) and the inner oxide (Part (B)) in Figure 6-3.

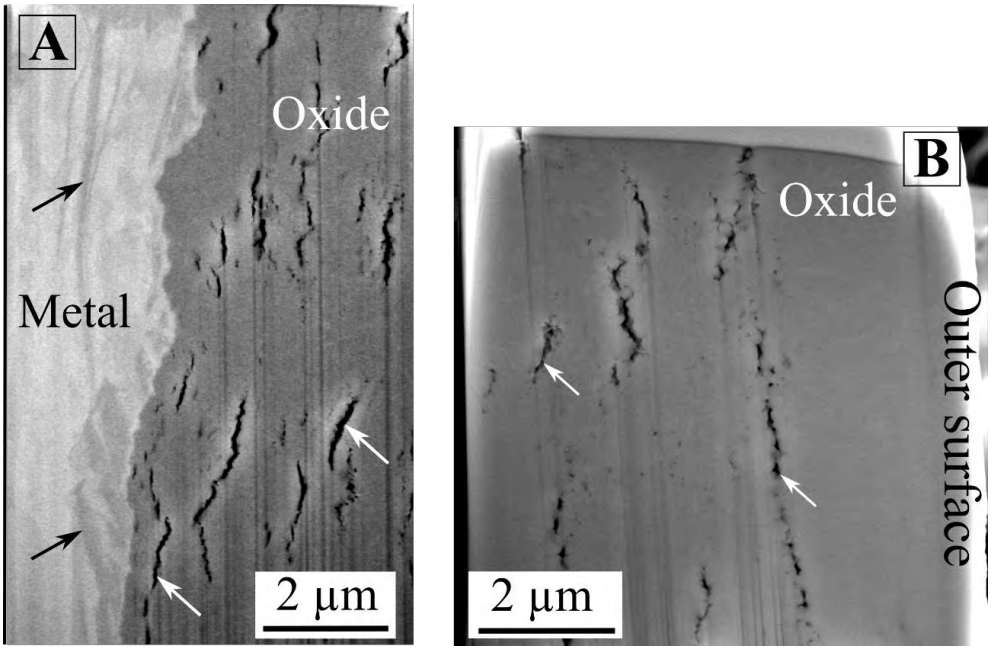

Figure 6-3 Example for the SE images obtained during the slice-and-view (A): at the metal-oxide interface; and (B): the outer oxide of the 4 cycle low-tin Zircaloy-4 sample. Black arrows mark the hydrides, white arrows indicate the cracks.

The 3D visualization of the outer 7 µm of the oxide is presented in Figure 6-4. In total 143 SE images have been collected along 2.6 µm distance in the Z direction, i.e. with step size of ~18.6 nm. Cracks in the oxide are coloured as green. The oxide matrix is not displayed here with colour but the entire bounding box of the reconstructions contains the oxide. Two region with different characteristics can be distinguished on the Figure: the outermost ~3 µm is dense and contains only 0.004 volume % of cracks, it is marked as oxide "from early oxidation" on the figure. This is an extremely low value and shows that practically no cracks were formed in the beginning of the oxidation. This dramatically changes in the oxide which formed after breakdown: large volumes of cracks were formed in the subsequent layer which contains 3.42 V% of cracks. The total volume fraction of the cracks in this visualized volume (i.e. in the whole 7 µm thick outermost region) is 2.52%. Cracks are not interconnected to each other; however they are elongated objects.

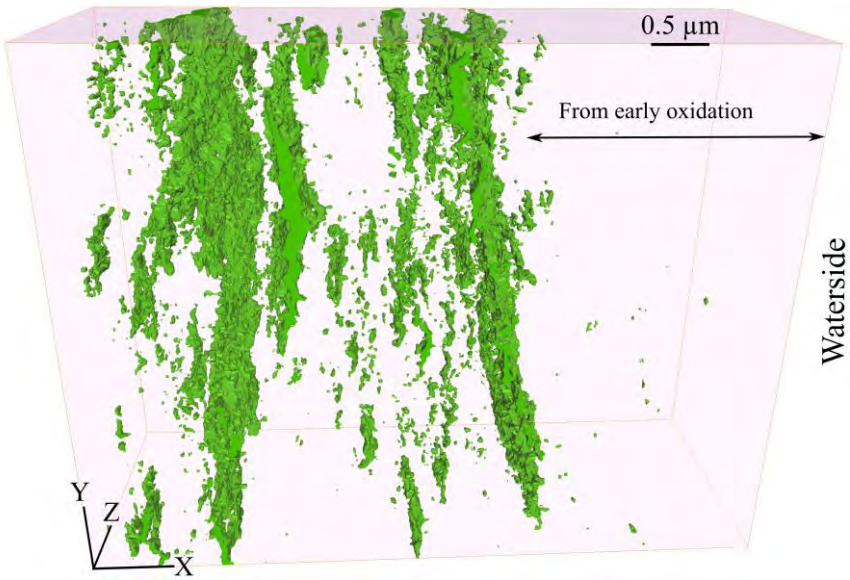

Figure 6-4 3D visualization of the cracks (green) in the outer region of the oxide (transparent pink) of the 4 cycle low-tin Zircaloy-4 sample. The size of the "bounding box": X=7.1 µm, Y=5.5 µm, Z=2.7 µm. The oxide that is formed in the beginning of the service is marked.

A snapshot of the reconstructed volume at the metal-oxide interface is presented in Figure 6-5. In total 64 SE images have been collected along about 1.7 µm distance in the Z direction, with step size of ~26.6 nm. The cracks in the oxide are displayed in green while the hydride phases in the metal in blue. The surrounding oxide is visualized in transparent pink in order to give a better view of the metal-oxide interface. Large and interconnected hydride phases are observed close to the interface. In the case of occurrence of some circumferential cracks close to each other, the oxide could create an interlinkage of the cracks by inducing radial cracks which connect these circumferential cracks to one another. This interlinkage was not observed in the 3D visualization. The total crack volume fraction of the oxide in this visualized volume is 3.21%, while if we consider only the innermost part of the oxide taken into account up to 1 µm from the interface, the measured value is 4.25%. The hydride volume fraction in the total volume of reconstructed metal is 16.75%, while up to 1 µm from the interface it is 26.3%.

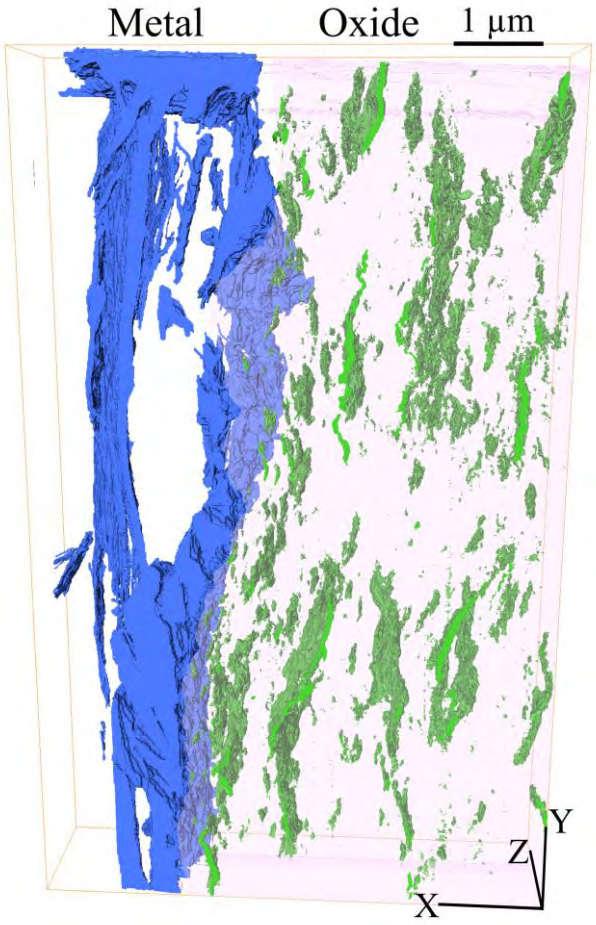

Figure 6-5 3D visualization of the hydrides (blue) in the metal; and the cracks (green) in the oxide (transparent pink) close to the metal-oxide interface of the 4 cycle low-tin Zircaloy-4 sample. The size of the bounding box: X=6.6 µm, Y=10.7 µm, Z=1.7 µm.

6.1.2. 3 cycle Zr-2.5Nb

6.1.2.1. Overview of the microstructure by SEM

Figure 6-6 shows SEM micrographs on the outer region of the 3 cycle Zr-2.5Nb sample showing the full oxide (Part (A)) and the metal-oxide interface (Part (B)), both showing a top-view of the segment. The average oxide thickness is 7.7 μm with 1 μm of standard deviation. The outermost 1-1.5 μm of the oxide has only small micro-cracks. In the rest of the oxide two types of cracks can be distinguished: small non-connected cracks and a long circumferential crack at around 1.5-2 μm away from the metal-oxide interface. The Nb-rich phases in the metal as well as in the oxide phase are well-observable on Part (B) of the Figure. These Nb-rich phases have been identified previously to have β-Zr structure. Their maximum Nb concentration is in the range of 18 - 20 at% [169]. Metallic Nb in the oxide can be observable by SEM up to 1.5-2 μm from the metal-oxide interface. The distribution of hydrides is observable on the SEM image in Figure 6-7 and it is clear that in the case of this sample there is no accumulation of hydrides close to the interface.

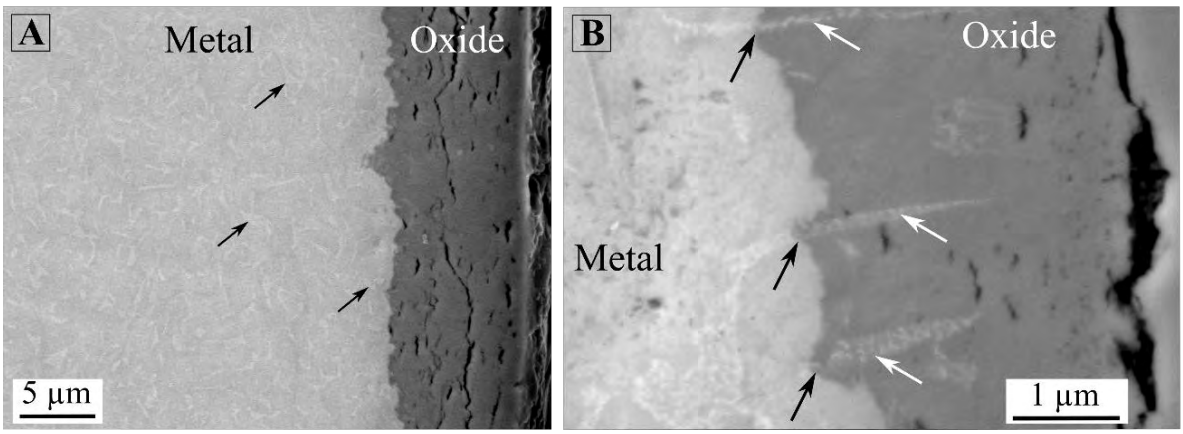

Figure 6-6 SE micrographs on the 3 cycle Zr-2.5Nb sample. (A): Outermost part of the cladding with the full oxide. Black arrows point to some of the Nb phases in the metal. (B): SE micrograph of the metal-oxide interface. White arrows show the Nb phases in the oxide phase. Black arrows indicate a more advanced oxide front in the metal surrounding the Nb phases.

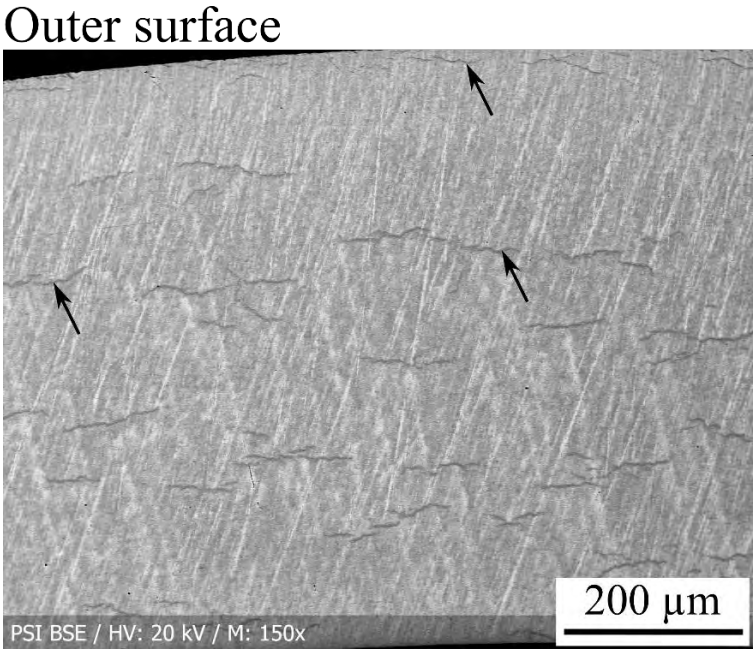

Figure 6-7 BSE image showing the hydride distribution in the 3 cycle Zr-2.5Nb cladding. Black arrows show some of the hydride phases.

6.1.2.2. Characterization of the cracks and Nb-phases in the oxide by FIB tomography

In the case of the 3 cycle Zr-2.5Nb sample only the oxide part close to the metal-oxide interface has been reconstructed in details, i.e. the metallic Nb phases and cracks are visualized. In the selected volume for 3D FIB no hydride phase was observed. Due to the fact that this study focuses on the effect of Nb phases on the crack formation in the oxide, the Nb in the metal has not been segmented and not presented here. The example SE image of the metal-oxide interface is presented in Figure 6-8. The different objects in the oxide have a well-distinguishable intensity. The SE image suggests that the Nb phases in the oxide stay metallic (i.e. un-oxidised) up to a certain distance in the oxide.

Figure 6-9 shows the result of the reconstruction. Along 1.3 µm in the Z direction 169 images were collected in order to obtain a high resolution, i.e. with the step size of ~7.5 nm. The metal part is displayed as well in a suggestive manner and in order to better understand the orientation

and the relative location of the oxide and the different objects. In this manner the shape of the interface is visible. In order to confirm that the Nb remains metallic in the oxide EDS measurements (not shown here) have been performed before and throughout the slicing of the sample in order to confirm that the observed phase is a Nb-rich phase. Furthermore TEM measurements and quantifications have confirmed that these Nb-rich objects in the oxide are still metallic. The ChemiSTEM map collected from the metal-oxide interface and the quantification can be found in Appendix III (Figure-AIII 3 and Table-AIII 1). The metallic Nb phases in the oxide are displayed in blue colour. Cracks are in brown. Based on the reconstructed volume the absence of cracks and dense oxide is observable at the interface at those sites where metallic Nb-phase is incorporated in the oxide. These crack-free areas can be found even up to 2-3 micrometres away from the interface. The cracking of the oxide at the time of formation, i.e. at the metal-oxide interface is observable at those parts of the oxide where no Nb-phase is present. The top view of the selected smaller volume in Figure 6-9 shows one example where the above described phenomenon can be better observed. The crack volume fraction of the oxide in the full reconstructed volume is 3.15% while this value is much lower, i.e. 0.25% close to the metal-oxide interface (up to 1 μm distance away from the metal-oxide interface). The oxide front seems to be more advanced at those areas where Nb-rich phases are present in the metal (please refer to Part (B) of Figure 6-6).

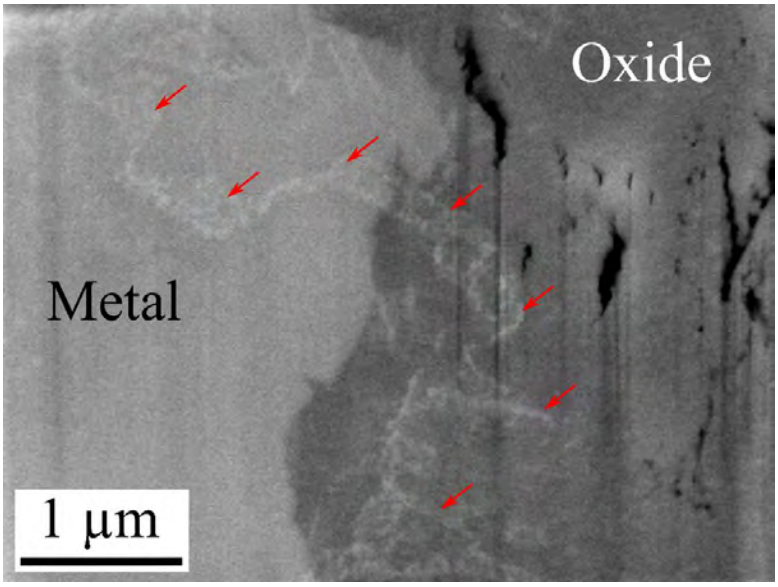

Figure 6-8 An example for the SE images obtained during the slice-and-view of the metal-oxide interface of the 3 cycle Zr-2.5Nb sample. A Nb-rich phase through the metal-oxide interface is marked by the red arrows.

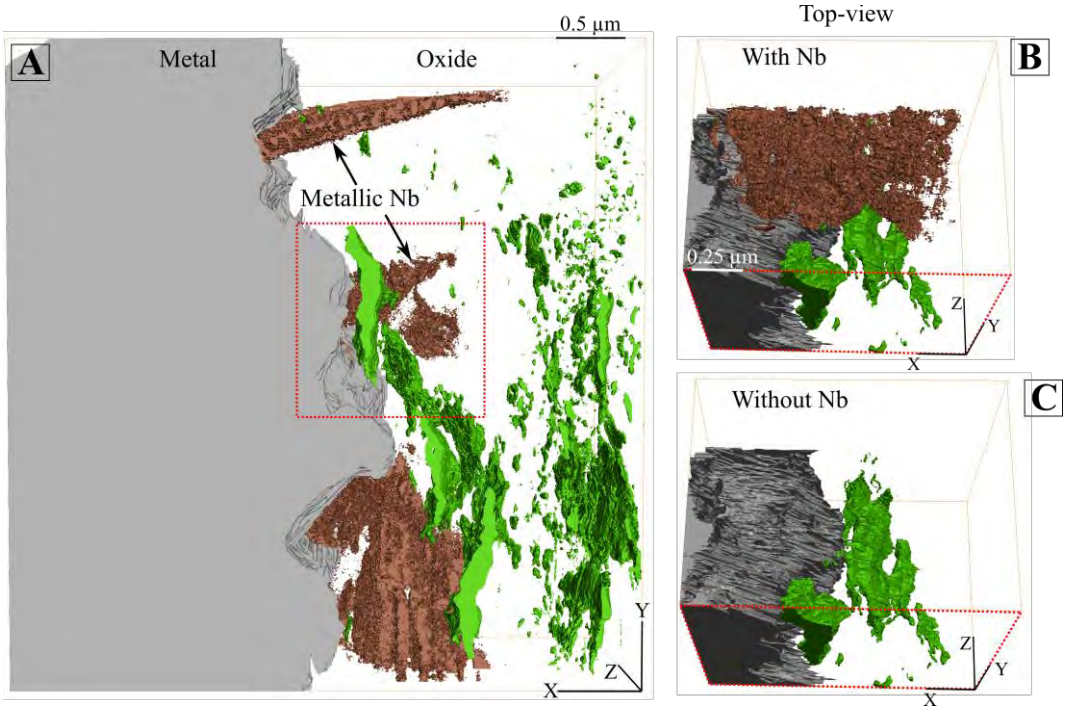

Figure 6-9 3D visualization of the cracks (green) and metallic Nb-phases (brown) in the oxide, and the metal (grey) close to the metal-oxide interface of the 3 cycle Zr-2.5Nb sample. (A): The size of the "bounding box": X=4.6 µm, Y=4.7 µm, Z=1.3 µm. The red dashed square shows a selected region that is displayed from a top-view orientation on (B) and (C). (B): Top-view orientation of a selected region with Nb, (C): without the Nb phases. The "bounding box" size in (B) and (C): X=1.6 µm, Y=1.4 µm, Z=1.2 µm

6.1.3. Discussion on the microstructural changes – Impact on hydrogen uptake

The crack microstructure in the different regions of the oxide layer has been revealed in both samples by FIB tomography. The general Discussion provides the description of the limitations of this technique.

The results in the case of the low-tin Zircaloy-4 sample show that the outermost 3 μm oxide is practically intact and cracks cannot be found in this part of the oxide in the range of the resolution of the FIB tomography technique. In the oxide which formed after this pre-transition oxide, both small and large cracks are observed parallel to the metal-oxide interface, i.e. in the circumferential direction. There is a sudden increase in the crack volume fraction from 0.004% in the first 3 μm layer (which is marked as "early oxidation" on Figure 6-4) to 3.4% in the oxide formed after. In the inner oxide the crack volume fraction is similar to this latter value which means that no significant increase of the crack volume fraction occurred at the last cycle. The value of 4.25 % crack volume fraction at the interface (up to 1 μm) tells us that the newly formed oxide is not highly protective and it is not highly stable against crack formation. This could strengthen the observation that the stress distribution of a less undulated interface can be correlated to an imperfect inner oxide. At the last stage of oxidation precipitated hydrides were also present in the metal and they can also contribute to the crack formation in a certain extent.

In the case of Zr-2.5Nb the outermost oxide is not visualized by FIB tomography therefore no exact value is given for the fraction of cracks at this site of the oxide. However, based on the SEM images, it is revealed that an intact outer layer exist in this case as well. This study focuses on the inner 2-3 μm of the oxide where Nb phases can be still found as metallic parts. In contrast

with the low-tin Zircaloy-4 sample, this material shows a decrease in the crack volume fraction in the 1 μm range of the oxide from the metal-oxide interface. This could mean that the lastly formed, fresh oxide is protective. However intact oxide at the interface has been observed only on those regions where metallic Nb phases are present.

The comparison of the crack volume fractions of the two samples at the different parts of the oxide is shown in Figure 6-10. The difference of the crack volume fraction between Zr-2.5Nb and low-tin Zircaloy-4 in the oxide at the metal-oxide interface is significant. This suggests that the formation of the cracks at the interface oxide is much less enhanced in the Zr-2.5Nb material. The presence of the metallic Nb-phases in the oxide could explain this phenomenon. The observations suggest that these phases act as composite members in the oxide increasing the mechanical properties and strengthen the oxide layer in the close environment of the interface. These Nb-phases are present in the oxide up to 1.5-2 μm away from the metal. Up to this distance the inner oxide is protected by these phases: cracks could be formed only in limited, Nb-free areas and the propagation of these small cracks may be prevented at this part of the oxide, i.e. no large, interconnected cracks are allowed to form. The higher amount of cracks in the more distant regions of the oxide could be also explained by the suggested interpretation: once the oxide layer is free of Nb-phases – i.e. more than 1.5-2 μm away from the interface – the oxide is not reinforced anymore. The relaxation of the oxide and propagation of the already formed cracks could occur. This could explain the formation of periodical crack-system of the oxides formed in Nb-containing claddings [172], and the occurrence of the two different crack types in the oxides. Another factor could be the absence of hydride phases in the metal as even in the distance of 2-3 μm hydrides were not observed. In Chapter 4 it has been demonstrated that hydride oxidation can increase the amount of cracks in the formed oxide. In the case of the 3 cycle Zr-2.5Nb the amount of hydrides do not contribute to the crack formation.

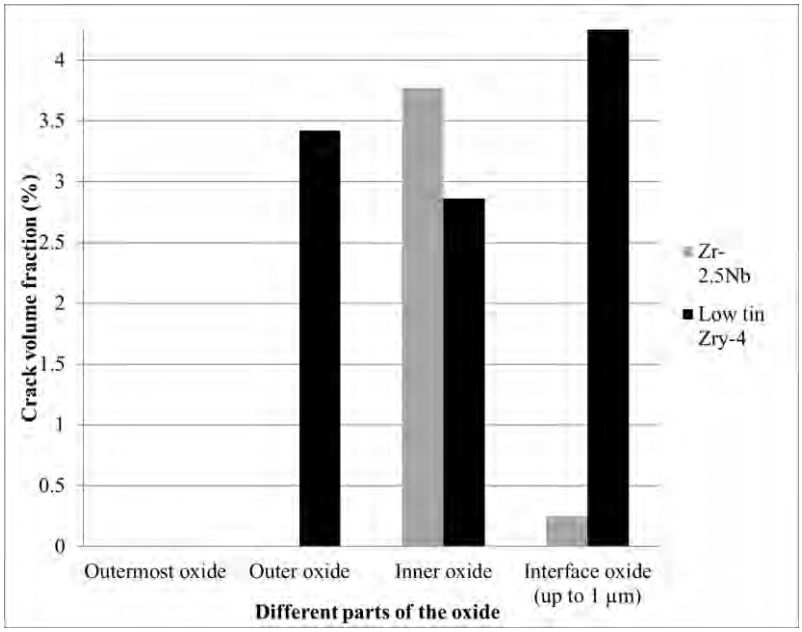

Figure 6-10 Crack volume fractions of the two samples at different sites of the oxide layer. Interface oxide: the oxide region up to the distance of 1 µm from the metal-oxide interface. Inner oxide: the full reconstructed oxides in Figure 6-5 and Figure 6-9 with the exception of the Interface oxide region. Its thickness is around 2 µm for both samples. Outer oxide: oxide marked as "from early oxidation" in Figure 6-4, thickness is 4 µm. Outermost oxide: The outermost 3 µm oxide in Figure 6-4. Note: the outer oxide and outermost oxide of Zr 2.5Nb are not available,

It has been shown (by SE micrographs and the 3D reconstruction as well) that the oxide front has progressed more ahead into the alloy where Nb phases are present. This leads to rougher interface in the case of the Zr-2.5Nb compared to that of low-tin Zircaloy-4.

Based on the above described phenomenon the influence of Nb on the oxide properties could be interpreted as follows:

1. The metal matrix around the Nb-phases oxidizes slightly faster than the metal matrix where Nb is not present. This leads to the formation of an undulated interface which will result in a better stress distribution in the oxide.

2. The metallic Nb-phases in the oxide can improve the mechanical properties of the oxide acting as a composite component which will prevent the material from cracking at the interface. Nb-phases seem to act as obstacles for the propagation of the already formed small cracks.

A schematic drawing of the oxide microstructure at the metal-oxide interface of Zr 2.5Nb is presented in Figure 6-11 that shows the above proposed explanation for the oxide's cracking behaviour.

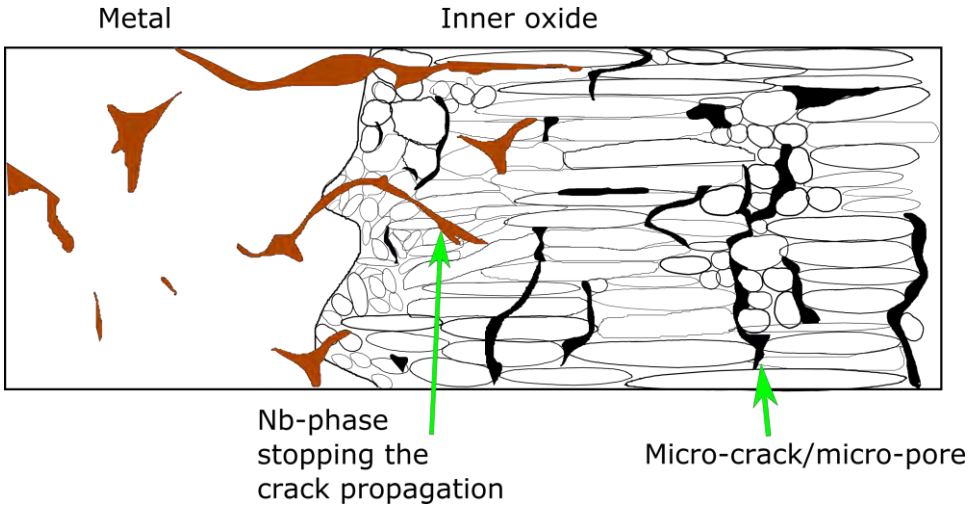

Figure 6-11 Schematic drawing of the microstructure of the oxide at the metal-oxide interface of Zr 2.5Nb. The Nb phases in the metal are in brown and the metallic Nb in the oxide as well. The metallic Nb-phases in the oxide are stopping the propagation of the cracks in the oxide. More cracks occur in those regions where Nb is not present.

6.1.4. Conclusions on the microstructural changes

The observations presented in this study and other studies in the literature as well have led to the conclusion that the critical factor responsible for the different performance of these two materials is the significantly different properties of their metal-oxide interface. A protective inner oxide is a prerequisite for the good HPU and oxidation properties. The large contrast in

the quality of the interface oxide layer has been demonstrated between the two samples. The interfaces show completely different microstructures: undulated and crack-free inner oxide have been found only in the Zr-2.5Nb sample. It is suggested that this latter could be due to the presence of the metallic Nb-phases in the inner oxide as well as the lack of large hydrides in the metal close to the interface. From the microstructural point of view it is suggested that, the significant difference regarding the resistance against cracking of the interface oxide regions of the two samples is one of the reasons for their different H-uptake properties.

6.2. Chemical changes in the material

In the following section EPMA quantitative point line-scans and qualitative elemental maps through the metal-oxide interface and on the full scale of the oxide are shown and described.
As before the behavior of the dissolved elements at the different regions of the samples is in the focus. As here the common alloying element is Fe this element will be in the centre of attention and its distribution in the metal and oxide as well as at their interface.
It is expected that the Zr(Fe, Cr)2 particles are already dissolved in a certain extent in the 4 cycle Zircaloy-4 sample. Based on the data in the literature regarding the dissolution of Nb in the Zr-Nb type claddings it is not expected that the Nb-phases are dissolved in the metal matrix in a large extent. Is known as well that Nb remains metallic in a certain distance (around 1.5-2 µm from the metal-oxide interface) in the oxide even when its surrounding is already oxidized. In other parts of the oxide, i.e. more than 2 µm away from the interface the Nb phases dissolve as well. However, it has been show that Nb remains metallic in the oxide (for more details refer to the Literature Review).

6.2.1. 4 cycle low-tin Zircaloy-4

6.2.1.1. Chemical analysis of the metal by EPMA

On Figure 6-12 a long point line-scan through the outer 300 µm of the base metal is shown. The Zr and O distribution and the alloying elements in at% and their ratio to Zr are presented. In the metal matrix, i.e. when SPPs are not included, the Fe concentration varies between 0.29 at and 0.36 at%, while the Cr content changes from 0.05 at% to 0.20 at%. The higher signals of Fe and Cr are coming from the SPPs. The highest measured element content is 2.03 at% Fe and 5.20 at% Cr. An EPMA elemental map is presented in Figure 6-13: it is clear that the diffusion of Fe from the SPPs is faster than that of Cr in this material as well. The matrix is already enriched of Fe. The metal-oxide interface is also visible on the map and it is well-observable that the composition of the metal is different close to the interface than in the bulk region. The large scale map of Fe in Figure 6-14 reveals that the high concentration zone at the outer side of the metal can be found practically all along the circumference. Therefore, the average element content is given for this two regions separately in Table 6-1. The thickness of the enriched interface region is about 2.5 µm therefore the average is given for this distance from the interface. In total 9-11 points are used for the calculation for this region. The bulk metal refers to the rest of the metal and 88-91 points have been collected. The results confirm that the metal side of the metal-oxide interface is enriched of Fe.

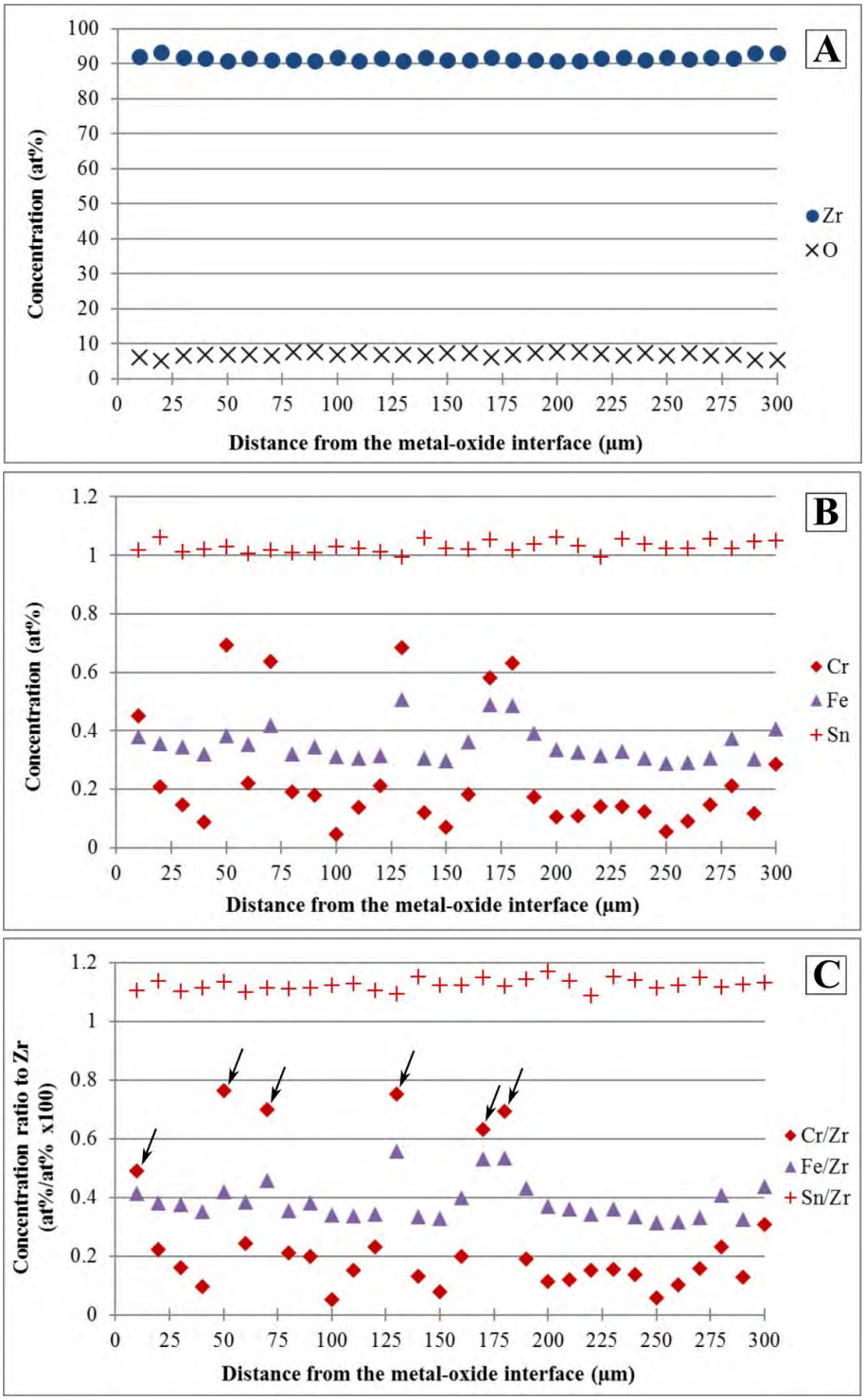

Figure 6-12 EPMA point line-scan in the outer 300 µm of the metal part of the 4 cycle low-tin Zircaloy-4 sample. (A): Zr and O; (B): Element concentrations in at%; (C): Element concentration ratios to Zr. Arrows indicate the increased element concentration due to the presence of an SPP in the vicinity of the measured point.

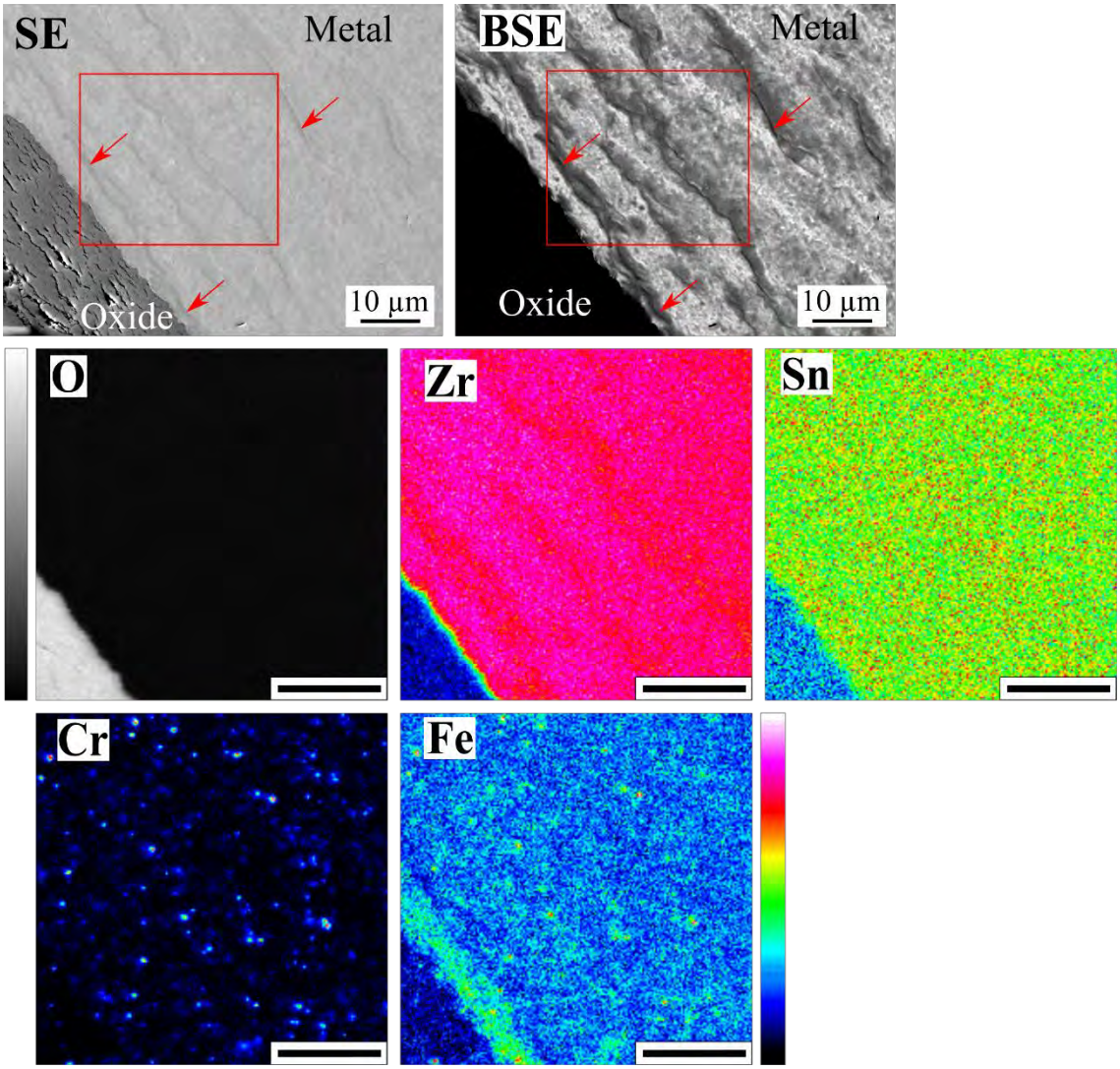

Figure 6-13 SE, BSE micrograph and elements maps on the metal and the metal-oxide interface of the 4 cycle low-tin Zircaloy-4 sample. Arrows indicate the hydrides. The scale bar is 5 µm.

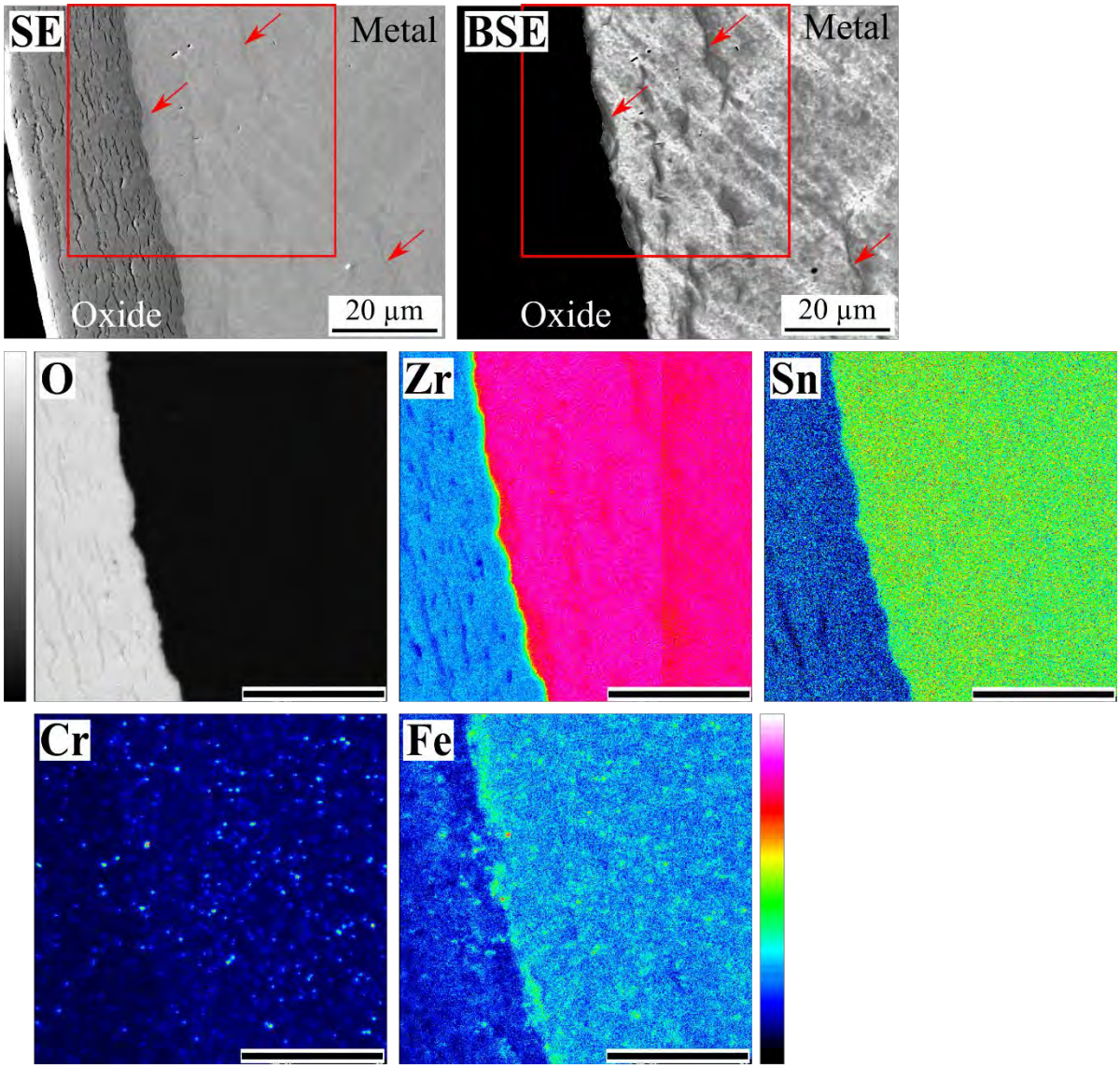

Figure 6-14 SE, BSE micrographs and large scale EPMA maps at the metal-oxide interface of the 4 cycle low-tin Zircaloy-4 sample. Arrows point to some of the hydrides. The scale bar is 20 µm.

Table 6-1 Average element concentrations in the bulk metal and close to the metal-oxide interface of the 4 cycle low-tin Zircaloy-4 sample. The SPPs are excluded from the calculation.

Phase	O (at%)	Zr (at%)	Sn (at%)	Cr (at%)	Fe (at%)
Bulk metal	6.38	92.12	1.01	0.14	0.33
Metal at the interface	6.59	91.80	1.01	0.16	0.47

6.2.1.2. Chemical analysis of the oxide and the metal-oxide interface by EPMA

Figure 6-15 shows one of the EPMA point line-scans measured on the oxide of the 4 cycle low-tin Zircaloy-4 sample. The metal-oxide interface is also included in the point line-scan. The full oxide layer is measured and presented in the Figure. Strong increment of the Fe concentration is observed at the outermost part of the oxide. This enriched layer is around 0.5-1 μm thick and the transition between the enriched layer and the rest of the oxide is quite sudden. The concentration of Fe changes at the metal-oxide interface as well: its transition from the metal to the oxide is not smooth and it can be described as a "step-like" transition having Fe enrichment in the metal part. The described variations in the Fe concentration are systematically observed. The other elements, namely Cr and Sn, behave as expected, sudden change in concentration or systematic behaviour in different sites of the sample is not observed. The elemental maps at the metal-oxide interface are presented in Figure 6-16 showing at higher magnification. Figure 6-17 the outer oxide of the sample. The elemental maps confirm the above described behaviour of Fe. The maps show that there are a low number of SPPs in the oxide scale and that the number of Fe-containing SPPs is less compared to Cr in the oxide as well. The maximum concentration measured for SPPs is 2.19 at% Cr – 0.94 at% Fe.

In order to give the average concentration of the oxide it needs to be given separately for the outer region and the bulk oxide. Although no difference was observed at the interface region of the oxide, it will be also separated in order to provide a data comparable with the other samples. Table 6-2 presents the composition of these regions where Interface oxide: up to 1.5 μm distance from the metal-oxide interface; Outer oxide: the outermost 1 μm; Intermediate oxide: between the other two regions. The average values are calculated from 8-9 points for the outer, 85-95 points for the intermediate, and 5-6 data points for the inner oxide regions in total. Based on the maps and the individual point line-scans Cr has a large range of concentration variation

in the oxide and the differences in the average values in the different oxide regions rather come from a random distribution than showing a systematic trend in the behaviour of Cr.

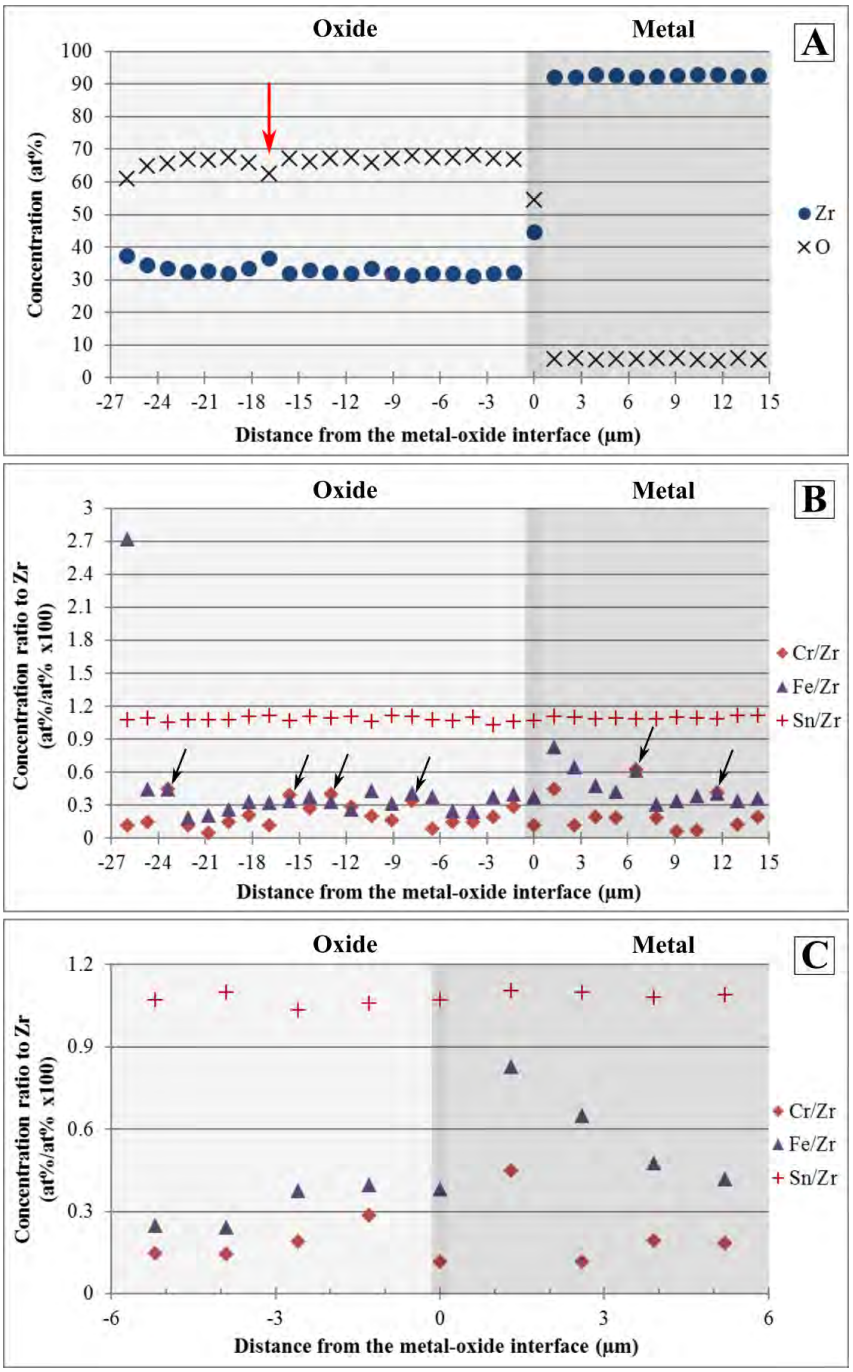

Figure 6-15 EPMA point line-scans through the metal-oxide interface of the 4 cycle low-tin Zircaloy-4 sample. (A): Zr and O distribution; (B): Cr, Fe, and Sn concnetration ratio over Zr. (C): The same as B showing only a narrower region at the interface. The point marked by a red arrow was most probably measured on a crack.

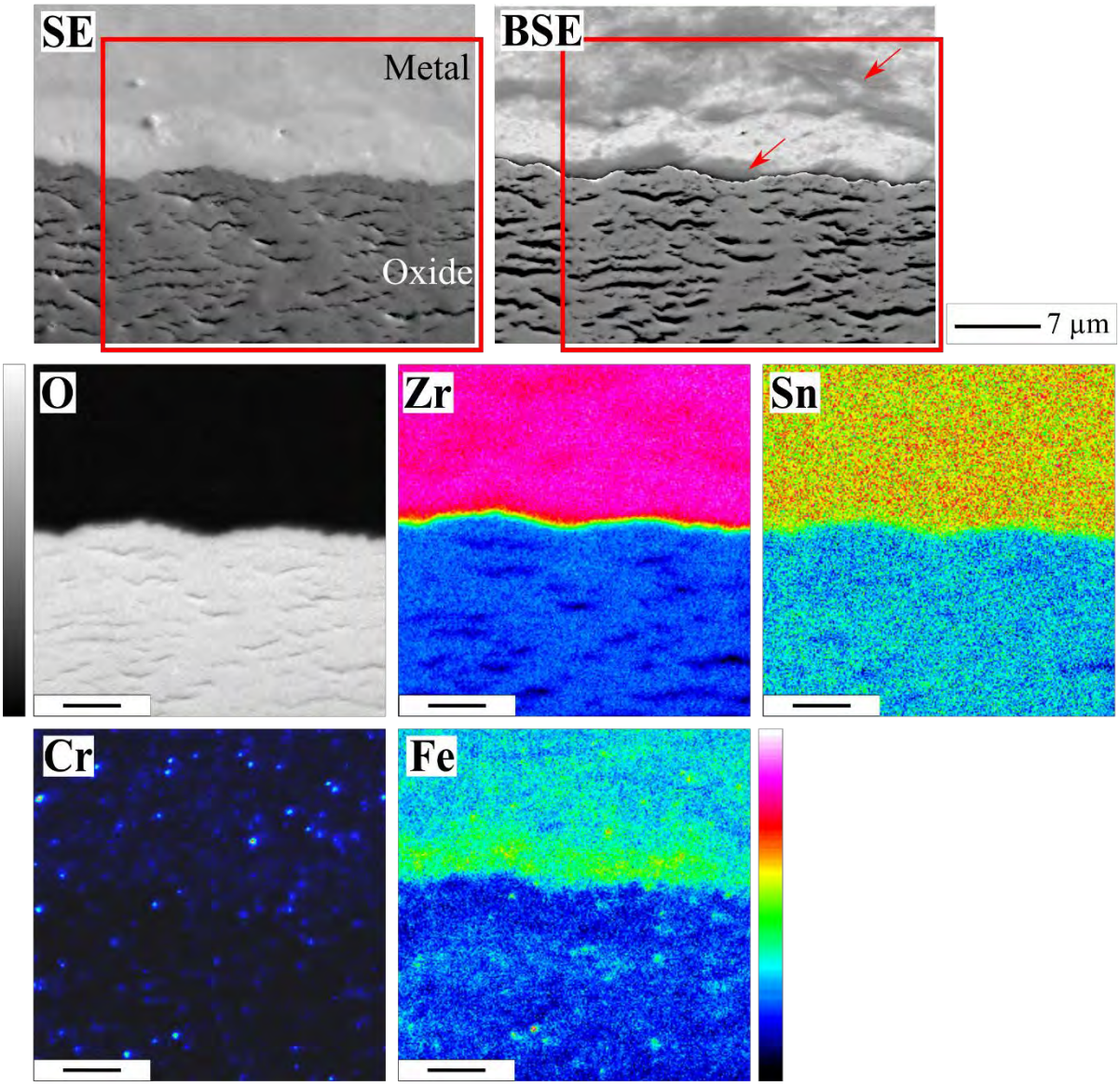

Figure 6-16 BSE image and EPMA elemental maps of Cr, O, and Fe at the metal-oxide interface of the 4 cycle low-tin Zircaloy-4 sample. Arrows indicate hydride phases. The scale bar is 5 µm.

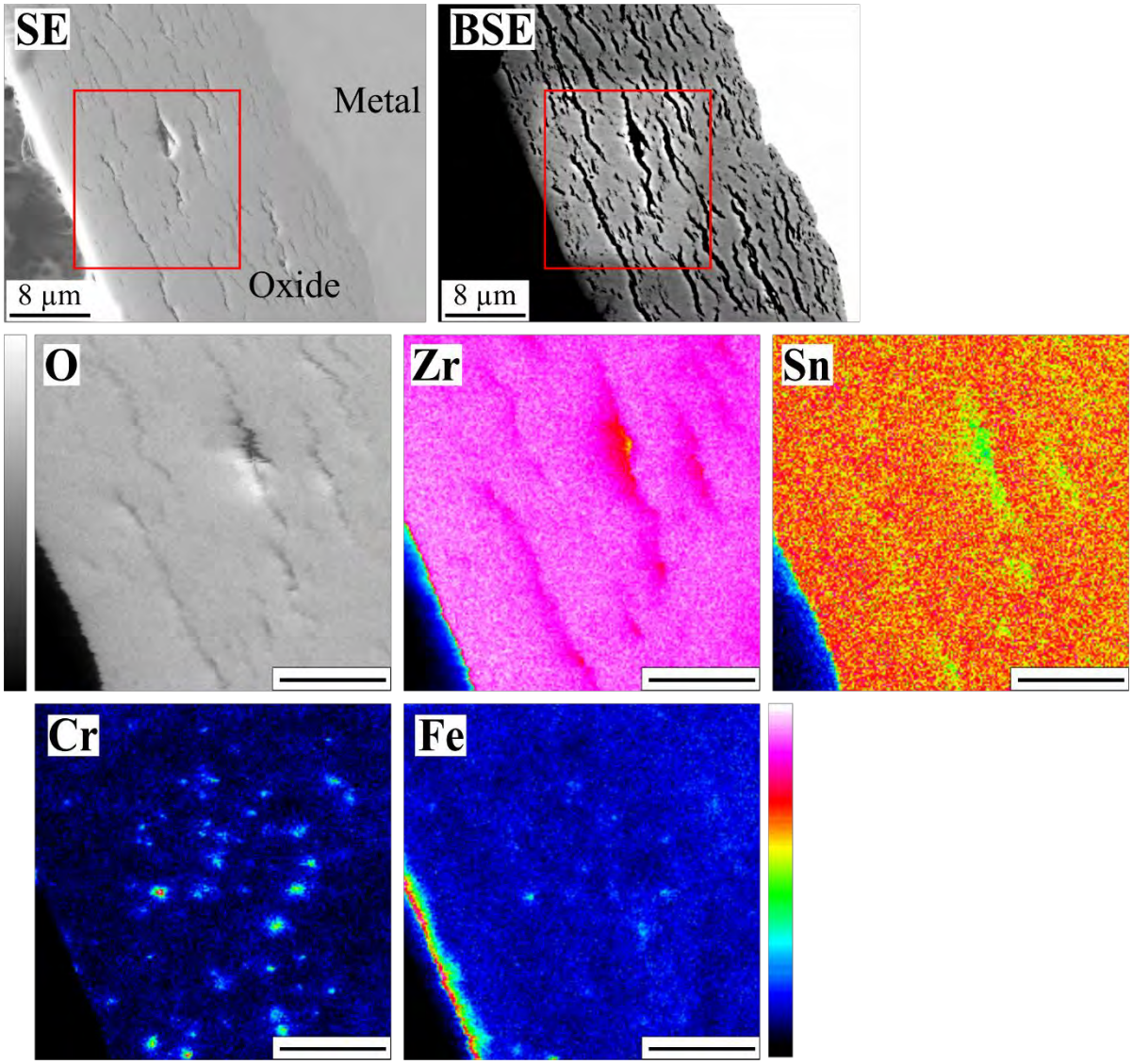

Figure 6-17 BSE image and EPMA elemental maps of Cr and Fe on the oxide (including the outermost oxide) of the 4 cycle low-tin Zircaloy-4 sample. The scale bar is 5 µm.

Table 6-2 Average concentrations of the different regions of the oxide matrix of the 4 cycle low-tin Zircaloy-4 sample. SPPs excluded. For definition of the layers please refer to the text.

Phase	O (at%)	Zr (at%)	Sn (at%)	Cr (at%)	Fe (at%)
Inner oxide	67.29	32.18	0.34	0.08	0.12
Intermediate oxide	67.15	32.34	0.35	0.05	0.10
Outermost oxide	64.15	35.10	0.39	0.03	0.27

6.2.2. 3 cycle Zr-2.5Nb

6.2.2.1. Chemical analysis of the metal by EPMA

An EPMA point line-scan on the outer 22 μm of the metal of the 3 cycle Zr-2.5Nb sample is shown in Figure 6-18. Part (A) shows both the Zr and O distribution. As expected Zr has a drop in its concentration value where the Nb phase is measured. Part (B) and (C) shows the Nb and Fe distribution in at% and as a ratio to Zr, respectively. The Nb signal varies in a large extent due to the Nb phases in the material which are homogeneously distributed. Fe has a little fluctuation between 0.09 at% and 0.15 at%. The elemental maps shown in Figure 6-19 confirm these observations. The average composition of the bulk and interface metal including all points for Nb and Fe (i.e. Nb-phases are included) is presented in Table 6-3. In total 125 points are used for the bulk and 7 for the interface region. The same Fe content is measured in the two regions however as the Zr and O values are different close to the interface, the ratio to Zr should be applied for comparison and it is given in the Discussion of this chapter.

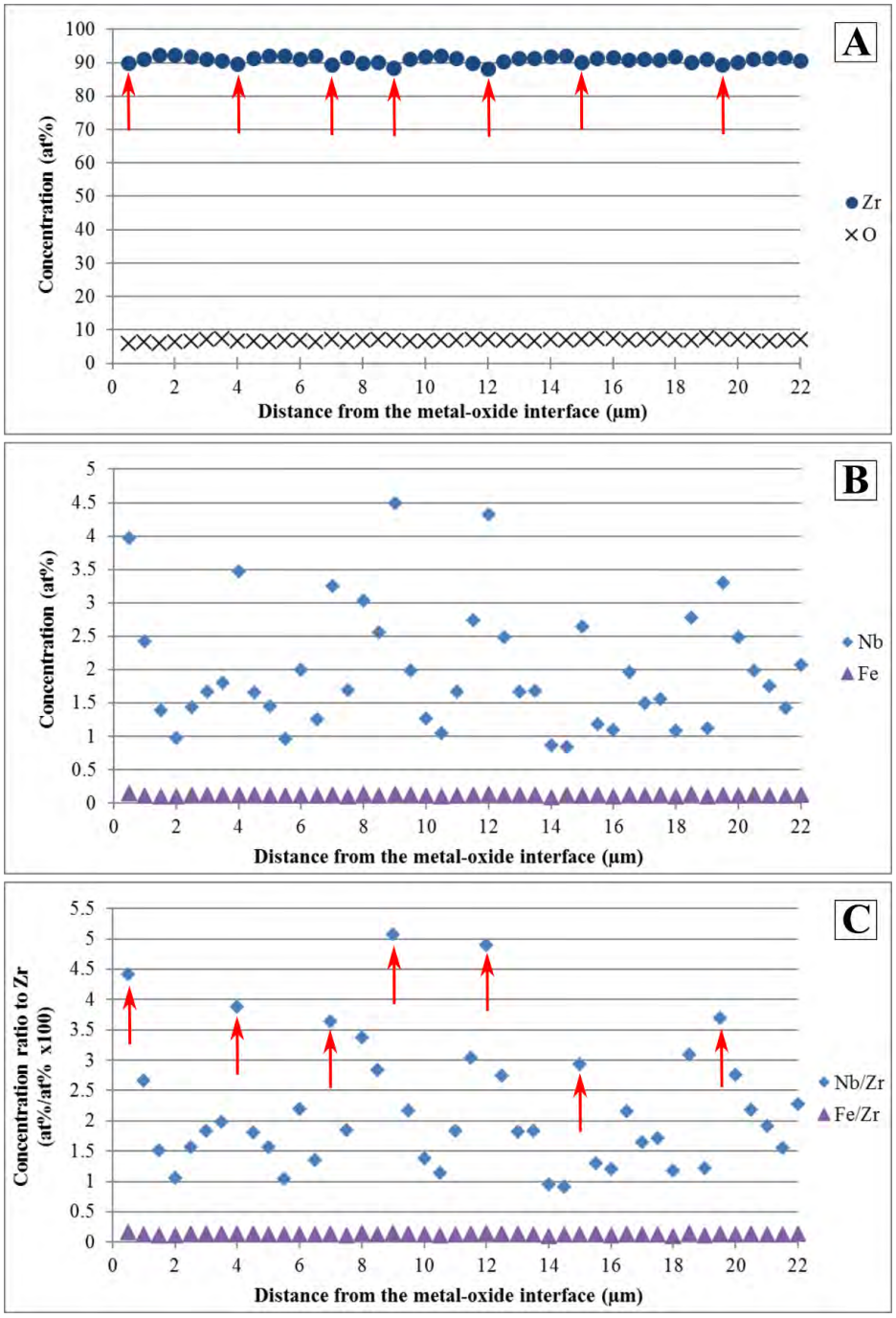

Figure 6-18 EPMA point line-scan on the metal of the 3 cycle Zr-2.5Nb. (A): Distribution of O and Zr; (B): distribution of Nb and Fe content in at%; (C): Nb and Fe concentration ratio to Zr is given. Arrows indicate the Nb-phases.

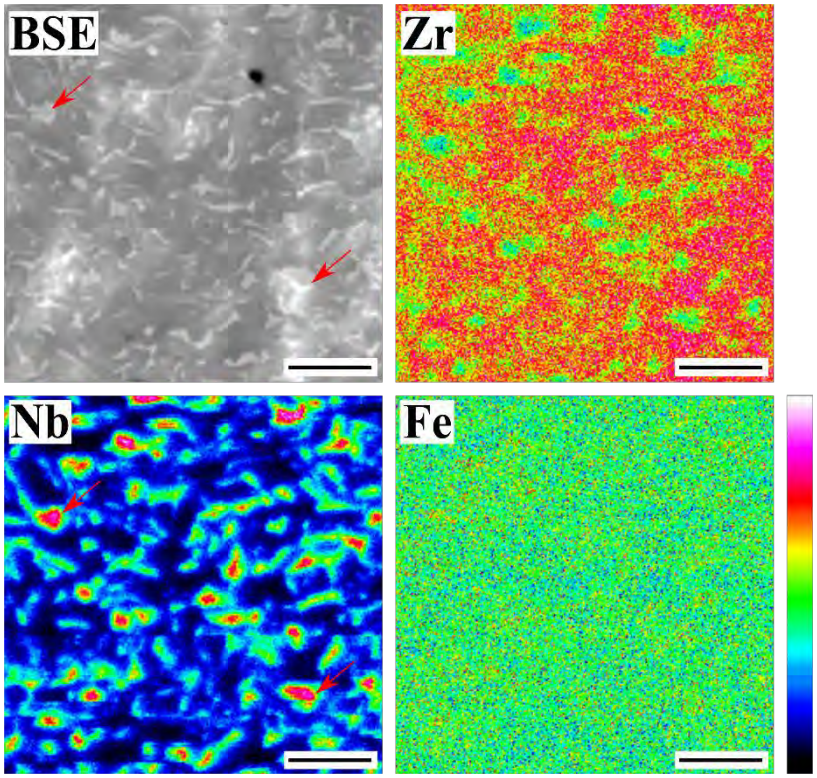

Figure 6-19 Elemental maps on the metal (around the centre of the cladding thickness) of the 3 cycle Zr-2.5Nb sample. Arrows indicate the Nb-phases. The scale bar is 5 µm.

Table 6-3 Average element concentrations in the bulk metal and close to the metal-oxide interface of the 3 cycle Zr-2.5Nb sample.

Phase	O (at%)	Zr (at%)	Nb (at%)	Fe (at%)
Bulk metal	7.00	90.52	2.34	0.13
Metal at the interface	11.53	86.45	1.88	0.13

6.2.2.2. Chemical analysis of the oxide and the metal-oxide interface by EPMA

The EPMA point line-scan on the full oxide as well as some part of the metal and the metal-oxide interface is presented in Figure 6-20. Nb shows some peaks in the oxide as well indicating that it does not dissolve fast in the oxide. In this sample as well the Fe content increases towards the outer oxide and the concentration is the highest in the outermost ~1.5 µm region. The elemental maps are presented in Figure 6-21 and shows that Fe is slightly accumulated also in

the surrounding areas of the large crack. The Fe map reveals that the oxide at the interface is depleted of Fe compared to the other regions of the oxide. In order to be able to observe this phenomenon only the Fe and Fe/Zr concentration is shown in Figure 6-22: two examples from different point line-scans are presented at the interface region. In other point line-scans as well either a slight minimum is observed at the interface (i.e. slight decrease on both sides of the interface) or a slight drop only in the oxide side of the interface. Due to the differences in the composition at the different regions of the oxide the average is given separately in Table 6-4. The “Inner oxide” is the oxide up to 1.5 μm from the metal-oxide interface and 5 points are used. The “Outermost oxide” is 1-2 μm of the outermost part depending on the local oxide thickness; calculated based on 6 data points. The “Intermediate oxide” describes the region in between the other two regions and it is calculated from 21 points.

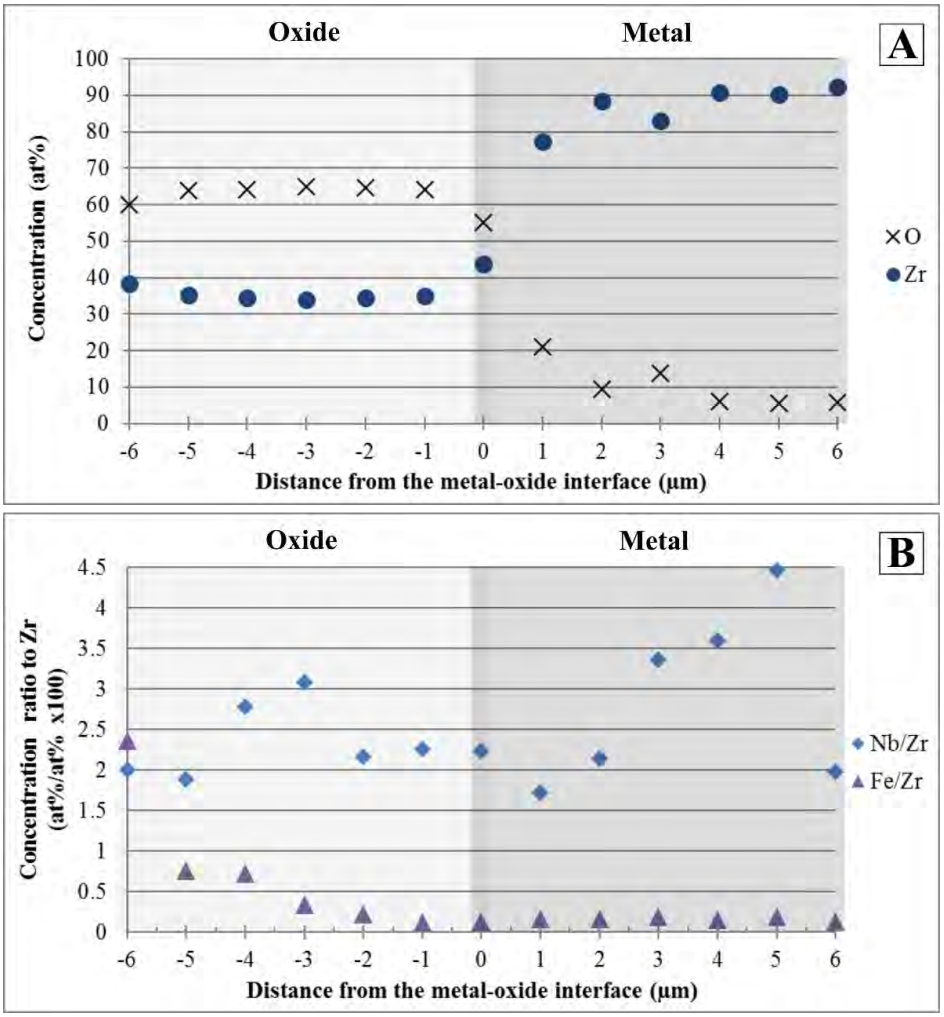

Figure 6-20 EPMA point line-scan on the oxide and the metal-oxide interface of the 3 cycle Zr-2.5Nb. (A): Distribution of O and Zr; (B): Nb and Fe concentration ratio to Zr is given.

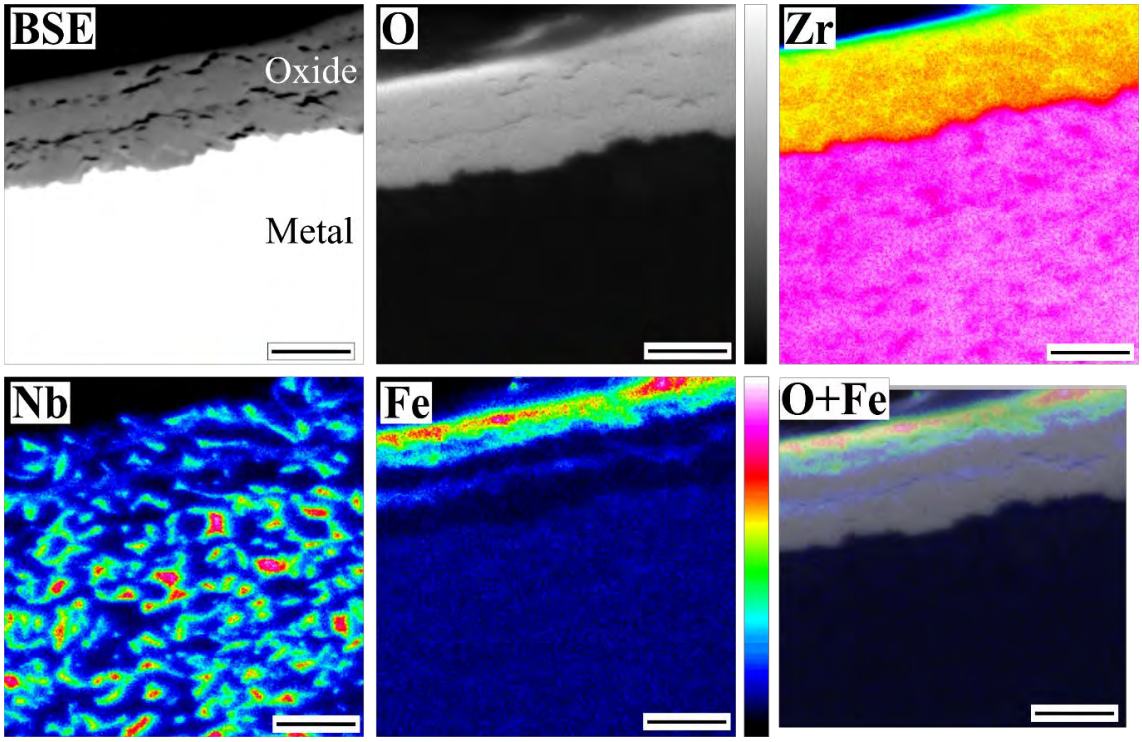

Figure 6-21 SE image and EPMA elemental maps of Nb and Fe on the metal and oxide (including the full oxide) of the 3 cycle Zr-2.5Nb sample. The scale bar is 5 µm.

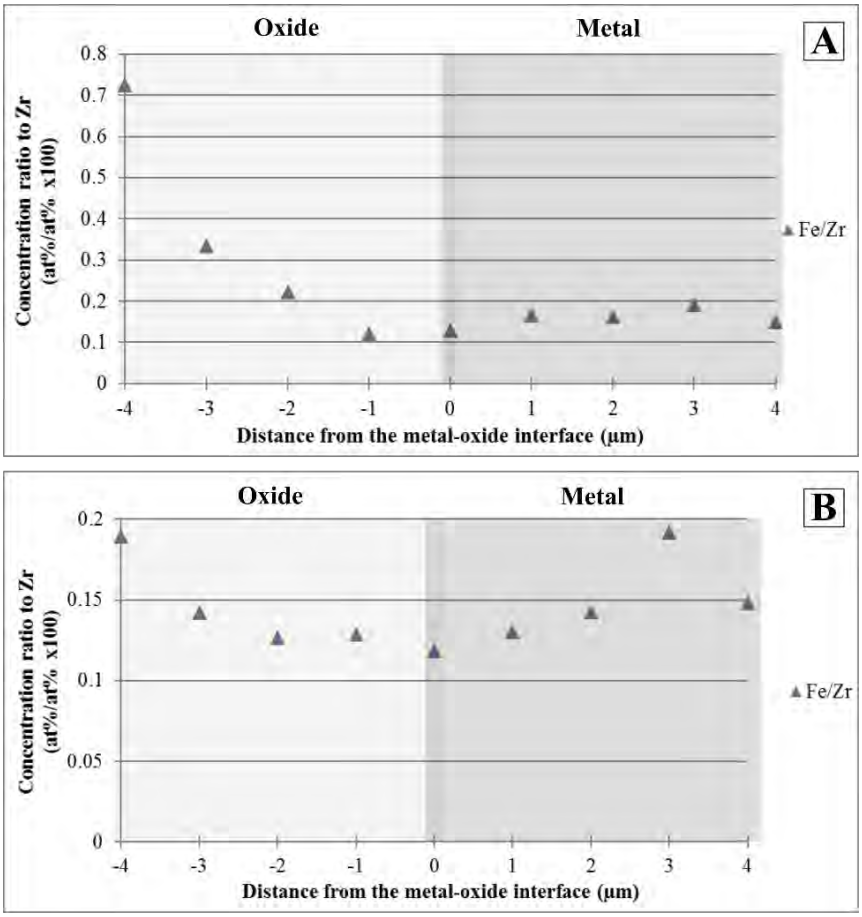

Figure 6-22 Two different EPMA point line-scans showing the Fe and Fe/Zr distribution through the metal-oxide interface of the 3 cycle Zr-2.5Nb.

Table 6-4 Average concentrations of the different regions of the oxide matrix of the 3 cycle Zr-2.5Nb sample. For definition of the different regions please refer to the text.

Phase	O (at%)	Zr (at%)	Nb (at%)	Fe (at%)
Inner oxide	64.51	34.62	0.82	0.04
Intermediate oxide	65.35	33.47	1.05	0.12
Outermost oxide	62.20	35.55	1.39	0.86

6.2.3. The effect of hydride phases on the chemical composition

In Chapter 5 it is demonstrated that at high burnup the hydride phases affect the distribution of Fe and Ni in the metal matrix.

In the case of the PWR materials direct point measurements as well as quantitative point line-scans have been carried out by EPMA on the hydrides and the metal matrix in order to compare their composition. TEM lamellae were not investigated in the case of these materials in the frame of this thesis. Although the EPMA maps suggest that there is a depletion of Fe at the site of the hydrides in both samples, the point measurements did not show a systematic difference. The reason could be the small size of the hydride phases in these samples. In the case of the 3 cycle Zr-2.5Nb sample there is no observable difference in the Nb content of the hydrides and the matrix.

6.2.4. Discussion on the chemical changes - Impact on the hydrogen uptake

The precision of the measurements and the detection limits for the PWR samples are presented in Table-AIII 2 in Appendix III. For detailed description of the limitations of the technique, please refer to the general Discussion of the thesis.

In order to better compare the EPMA results the average concentration ratios to Zr are presented in the different regions of the metal and oxide for both of the PWR materials in Figure 6-23. (Refer to Figure-AIII 1 and Figure-AIII 2 in Appendix III for the graphs of the oxide and metal parts separately.) The individual line scans which were presented before as well as these graphs demonstrate that the distribution of Fe shows a different behaviour at the metal-oxide interface of the two materials: in the Zircaloy-4 sample the concentration of Fe in the metal and in the oxide part is different and a step-like transition through the interface is observed. This means

that an Fe enriched layer can be found in the metal close to the interface while in the oxide side of the interface lower concentration of Fe is found. This suggests that once the Fe rich metal layer is incorporated in the oxide it is possible that the Fe diffuses to the outer surface. Therefore, the presence of an active process is expected which acts as the driving force for the diffusion of Fe to the outer surface. This assumption also corresponds with the accumulation of Fe on the outermost surface of the oxide. This aspect is further discussed in the general Discussion of the thesis. A detailed study on Zircaloy-2 and 4 samples with extremely different SPP size distributions have been presented by [198], [148]. It has been demonstrated that samples with large SPPs pick up significantly more hydrogen and it was explained by the role of the un-oxidized SPP helping the diffusion of hydrogen through the oxide and into the metal. It has been reported that the Zr_2Fe molecule and also the $Zr(Fe, Cr)_2$ type of particle can absorb hydrogen up to 3 atoms per molecule [199], [200], [201]. The measured concentration of Fe in the Fe-accumulated area of the metal part of the interface is similar or even higher than that of the measured concentrations of the Fe-containing SPPs or "hot-spots" in the metal. It should be mentioned that EPMA is not the most suitable technique in the accurate measurement of the concentration of the SPPs due to the large specimen-beam interaction volume, i.e. we can rather accept this data as an averaged value coming from the mixture of the SPP and the metal matrix. Therefore, we can expect that the Fe concentration in the Fe-rich region is not as high as in an SPP.

In contrast, in the case of the Zr-2.5Nb sample no Fe enrichment has been observed at the metal side. The Fe seems to be homogeneously distributed in the metal part and the transition from the metal to the oxide through the interface seems to be rather smooth without any sudden change in Fe content. However, once the point line-scan is magnified at the area of the metal-oxide interface, a trend of a slight decrease of Fe in the metal part towards the interface is observable in some of the point line-scans. A minimum is revealed in the concentration of Fe around the interface, i.e. it is followed by a steady increase in the oxide towards the outer surface. As the EPMA beam diameter is around 100 nm range, the spatial resolution of the point measurements and the maps are limited and measurements at the interface give a mixed signal coming partially from the metal and the oxide sides, also depending on the geometry of the interface under the measured area. However, a well-observable difference in behaviour of Fe is revealed at the metal-oxide interface for the two samples which suggests that these are indeed the trends of the element distribution after the given irradiation time. The behaviour of dissolved Fe at the metal-oxide interface leads to the conclusion that the quality of the interface differs to a high degree in the two samples. The responsible factor could be the difference in the electric conductivity of the oxide or the different stress distribution at the interface. It is has been shown that the HPU and the oxidation is lower if the oxide has a higher conductivity [60]. However, these statements need further studies in the future to be confirmed.

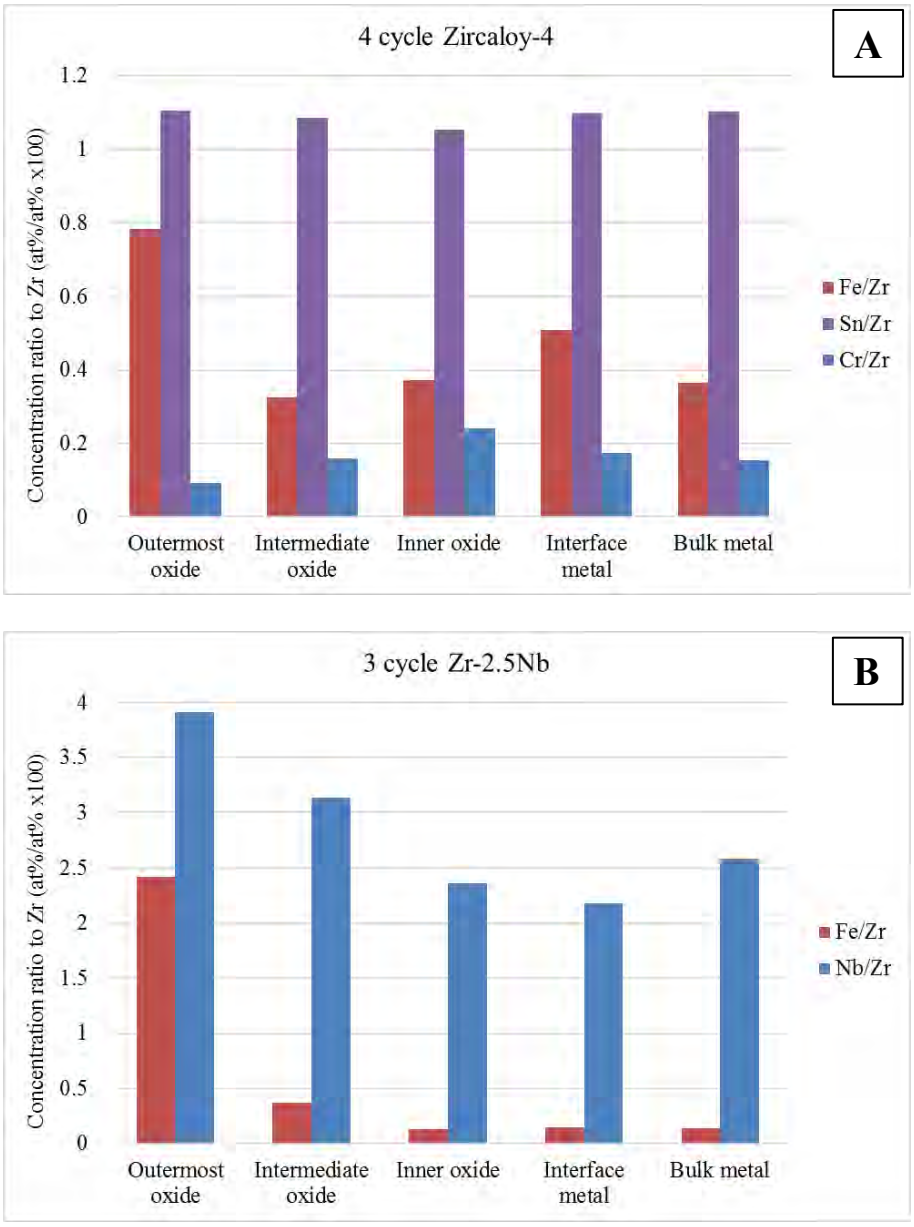

Figure 6-23 The average concentration ratios to Zr in the different regions of the oxide and the metal for the 4 cycle Zircaloy-4 (A) and the 3 cycle Zr-2.5Nb (B).

As it was already discussed, the undulation of the metal-oxide interface is different for the two investigated materials [169]. It has been shown by several studies that the undulation of the interface has an effect on the stress distribution in the oxide [139] [69], [138]. Changes in the compressive and tensile stresses have been revealed in an undulated interface by modelling [138]. It is also claimed that the differences in the stresses have an influence on the diffusion

coefficient of oxygen [69]. In our best knowledge there is no study on the topic of how the changes in the stress distribution at the interface would influence the diffusion of other elements. Further study is necessary to conclude on this question. However, it is logical to assume that the diffusion coefficient of other elements would be also altered by the stress build-up in an undulated interface. Therefore it is likely that the observed differences of Fe at the metal-oxide interfaces of the irradiated low-tin Zircaloy-4 and Zr-2.5Nb is due to the fact that their interface roughness is very different. The possible cause of the different interface-roughness of the two samples is further discussed in section 6.1.3.

In the case of the outer oxide region Fe shows similar behaviour in both samples: its concentration increases towards the outer oxide. It is worth reminding that no additional Fe has been injected in the coolant. No crud was observed on the surface of the Zr-2.5Nb segment. It is possible that the amount of crud was so small and the crud was so loose, that during the transport and hot cell handing it was already removed. Although we cannot exclude this factor, it is not expected that the Fe in the outer surface is coming from the reactor environment. As it was mentioned, it is known that Fe and Cr are tend to diffuse to the outer surface of the oxide once the SPPs are incorporated in the oxide even without irradiation [105]. The same behaviour of Fe and Cr was presented in a study on binary Zr alloys by [104]. The fact that Fe accumulation was not observed in those binary alloys which did not contain Fe, suggest that the Fe-rich layer is not a contamination from the environment [104].This aspect is discussed in the Discussion chapter. High amount of Cr was not detectable at the outer part of the oxide in the low-tin Zircaloy-4 after 4 years of irradiation. This implies that the Cr is not dissolved from the precipitates in the metal in a large extent and that the particles in the oxide are still rich in Cr. This shows that the dissolution of Cr is a much slower process even in the oxide phase. In Chapter 5 Cr enriched outer surface was revealed on the LK3/L type Zircaloy-2 claddings only

at high burnups (6 and 9 cycle claddings) while Fe enriched outer oxides have been systematically observed after all measured service times (3, 6, and 9 cycles) in BWR. Therefore, its effect on the cladding's behaviour is described in the Discussion.

Other studies in the literature discussing the effect of dissolved Fe and Nb in the oxide scale has drawn the conclusion that these elements will supress the hydrogen diffusion if they are present with a lower valence state than Zr^{4+} [152]. In the case of Nb it is claimed that it has a higher oxidation state (5+) when it is dissolved in the surface region of the oxide. The advantageous effect of Nb^{5+} is explained by an increase in the electron concentration in this region due to the dissolved Nb causing an enhanced reduction of protons at the water-oxide interface [152].

6.2.5. Conclusions on the chemical changes

In the best of our knowledge it is the first time that Fe enriched region has been shown at the metal part of the metal-oxide interface on the irradiated low-tin Zircaloy-4 material. Therefore very little is available on this topic in the current literature. It is in general accepted that Fe-containing SPPs at the metal-oxide interface could help the H to access the metal. It could be that the Fe enriched metal plays the same role and helps the hydrogen uptake. However, more research and modelling are needed to understand and explain the influence of this region in the HPU and the oxidation.

Fe accumulation in the outer surface of the oxide has been observed in all type of claddings in both BWR (Chapter 5) and in PWR (Chapter 6). Given these points, this is a general

phenomenon in Zr-based claddings containing Fe as alloying element and it is independent of reactor type.

In conclusion, the effect of Fe on the HPU and oxidation depends on many parameters and it is a rather complex issue. Based on the results presented here and other studies in the literature a suggestion can be given here, namely that the dissolved Fe may have two effects on the properties of the materials:

i. Fe accumulated at the metal side of the interface could increase the HPU.

ii. Dissolved Fe accumulated at the outer surface of the cladding could have a positive effect on the HPU by lowering the amount of hydrogen entering the oxide.

Further study is needed to confirm these assumptions.

7. COMPARISON OF THE DIFFERENT REACTORS AND DIFFERENT MATERIALS

In the previous chapters the results were discussed separately for the samples from the different reactors. The environments of BWR and PWR are very different. Not only the pressure and the temperature are not the same but the water chemistry is also a factor (discussed in the introduction). Therefore it would be expected that several aspects of the behaviour of the claddings will not be comparable. As an example, it has been observed that in the PWR, the oxide thickness increases from the bottom of the rod to the top, as shown in Figure 8 of [13], this not being the case for BWR behaviour (Figure 3 of the same reference). As mentioned already, the aim of the thesis is to find additional factors which are responsible for the increased H-uptake at high burnups (when it occurs). Although it has been possible to study the claddings with different residence time in BWR, and draw a first conclusion about the hydrogen uptake phenomenon, the study of claddings from PWR and comparison between the two families of reactor claddings will bring a much more comprehensive understanding of the phenomenon.

This means that it is important to be able to identify that among these factors, which ones are the reactor specific characteristics and which are the general, i.e. reactor-independent phenomena. In this manner some aspects from BWR results can be compared with the PWR samples, e.g. the behaviour of Fe and the crack microstructure of the oxide as well as the role of the hydride phases on the chemical composition and the oxide microstructure. This chapter is dealing with these factors in order to separate the general behaviour from the reactor specific ones for different Zr-based materials. First the behaviour of Fe and Cr in the two Zircaloy type claddings will be discussed from two different reactors. Then, the crack and hydride volume fractions of all claddings are discussed. As the last point the comparison of the two PWR type materials will be given. It is worth noting that due to the fact that the LK3/L and the Zr-2.5Nb

samples originate from different types of reactors and their composition is significantly different, their compositional changes cannot be compared.

The aim here is to find those phenomena which are present in any alloy in any reactor that can bring a hint to the mechanism of H uptake and its modification with residence time.

7.1. Compositional changes in the claddings in BWR and PWR

The fact that the samples have served in different types of reactors enormously increases the number of possible factors influencing the behaviour. An important conclusion from the previous chapters is that many phenomena occur simultaneously during the service and among these the rate limiting factor could change at the different stages of the service and in different reactors. This work focuses only on irradiated materials and studies samples coming from fission reactors. The number of samples to be studies is indeed quite limited due to this fact, and already quite demanding to examine. In other words, it is not possible to study a reduced number of parameters at a time. However, studying the same cladding from the same reactor and the same elevation and position in the fuel assembly after different cycles is the most optimum possibility to better understand the evolution of the material both from the compositional and the microstructural point of view. This has been indeed provided from the BWR materials in this study. Together with the information regarding the oxide growth and the amount of extra hydrogen in the sample after each stage it is possible to better understand the dynamics of the material change and correlate the overall evolution of the material to the HPU and oxidation properties. In the case of the PWR materials, in this study, one dataset is available after a certain burnup. The oxide thickness and H-content after different cycles are not reported in the case of the PWR claddings presented in this thesis. Therefore, the knowledge regarding

their evolution in time is not as detailed as for the LK3/L cladding. The examination of the PWR materials was performed as a comparative observation, with the aim of searching for similar characteristic microstructural features. Thus one data set was considered due to the available time for this study. These materials provide a good basis for comparison to the LK3/L samples which helps to better understand which phenomena occur in both types of reactors.

It could be criticized that although the observations lead to similar apparent behaviours, their role on the HPU and oxidation would be different in the two reactors. As the number of samples studied in the case of PWR material is not high, this aspect remains to be further explored. However, trends observed show the opposite and give rise to the deduction that it is possible to draw conclusions which are valid for all materials and are independent of reactor type.

7.1.1. Comparison of LK3/L Zircaloy-2 and low-tin Zircaloy-4 – Role of the alloy composition in different reactor conditions

In order to compare the behaviour of materials in the two reactors, we should select those samples which have similar burnups. The burnup of the 4 cycle low-tin Zircaloy-4 is 51.1 MWD/kgU which is closest to the burnup of the 3 cycle LK3/L sample, i.e. 44.6 MWd/kgU. It must be reminded that the two claddings are oxidized at different temperatures, the BWR cladding having a surface temperature in the range of 290°C, whereas the surface temperature in the case of PWR cladding would be between 20 to 40°C higher.

As a remainder, the compositions of the two alloys are presented in Table 7-1. Zircaloy-4 does not contain any Ni and it has higher Fe and slightly lower Cr and Sn concentrations, in comparison with Zircaloy-2. This also means that instead of the two types of precipitates, in

this material only one type is present. It is also interesting to note that the total alloying element content of the LK3/L is surprisingly close to that of the low-Sn Zircaloy-4 selected in this study. In other words the sum of Fe+Cr (+Ni), in the two claddings is 0.557 for LK3/L and 0.542 at% for Zircaloy-4. Furthermore, the Cr contents are very similar. It is clear that although they have spent similar times in the reactor the oxidation of the PWR material is much faster and the H content is also higher; this being partly due to the higher reactor temperature in the KKG PWR. The HPUF is similar (~19-20%) for both samples. So we could claim that despite the fact that the two claddings come from different reactors and are not exactly similar alloys, they are surprisingly comparable.

Table 7-1 The composition of the LK3/L and Zircaloy-4 claddings with Zr in balance.

Alloy		Sn	Fe	Cr	Ni	Fe+Cr (+Ni)
LK3/L Zircaloy-2	wt%	1.34	0.18	0.11	0.05	0.34
	at%	1.02	0.29	0.19	0.077	0.557
Low-tin Zircaloy-4	wt%	1.20	0.22	0.107	-	0.327
	at%	0.914	0.356	0.186	-	0.542

7.1.1.1. Comparison of metal part of the two types of claddings

The EPMA point measurements of the two irradiated samples have shown that the content of Cr and Sn are indeed similar (between the two claddings) but slightly less in the Zircaloy-4 metal matrix: 0.12 at% of Cr in 3 cycle Zircaloy-2 and 0.14 at% in 4 cycle Zircaloy-4; 1.14 at% of Sn in Zircaloy-2 and 1.01 at% Sn in 4 cycle Zircaloy-4,Fe is slightly higher in the Zircaloy-4 (0.33 at%) compared to the 0.22 at% Fe content of Zircaloy-2. The maximum measured element content of an SPP is observed to be much higher in the PWR cladding: 5.2 at% Cr with 2.03 at% Fe compared to the 1.68 at% Cr and 0.36 at% Fe in LK3/L, i.e. it is around 3 times

more Cr and more than 5.6 times higher Fe. Significant difference is observed regarding two aspects of the metal. In the Zircaloy-4 large hydride phases are already formed at the metal-oxide interface at this stage of the service. Although an Fe-enriched band is observed at the interface region of the metal in both materials it is thicker in the case of the Zircaloy-4 and it contains higher amount of Fe, namely 0.47 at% which is 1.7 times higher than in the LK3/L sample with 0.27 at% (comparing the average Fe concentration ratios to Zr at the interface region of the metal). The evolution of this Fe rich interface region has been presented for Zircaloy-2 and it is revealed that after an increase in concentration in the 6 cycle sample, the Fe accumulation disappears from this region at higher burnup (i.e. in the 9 cycle cladding). Therefore, it is possible to conclude that Fe accumulation at the metal side of the interface seems to be a general phenomenon in the Zircaloy type materials at medium burnups and it is no more present at high burnups. Although the Fe enrichment near the metal-oxide interface could be linked to the oxide transitions and to the stress, this correlation has not been studied in this thesis, and therefore it will not be discussed.

7.1.1.2. Comparison of the oxide part of the two types of claddings

The oxide layer of the Zircaloy-4 is different from the 3 cycle LK3/L:

(1) The SPPs are mostly dissolved in the latter while there are still some Cr hot-spots in the oxide of the PWR cladding. To better compare the Cr SPPs in the oxides of the two samples, EPMA maps of Cr are presented in Figure 7-1 with the similar magnification.

(2) Comparing the oxide matrix of the two samples: around 2 times higher Cr content is measured in the Intermediate oxide matrix of the 4 cycle Zircaloy-4 sample (ratios to Zr are taken into account): as it is 0.028 at% in the case of 3 cycle Zircaloy-2, and 0.05 at% in the Zircaloy-4. The Cr content is also higher for the Zircaloy-4 (0.03 at%) in the Outermost oxide

than for Zircaloy-2 (0.024 at%). In the Inner oxide the difference is even higher (double): 0.08 at% for Zircaloy-4 and 0.04 at% in Zircaloy-2. A very possible explanation is the fact that the number of SPPs in the Zircaloy-4 is much higher and therefore, during the EPMA point analysis, the electron beam interaction volume will absolutely encompass partly these SPPs, although it is aimed to measure the matrix.

(3) The Fe content is also higher throughout the oxide scale of the Zircaloy-4. The average content taking the ratios to Zr is 2.4 times higher in its Inner oxide showing 0.12 at% compared to the 0.056 at% Fe in the case of Zircaloy-2. For the Intermediate oxide: 0.10 at% and 0.077 at% was measured as average Fe content in Zircaloy-4 and Zircaloy-2, respectively. Around 2.8 times higher Fe content is measured in the Outermost oxide of Zircaloy-4 (0.27 at%) than that of Zircaloy-2 (0.094 at%). Both samples show Fe enriched outer oxide. This observation confirms that this behaviour of Fe is not reactor or material specific.

For the better comparison the average element distribution in the metal and oxide is presented for both materials in Figure 7-2.

(4) As expected, Sn content is lower in all regions of the oxide of the low-tin sample: 0.34 at% and 0.43 at% in the Inner oxides of Zircaloy-4 and Zircaloy-2, respectively. In the Intermediate oxide: 0.35 at% (Zircaloy-4) and 0.4 at% (Zircaloy-2). While there is a slight difference in the Outermost oxide with Zircaloy-4 having 0.39 at% Sn compared to the measured 0.4 at% in the case of Zircaloy-2.

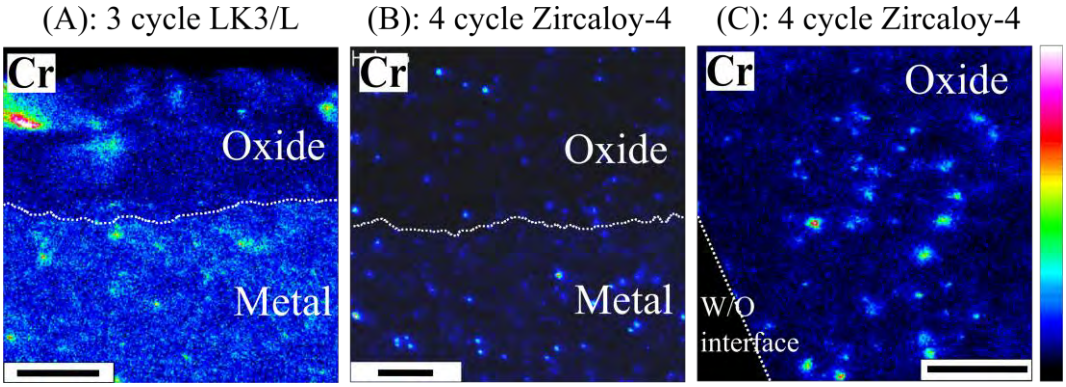

Figure 7-1 EPMA maps of Cr with similar magnifications, the scale bars show 5 µm. (A): 3 cycle LK3/L Zircaloy-3 where the full oxide is shown. The white dashed line indicates the metal-oxide interface. (B): 4 cycle low-tin Zircaloy-4 metal-oxide interface. Dashed line indicates the interface. (C): the outer region of the oxide of Zircaloy-4 is shown. The white line indicates the water-oxide interface. The comparison shows the presence of bigger number of Zr (Fe, Cr)$_2$ SPPs in Zircaloy-4 cladding.

Regarding the Ni concentration and behaviour, in the BWR material, it has been claimed that Ni shows a deleterious effect on the HPU of the cladding. However the comparison of the early stages of reactor life of LK3/L in BWR and Zircaloy-4 in PWR gives the following conclusion: in 3 cycle LK3/L where some of the Ni-containing SPPs are still present in the material and also some dissolution of Ni has occurred already, this material shows lower oxidation rate compared to the Zircaloy-4; with lower H content. Therefore it can be concluded that Ni does not have a significantly deleterious effect on the behaviour in the early stages of service life. It is clear that the PWR cladding is exposed to a higher oxidation temperature; however, the two alloys can be compared.

Although there is only one irradiation condition for the PWR material, some conclusions can be extrapolated due to the material available in the literature. It has been observed in other studies that Zircaloy-4 shows accelerated corrosion at higher burnups and the evolution of its oxide layer and H-pickup is also described [172]. Some explanations are suggested for the

increased corrosion of the material, such as hydride precipitation in metal [175], [176], [177], [15]; concentration of Sn [202], [155]; SPP dissolution [203], [204]; effect of Li [205], [206]. The LK3/L Zircaloy-2 material shows an increased corrosion between the 7th and the 9th cycles.

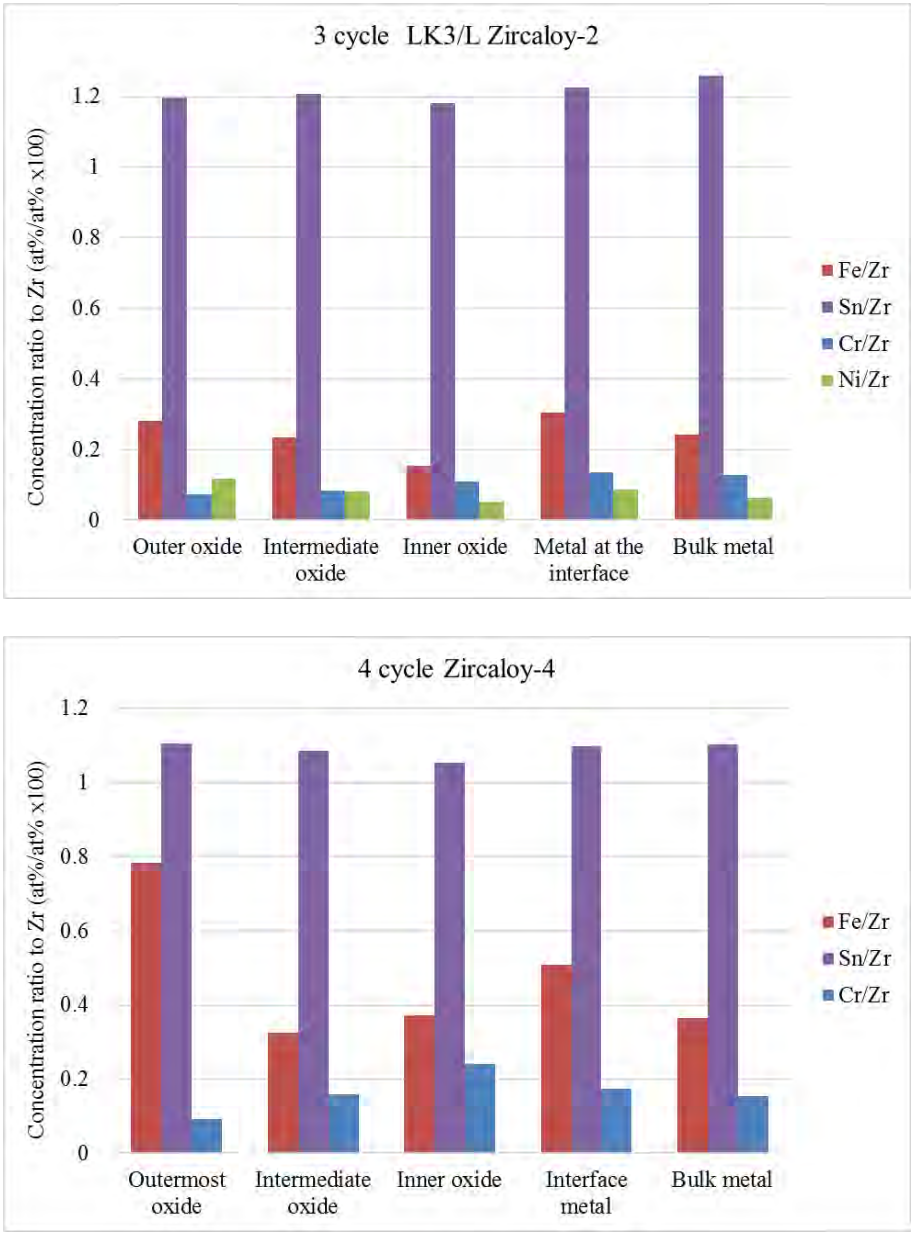

Figure 7-2 Average element concentrations in the different parts of the metal and oxide for both the 3 cycle LK3/L Zircaloy-2 and the 4 cycle low-tin Zircaloy-4.

7.2. Microstructural changes of the claddings in BWR and PWR

As observed in different chapters, the microstructure of the oxide, the crack morphology and volume fraction have been taken into consideration to compare the different materials. In this section this aspect will be considered for different alloys. Many different parameters are potential sources for crack formation in general (e.g. transition in the oxidation kinetics [65], [207]; stress induced cracking [21], [188]; cracking due to hydride oxidation [208], [209]; SPP oxidation induced micro-cracks [188], [104]). Although there are several other responsible factors which could be alloy specific (i.e. micro-crack formation during oxidation of SPPs in Zircaloys or the role of Nb phases on improved crack formation) the crack formation is inevitable and it is due to the internal stresses under the above mentioned conditions. Although the causes of cracking can be different in the three types of claddings, the crack volume fraction can be investigated independently of its origins.

Therefore in the following the crack volume fractions in all studied samples are directly compared and correlated to the cladding behaviour. In order to use a parameter which can be present in all different cladding hydride phases are also measured. It has been revealed that if these hydrides are sufficiently large they could induce cracks in the oxide while they oxidize. The following chapter discusses this issue in more details in order to answer whether this is a general phenomenon.

7.2.1. Comparison of the hydride and crack volume fractions

As it has been observed in previous chapters, a correlation can be found between the volume of hydrides at the metal-oxide interface and the crack volume immediately at the interface oxide. In this part, all claddings studied are considered independent of their origin (BWR or PWR) or

their number of cycles, to search for a direct correlation between hydride volume fraction and oxide micro-crack structure. It is worth noting that in the following the terms “inner oxide” and “interface oxide” should be distinguished from each other.

A comparison of the crack volume fractions at the inner regions (by inner regions we mean the inner oxide and the interface oxide) of the oxides in both PWR and BWR materials is presented with the aim to reveal the influence of this factor on the behaviour of the cladding. In order to better understand the correlation between the amount of hydride phases in the metal and the cracks formed in the oxide these values are compared at the metal-oxide interface where the oxidation of metal matrix and hydrides occurs. A prediction for the further crack production as a function of the amount of hydride phases at the metal-oxide interface is suggested.

7.2.1.1. Comparison of the oxide crack volume fractions of the BWR and PWR claddings

The volume fraction of cracks in the different regions of the oxide can be compared in all the alloys presented. For this reason the analysed thickness of the oxide regions and their distance from the metal-oxide interface should be the same for all samples. As it has been discussed in the previous chapters all claddings show a dense, practically crack free outer oxide (outermost 3 µm in the LK3/L materials, while it is 2.5-3 µm for low-tin Zircaloy-4 and 1-1.5 µm in Zr-2.5Nb). This region, which is correlated in previous chapters to the oxide formed on a hydride free metal, does not contain cracks and it is similar in most alloys. It is therefore not compared in more details, in this part, as it does not provide any correlation to the changes in the oxide structure, although it is a very important conclusion about the oxide microstructures. In the following the inner oxides are discussed.

The values extracted from the 3D FIB results of inner oxides of all alloys are shown in Figure 7-3. In this study, the Interface oxide is defined as the distance up to 1 µm from the interface.

The Inner oxide will be a 2 μm thick region from 1 to 3 μm distance from the interface. The 6 cycle LK3/L makes an exception: its inner region will represent only 1 μm thick oxide starting as others from 1 μm distance from the interface. This is due to the thin (only 2 μm) oxide layer formed during the 6^{th} cycle.

It is interesting to note that the Nb-containing sample has the highest crack V% in the inner region (3.77%), even higher than in the same region of the 9 cycle Zircaloy-2 (2.83%). In this region the 6-cycle LK3/L as well as the 4 cycle Zircaloy-4 samples show similar values: 2.73 % and 2.86%, respectively. The lowest values in both the inner oxide and interface oxide are shown by the 3 cycle LK3/L sample (0.25% and 0.068% respectively) which also shows the best oxidation and HPU behaviour. However, based on the comparison of the volume fractions at the interface oxide it is clear that there is a correlation between the performance of the cladding (its hydrogen uptake) and the amount of cracks at this region. In other words the claddings which perform the best have the lowest crack volume fraction at the interface oxide and vice versa. In other words, the claddings with the lowest crack volume fractions at the interface oxide region (3 cycle Zr-2.5Nb with 0.25% and 3 cycle LK3/L with 0.068% of cracks) show very satisfactory performance. The 9 cycle LK3/L which shows increased oxidation and HPU has much higher V% of cracks (namely 8.32%) compared to the other samples, such as 6 cycle LK3/L with 2.3%, and 4 cycle Zircaloy-4 with 4.25% crack volume fractions at the Interface oxide. This observation confirms that the interface region has a high influence on the behaviour and the protectiveness of the oxide from the microstructural point of view and its microstructure is representative of its protectiveness. It seems that the inner oxide region shown in the Figure 7-3 does not show such a representative correlation. Therefore, in the following the metal microstructure is discussed and the focus stays on the Interface oxide region only.

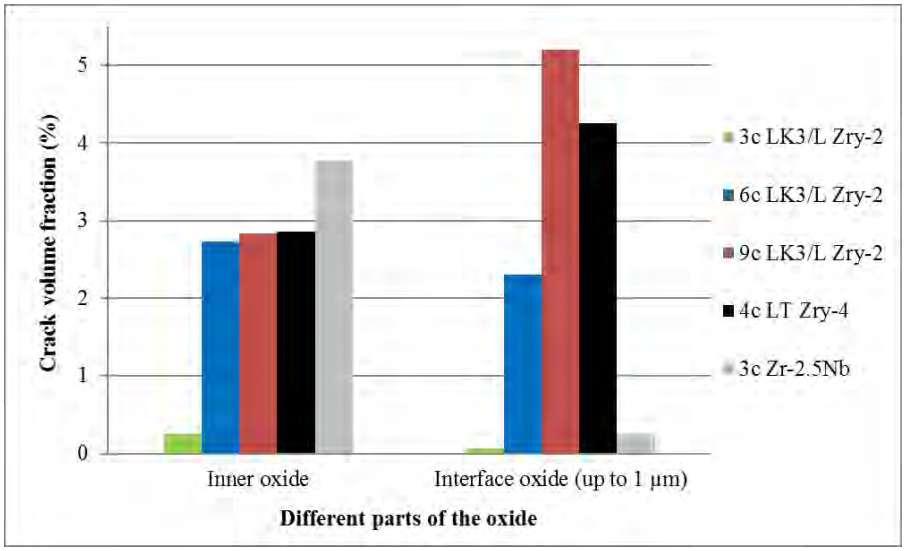

Figure 7-3 Comparison of the crack volume fraction of all measured cladding grades and cycles in the inner and the interface oxide. Interface oxide: up to 1 µm from the metal-oxide interface; Inner oxide: the region between 1-3 µm from the metal-oxide interface. Note: for the Inner oxide on 6 cycle LK3/L: 1-2 µm from the metal-oxide interface. It must be noted that the interface oxide seems to play a very important role on the behaviour of the cladding.

7.2.1.2. Comparison of the metal-oxide interface regions of the BWR and PWR claddings

The interface region of the metal and the oxide is compared in all samples: the amount of cracks as a function of the amount of the hydride phases are presented in Figure 7-4. A certain correlation can be seen based on this figure. The lower the amount of hydride phases the lower the crack volume fraction. It is interesting to note that the phenomena seem to be independent from the burnup, or cycle or even the type of alloy and reactor environment.

The best fit on the points of Figure 7-4 is an exponential function. This suggests that once the hydride phases reach a certain amount (in V% at the interface) the amount of cracks induced due to their subsequent oxidation in the oxide could be deleterious for the cladding. An exponential function has been fitted on the dataset in order to give a rough estimation for the further crack production. It has to be emphasized that 5 data points are statistically not very

high and more data is needed to give an accurate prediction. However the handling of the irradiated rods and the preparation of the segments as well as the production of the 3D datasets are very time-consuming processes, knowing that for certain sets of data, the measurements were repeated more than once or even twice, to obtain certainty about the results.

Due to the limited time of the PhD project the production of a larger amount of dataset was not feasible. The fit function ($V_{crack} = 0.1304\, e^{0.1362 V_{hydride}}$ where V_{crack} and $V_{hydride}$ are the volume fraction of cracks and hydrides at the metal-oxide interface) is plotted in Figure 7-5. Theoretically; if no significant change occurs in the influencing parameters of the crack formation; based on this plot the amount of cracks which is present in the last sample in the row, i.e. the 9 cycle LK3/L material would double in the Interface oxide with the increase of only 6% in the hydride volume fraction. The 4 cycle Zircaloy-4 sample has practically the same hydride volume fraction (26.35%) at the interface as the 9 cycle LK3/L cladding (26.30%) while their H content differ by more than a factor of two: 209 ppm in the 4 cycle Zircaloy-4 and 595 ppm in the 9 cycle LK3/L cladding. As it is shown in Figure 7-6 A and B the relationship between the total H content of the segments and their hydride volume fractions or their crack volume fraction at the metal-oxide interface does not show such a strong correlation for each of the materials presented: although 4 cycle low-tin Zircaloy-4 contains almost 3 times less H than the 9 cycle LK3/L, they show similar hydride volume fraction at the interface). Furthermore, part B of the Figure shows that even though the H contents of the 6 cycle LK3/L (202 ppm) and the 4 cycle low-tin Zircaloy-4 (209 ppm) are similar, their crack volume fractions at the interface show a significant difference (2.30% in 6 cycle LK3/L and 4.25% in Zircaloy-4). This latter also confirms that the total H content is not the determinant factor in the crack volume fraction.

One of the explanations for the similar hydride V% of the 9 cycle LK3/L and the 4 cycle Zircaloy-4 close to the metal-oxide interface, that is presented in Figure 7-4, could be that only in the case of LK3/L cladding an inner liner is present and it has been shown that a large amount of hydrogen is absorbed by the liner (Figure 4-27 of Chapter 4). Depending on whether the liner acts as a sink for hydrogen during service this could result in two scenarios:

1. If the hydrides accumulate in the liner in reactor and service temperature as well: The cladding has a lower effective hydrogen concentration than if it would be without the liner. This could lead to a reduced hydride volume fraction at the metal-oxide interface as for the 9 cycle cladding.
2. If the hydrides do not accumulate in the liner during service: This means that during the service the volume fraction of the hydrides was higher at the interface region due to the temperature gradient. In this case the data point corresponding to the 9 cycle LK3/L sample would shift to the right in the X axis and would implement a less drastic crack production having a less steep function fit.

The terminal solid solubility (TSS) limit of hydrogen in Zr is presented in Figure 7-7 from references [210] and [211]. The TSS is not the same for precipitation and dissolution of hydrides, therefore TSSP (for precipitation) and TSSD (for dissolution) are given. The solid solubility limit of H is 47 ppm at 300 °C for pure Zr and slightly higher for Zircaloy-2: 60 ppm at service temperature [111]. The excess hydrogen precipitates in the form of zirconium-hydrides with different composition and crystal structure [24]. Although a temperature gradient is present from the hotter liner to the cooler outer part of the cladding with around a 20 °C difference, the inner liner can still act as a sink of hydrogen during the service due to the compositional differences. The liner does not contain alloying elements therefore it has a higher

affinity for hydrogen. It is worth reminding that the inner liner is included in LK3/L, in order to enhance the Pellet-Cladding Interaction (PCI) resistance [181].

It is important to emphasize again that the crack volume fraction of the interface oxide is only one parameter among the several factors governing the properties. To correlate this volume fraction to the hydride volume fraction at the metal side of the interface seems to provide a means to determine the cladding uptake behaviour independent of reactor and type of cladding. This if it is further examined and re-confirmed would be a useful means to evaluate the extent of degradation of material. In contrast to the hydrogen content of the cladding, this parameter is much more realistic in conjunction with the structure of the interface, knowing that the oxidation and uptake phenomena take place at this very site. In other words, as mentioned above, although a cladding could have high hydrogen content, due to the lower hydride concentration at the interface, it could show lower crack volume fraction in the oxide, and thus could show a better overall resistance to degradation.

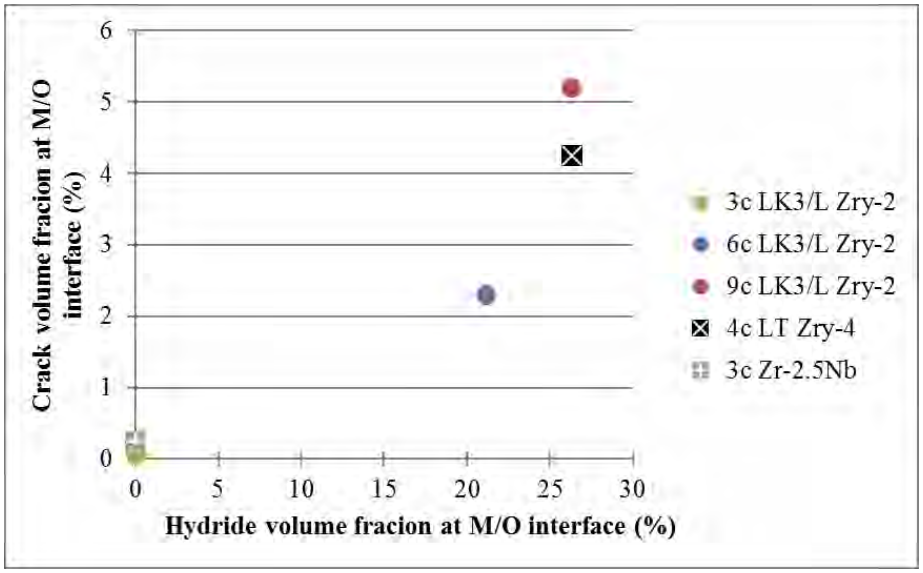

Figure 7-4 The crack volume fraction in the oxide as a function of the volume fraction of hydrides in the metal. Both parameters are taken into account close to, i.e. up to 1 µm from the metal-oxide interface.

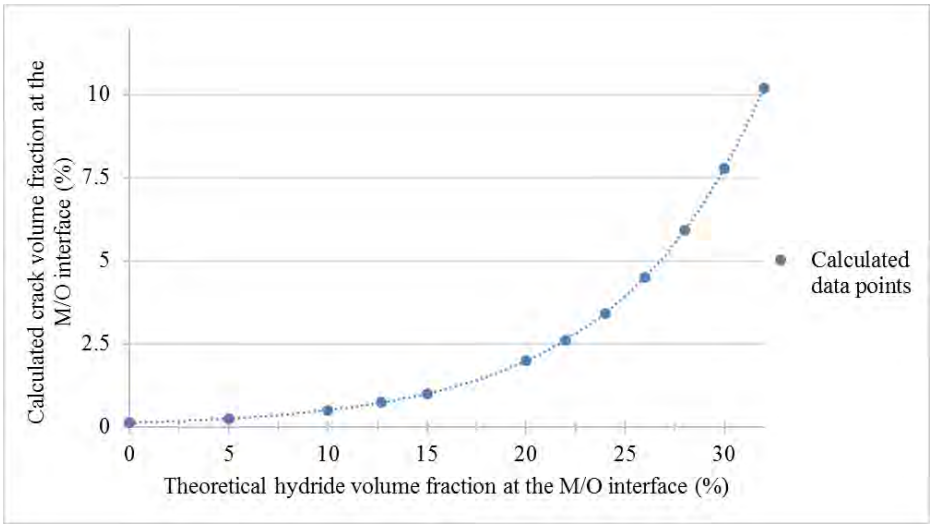

Figure 7-5 The calculated values for the crack volume fraction of oxides as a function of the hydride volume fraction of the oxidizing metal based on the values presented in Figure 7-4. Both values apply to the metal-oxide interface region.

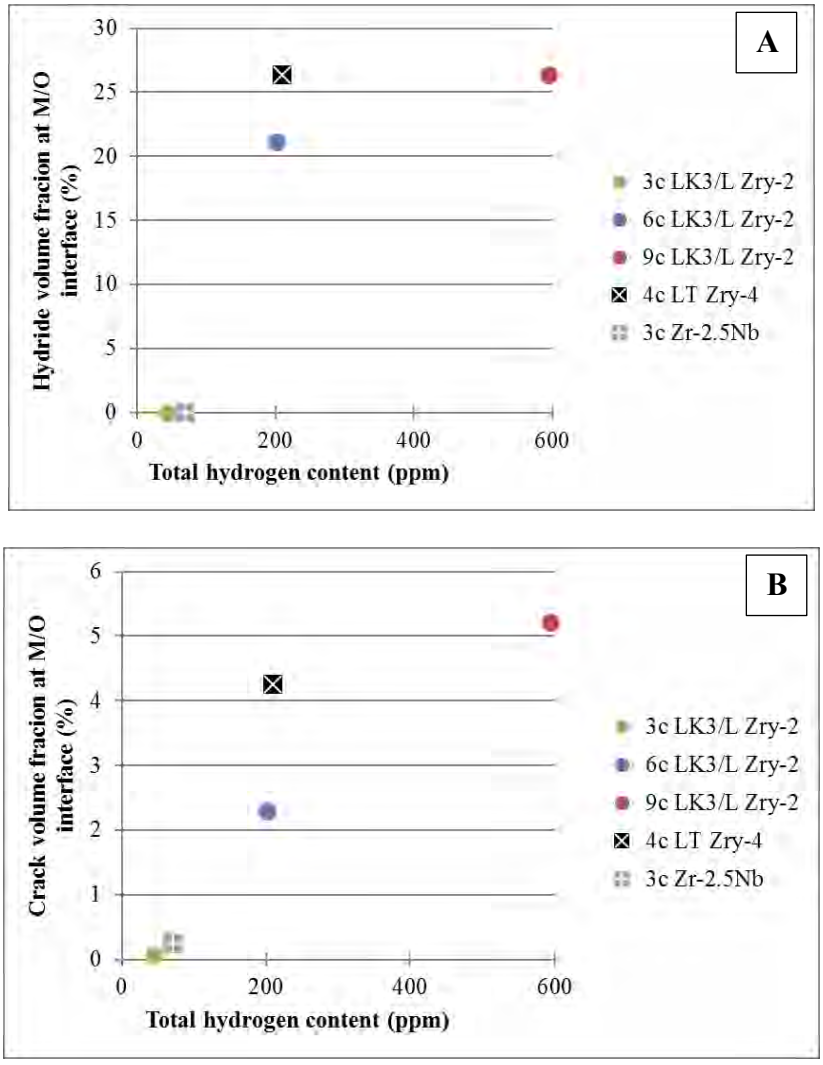

Figure 7-6 (A): The hydride volume fraction at the metal-oxide interface as a function of the total hydrogen content. (B): The crack volume fraction at the metal-oxide interface as a function of total hydrogen content.

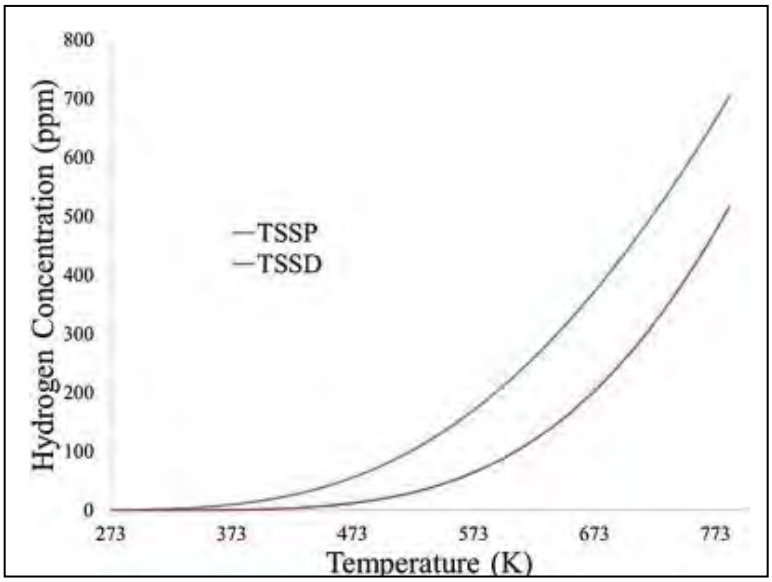

Figure 7-7. Terminal solid solubility (TSS) of H in Zr [211] where TSSP and TSSD are the graphs for the hydride precipitation and dissolution, respectively.

7.3. Comparison of low-tin Zircaloy-4 and Zr-2.5Nb claddings – Role of composition under the same reactor conditions

The detailed comparison of the compositional differences of the two claddings and its influence on their different behaviour has been already discussed in the Discussion section of Chapter 6. Some suggestions have been proposed as the cause of the better performance of Zr-2.5Nb cladding. These are the following: not significant dissolution of the Nb-phases occurs in the metal while dissolution of the SPPs are faster in the Zircaloy-4 type sample. Nb phases remain metallic in the oxide up to a certain distance increasing the conductivity of the oxide and reinforce the oxide structure against cracking while SPPs dissolve relatively fast after their oxidation in Zircaloy type of materials. The oxide close to the metal-oxide interface has shown significantly higher crack volume fraction in Zircaloy-4 sample. The dissolved Nb and Fe in the oxide scale are both claimed to improve the H-uptake properties. It influences the oxidation

as well, as an example it has been revealed that a low-tin Zircaloy-4 sample irradiated to 31 MWd/kgU with higher Fe content has a significantly reduced oxidation compared to the lower Fe addition [161]. It has been also shown by other studies that the Zr-Nb type claddings are more suitable for the PWR environment also due to the fact that Zircaloy-4 shows accelerated corrosion in reactor while this is not observed in the case of Zr-Nb type claddings [172]. The very small crack volume fraction of Zr-Nb type cladding compared with the Zircaloy-4 is clearly an indication of the protectiveness of the oxide layer of the Zr-Nb type material.

8. DISCUSSION

In this thesis every chapter is followed by a detailed discussion which provides a critical overview and the possible interpretation of the results. The reader is asked to refer to these pages for more detailed discussion of each specific topic. In this final discussion the most important results and outcomes of the thesis are briefly discussed in order to give a final overview. The first part of this chapter deals with the scope of the techniques used to study the materials and discusses the limitations and the possible sources of error. The second part, which is the core of this chapter, discusses the scientific findings.

8.1. Discussion of the main characterization techniques

8.1.1. FIB tomography

FIB tomography gives not only the shape of the visualized objects in three-dimensions but it also provides quantification of the volume fraction of the objects. During the slice-and-view process a layer with a certain thickness is removed along the slicing direction by ion milling (in this thesis this direction is selected as the Z axis); this is defined as the “slice thickness”. The optimal thickness of the layers removed is dependent on the morphology and the volume of the objects studied. It was recommended that around 8-10 slices from the smallest object in the reconstruction gives an acceptable resolution in the z-direction of the visualization [212]. It is worth noting that there is a limit in the size below which it is not possible to reveal an object in 3D by FIB, due to the limit in the slice thickness possible to cut with FIB.

In this study, the average slice thicknesses of the shown reconstructions changed between 8 nm and 32.5 nm. Therefore, objects with a size below 0.064 μm and 0.26 μm in the z-direction

occurred in less than 8 images and the resolution of these objects in the z-direction are below the mentioned limit. It means that small pores of the oxide could not be revealed with the same accuracy as the cracks with bigger sizes. However, the mentioned limit is a recommendation and rather an empirical observation than a strict rule. These small micro-cracks are well-recognizable in the 2D micrographs and even with less number of images it is possible to visualize them in the 3D reconstruction. Not only the size of the objects can limit the accuracy of the FIB tomography technique but also the resolution in x-y direction limited by the resolution of the SE or BSE images taken after each slice and the sharpness of the images. The images have been taken with relatively low magnification as the size of the objects of interest (e.g. hydrides and micro-cracks) are mostly in the μm range in the x-y direction.

Taking into account the above mentioned limitations and the sizes of the objects analysed in this study, it is possible to claim that the result of the 3D reconstructions, i.e. the shapes and the quantification of the volumes of the different objects (cracks in the oxide and hydrides in the metal) are reliable, within the resolution limits as mentioned.

The current study shows that FIB tomography offers a powerful technique for the investigation of the microstructural changes in the material. It can be used to show how these changes are related to the oxidation phenomenon.

8.1.1.1. Error estimation of the FIB tomography results

During the slice-and-view process the following parameters could be selected in the FIB software: the width of the slices (and SEM images, i.e. X value of 3D reconstructions), the depth of the cut (Y value) and the frequency of the imaging. Therefore, it was not possible to directly control the slice thickness (Z value), but rather indirectly with this last parameter.

In this study, constant slice thickness was assumed and it was calculated as an average slice thickness in the end of the image stack collection (i.e. total Z length of the milled volume per number of slices). Due to the destructive method, objects (e.g. small pores) which have smaller size than the slicing step size may not have been captured. However the total volume of these undetected objects is assumed to be negligible if the slice thickness is small enough.

It is not expected that between two slices the shape of the cracks would change significantly, especially as the slice thickness was rather small during the slicing of the samples. Furthermore, the SE image gives depth information as well, as it has an interaction volume of a few nm at the low (5-10 kV) acceleration voltage which was used. Therefore, it is assumed that the errors caused by the changes in the shape of the objects can be neglected. The largest error could come from the segmentation error, i.e. if during this step more or less number of pixels is associated to the object. This leads to an overestimation or underestimation of the contour of the object. Based on the comparison of the original and the segmented images, it was assumed that on average only a few pixels have been segmented imprecisely around the object, especially on those cases where the boundary between two adjacent phases were not well-defined. The segmentation was done either entirely manually or the automatic segmentation was followed by a manual “cleaning” step. Each image of all image stacks have been reviewed manually after segmentation. Therefore, the segmentation is considered as highly accurate. However, in the case of large datasets as the image stacks, it is unavoidable that either extra pixels have been associated with the object or at some sites some pixels were missed out from the segmentation. A test has been made by shrinking or enlarging the segmentation of a given object therefore decreasing or increasing its volume. The volumes after the different segmentations have been calculated in order to estimate the volume change due to the different segmentation scenarios and therefore to determine the error in volumes that could occur due to the image segmentation.

This error is estimated to be around ± 15-30% in the present work, however the upper limit is rather an overestimation which is caused by the estimation procedure itself; we do not expect an error higher than ± 20% in most cases.

It is worth noting that the reconstructions have been produced by two different software products. The majority of the reconstructions on the LK3/L claddings were done by ImageJ and the rest of the 3D visualizations with Avizo. This change was justified by the time reduction of the computational process for the reconstruction, especially the segmentation of the images. A test confirmed that the two software give practically the same volumes if the same "label" file is reconstructed with them. Therefore, the change in software did not introduce an extra factor of uncertainty or error.

Taking into account the above error estimation, and knowing that a comparative study is performed, FIB tomography gives reliable and acceptable statistics to estimate the volume of the objects investigated. The operator does not contribute to the error when comparing two datasets, as all data was analysed by the same operator.

8.1.2. EPMA and ChemiSTEM

One of the greatest advantages of the EPMA technique is the possibility to analyse the large scale chemical compositions with very high sensitivity providing quantitative information. Although EPMA measurements have intrinsically a certain limit of precision, the use of EPMA in this study allowed to provide the most accurate quantification from the largest surface area possible for such highly irradiated material.

One of the drawbacks of EPMA is the relatively long measurement time as the elements are detected separately by several diffraction crystals. Furthermore, the spatial resolution of EPMA

is much more limited compared to STEM due to the fact that in the EPMA bulk samples are used and interact with the beam, resulting in a larger interaction volume than in the STEM where the sample is a thin film. Also, the acceleration voltage of the incident beam in EPMA (15 to 30 keV); as well as the penetration depth of the beam as a function of this incident energy, induces an interaction volume which will be larger in comparison to TEM.

Therefore, it is not possible to resolve small features in the nanometric range. The trends and changes in concentrations reported in this study can be measured reliably by EPMA and the above mentioned limitations have been taken into account while presenting the data. In contrast, TEM is the most appropriate technique for characterization in the nanometric range of the material. Therefore the high resolution chemical analysis and the accurate quantification of the SPPs and GB segregation have been carried out by TEM. While ChemiSTEM has a higher spatial resolution, its detection limit is lower than that of EPMA. Furthermore, the areas analysed are much smaller. Independent of limitations of the techniques used, the obtained results point to specific trends.

8.2. Discussion of the scientific findings

In this study fuel claddings irradiated in a BWR (KKL) and a PWR (KKG) with different burnups were studied to correlate microstructure and chemistry to the changes of behaviour at high burnup. The aim of this study has not been to examine other structural components of the reactor.

One of the main objectives of this dissertation is a full characterization of an extreme high burnup cladding in order to observe the highest possible level of compositional and microstructural degradation of the material. For this reason a 9 cycle LK3/L Zircaloy-2 was available. To better understand the different levels of degradation, two other samples are studied

from the same batch and from the same BWR: a 3 cycle (medium burnup) and a 6/7 cycle (high burnup) cladding. The datasets from all the BWR samples are then compared in order to comprehend the dynamics of the chemical and structural evolution of the material and to observe what the major differences at high and extreme burnups are compared to the medium irradiated or even the un-irradiated material. Several aspects have been found to be quite similar after each stage of irradiation while other factors observed to be significantly different between the lower and higher burnup regions. Therefore apparent trends are established in this work and will be describe in this chapter.

In order to be able to separate those phenomena which are reactor or alloy specific, it is necessary to characterize other claddings from different reactor, i.e. PWR, displaying different HPU and oxidation behaviours. In this manner some of the possible causes of the increased HPU and oxidation at high burnups could be revealed as generalities for both reactors. The main aim of the dissertation is to suggest which factors could be responsible for the reduced protectiveness at the late life of the cladding.

A critical argument could be the low number of available samples in the case of the PWR claddings and that it may not be enough to reach a general conclusion. However, the fact that even with a relatively low amount of data, some trends and some similarities between the BWR and PWR claddings have already revealed themselves is convincing. This indicates that the observations on the 4 cycle Zircaloy-4 and the 3 cycle Zr-2.5Nb samples are indeed representative and can be used for the comparison to the other samples from BWR.

Therefore in the following the observed generalities and differences in the two reactors as well as their possible interpretation is described.

8.2.1. Behaviour of Fe in BWR and in PWR

As a reminder, the Fe distribution of the different regions of the studied samples is presented below in Figure 8-1. For the LK3/L cladding all studied cycles are shown together in one graph.

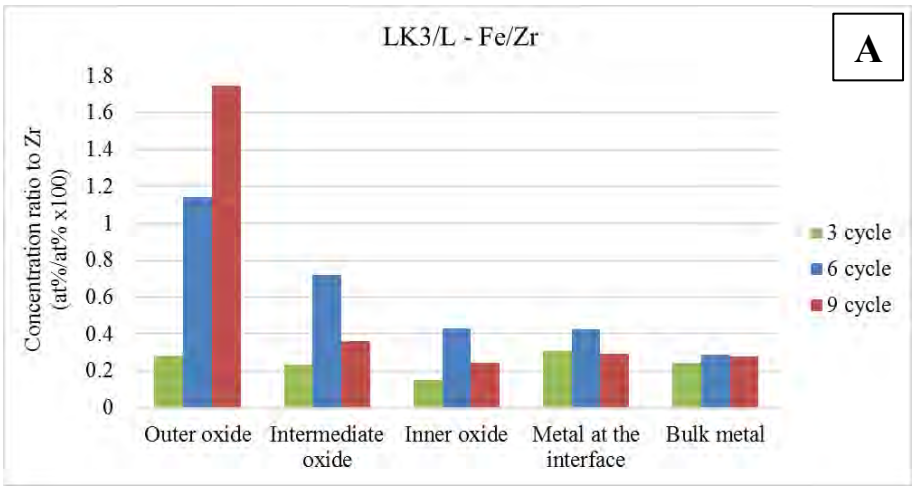

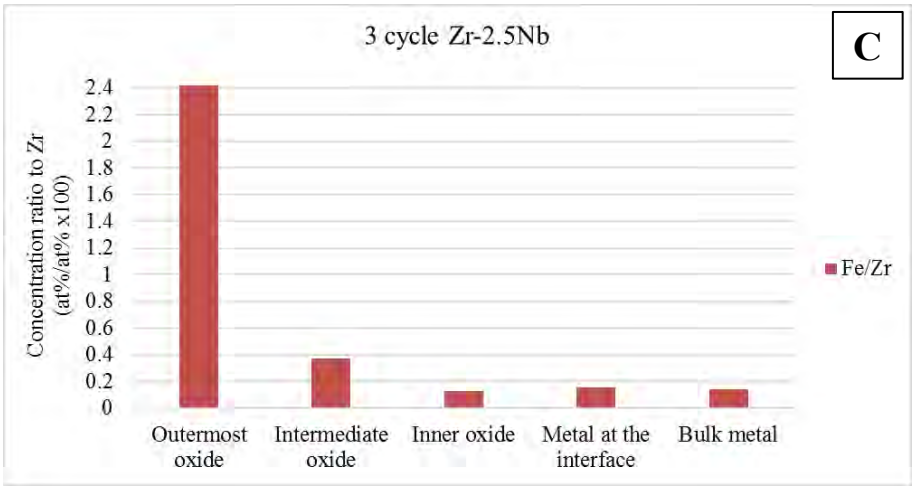

Figure 8-1 (A): Evolution of Fe in the LK3/L cladding with different service time. Fe distribution in 4 cycle Zircaloy-4 (B) and 3 cycle Zr-2.5Nb (C) samples. Average data is given based on EPMA point line-scans with SPPs excluded.

A. Some generalities have been observed in the case of Fe in the metal:

- Fe seems to behave in a very similar way in both fuel claddings of Zircaloy-2 and Zircaloy-4 in the medium and high burnup regions independent of reactor. An Fe accumulated region is revealed by EPMA in the metal in the vicinity of the interface in the 3 and 6 cycle LK3/L and in the 4 cycle low-tin Zircaloy-4 samples. The PWR cladding showed the highest Fe concentration in this region, followed by the 6 cycle LK3/L sample. In other words, the same phenomena were observed in two different types of alloys which have experienced two significantly different environments and conditions as well as after different service times. This indicates that it is a general behaviour of Fe in medium and high burnup materials independent of reactor type. As it was not observed in the 9 cycle LK3/L sample, it is suggested that this accumulation is not stable at extreme high burnups. To the best of our knowledge this Fe accumulation at the metal side of the metal-oxide interface was not reported previously in the literature.

- This accumulation is observed in samples showing different oxidation and HPU behavior. The oxide layer of the LK3/L cladding is still protective after 3 cycles and its HPU is very low, this is not the case in the 6 cycle sample. It is known from the literature that the low-tin Zircaloy-4 as cladding in PWR, shows accelerated corrosion at this stage of burnup. This indicates that: a. the Fe-rich region is stable even during the fast corrosion of the metal; and b. the accumulation of Fe at the interface may not be the rate limiting factor on the oxidation or the HPU. If it would have a significantly negative effect on the HPU and the oxidation then between the 3rd and 5th cycles an obvious increase in HPU should occur in the LK3/L cladding: we can assume that after 5 cycles the Fe rich region is still present and as the H content is relatively low (90 ppm) it can be concluded that the HPUF has not increased.

B. Fe shows similarities in the oxide as well:

- All samples investigated show an increasing Fe content towards the outermost oxide region. Fe accumulation has also been observed in free surfaces such as cracks in the high burnup materials. This phenomenon is independent of alloy, service time and reactor type. The Fe concentration shows an increasing tendency in this layer with the number of cycles in the LK3/L samples, i.e. the phenomenon increases with time.
- It must be mentioned that the origin of this layer is under debate in the scientific community and the driving force for Fe to diffuse out to the outer oxide has not been identified yet. In fact, the question whether this Fe comes from the alloy or from the reactor environment (e.g. water chemistry, or as corrosion product of pressure vessels, stainless steel pipes, or other components, etc.) is still under discussion. In the case of BWR iron and zinc are normally injected in the coolant in small quantities and an Fe-

Zn rich crud is developed on the surface of the material. It is claimed that the Fe which is the component of the crud would diffuse to the outer regions of the oxide or in the cladding itself. The fact that previous studies ([103], [104], [105]) clearly showed that Fe diffuses out from the SPPs once it is incorporated in the oxide layer even in the absence of irradiation and furthermore it diffuses out to the free surface of the oxide indicates the opposite of the previous statement and it suggest that this is an intrinsic behaviour of Fe in zirconia. The irradiation could enhance this behaviour due to the fact that Fe starts to dissolve from the SPPs already in the metal and this is being subsequently oxidized. It is to be emphasized that studies (references [103], [104]) on binary alloys such as Zr-1%Fe, Zr-1%Ni, Zr-1%Cr, Zr-0.6%Nb oxidized in autoclave reported Fe rich outer oxide surface only in the case of Zr-1%Fe, other alloys did not show Fe-accumulation. This is a very important observation proving that this Fe did not come from the environment and it was not a contamination as it is discussed in more details in reference [104] as well. To the best of our knowledge this statement has not been disproven based on the previous literature. In other words, Fe contamination has not been published on Fe-free alloys (containing other types of SPPs) if Fe was not injected in the water. It is also an important factor that in PWR Fe is not injected in the coolant. Although Fe is a typical corrosion product of the reactor components and therefore it could be present in the coolant, no crud has been observed in this study on the examined PWR claddings, i.e. during the time of service in KKG there was no crud deposition on the investigated claddings [from private communication].

- It was claimed that dissolved Fe in the monoclinic oxide has a positive influence on the HPU by: reducing the potential gradient through the oxide, or reducing the mobility of interstitial protons in the oxide [141], [153]. This could mean that with increasing

dissolved Fe concentration the HPU would become lower if other factors are not influencing the process. However, many different deteriorating factors are present at high burnups.

8.2.2. Behaviour of Ni during long-time service in BWR

As Ni is claimed to have a detrimental effect on the HPU of some of the claddings, the study of its behaviour and its evolution with time could give an important hint for the better understanding of the increased HPU of some of the claddings at late life. It is demonstrated that not only the metallic Ni could increase the HPU of the cladding but oxidized Ni as well through charge compensation [131].

In order to observe the evolution of Ni in the LK3/L material from low to extremely high burnups, all of the obtained EPMA point analysis data for Ni is presented on all the studied LK3/L samples in Figure 8-2. The Ni distribution is given in the different regions of the oxide and metal.

The LK3/L alloy shows good HPU properties in the first 3 cycles when Ni is present both in the SPPs and dissolved in the metal. The 6 cycle cladding has a much larger HPUF and depending on the amount of metallic and dissolved Ni, Ni could indeed contribute to the degradation of the HPU properties at high burnups. On the other hand there is a low chance that metallic Ni would still significantly influence the HPU at the extreme high burnup stages as e.g. in the 9 cycle sample most of the Ni containing SPPs are dissolved. The EPMA results confirm this statement as well as the ChemiSTEM maps in the oxide part of the interface in the areas studied. However it is possible that the oxidized Ni in the vicinity of the metal-oxide interface would increase the HPU based on the observation that the dissolved Ni content

increases in the “inner oxide” region (i.e. up to 1.5 µm from the interface) from the medium to high burnups (i.e. it is higher after 6 and 9 cycles than after 3 cycles).

When we would like to further understand the effect of Ni it could be a good approach to compare a sample with similar composition with and without Ni. Therefore, Zircaloy-4 and Zircaloy-2 claddings have been compared. In the case of this study, however, one has to be careful due to the fact that the available Ni-free sample was exposed to a much harsher environment and the temperature of the two claddings at the surface can differ significantly.

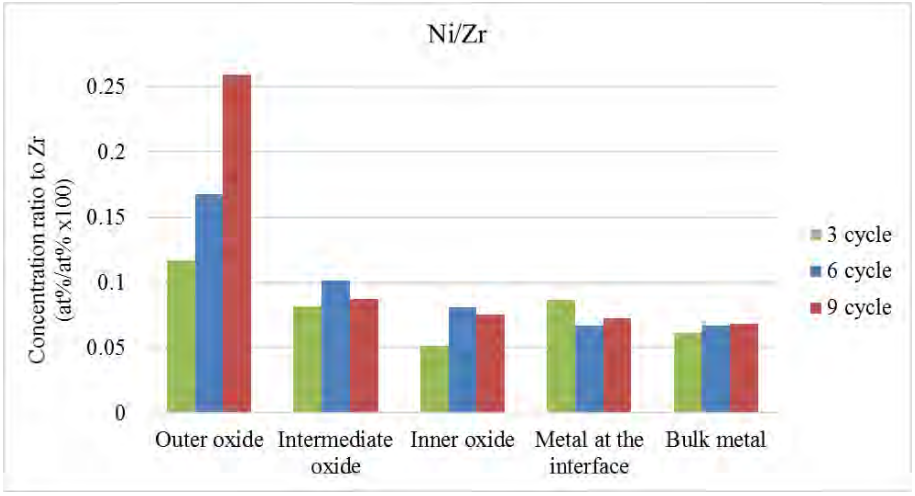

Figure 8-2 Evolution of Ni of the LK3/L cladding with different service time. Average data is given based on EPMA point line-scans with SPPs excluded.

8.2.3. Behaviour of Cr in BWR and in PWR

The Cr distribution of the different regions in all studied samples is presented in Figure 8-3. For the LK3/L cladding all studied cycles are shown together in one graph.

Cr is present in the form of SPPs in the beginning of the service in both Zircaloy-2 and Zircaloy-4 type materials. Cr is the last element that dissolves from the SPPs, therefore it was detected in both dissolved form in the matrix and in a form of some remnant SPPs even after extremely high burnup. Therefore, Cr could be one of the possible reasons why the LK3/L cladding still does not show extreme rapid oxidation even after 9 cycles. On the other hand some authors claimed that the intermetallic Fe-Cr SPPs in the barrier layer increases the HPU by offering an easy route to the metal [148], [71], [146]. However, this process is expected to be less active at late life of the cladding when only a very few remnant SPPs are available. Therefore, it is not likely that Cr would have a negative effect on the HPU of the LK3/L cladding at late life.

It is worth mentioning that in the above referred studies, the effect of the SPPs, i.e. Fe and Cr together, was studied rather than the effect of Cr. In general, little is available in the literature on the effect of Cr alone.

The evolution of Cr in the LK3/L cladding was already discussed in Chapter 5 – Section 5.3. It is interesting to note that its distribution is different in the two cladding types. Cr shows a maximum concentration in the “inner oxide” region of the 4 cycle low-tin Zircaloy-4. Further study is needed to understand what could cause such distribution, and that whether Cr is metallic in this region, and what could be the effect of this on the cladding’s behaviour.

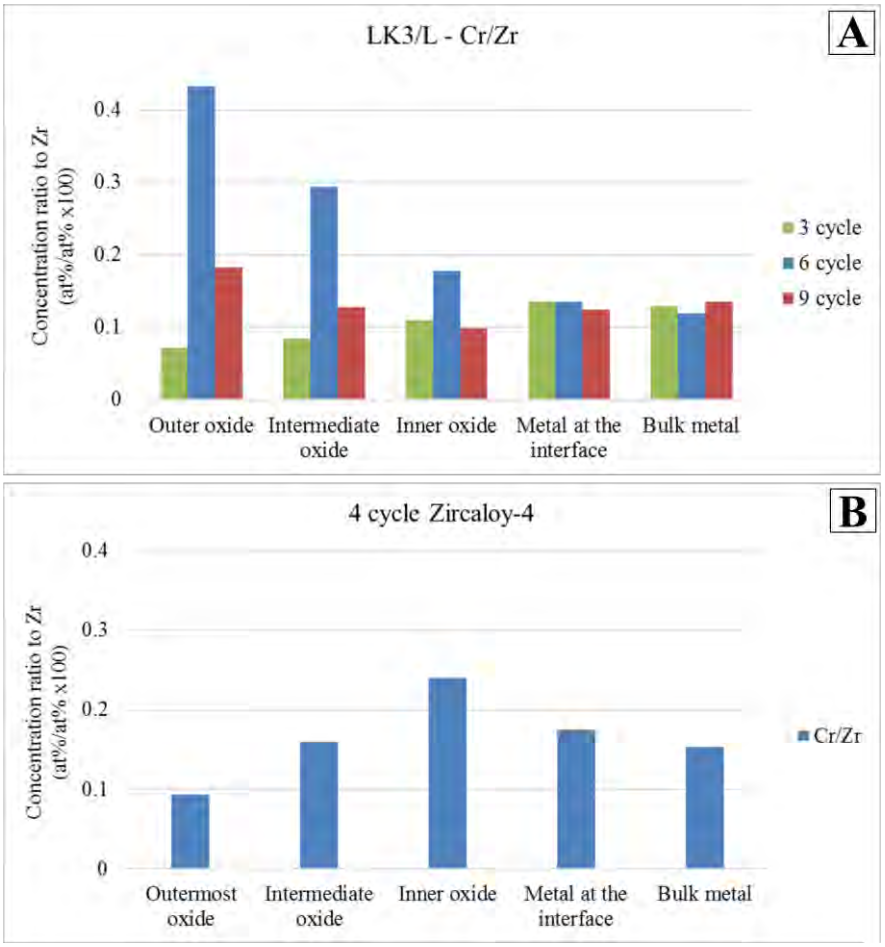

Figure 8-3 (A): Evolution of Cr in the LK3/L cladding with different service time. (B): Cr distribution in 4 cycle Zircaloy-4 sample. Average data is given based on EPMA point line-scans with SPPs excluded.

8.2.4. Behaviour of Nb and its effect at medium burnup

The Zr-2.5Nb cladding was studied after 3 cycles and its distribution in the sample's different regions is shown in Figure 8-4. Nb is present as a second phase in the material. These large Nb phases seem to be very stable against irradiation-induced dissolution, and they were observed throughout the whole sample. For this reason, during the EPMA point line-scans some signal of Nb was always detected and for the evaluation it was not possible to clearly separate the Nb from the metal or the oxide matrix.

In average, Nb shows higher concentration at the outermost 1-2 µm region of the oxide compared to the rest of the oxide layer. It was suggested that dissolved Nb in the oxide with a valence state lower than 4+ would lower the interstitial proton diffusivity and lower the HPU [152]. A higher oxidation state of Nb (i.e. 5+) would occur when it is dissolved in the surface region of the oxide which would increase the electron concentration in this region and help reduction of protons at the water-oxide interface [152], [172].

This current study confirms that although the Nb remains metallic in the oxide up to 2 µm it seems to be dissolved in the rest of the oxide. Furthermore the site of proton reduction could be the water-oxide interface as a higher Nb/Zr ratio was observed at this outer oxide region. This could be one of the explanations for the low oxidation and HPU of the Zr-2.5Nb cladding under PWR conditions.

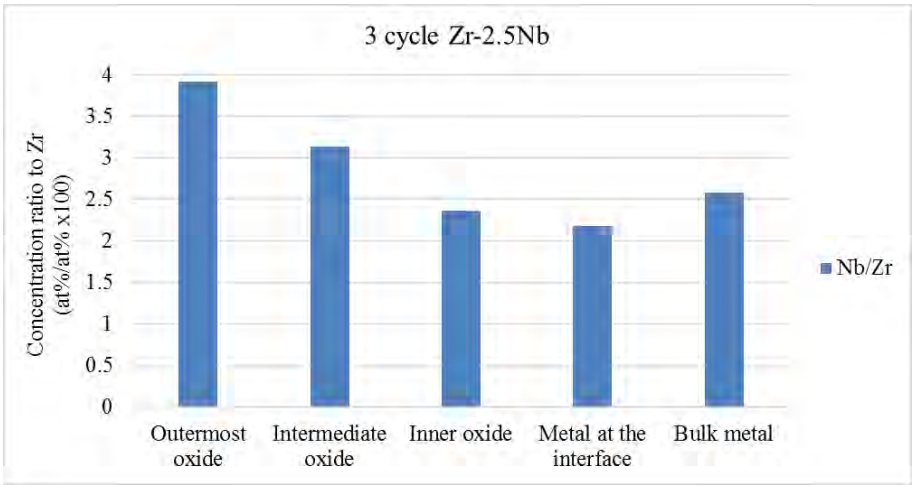

Figure 8-4 Nb distribution in the Zr-2.5Nb sample. Average data is given based on EPMA point line-scans.

8.2.5. Crack formation in the oxide scale and the effect of hydride precipitates

FIB tomography on the different alloys showed how the crack volume fraction evolves in the vicinity of the metal-oxide interface (up to 1 μm in this study) and in other parts of the oxide layer after different residence times; for the LK3/L cladding in BWR. It also provided the value of the crack volume fraction in the 3 cycle Zr-2.5Nb and 4 cycle low tin ZIrcaloy-2 claddings taken from PWR. When we correlate the protectiveness of the oxide (e.g. taking the crack volume fraction as one of the determinant factors) to the HPU and oxidation properties of the material, it is found that the nature of oxide layer at the metal-oxide interface can have a correlation with the oxidation rate and thus the cladding's properties, while the structure of the rest of the oxide seems to have no significant influence on the cladding's behaviour and seems to be a negligible parameter. It has been found that the claddings with the best performance have a practically crack-free interface oxide both in BWR and PWR. As an example, the oxide at metal-oxide interface of 3 cycle LK3/L sample is practically crack-free. However, in this example the whole oxide is mostly crack-free, and one of the reasons behind this is the absence of hydrides in the metal. Another example is the 3 cycle Zr-2.5Nb sample: the bulk oxide shows high crack volume fraction, while the interface oxide is almost entirely crack-free. Both samples show good in-reactor performance. Although the oxide at the metal-oxide interfaces of these two samples is intact, the reason behind this could be different in the two cases. In the case of the Zr-2.5Nb cladding, the suggested explanation is that the metallic Nb phases in the inner region of the oxide act as obstacles for crack propagation and they mechanically strengthen the oxide. In the outer regions of the oxide, this effect is not available as the Nb phases are oxidized; therefore cracks propagate in the bulk oxide.

Even though, the origin of the crack-free interface oxide could be different in these samples the intact interface oxide leads to the same result, i.e. low HPUF and good oxidation properties.

Direct correlation has been found between the amount of cracks in the oxide and the amount of hydride phases in the metal at the interface in the case of all studied claddings. For the ease of reading the graph is presented again in Figure 8-5. The results presented here confirm the hypothesis previously described in the literature that the presence of hydride phases could modify the corrosion kinetics and promote crack formation in the forming oxide [172], [175], [178]. Regarding this phenomenon, studies have been published only on PWR materials, but not on BWR claddings. In order to understand whether this phenomenon occurs also in BWR, data is provided in this thesis on BWR samples which confirmed the generality of this phenomenon. Furthermore, the results presented here demonstrate the effect of hydride-oxidation on the crack formation in a quantitative manner.

The effect of crack volume fraction seems to be a factor highly influencing the oxidation and HPU properties at each stage of the service, in all alloys, and in both reactor types.

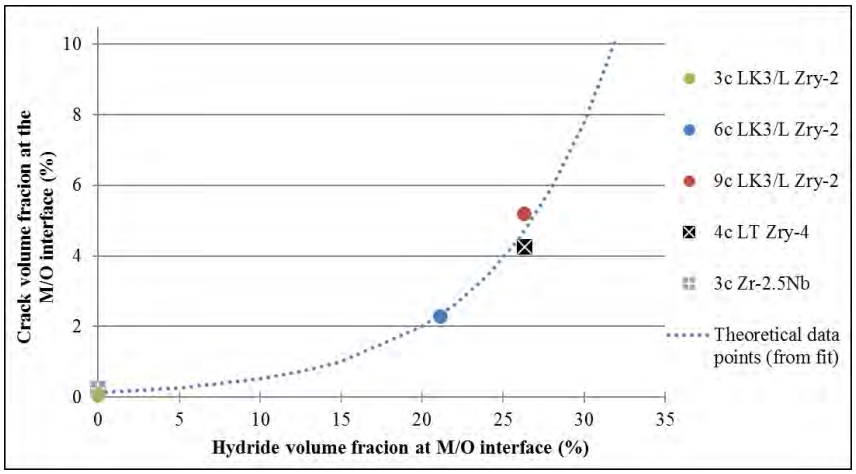

Figure 8-5 The crack volume fraction in the oxide as a function of the volume fraction of hydrides in the metal. Values are taken from up to 1 µm from the metal-oxide interface. The fitted curve is also presented.

9. CONCLUSIONS

In this thesis the microstructure and chemical composition of three different Zr-based cladding alloys which served in two reactors were characterized. Three different microscopy techniques were applied, as SEM, 3D FIB tomography and TEM for microstructural investigations; EPMA, ChemiSTEM for compositional measurements. For BWR samples an LK3/L type Zircaloy-2 cladding was investigated after 4 different residence times; and for PWR a low-tin Zircaloy-4 was analysed after 4 cycles and a Zr-2.5% Nb after 3 cycles. In the literature numerous studies of the oxidation and HPU can be found on Zr-based alloys however most of these are in autoclave due to the difficulties when handling radioactive materials. Therefore there is a great need for studies on in-reactor materials. One of the aims of this thesis is to contribute to the sources of information on these materials. The main aim is, however, to find important parameters that are responsible for the changes of behaviour of the material, e.g. increased H-uptake in LK3/L Zircaloy-2 at late life stages or accelerated corrosion of Zircaloy-4 in reactor. The microstructural and compositional evolution of the LK3/L cladding were revealed in micrometric and nanometric levels starting from un-irradiated stage up to extremely high burnup, i.e. 9 cycle. This helps to understand the changes of the material as a function of the residence time.

The main focuses during this study were: the evolution of the hydride phases, i.e. their size and their distribution in the cladding, and the role of their oxidation; the evolution of the oxide scale and its microstructural changes such as crack formation. Also the overall chemical changes and the large scale element distributions in the oxide, the metal, and the vicinity of the metal-oxide interface; changes in nanometric scale i.e. in the metal GBs, in the SPPs, and in the hydrides. The relevance of these observations comes from the fact that the H-uptake and oxidation

properties of the cladding is known after the different cycles measured, therefore a correlation between the chemical and microstructural changes and the changes in the material's properties in reactor can be drawn. Another aim of the thesis is to separate those influencing parameters that are general from those which are material- or reactor-specific. The samples from PWR have been investigated with this aim.

The main observations can be highlighted as follows:

A. Based on the FIB tomography results:

- Regardless of reactor type or alloy composition the outermost 2-3 μm region of the oxide layer is intact and contains no cracks or only micro-pores. The TEM micrographs (where available) also confirm this observation. Based on this finding, it is concluded that all claddings studied had protective oxide in the beginning of their service. This could be responsible for their good H-uptake and corrosion properties in early life. This outer layer does not change with further service; however radial cracks occur in this region with the subsequent growth of the oxide layer, offering a fast route for all oxidizing species to the deeper regions of the material.
- The crack volume fraction increases with the length of residence time in the reactor in the case of LK3/L Zircaloy-2 and this can be correlated to the reduced protectiveness of the cladding against H-uptake and oxidation towards the extreme high burnup region. This is suggested to be one of the causes for increased H-uptake at high burnups.

- In the metal it is observed that the size of the hydride phases and their volume fraction at the metal-oxide interface increased with residence time. This means that it is more likely that the additional hydrogen absorbed by the metal participate in the growth of

the hydrides that are already present at the interface rather than precipitating as new hydride.

- It is revealed that the volume fraction of hydrides in the vicinity of the metal-oxide interface is a useful parameter to correlate to the microstructure of the oxide in the vicinity of the interface. We suggest that the main parameter to be taken into account regarding the effect of hydrides is not necessarily the total hydrogen content but rather the volume fraction of hydrides at the metal-oxide interface.
- Regardless of reactor condition and alloy type, those samples which had a higher volume fraction of hydride phases in the metal in the vicinity of the metal-oxide interface also exhibited high crack volume fraction in the oxide close to the interface (i.e. 6 and 7 cycle LK3/L Zircaloy-2, 4 cycle low-tin Zircaloy-4). On the other hand, samples with low amount of hydride phases or no hydrides at the interface (i.e. 3 cycle LK3/L Zircaloy-2, 3 cycle Zr-2.5Nb) show low or extremely low fraction of cracks in the interface oxide (up to 1 μm from the interface). A clear, quantitative correlation has been shown for first time, to the best of our knowledge, between these two parameters and the role of hydride oxidation on the crack formation in the oxide can be revealed.
- In the case of LK3/L Zircaloy-2 cladding the turning point where the material shows considerable changes in microstructure and reduced protectiveness seems to occur between 6 and 9 cycles. However, even after 9 cycles the cladding does not show extremely rapid oxidation and H-uptake.
- A reduced level of undulation of the metal-oxide interface from 3 cycles to 6 and 9 cycles was observed (in LK3/L). Furthermore, straighter interface was revealed in the case of the 4 cycle low-tin Zircaloy-4 cladding compared to the 3 cycle Zr-2.5Nb.

B. Based on the EPMA results:

- The chemical composition of the metal-oxide interface and the oxide evolves significantly and dynamically with the time spent in the reactor in the case of the LK3/L material.
- Increasing amount of dissolved O in the metal at the interface of the LK3/L cladding was observed by EPMA.
- Independent of reactor type and alloy composition a trend of increasing concentration of Fe towards the outer surface of the oxide is observed. As a consequence, an Fe-rich region is present in the outermost oxide in all claddings, i.e. independent of the presence of crud. Ni (where it is present) shows similar behaviour but much less enhanced.
- Increased Ni content is observed in the inner oxide (up to 1.5 μm from the metal-oxide interface) at high burnup LK3/L claddings compared to medium burnup.
- Remnant SPPs of Cr are still present in the LK3/L cladding even after extremely high burnup. However, they contain in most cases very little Cr. Due to their average size, the composition can be determined by TEM.

C. Based on the ChemiSTEM results:

- All LK3/L claddings show segregation of Fe and Ni at the metal GBs both in un-irradiated stage and after irradiation. Sn shows segregation in metal GBs and in the adjacent oxide part as well only above high burnups (i.e. 7 and 9 cycles). The element content in the GBs seems to increase with the number of cycles. Cr shows limited segregation after 9 cycles in the metal GBs.
- In the case of 9-cycle LK3/L, the Sn segregation was observed in one sample, at the metal oxide interface and its trace was also continued into the oxide.

- Hydrides are depleted of Fe, Ni, and Sn compared to the surrounding metal matrix at extreme high burnups (9 cycle LK3/L). As the hydrides are large at this stage, this causes additional enrichment of the alloying elements in the metal matrix. As the elements have low solid solubility in the metal this phenomenon could promote the segregation of these elements at the GBs.
- The oxide of the LK3/L cladding is sub-stoichiometric after 3 cycles and stoichiometric after 9 cycles.

Based on these observations the most important conclusions are the following:

1. The microstructure and composition of a cladding which is exposed to irradiation change dynamically and continuously in light water reactors. Numerous different processes are active and many potential influencing parameters are present parallel with each other. The most significant parameter influencing the H-uptake and the oxidation of the material at a given time could change from cycle to cycle.

2. An oxide layer with no or low amount of micro-cracks is protective against rapid oxidation and H-uptake. In general a more porous oxide is less protective and also mechanically weaker. The increasing crack volume fraction in the innermost regions of the oxide is one of the parameters influencing the material's late-life H-pickup and oxidation properties.
3. Oxidation of hydrides in the metal at the metal-oxide interface promotes the production of cracks in the forming oxide. If large hydrides are present, this phenomenon plays significant role in the reduction of protectiveness. Formation of large hydrides and their subsequent oxidation therefore is a HPU increasing factor at high burnups.

4. In Zr-2.5% Nb the presence of the metallic Nb phases in the oxide in the vicinity of the metal-oxide interface improves the resistance against cracking as these phases act as composite components and strengthen the oxide's mechanical properties. Furthermore they act as obstacles for the propagation of the already formed cracks in the oxide. This is one of the causes of the cladding's high performance in PWRs.
5. This study confirms that an undulated metal-oxide interface can be correlated to a more protective behaviour than that of a straight interface. The undulation of the interface is reduced in the 6 and 9 cycle samples compared to the 3 cycle cladding. This can be correlated to the higher oxidation and HPU of the LK3/L cladding at high and extreme high burnups.

6. Increasing levels of O in the interface metal of the LK3/L samples at high burnups are correlated to faster oxidation.
7. Irradiation induced high level dissolution of SPPs at extreme high burnups reduces the protectiveness of the cladding against increased oxidation in the LK3/L type materials and most probably in other Zircaloy type claddings. However, the presence of the Cr remnant SPPs in the 9 cycle LK3/L cladding could still play a protective effect against very rapid oxidation.
8. The presence of dissolved Fe^{3+} in the monoclinic oxide was claimed by other researchers, to positively influence the H-uptake properties. In this current study increasing dissolved Fe content was observed in the outermost oxide of the LK3/L claddings with increasing burnup. We can assume a high oxidation state of Fe in this region and therefore assume a protective outer layer. However, even if this assumption is correct, the protectiveness of this layer may be relevant only at the beginning of the

service. At later stages, e.g. high burnups, other processes could overcome this effect. This point needs further clarification and confirmation in future studies.

9. The speciation of Ni has been examined, and their role on the H uptake has been discussed by other researchers. Ni is considered to increase the HPU in metallic state or in oxidized form (Ni^{2+}) in the regions of the oxide close to the interface. The current study indicates increasing Ni concentration in the inner 1.5 μm region of the oxide of the LK3/L Zircaloy-2 claddings towards high burnups. This can be one of the causes of the increased HPU at late-life stages of the cladding.
10. Cr dissolves slowly from the SPPs and it is still observable as remnants at extreme high burnups. This could be one factor that still protects the cladding against extreme rapid oxidation even after the designed life-time of the LK3/L cladding.
11. Metallic Fe and Ni at the interface was claimed to offer a fast route for hydrogen ingress. GB segregation of these elements with increasing concentration towards high burnups could be an HPU-increasing factor. The large hydride phases at high burnups reject these elements, and could promote the GB segregation of these elements.
12. Sn segregates at the metal GBs only at high burnups. The segregation continues to the oxide side of the metal-oxide interface. The effect of Sn segregation in the oxide could help the tetragonal to monoclinic transformation of the oxide degrading the oxidation properties. This could be one of the responsible parameters for the faster corrosion of the LK3/L alloy after long residence times.
13. The formation of a stoichiometric oxide at high burnup indicates a reduced oxide conductivity leading to higher H-pickup at late life. On the other hand, even at high burnups a less charging oxide layer was observed at the interface of the LK3/L

claddings, indicating the presence of an inner layer with higher conductive properties. This topic is being studied as the continuation of this project.

High level of porosity in the oxide and large hydride phases in the metal at the interface, straight metal-oxide interface, higher O concentration of the interface metal, high level of SPP-dissolution, segregation of Fe, Ni, Sn and slightly Cr in the metal grain boundaries, increased Ni concentration in the inner oxide, Sn segregation at the interface oxide, stoichiometric oxide were identified as the causes of increased H-uptake of the LK3/L cladding at extreme high burnups. Although all of these factors are present after 9 cycles, the cladding does not show extremely fast oxidation and H-uptake even beyond the designed service time.

APPENDIX I

Oxide charging during slice-and-view

Figure-AI 1 shows the observed charging phenomenon of 3, 6, and 9 cycle oxides. The oxide close to the interface (i.e. within 0.5 µm in the 6 cycle and 1 µm in the 9 cycle sample) such charging was not observed.

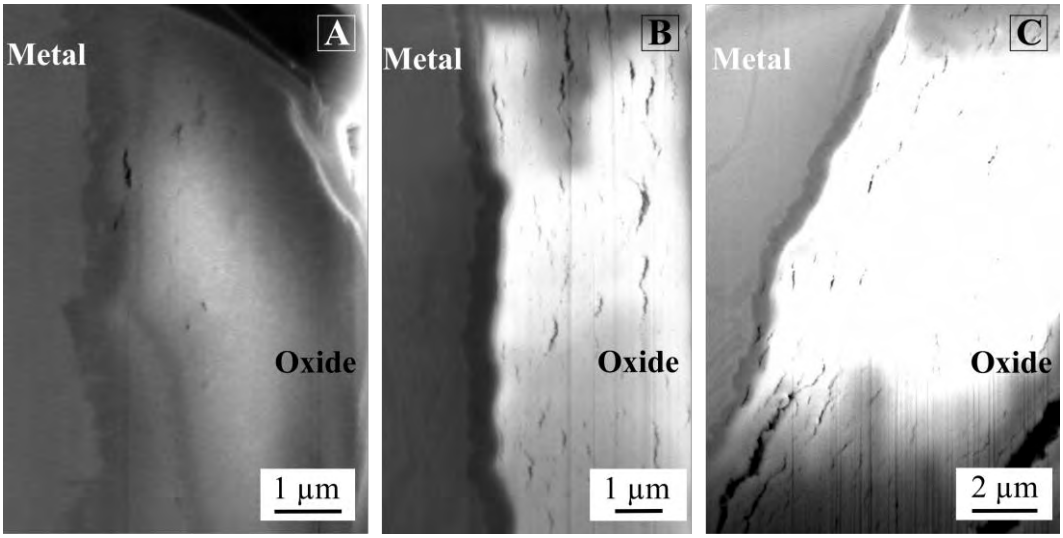

Figure-AI 1 Example SE images of the charging phenomenon during the FIB cuts in the (A): 3, (B): 6 and (C): 9 cycle samples.

Void fraction in oxide created by the hydrides in the metal

The following equations were used to calculate the void fraction that were created in the oxide by the oxidation of the hydrides at the interface:

For a given volume of metal matrix and hydride, we could write:

$$Vm + VHyd = VTmet$$

$$VTm\ x\ 1.546 = VTox$$

$$Vm + VHyd\ x\ 0.843 = VTZr$$

$$VTZr\ x\ 1.546 = VPureOx$$

$$VTox - VpureOx = \Delta\, Vvoid$$

$$\frac{\Delta Vvoid}{Vpureox}\ x\ 100 = Vf$$

Where: V_m is the volume of matrix, V_{Hyd} volume of hydride, V_{Tmet} volume of total hydride and matrix in the metal. V_{Tox} is the volume of the oxide assuming that all was zirconium. V_{TZr} is the real volume of Zr in the metal, and V_{PureOx} is the volume of oxide if no hydride was in it. $\Delta\, Vvoid$ is the volume difference due to voids, Vf is the volume fraction of voids in the oxide. All numbers should be in micrometre cubed. The values from the 3D reconstruction have been used for calculation.

APPENDIX II

The validation of data obtained by EPMA at the metal-oxide interface – Exclusion of artefacts

The quantitative EPMA point line-scan measurements and the qualitative maps through the metal-oxide interface showed a drop in the concentration of some of the elements (e.g. Fe) in the oxide compared to the metal in the vicinity of the metal-oxide interface. As this phenomenon was not expected, the possibility of an artefact from sample preparation had to be excluded. The fact that the oxide and the matrix have different hardness, the oxide could be polished slower than the metal. A physical manifestation of this would be a level difference in the metal and oxide at the metal-oxide interface. Two methods were used to exclude this artefact and the 3 cycle LK3/L sample was used as the concentration drop is the most apparent in this sample:

1. As one method, after the EPMA measurement the used sample was cut by FIB in the cross-sectional direction to the measured surface. Pt was first deposited by electron beam on top of the area before the FIB was used, in order to avoid any damage and modification of the surface. A gentle 300 pA FIB current was used as the last step for polishing. An image of the metal-oxide interface showing no such level-difference between the metal and the oxide is presented in Figure-AII 1.

2. The sample was measure a second time with different sample preparation. The side of the segment was cut and polished by FIB and subsequently analysed by EPMA. As a last polishing step 700 pA FIB current was applied. The polished surface is shown in Figure-AII 2. The EPMA provided the same results on this region of the sample a well.

Therefore, the possibility that the concentration drop is caused by an artefact is excluded.

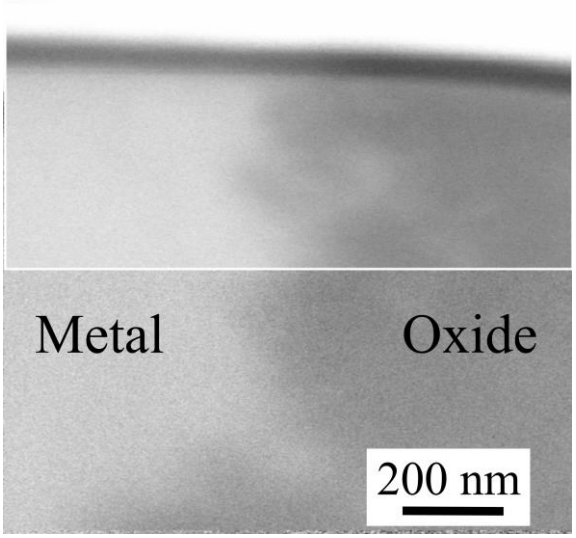

Figure-AII 1 High magnification SE image of the metal-oxide interface of the 3 cycle LK3/L sample. No surface level difference is observable between the metal and the oxide at the metal-oxide interface.

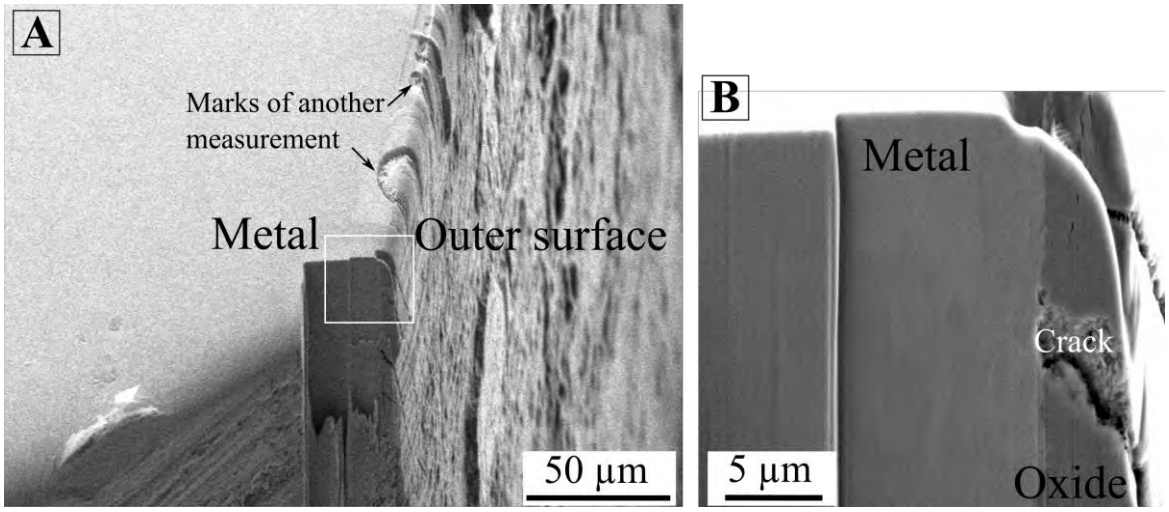

Figure-AII 2 SE images of FIB cut and polish on the side of the 3 cycle LK3/L segment. (A): low magnification image of the cut where the white square marks the polished region. (B): image of the FIB-polished region. The polished surface was subsequently measured by EPMA.

Precision of the EPMA quantifications

Table-AII 1 presents the precision of the quantitative EPMA analysis for the metal and oxide phases.

Table-AII 1 Precision of the quantitative EPMA analyses in the metal and in the oxide. "ZrO_2 KKL-H6-SB" specimen was used as a standard for measuring O, Sn, Zr and "SRM661 Standard material" for Cr, Fe, and Ni. The data is based on one long EPMA point line-scan.

	Concentration range (wt%)	95% confidence limit (wt%)	Standard deviation	Detection limit (wt%)
Metal				
O	1.04 - 1.46	0.131	0.153	0.100
Cr	0.05 - 0.14	0.082	0.031	0.043
Fe	0.16 - 0.22	0.088	0.023	0.050
Ni	0.01 - 0.07	0.091	0.021	0.045
Zr	98.01 - 98.32	0.585	0.114	0.043
Sn	1.32 - 1.38	0.097	0.025	0.047
Oxide				
O	23.98 - 27.02	0.291	0.934	0.072
Cr	0.03 - 0.17	0.078	0.051	0.045
Fe	0.15 - 0.39	0.100	0.083	0.053
Ni	0.01 - 0.08	0.084	0.020	0.048
Zr	73.79 - 74.80	0.517	0.301	0.041
Sn	0.98 - 1.01	0.086	0.010	0.047

Additional data for 9 cycle oxide – Line-scan of the oxide at the metal-oxide interface

Due to the loss of sample, no direct point measurement is available on the 9 cycle LK3/L oxide in the vicinity of the metal oxide interface. As maps were taken before the sample was damaged, the maps were quantified, i.e. a QMap was created, providing semi-quantitative data. A line-scan on this map is shown in Figure-AII 3. Based on this and other line-scans and semi-

quantitative data, the 9 cycle sample's oxide is stoichiometric not only in the bulk region but also at the interface.

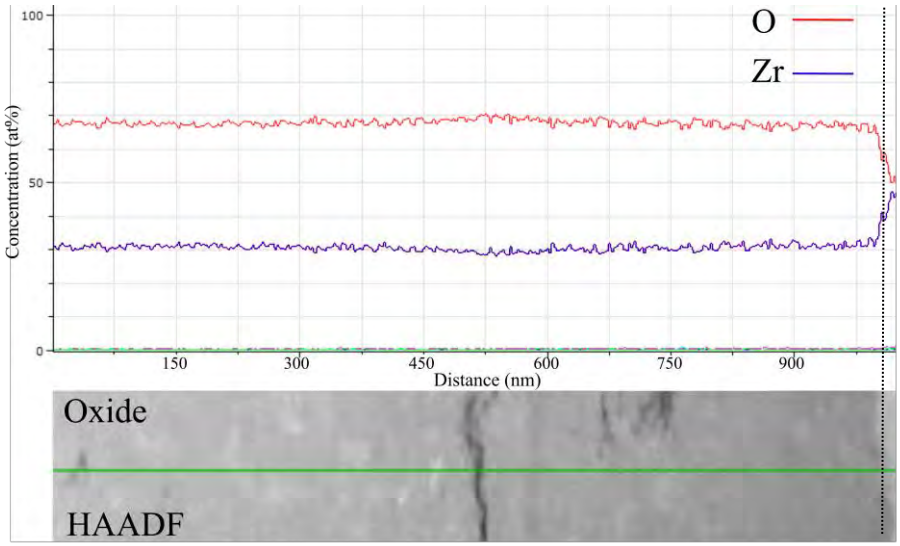

Figure-AII 3 Line-scan on a QMap of the 9 cycle LK3/L oxide showing O and Zr in the vicinity of the metal-oxide interface (marked by the dashed line). The data corresponds to the green line on the HAADF image below.

Comparison of obtained results by EPMA and ChemiSTEM

In Figure-AII 4 ChemiSTEM data of the metal matrix is compared to the EPMA "Metal close to the metal-oxide interface" region. The average values are compared and the element concentration ratio to Zr is used. The ChemiSTEM results show about 2.7 times higher Fe concentration in the case of the 3 cycle sample. This is due to the fact that the TEM lamella was prepared at the metal-oxide interface which, based on the EPMA results, contains high concentrations of Fe. EPMA has a larger volume of interaction than TEM therefore it is less accurate to measure small-scale regions and signals from the surrounding phases could also occur. In the case of the other cycles, EPMA and TEM provide data which is not significantly different. In Figure-AII 5 the oxide matrix element concertation is compared between the two

techniques. In the case of the 3 and 6/7 cycle the “Inner oxide” region is used from the EPMA measurements as the TEM lamella was prepared at the metal-oxide interface. However in the case of the 9 cycle sample the TEM lamella prepared at the outermost oxide is compared, i.e. the “Outermost oxide” region of the EPMA data is used. Around 3 times higher Fe concentration measured by the ChemiSTEM in the 3 cycle sample which can be explained based on the same consideration as before in the case of the metal matrix. The ChemiSTEM results of Sn show variation for both the metal and the oxide matrices which is not observable in the EPMA values. This variation is significant in the case of the 7 and 9 cycle oxides. This could be due to the local fluctuations of Sn in a nanometric scale resulting scatter in the TEM data.

In Figure-AII 6 it is shown that the ChemiSTEM measurement provide significantly higher values for the SPP concentrations at high and extreme high burnups. This is expected due to the much smaller interaction volume of the beam with the sample. It is very important to note that for each graph the maximum SPP concentration is given and this value is not necessarily representative of the of the average concentrations, especially in the case of the higher burnup samples where the average is significantly below the maximum value. Therefore, Figure-AII 6 should not be interpreted as an evolution of the SPP concentration.

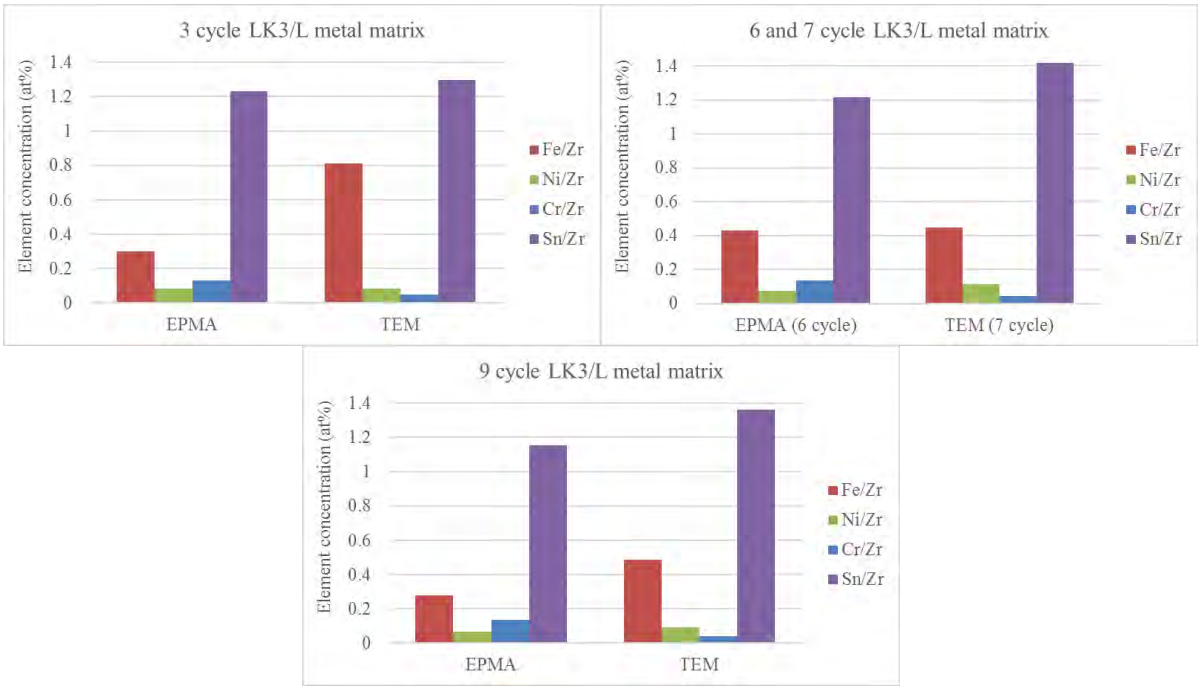

Figure-AII 4 Comparison of the obtained results for the metal matrix by EPMA and TEM after the measured cycles. The average values are compared. In the case of the 3 and 6/7 cycles the "metal close to the metal-oxide interface" region is taken into account from the EPMA data. Bulk metal is taken for the 9 cycle sample.

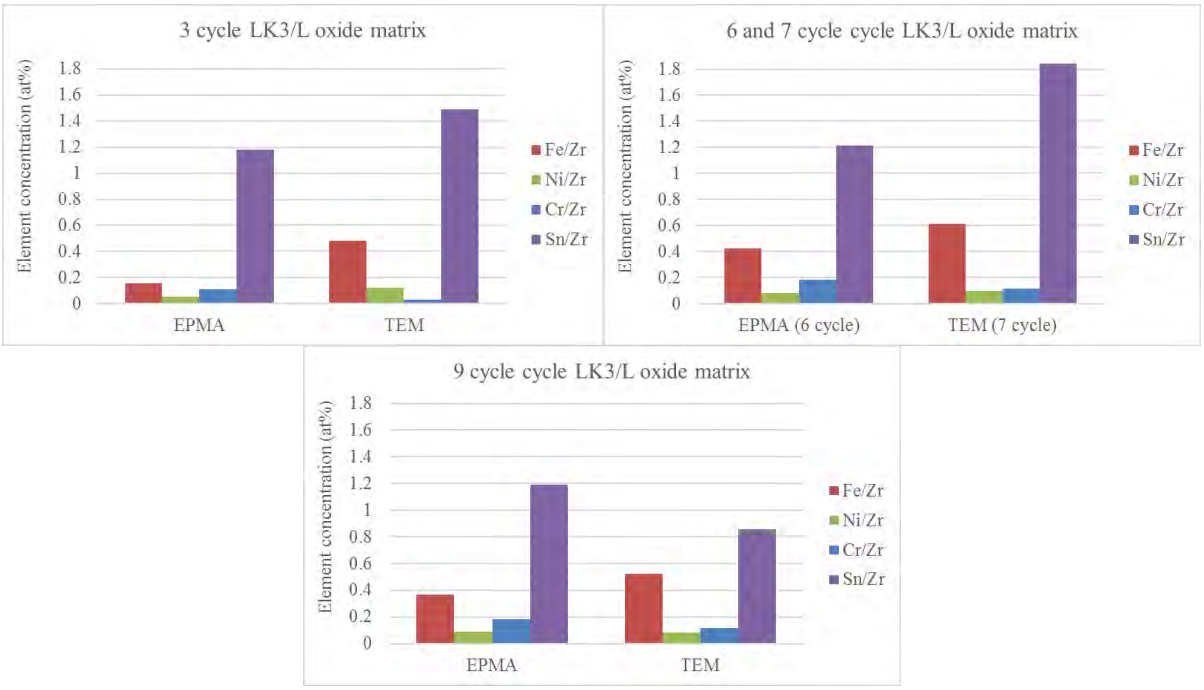

Figure-AII 5 Comparison of the obtained results for the oxide matrix by EPMA and TEM after the measured cycles. The average values are compared. In the case of the 3 and 6/7 cycles the "Inner oxide" region is taken into account from the EPMA data. Outermost oxide is taken for the 9 cycle sample as the TEM sample from which the data is presented is prepared at this region.

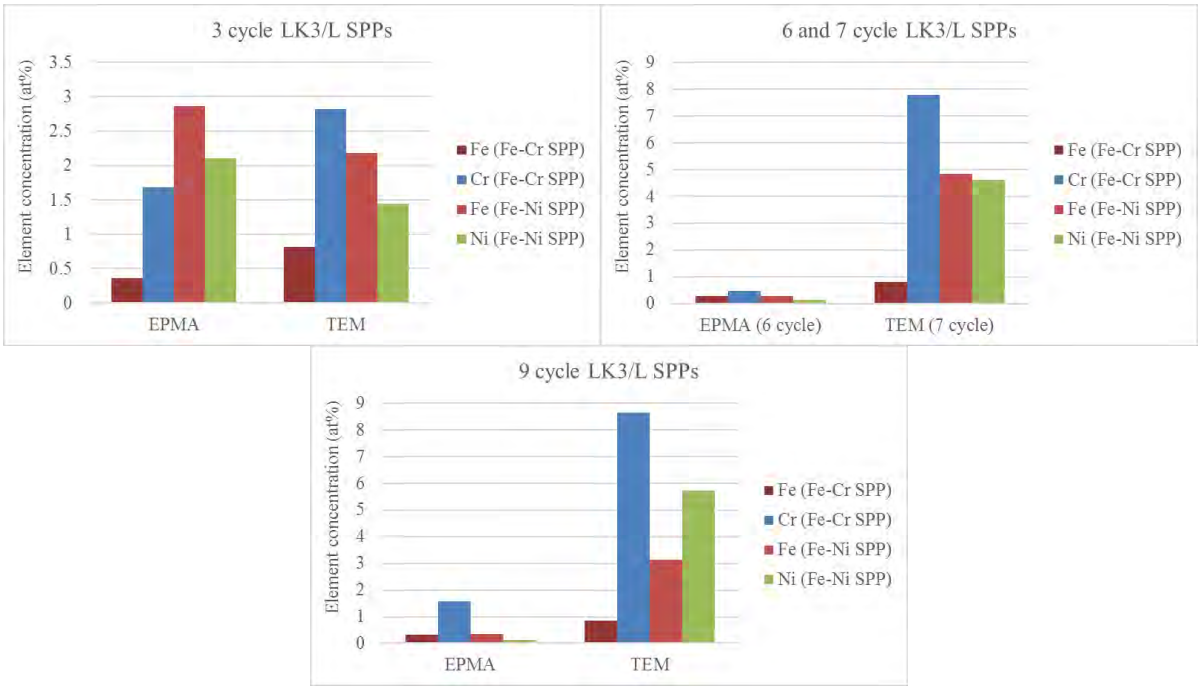

Figure-AII 6 Comparison of the obtained results for the SPPs by EPMA and TEM after the measured cycles of the LK3/L cladding. The maximum measured values are compared. These SPP concentration values do not represent the highest compositions expected, in particular in the case of the 3 cycle LK3/L sample.

Alloying element evolution of LK3/L cladding – additional data

The comparison of the changes in composition with for metal and oxide is shown in Figure-AII 7 and Figure-AII 8. Data is given in at%.

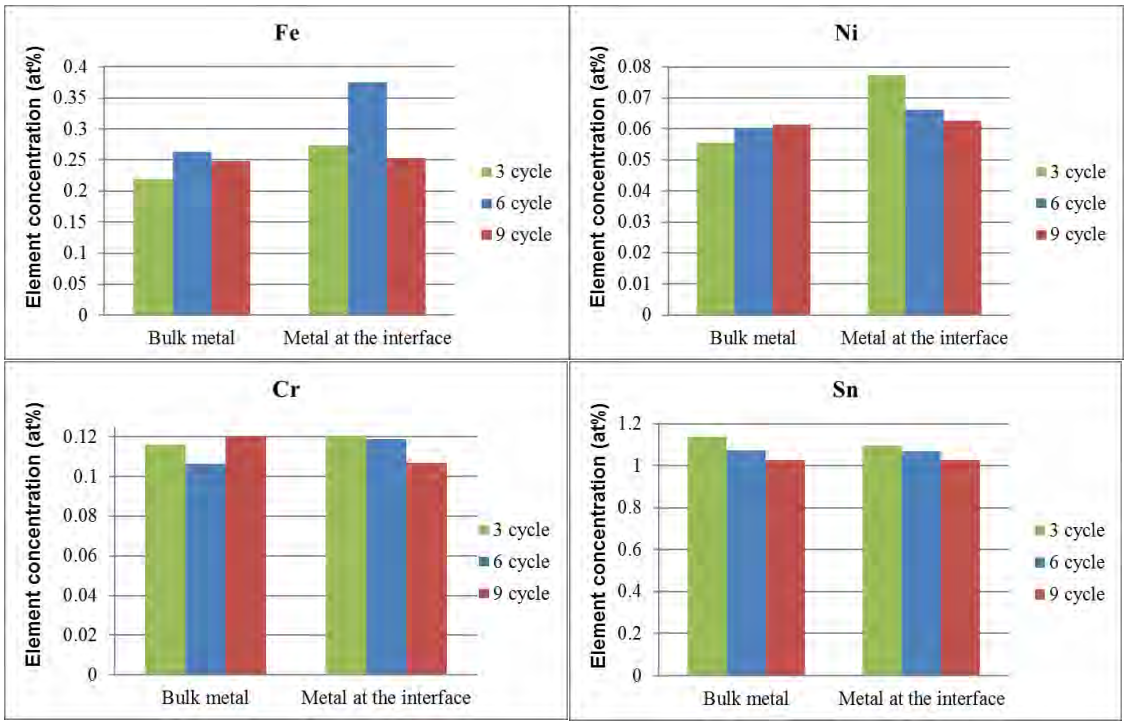

Figure-AII 7 Alloying element evolution of the cladding with time in the metal matrix based on the EPMA point line-scans. Note: these are not the ratios of alloying element to Zr, but direct measurements.

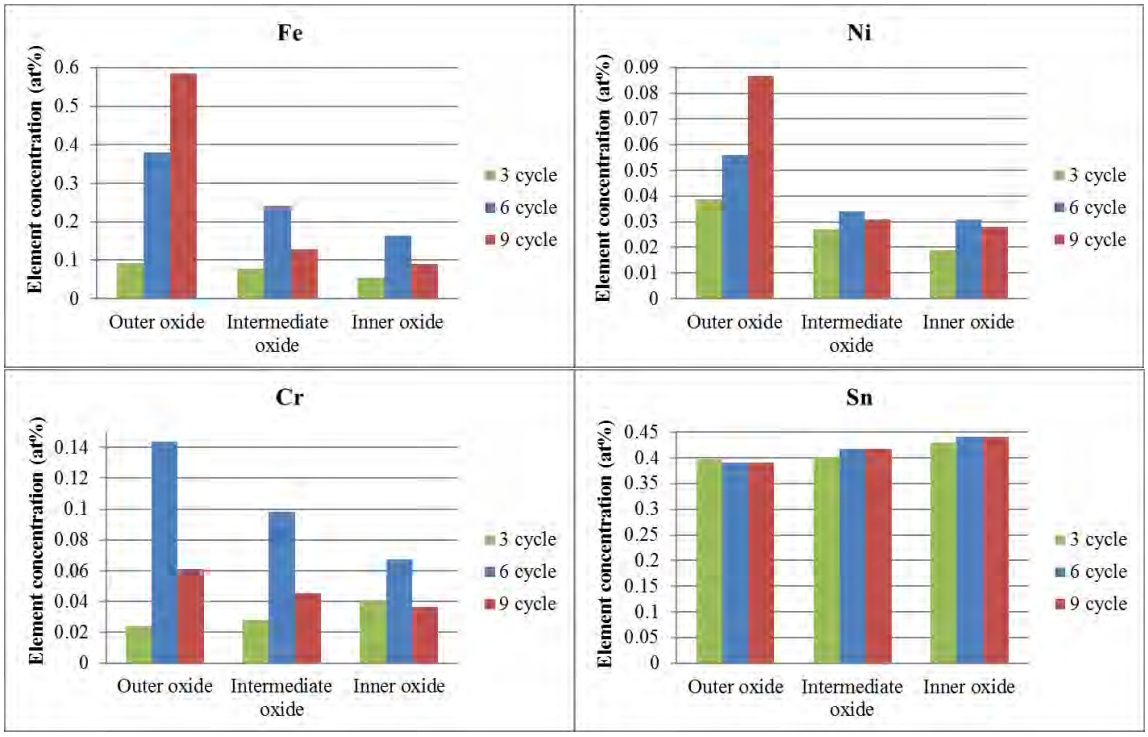

Figure-AII 8 Alloying element evolution of the cladding with time in the oxide based on the EPMA point line-scans. Note: these are not the ratios of alloying element to Zr, but direct measurements.

APPENDIX III

Complementary information regarding the PWR materials

The average element concentrations in at% is shown for the 4 cycle Zircaloy-4 and 3 cycle Zr-2.5Nb claddings in Figure-AIII 1and in Figure-AIII 2.

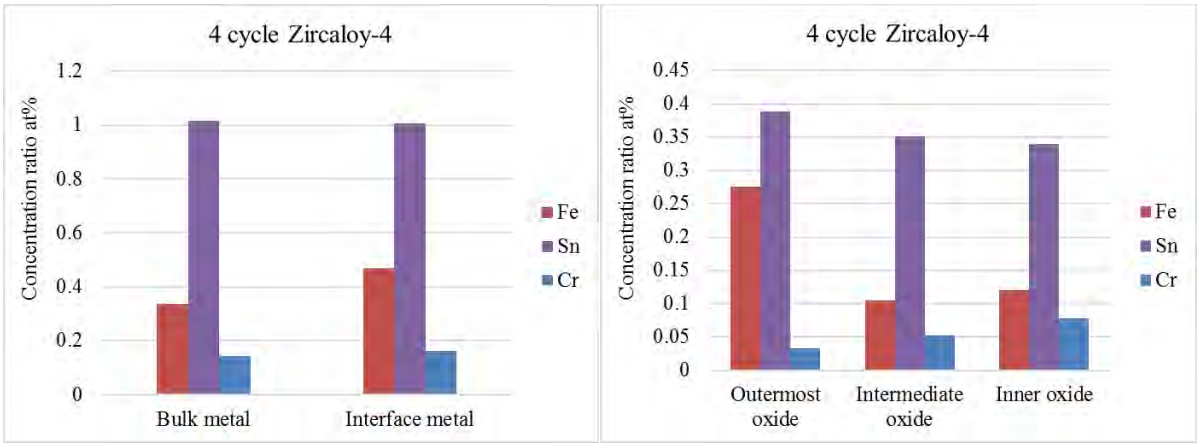

Figure-AIII 1 Average element concentrations in the different regions of the metal and the oxide of the 4 cycle Zircaloy-4 sample.

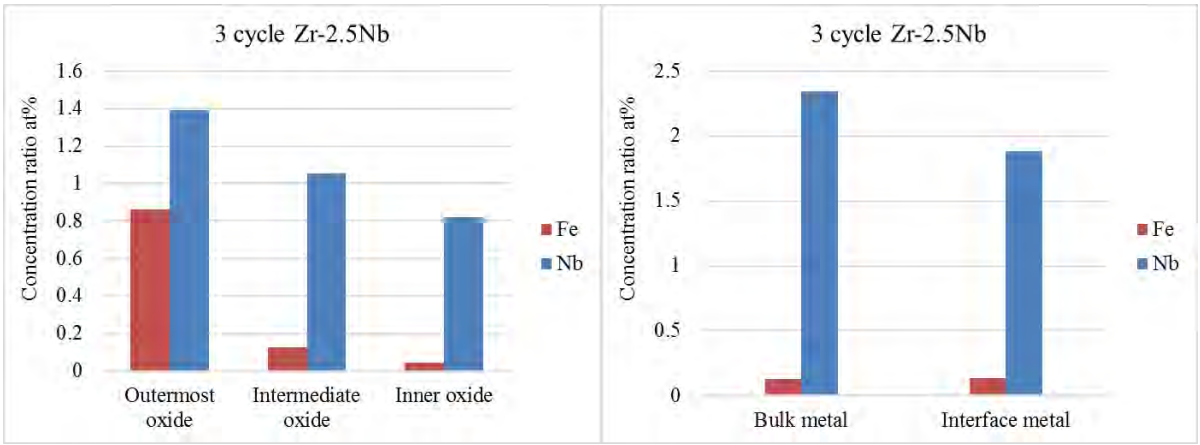

Figure-AIII 2 Average element concentrations in the different regions of the metal and the oxide of the 3 cycle Zr-2.5Nb sample.

The HAADF image and ChemiSTEM maps of the 3 cycle Zr-2.5Nb sample are provided in Figure-AIII 3. The semi-quantitative data (based on QMap point analysis) on the different phases of the sample is given in Table-AIII 1.

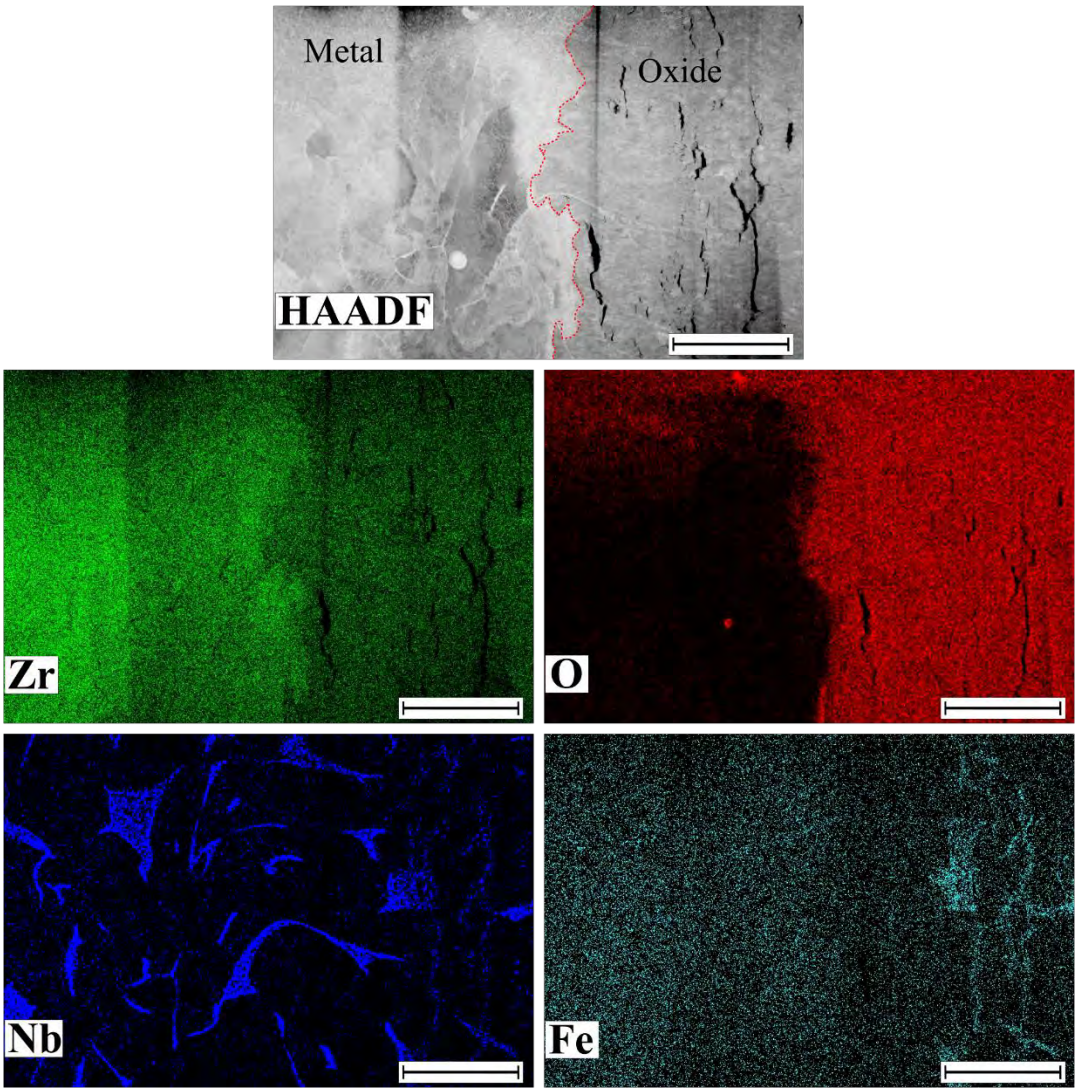

Figure-AIII 3 ChemiSTEM micrograph on the metal-oxide interface of the 3 cycle Zr-2.5Nb TEM lamella. The red dotted line on the HAADF image marks the interface. The scale bar is 2 µm.

Table-AIII 1 The maximum measured Nb concentration and measure oxide matrix away from the interface. The average of 4-4 points is shown, they were collected from the Metal-oxide interface as well as away from the interface region. Standard deviation is shown in brackets.

Phase	O (at%)	Zr (at%)	Fe (at%)	Nb (at%)
One data point away from the metal-oxide interface				
Oxide matrix	57.66	42.25	0.09	0.01
Nb rich phase in oxide	29.68	41.18	0.35	28.78
Average of 4-4 data points				
Oxide matrix	57.16 (1.2)	42.71 (1.2)	0.09 (0.0)	0.04 (0.05)
Nb rich phase in oxide	47.13 (12.7)	36.41 (3.3)	0.29 (0.14)	16.17 (10.3)

The precision of the EPMA measurements of the Zr-2.5Nb sample is given in Table-AIII 2.

Table-AIII 2 Precision of the quantitative EPMA analyses in the metal and in the oxide of the Zr-2.5Nb sample. The data was calculated for one long EPMA point line-scan.

	Concentration range (wt%)	95% confidence limit (wt%)	Standard deviation	Detection limit (wt%)
Metal				
O	0.98-1.48	0.149	0.092	0.108
Zr	88.12-94.2	0.639	1.481	0.036
Fe	0.06-0.12	0.023	0.013	0.015
Nb	1.5-7.1	0.208	1.356	0.078
Oxide				
O	22.48-24.23	0.280	0.572	0.071
Zr	64.56-71.14	0.538	2.219	0.034
Fe	0.074-0.93	0.026	0.302	0.014
Nb	1.71-5.67	0.206	1.353	0.068

REFERENCES

[1] D. O. Northwood, "The development and applications of zirconium alloys," *Materials and Design,* vol. 6, no. 2, pp. 58-70, 1985.

[2] H. Weidinger, "Zr-alloys, the nuclear material for water reactor fuel. A survey and update with focus on fuel for pressurized water reactor systems," in *7th International Conference on WWER Fuel Performance, Modelling and Experimental Support*, Albena, Bulgaria, 2007.

[3] D. R. Olander and A. T. Motta, "A new book: Light-water reactor materials," in *Nuclear Engineering and Technology 37*, 2005.

[4] K. L. Murty and I. Charit, An Introduction to Nuclear Materials: Fundamentals and Applications, John Wiley and Sons, 2013.

[5] "CLP Holdings Limited," 2013. [Online]. Available: https://www.clpgroup.com/NuclearEnergy/Eng/power/power4_1_2.aspx. [Accessed 28 July 2019].

[6] C. R. F. Azevedo, "Selection of fuel cladding material for nuclear fission reactors," *Engineering Failure Analysis,* vol. 18, no. 8, pp. 1943-1962, 2011.

[7] P. Aaltonen and H. Hanninen, "Water chemistry and behavior of materials in PWRs and BWRs," IAEA-TECDOC-965, 1997.

[8] D. Lister and S. Uchida, "Determining water chemistry conditions in nuclear reactor coolants," *Journal of Nuclear Science and Technology,* vol. 52, no. 4, pp. 451-466, 2015.

[9] F. A. Sarott, “Water chemistry in boiling water reactors - A Leibstadt-specific overview,” *CHIMIA International Journal for Chemistry,* vol. 59, no. 12, pp. 923-928, 2005.

[10] M. Lips, “Water Chemistry in Pressurized Water Reactors - A Gösgen-Specific Overview,” *CHIMIA International Journal for Chemistry,* vol. 59, no. 12, pp. 929-937, 2005.

[11] T. Series, Safety Aspects of Water Chemistry in Light Water Reactors, vol. 489, Vienna: INTERNATIONAL ATOMIC ENERGY AGENCY, 1988.

[12] B. Cox, V. G. Kritsky, C. Lemaignan, V. Polley, I. G. Ritchie, H. Ruhmann, V. N. Shishov, Y. K. Bibilashvili and A. V. Nikulina, Waterside corrosion of zirconium alloys in nuclear power plants, Vienna: IAEA-TECDOC-996, 1998.

[13] S. Abolhassani, S. Bart, J. Bertsch, M. Grosse, L. Hallstadius, A. Hermann, G. Kuri, G. Ledergerber, C. Lemaignan, M. Martin, S. Portier, C. Proff, R. Restani, S. Valance, S. Valizadeh and H. Wiese, “Corrosion and Hydrogen Uptake in Zirconium Claddings Irradiated in Light Water Reactors,” *Zirconium in the Nuclear Industry: 17th Volume,* pp. 540-573, 2015.

[14] S. Valizadeh, G. Ledergerber, S. Abolhassani, D. Jädernäs, M. Dahlbäck, E. V. Mader, G. Zhou, J. Wright and L. Hallstadius, “Effects of secondary phase particle dissolution on the in-reactor performance of BWR cladding,” *Zirconium in the Nuclear Industry: 16th International Symposium,* pp. 729-753, 2012.

[15] M. Blat, L. Legras, D. Noel and H. Amanrich, “Contribution to a better understanding of the detrimental role of hydrogen on the corrosion rate of Zircaloy-4 cladding

materials," *Zirconium in the Nuclear Industry: Twelfth International Symposium. ASTM International,* pp. 563-591, 2000.

[16] B. Cox, "Some thoughts on the mechanisms of in-reactor corrosion of zirconium alloys," *Journal of Nuclear Materials,* vol. 336, no. 2, pp. 331-368, 2005.

[17] F. Garzarolli and P. Rudling, "Mechanistic reasons for the differences in oxidation and hydriding behaviour between out-reactor and in-reactor," ASTM International, 2017.

[18] J. Koutsky and J. Kocik, "7. Radiation damage to zirconium and its alloys," in *Radiation damage of structural materials*, 1994.

[19] T. Isobe, T. Murai and Y. Mae, "Anodic protection provided by precipitates in aqueous corrosion of Zircaloy," *Zirconium in the Nuclear Industry: Eleventh International Symposium,* vol. 1295, pp. 203-217, 1996.

[20] K. Hauffe and J. Hinrichs, Oxidation of metals and alloys, New York: Plenum Press, 1965.

[21] H. E. Evans, "Stress effects in high temperature oxidation of metals," *International materials reviews,* vol. 40, no. 1, pp. 1-40, 1995.

[22] N. Ramasubramanian, P. Billot and S. Yagnik, "Hydrogen evolution and pickup during the corrosion of zirconium alloys: a critical evaluation of the solid state and porous oxide electrochemistry," *Zirconium in the Nuclear Industry: Thirteenth International Symposium,* pp. 222-244, 2002.

[23] J. S. Bradbrook, G. W. Lorimer and N. Ridley, "The precipitation of zirconium hydride in zirconium and Zircaloy-2," *Journal of Nuclear Materials,* vol. 42, no. 2, pp. 142-160, 1972.

[24] R. M. Lobo, A. H. P. Andrade and M. Castagnet, “Hydride embrittlement in zircaloy components,” in *International Nuclear Atlantic Conference - INAC*, Belo Horizonte, MG, Brazil, 2011.

[25] R. A. Castelli, “Nuclear Corrosion Modelling,” *The Nature of CRUD,* p. 978, 2009.

[26] D. E. Janney and D. L. Porter, “Characterization of phases in ‘crud’from boiling-water reactors by transmission electron microscopy,” *Journal of nuclear materials,* vol. 362, no. 1, pp. 104-115, 2007.

[27] T. R. Allen, R. J. M. Konings and A. T. Motta, “Corrosion of zirconium alloys,” *Comprehensive nuclear materials,* vol. 5, pp. 49-68, 2012.

[28] J. W. Yeon, Y. Jung and S. I. Pyun, “Deposition behaviour of corrosion products on the Zircaloy heat transfer surface,” *Journal of nuclear materials,* vol. 354, no. 1-3, pp. 163-170, 2006.

[29] S. Abolhassani, D. Gavillet, F. Groeschel, P. Jourdain and H. U. Zwicky, “Recent observation on the evolution of the secondary phase particles in Zircaloy-2 under irradiation in a BWR up to a high burn-up,” in *International Topical Meeting; LWR Fuel Performance meeting*, Park City, USA, pp. 470-484, 2000.

[30] E. Steinberg, H. G. Weidinger and A. Schaa, “Analytical approaches and experimental verification to describe the influence of cold work and heat treatment on the mechanical properties of zircaloy cladding tubes,” *Zirconium in the Nuclear Industry,* pp. 106-121, 1984.

[31] J. P. Gros and J. F. Wadier, “Precipitate growth kinetics in Zircaloy-4,” *Journal of Nuclear Materials,* vol. 172, no. 1, pp. 85-96, 1990.

[32] T. Andersson, T. Thorvaldsson, A. Wilson and A. M. Wardle, “Influence of Thermal Processing and Microstructure on the Corrosion Behaviour of Zicaloy-4 Tubing,” in *IAEA Int. Symp. on Improvements in Water Reactor Fuel Technology and Utilization*, Stockholm, 1987.

[33] G. Ledergerber, S. Valizadeh, J. Wright, M. Limbäck, L. Hallstadius, D. Gavillet, S. Abolhassani, F. Nagase, T. Sugiyama, W. Wiesenack and T. Tverberg, “Fuel performance beyond design - Exploring the limits,” *in LWR Fuel Performance Meeting/Top Fuel/WRFPM 2010,* pp. 513-524, 2010.

[34] J. H. Schemel, “Zirconium Alloy Fuel Clad Tubing,” *Publication of Sandvik Special Metals,* vol. 46, pp. 225-231, 1989.

[35] Z. Duan, H. Yang, Y. Satoh, K. Murakami, S. Kano, Z. Zhao, J. Shen and H. Abe, “Current status of materials development of nuclear fuel cladding tubes for light water reactors,” *Nuclear Engineering and Design,* vol. 316, pp. 131-150, 2017.

[36] J. H. Schemel, ASTM Manual on Zirconium and Hafnium (Vol. 639), ASTM International, 1977.

[37] T. Alam, M. K. Khan, M. Pathak, K. Ravi, R. Singh and S. K. Gupta, “A review on the clad failure studies,” *Nuclear Engineering and Design,* vol. 241, no. 9, pp. 3658-3677, 2011.

[38] C. Lemaignan, “Zirconium alloys: properties and characteristics,” in *Comprehensive Nuclear Materials*, vol. 2, Elsevier, 2012, pp. 217-232.

[39] R. M. Krishnan and M. K. Asundi, “Zirconium alloys in nuclear technology,” *Proceedings of the Indian Academy of Sciences Section C: Engineering Sciences,* vol. 4, no. 1, pp. 41-56, 1981.

[40] D. Charquet, R. Hahn, E. Ortlieb, J. P. Gros and J. F. Wadier, "Solubility limits and formation of intermetallic precipitates in ZrSnFeCr alloys," *Zirconium in the Nuclear Industry: Eighth International Symposium,* pp. 405-422, 1989.

[41] Y. I. Jung, Y. N. Seol, B. K. Choi, J. Y. Park and Y. H. Jeong, "Effect of Cr on the creep properties of zirconium alloys," *Journal of Nuclear Materials,* vol. 396, no. 2-3, pp. 303-306, 2010.

[42] Z. G. Zhang, Z. H. Feng, X. J. Jiang, X. Y. Zhang, M. Z. Ma and R. P. Liu, "Microstructure and tensile properties of novel Zr--Cr binary alloys processed by hot rolling," *Materials Science and Engineering: A,* vol. 652, pp. 77-83, 2016.

[43] M. I. Bethune and C. D. Williams, "The α (α+ β) boundary in the zr-nb system," *Journal of Nuclear Materials,* vol. 29, no. 1, pp. 129-132, 1969.

[44] N. S. McIntyre, R. D. Davidson, C. G. Weisener, G. M. Good, G. R. Mount, B. D. Warr and M. Elmoselhi, "Migration of hydrogen through thin films of ZrO2 on Zr--Nb alloy," *Journal of Vacuum Science & Technology A: Vacuum, Surfaces, and Films,* vol. 9, no. 3, pp. 1402-1405, 1991.

[45] T. B. Massalski, "Binary alloy phase diagrams ASM International," *Materials Park, OH,* pp. 1442-1446, 1990.

[46] J. P. Abriata, J. C. Bolcich and D. Arias, "The Sn- Zn (Tin-Zirconium) System," *Journal of Phase Equilibria,* vol. 4, no. 2, pp. 147-154, 1983.

[47] D. Arias and J. P. Abriata, "The Fe- Zr (Iron-Zirconium) system," *Bulletin of Alloy Phase Diagrams,* vol. 9, no. 5, pp. 597-604, 1988.

[48] D. Arias and J. P. Abriata, "The Cr- Zr (Chromium-Zirconium) system," *Journal of Phase Equilibria,* vol. 7, no. 3, pp. 237-244, 1986.

[49] P. Nash and C. S. Jayanth, “The Ni- Zr (nickel-zirconium) system,” *Journal of Phase Equilibria,* vol. 5, no. 2, pp. 144-148, 1984.

[50] J. P. Abriata and J. C. Bolcich, “The Nb- Zr (Niobium- Zirconium) system,” *Journal of Phase Equilibria,* vol. 3, no. 1, pp. 34-44, 1982.

[51] P. Kofstad, “Defects and transport properties of metal oxides,” *Oxidation of Metals,* vol. 44, no. 1-2, pp. 3-27, 1995.

[52] K. R. Lawless, “The oxidation of metals,” *Reports on Progress in Physics,* vol. 37, no. 2, p. 231, 1974.

[53] A. Couet, “Hydrogen pickup mechanism of Zirconium alloys - PhD Dissertation,” Pennsylvania State University, Graduate School Department of Nuclear Engineering, 2014.

[54] C. Anghel, “Modified oxygen and hydrogen transport in Zr-based oxides,” Doctoral dissertation, KTH Royal Institute of Technology, Stockholm, Sweden, 2006.

[55] T. Arima, K. Moriyama, N. Gaja, H. Furuya, K. Idemitsu and Y. Inagaki, “Oxidation kinetics of Zircaloy-2 between 450 C and 600 C in oxidizing atmosphere,” *Journal of Nuclear Materials,* vol. 257, no. 1, pp. 67-77, 1998.

[56] R. Stevens, Zirconia and zirconia ceramics, Manchester, UK: Twickenham : Magnesium Elektron, 1986.

[57] J. Godlewski, P. Bouvier, G. Lucazeau and L. Fayette, “Stress distribution measured by Raman spectroscopy in zirconia films formed by oxidation of Zr-based alloys,” *Zirconium in the Nuclear Industry: Twelfth International Symposium,* pp. 877-900, 2000.

[58] R. C. Garvie and M. F. Goss, “Intrinsic size dependence of the phase transformation temperature in zirconia microcrystals,” *Journal of Materials Science,* vol. 21, no. 4, pp. 1253-1257, 1986.

[59] A. T. Motta, A. Couet and R. J. Comstock, “Corrosion of zirconium alloys used for nuclear fuel cladding,” *Annual Review of Materials Research,* vol. 45, pp. 311-343, 2015.

[60] A. Couet, A. Motta and R. Comstock, “Effect of alloying elements on hydrogen pickup in zirconium alloys,” in *Zirconium in the Nuclear Industry: 17th Volume*, 2015.

[61] A. T. Fromhold, Theory of Metal Oxidation. Vol. I. Fundamentals, Amsterdam, New York and Oxford: North Holland Publishing Co., 1976.

[62] P. Kofstad, High temperature corrosion, Crown House, Linton Road, Barking, Essex IG 11 8 JU, UK: Elsevier Applied Science Publishers, 1988.

[63] C. Wagner, “Diffusion and high temperature oxidation of metals,” *Atom movements,* pp. 153-173, 1951.

[64] G. A. Eloff, C. J. Greyling and P. E. Viljoen, “The role of space charge in the oxidation of Zircaloy-4 between 350 and 450deg C in air,” *Journal of nuclear materials,* vol. 199, no. 3, pp. 285-288, 1993.

[65] A. Yilmazbayhan, A. T. Motta, R. J. Comstock, G. P. Sabol, B. Lai and Z. Cai, “Structure of zirconium alloy oxides formed in pure water studied with synchrotron radiation and optical microscopy: relation to corrosion rate,” *Journal of Nuclear Materials,* vol. 324, no. 1, pp. 6-22, 2004.

[66] G. P. Sabol and S. B. Dalgaard, “The origin of the cubic rate law in zirconium alloy oxidation,” *Journal of the Electrochemical Society,* vol. 122, no. 2, pp. 316-317, 1975.

[67] H. A. Porte, J. G. Schnizlein, R. C. Vogel and D. F. Fischer, "Oxidation of zirconium and zirconium alloys," *Journal of the Electrochemical Society,* vol. 107, no. 6, pp. 506-515, 1960.

[68] A. Motta, M. G. da Silva, A. Yilmazbayhan, R. Comstock, R. Cai and B. Lai, "Microstructural characterization of oxides formed on model Zr alloys using synchrotron radiation," *Zirconium in the Nuclear Industry: 15th International Symposium,* pp. 486-506, 2009.

[69] C. C. Dollins and M. Jursich, "A model for the oxidation of zirconium-based alloys," *Journal of Nuclear Materials,* vol. 113, no. 1, pp. 19-24, 1983.

[70] M. Tupin, M. Pijolat, F. Valdivieso, M. Soustelle, A. Frichet and P. Barberis, "Differences in reactivity of oxide growth during the oxidation of Zircaloy-4 in water vapour before and after the kinetic transition," *Journal of Nuclear Materials,* vol. 317, no. 2-3, pp. 130-144, 2003.

[71] P. Bossis, G. Lelievre, P. Barberis, X. Iltis and F. Lefebvre, "Multi-scale characterization of the metal-oxide interface of zirconium alloys," *Zirconium in the Nuclear Industry: Twelfth International Symposium,* pp. 918-945, 2000.

[72] M. Tupin, C. Bataillon, J. P. Gozlan and P. Bossis, "High temperature corrosion of Zircaloy-4 followed by in-situ impedance spectroscopy and chronoamperometry. Effect of an anodic polarisation," in *Electrochemistry in light water reactors: Reference electrodes, measurement, corrosion and tribocorrosion issues*, vol. 49, Elsevier, 2007, pp. 134-163.

[73] T. Pauporte and J. Finne, “Impedance spectroscopy study of anodic growth of thick zirconium oxide films in H2SO4, Na2SO4 and NaOH solutions,” *Journal of applied electrochemistry,* vol. 36, no. 1, pp. 33-41, 2006.

[74] A. T. Fromhold, Theory of Metal Oxidation: Space charge, North-Holland, 1980.

[75] A. T. Motta, “Waterside corrosion in zirconium alloys,” *JOM,* vol. 63, no. 8, pp. 59-63, 2011.

[76] P. Bossis, F. Lefebvre, P. Barberis and A. Galerie, “Corrosion of zirconium alloys: Link between the metal/oxide interface roughness, the degradation of the protective oxide layer and the corrosion kinetics,” *Materials science forum,* vol. 369, pp. 255-262, 2001.

[77] N. Ni, S. Lozano-Perez, M. L. Jenkins, C. English, G. D. W. Smith, J. M. Sykes and C. R. M. Grovenor, “Porosity in oxides on zirconium fuel cladding alloys, and its importance in controlling oxidation rates,” *Scripta Materialia,* vol. 62, no. 8, pp. 564-567, 2010.

[78] C. Gibert, “Irradiation and lithium presence influence on the crystallographic nature of zirconia in the framework of PWR zircaloy 4 fuel cladding corrosion study,” CEA/Saclay, 1999.

[79] H. Göhr, J. Schaller, H. Ruhmann and F. Garzarolli, “Long-term in situ corrosion investigation of Zr alloys in simulated PWR environment by electrochemical measurements,” in *Zirconium in the Nuclear Industry: Eleventh International Symposium*, 1996.

[80] E. Polatidis, P. Frankel, J. Wei, M. Klaus, R. J. Comstock, A. Ambard, S. Lyon, R. A. Cottis and M. Preuss, “Residual stresses and tetragonal phase fraction characterisation

of corrosion tested Zircaloy-4 using energy dispersive synchrotron X-ray diffraction," *Journal of Nuclear Materials,* vol. 432, no. 1-3, pp. 102-112, 2013.

[81] B. Cox and Y. M. Wong, "A hydrogen uptake micro-mechanism for Zr alloys," *Journal of Nuclear Materials,* vol. 270, no. 1-2, pp. 134-146, 1999.

[82] N. Ramasubramanian, V. Perovic and M. Leger, "Hydrogen Transport in the Oxide and Hydrogen Pickup by the Metal During Out-and In-Reactor Corrosion of Zr-2.5 Nb Pressure Tube Material," *Zirconium in the Nuclear Industry: Twelfth International Symposium,* pp. 853-876, 2000.

[83] K. Li, T. Aarholt, J. Liu, H. Hulme, A. Garner, M. Preuss, S. Lozano-Perez and C. Grovenor, "3D-characterization of deuterium distributions in zirconium oxide scale using high-resolution SIMS," *Applied Surface Science,* vol. 464, pp. 311-320, 2019.

[84] B. de Gabory and A. T. Motta, "Structure of Zircaloy 4 oxides formed during autoclave corrosion," in *ANS LWR Fuel Performance Meeting, TopFuel*, 2013.

[85] H. Li, M. G. Glavicic and J. A. Szpunar, "A model of texture formation in ZrO2 films," *Materials Science and Engineering: A,* vol. 366, no. 1, pp. 164-174, 2004.

[86] N. Petigny, P. Barberis, C. Lemaignan, C. Valot and M. Lallemant, "In situ XRD analysis of the oxide layers formed by oxidation at 743 K on Zircaloy-4 and Zr-1NbO," *Journal of Nuclear Materials,* vol. 280, no. 3, pp. 318-330, 2000.

[87] B. D. Warr, M. B. Elmoselhi, S. B. Newcomb, N. S. McIntyre, A. M. Brennenstuhl and P. C. Lichtenberger, "Oxide characteristics and their relationship to hydrogen uptake in zirconium alloys," in *Zirconium in the Nuclear Industry: Ninth International Symposium*, West Conshohocken, PA, 1991.

[88] X. Iltis, F. Lefebvre and C. Lemaignan, “Microstructural study of oxide layers formed on Zircaloy-4 in autoclave and in reactor part II: Impact of the chemical evolution of intermetallic precipitates on their zirconia environment,” *Journal of Nuclear Materials,* vol. 224, no. 2, pp. 121-130, 1995.

[89] B. Hutchinson, B. Lehtinen, M. Limbäck and M. Dahlbäck, “A study of the structure and chemistry in Zircaloy-2 and the resulting oxide after high temperature corrosion,” in *Zirconium in the Nuclear Industry: 15th International Symposium*, West Conshohocken, PA, 2009.

[90] A. Yilmazbayhan, E. Breval, A. T. Motta and R. J. Comstock, “Transmission electron microscopy examination of oxide layers formed on Zr alloys,” *Journal of Nuclear Materials,* vol. 349, no. 3, pp. 265-281, 2006.

[91] D. Hudson, N. Ni, S. Lozano-Perez, D. Saxey, C. English, G. D. Smith, J. Sykes and C. Grovenor, “The atomic scale structure and chemistry of the Zircaloy-4 metal-oxide interface,” in *14th International Conference on Environmental Degradation of Materials in Nuclear Power Systems Water Reactors 2009*, Virginia Beach, VA, 2009.

[92] N. Ni, S. Lozano-Perez, J. Sykes and C. Grovenor, “Quantitative EELS analysis of zirconium alloy metal/oxide interfaces,” *Ultramicroscopy,* vol. 111, no. 2, pp. 123-130, 2011.

[93] Y. Dong, A. T. Motta and E. A. Marquis, “Atom probe tomography study of alloying element distributions in Zr alloys and their oxides,” *Journal of Nuclear Materials,* vol. 442, no. 1-3, pp. 270-281, 2013.

[94] B. de Gabory, A. T. Motta and K. Wang, “Transmission electron microscopy characterization of Zircaloy-4 and ZIRLO™ oxide layers,” *Journal of Nuclear Materials,* vol. 456, pp. 272-280, 2015.

[95] P. Chemelle, D. B. Knorr, J. B. Van Der Sande and R. M. Pelloux, “Morphology and composition of second phase particles in Zircaloy-2,” *Journal of Nuclear Materials,* vol. 113, no. 1, pp. 58-64, 1983.

[96] D. Pecheur, F. Lefebvre, A. T. Motta, C. Lemaignan and D. Charquet, “Oxidation of intermetallic precipitates in Zircaloy-4: Impact of irradiation,” in *Zirconium in the Nuclear Industry: Tenth International Symposium*, West Conshohocken, PA, 1994.

[97] D. Pecheur, F. Lefebvre, A. T. Motta, C. Lemaignan and J. F. Wadier, “Precipitate evolution in the Zircaloy-4 oxide layer,” *Journal of Nuclear Materials,* vol. 189, no. 3, pp. 318-332, 1992.

[98] A. Froideval, S. Abolhassani, D. Gavillet, D. Grolimund, C. Borca, J. Krbanjevic and C. Degueldre, “Microprobe analysis of neutron irradiated and autoclaved zirconium niobium claddings using synchrotron-based hard X-ray imaging and spectroscopy,” *Journal of Nuclear Materials,* vol. 385, no. 2, pp. 346-350, 2009.

[99] K. Sakamoto, K. Une and M. Aomi, “Chemical state of alloying elements in oxide layer of Zr-based alloys,” in *Light Water Reactor Fuel Performance Meeting - Top Fuel 2010*, La Grange Park, IL, 2010.

[100] K. Sakamoto, K. Une, M. Aomi and K. Hashizume, “Depth profile of chemical states of alloying elements in oxide layer of Zr-based alloys,” *Progress in Nuclear Energy,* vol. 57, pp. 101-105, 2012.

[101] C. Proff, S. Abolhassani and C. Lemaignan, “Oxidation behaviour of zirconium alloys and their precipitates - A mechanistic study,” *Journal of Nuclear Materials,* vol. 432, no. 1-3, pp. 222-238, 2013.

[102] A. Couet, A. T. Motta, B. de Gabory and Z. Cai, “Microbeam X-ray absorption near-edge spectroscopy study of the oxidation of Fe and Nb in zirconium alloy oxide layers,” *Journal of Nuclear Materials,* vol. 452, no. 1-3, pp. 614-627, 2014.

[103] C. Proff, S. Abolhassani, M. M. Dadras and C. Lemaignan, “In situ oxidation of zirconium binary alloys by environmental SEM and analysis by AFM, FIB, and TEM,” *Journal of Nuclear Materials,* vol. 404, no. 2, pp. 97-108, 2010.

[104] C. Proff, S. Abolhassani and C. Lemaignan, “Oxidation behaviour of binary zirconium alloys containing intermetallic precipitates,” *Journal of Nuclear Materials,* vol. 416, no. 1-2, pp. 125-134, 2011.

[105] S. Abolhassani, M. Dadras, M. Leboeuf and D. Gavillet, “In situ study of the oxidation of Zircaloy-4 by ESEM,” *Journal of nuclear materials,* vol. 321, no. 1, pp. 70-77, 2003.

[106] G. Sundell, M. Thuvander and H.-O. Andrén, “Enrichment of Fe and Ni at metal and oxide grain boundaries in corroded Zircaloy-2,” *Corrosion Science,* vol. 65, pp. 10-12, 2012.

[107] A. Couet, A. T. Motta and R. J. Comstock, “Hydrogen pickup measurements in zirconium alloys: Relation to oxidation kinetics,” *Journal of Nuclear Materials,* vol. 451, no. 1, pp. 1-13, 2014.

[108] E. Hillner, “Hydrogen absorption in Zircaloy during aqueous corrosion, effect of environment,” Westinghouse Electric Corp. Bettis Atomic Power Lab., Pittsburgh, 1964.

[109] F. Garzarolli, B. Cox and P. Rudling, “Optimization for Zry-2 for High Burnups,” *Zirconium in the Nuclear Industry: 16th International Symposium. ASTM International,* pp. 711-728, 2012.

[110] K. Takahashi, T. Iwasaki and M. Inagaki, “Effects of additive elements and precipitate behavior in oxide films on hydrogen pick-up of zirconium alloys,” in *LWR fuel performance meeting*, 2014.

[111] K. Une and S. Ishimoto, “Terminal solid solubility of hydrogen in unalloyed zirconium by differential scanning calorimetry,” *Journal of Nuclear Science and Technology,* vol. 41, no. 9, pp. 949-952, 2004.

[112] K. Une and S. Ishimoto, “Dissolution and precipitation behavior of hydrides in Zircaloy-2 and high Fe Zircaloy,” *Journal of nuclear materials,* vol. 322, no. 1, pp. 66-72, 2003.

[113] O. Courty, A. T. Motta and J. D. Hales, “Modeling and simulation of hydrogen behavior in Zircaloy-4 fuel cladding,” *Journal of Nuclear Materials,* vol. 452, no. 1-3, pp. 311-320, 2014.

[114] K. Colas, A. T. Motta, M. Daymond and J. Almer, “Mechanisms of hydride reorientation in zircaloy-4 studied in situ,” in *Zirconium in the Nuclear Industry: 17th Volume*, ASTM International, 2015, pp. 1-31.

[115] E. Zuzek, J. P. Abriata, A. San-Martin and F. D. Manchester, “The H-Zr (hydrogen-zirconium) system,” *Bulletin of alloy phase diagrams,* vol. 11, no. 4, pp. 385-395, 1990.

[116] A. Steuwer, J. R. Santisteban, M. Preuss, M. J. Peel, T. Buslaps and M. Harada, “Evidence of stress-induced hydrogen ordering in zirconium hydrides,” *Acta Materialia,* vol. 57, no. 1, pp. 145-152, 2009.

[117] L. Lanzani and M. Ruch, “Comments on the stability of zirconium hydride phases in Zircaloy,” *Journal of Nuclear Materials,* vol. 324, no. 2-3, pp. 165-176, 2004.

[118] E. Tulk, M. Kerr and M. R. Daymond, “Study on the effects of matrix yield strength on hydride phase stability in Zircaloy-2 and Zr 2.5 wt\% Nb,” *Study on the effects of matrix yield strength on hydride phase stability in Zircaloy-2 and Zr 2.5 wt\% Nb,* vol. 425, no. 1-3, pp. 93-104, 2012.

[119] J. H. Root, W. M. Small, D. Khatamian and O. T. Woo, “Kinetics of the δ to γ zirconium hydride transformation in Zr-2.5 Nb,” *Acta Materialia,* vol. 51, no. 7, pp. 2041-2053, 2003.

[120] A. I. Kolesnikov, A. M. Balagurov, I. O. Bashkin, A. V. Belushkin, E. G. Ponyatovsky and M. Prager, “Neutron scattering studies of ordered gamma-ZrD,” *Journal of Physics: Condensed Matter,* vol. 6, no. 43, p. 8977, 1994.

[121] A. C. Switendick, “Electronic structure of gamma phase zirconium hydride,” *Journal of the Less Common Metals,* vol. 103, no. 2, pp. 309-315, 1984.

[122] M. P. Cassidy and C. M. Wayman, “The crystallography of hydride formation in zirconium: II. The delta→ epsilon transformation,” *Metallurgical and Materials Transactions A,* vol. 11, no. 1, p. 57, 1980.

[123] K. G. Barraclough and C. J. Beevers, “Some observations on the phase transformations in zirconium hydrides,” *Journal of Nuclear Materials,* vol. 34, no. 2, pp. 125-134, 1970.

[124] M. B. Elmoselhi, K. Tashiro and A. C. Wallace, “Hydrogen Ingress Into Zirconium Alloys as a Life-Limiting Factor—Methods of In-Line Monitoring, Prediction and Control,” in *2012 20th International Conference on Nuclear Engineering and the ASME 2012 Power Conference*, 2012.

[125] A. T. Motta and L. Q. Chen, “Hydride formation in zirconium alloys,” *JOM,* vol. 64, no. 12, pp. 1403-1408, 2012.

[126] G. Sundell, M. Thuvander, P. Tejland, M. Dahlbäck, L. Hallstadius and H. O. Andrén, “Redistribution of alloying elements in Zircaloy-2 after in-reactor exposure,” *Journal of Nuclear Materials,* vol. 454, no. 1, pp. 178-185, 2014.

[127] A. Couet, A. T. Motta and A. Ambard, “The coupled current charge compensation model for zirconium alloy fuel cladding oxidation: I. Parabolic oxidation of zirconium alloys,” *Corrosion Science,* vol. 100, pp. 73-84, 2015.

[128] A. Garner, P. Frankel, J. Partezana and M. Preuss, “The effect of substrate texture and oxidation temperature on oxide texture development in zirconium alloys,” *Journal of Nuclear Materials,* vol. 484, pp. 347-356, 2017.

[129] B. D. C. Bell, S. T. Murphy, R. W. Grimes and M. R. Wenman, “The effect of Nb on the corrosion and hydrogen pick-up of Zr alloys,” *Acta Materialia,* vol. 132, pp. 425-431, 2017.

[130] Q. Auzoux, P. Bouffioux, A. Machiels, S. Yagnik, B. Bourdiliau, C. Mallet, N. Mozzani and K. Colas, “Hydride reorientation and its impact on ambient temperature mechanical properties of high burn-up irradiated and unirradiated recrystallized Zircaloy-2 nuclear fuel cladding with an inner liner,” *Journal of Nuclear Materials,* vol. 494, pp. 114-126, 2017.

[131] G. Kuri, H. Ramanantoanina, J. Bertsch, M. Martin and I. Panas, “Chemical state and atomic scale environment of nickel in the corrosion layer of irradiated Zircaloy-2 at a burn-up around 45 MWd/kg,” *Corrosion Science,* vol. 143, pp. 200-211, 2018.

[132] M. Christensen, W. Wolf, C. M. Freeman, E. Wimmer, R. B. Adamson, L. Hallstadius, P. E. Cantonwine and E. V. Mader, "Effect of alloying elements on the properties of Zr and the Zr-H system," *Journal of Nuclear Materials,* vol. 445, no. 1-3, pp. 241-250, 2014.

[133] J. L. Béchade, R. Brenner, P. Goudeau and M. Gailhanou, "Influence of temperature on X-ray diffraction analysis of ZrO2 oxide layers formed on zirconium based alloys using a synchrotron radiation," *Materials Science Forum,* vol. 404, pp. 803-808, 2002.

[134] N. Ni, S. Lozano-Perez, J. Sykes and C. Grovenor, "Multi-scale characterisation of oxide on zirconium alloys," *Materials at High Temperatures,* vol. 29, no. 3, pp. 166-170, 2012.

[135] M. Preuss, P. Frankel, S. Lozano-Perez, D. Hudson, E. Polatidis, N. Ni, J. Wei, C. English, S. Storer, K. Chong, M. Fitzpatrick, P. Wang, J. Smith, C. Grovenor, G. Smith, J. Sykes, B. Cottis, S. Lyon, L. Hallstadius, R. Comstock, A. Ambard and M. Blat-Yrieix, "Studies regarding corrosion mechanisms in zirconium alloys," *Zirconium in the Nuclear Industry: 16th International Symposium,* pp. 649-681, 2012.

[136] C. Roy and B. Burgess, "A study of the stresses generated in zirconia films during the oxidation of zirconium alloys," *Oxidation of Metals,* vol. 2, no. 3, pp. 235-261, 1970.

[137] P. Goudeau, D. Faurie, B. Girault, P. O. Renault, E. Le Bourhis, P. Villain, F. Badawi, O. Castelnau, R. Brenner, J. L. Béchade, G. Geandier and N. Tamura, "Strains, stresses and elastic properties in polycrystalline metallic thin films: in situ deformation combined with x-ray diffraction and simulation experiments," *Materials Science Forum,* vol. 524, pp. 735-740, 2006.

[138] M. Parise, O. Sicardy and G. Cailletaud, “Modelling of the mechanical behavior of the metal--oxide system during Zr alloy oxidation,” *Journal of Nuclear Materials,* vol. 256, no. 1, pp. 35-46, 1998.

[139] H. E. Evans, D. J. Norfolk and T. Swan, “Perturbation of parabolic kinetics resulting from the accumulation of stress in protective oxide layers,” *Journal of the Electrochemical Society,* vol. 125, no. 7, pp. 1180-1185, 1978.

[140] J. Schefold, D. Lincot, A. Ambard and O. Kerrec, “The Cyclic Nature of Corrosion of Zr and Zr-Sn in High-Temperature Water (633 K) A Long-Term In Situ Impedance Spectroscopic Study,” *Journal of The Electrochemical Society,* vol. 150, no. 10, pp. B451-B461, 2003.

[141] K. Une, K. Sakamoto, M. Aomi, J. Matsunaga, Y. Etoh, I. Takagi, S. Miyamura, T. Kobayashi and K. Ito, “Hydrogen Absorption Mechanism of Zirconium Alloys Based on Characterization of Oxide Layer,” *Zirconium in the Nuclear Industry: 16th International Symposium,* vol. 8, no. 5, pp. 401-432, 2011.

[142] D. Khatamian and F. D. Manchester, “An ion beam study of hydrogen diffusion in oxides of Zr and Zr-Nb (2.5 wt%): I. Diffusion parameters for dense oxide,” *Journal of Nuclear Materials,* vol. 166, no. 3, pp. 300-306, 1989.

[143] J. H. Austin, T. S. Elleman and K. Verghese, “Tritium diffusion in Zircaloy-2 in the temperature range -78 to 204 °C,” *Journal of Nuclear Materials,* vol. 51, no. 3, pp. 321-329, 1974.

[144] M. B. Elmoselhi, B. D. Warr and S. McIntyre, “A study of the hydrogen uptake mechanism in zirconium alloys,” *Zirconium in the Nuclear Industry: Tenth International Symposium,* pp. 62-79, 1994.

[145] D. Khatamian, “Diffusion of Hydrogen in the Oxides of Annealed Zr-1Nb, Zr-2.5Nb and Zr-20Nb Alloys,” *International journal of research in physical chemistry and chemical physics,* vol. 181, no. 1-2, pp. 999-1004, 1993.

[146] K. Baur, F. Garzarolli, H. Ruhmann and H. J. Sell, “Electrochemical examinations in 350 C water with respect to the mechanism of corrosion-hydrogen pickup,” *Zirconium in the Nuclear Industry: Twelfth International Symposium,* pp. 836-852, 2000.

[147] A. Couet, A. Motta, A. Ambard and R. Comstock, “Hydrogen pickup mechanism in zirconium alloys,” *Zirconium in the Nuclear Industry: 18th International Symposium,* pp. 312-349, 2018.

[148] Y. Hatano, M. Sugisaki, K. Kitano and M. Hayashi, “Role of intermetallic precipitates in hydrogen transport through oxide films on Zircaloy,” *Zirconium in the Nuclear Industry: Twelfth International Symposium,* pp. 901-917, 2000.

[149] B. Cox, “Zirconium intermetallics and hydrogen uptake during corrosion,” Atomic Energy of Canada Ltd., 1987.

[150] G. Sundell, M. Thuvander, A. K. Yatim, H. Nordin and H. O. Andren, “Direct observation of hydrogen and deuterium in oxide grain boundaries in corroded Zirconium alloys,” *Corrosion Science,* vol. 90, pp. 1-4, 2015.

[151] K. Kakiuchi, N. Itagaki, T. Furuya, A. Miyazaki, Y. Ishii, S. Suzuki, T. Terai and M. Yamawaki, “Role of iron for hydrogen absorption mechanism in zirconium alloys,” *Zirconium in the Nuclear Industry: Fourteenth International Symposium,* pp. 349-366, 2005.

[152] K. Une, K. Sakamoto, J. Matsunaga, Y. Etoh, M. Aomi, I. Takagi, K. Sawada and H. Watanabe, "Controlling Factors in Hydrogen Absorption of Zirconium Alloys," in *Proceedings of TopFuel 2012*, Manchester, UK, 2012.

[153] Y. R. Than, M. R. Wenman, B. D. C. Bell, S. R. Ortner, H. Swan and R. W. Grimes, "Modelling and experimental analysis of the effect of solute iron in thermally grown Zircaloy-4 oxides," *Journal of Nuclear Materials,* vol. 509, pp. 114-123, 2018.

[154] K. Park and D. R. Olander, "Oxygen diffusion in single-crystal tetragonal zirconia," *Journal of the Electrochemical Society,* vol. 138, no. 4, pp. 1154-1159, 1991.

[155] F. Garzarolli, H. Stehle and E. Steinberg, "Behavior and properties of zircaloys in power reactors: A short review of pertinent aspects in LWR fuel," *Zirconium in the Nuclear Industry: Eleventh International Symposium,* pp. 12-32, January 1996.

[156] F. Garzarolli, I. Pohlmeyer, E. Steinberg and S. rapp-Pritsching, "Long time out of pile corrosion of Zircaloy-4 in 350 C water," in *IAEA Technical Committee Meeting on External Cladding Corrosion in Water Power Reactors*, Cadarache, 1985.

[157] F. Garzarolli, "Progress in understanding PWR fuel rod waterside corrosion," Kraftwerk Union Aktiengesellschaft, Erlange, West Germany, 1985.

[158] V. F. Urbanic, B. Cox and G. J. Field, "Long-term corrosion and deuterium uptake in CANDU-PHW pressure tubes," *Zirconium in the Nuclear Industry,* pp. 189-203, 1987.

[159] M. Limbäck, M. Krammen, P. Rudling, R. Pati and A. Garde, "Corrosion and hydriding performance of Zircaloy-2 and Zircaloy-4 cladding materials in PWRs," in *Proceedings of the International Topical Meeting on Light Water Reactor Fuel Performance*, 1994.

[160] G. P. Sabol, R. J. Comstock, R. A. Weiner, P. Larouere and R. N. Stanutz, “In-reactor corrosion performance of ZIRLO™ and zircaloy-4,” *Zirconium in the nuclear industry: Tenth International Symposium,* pp. 714-744, 1994.

[161] A. Seibold, F. Garzarolli and R. Manzel, “Optimized Zry-4 with enhanced Fe and Cr content and DUPLEX cladding: the answer to corrosion in PWRs,” in *TopFuel-1995*, 1995.

[162] A. Seibold, F. Garzarolli and R. Manzel, “Material development for siemens fuel elements,” in *International Topical Meeting on Light Water Reactor Fuel Performance*, American Nuclear Society, Park City, Utah, 2000.

[163] A. Seibold and F. Garzarolli, “Influence of composition and condition on in-PWR behavior of Zr-Sn-Nb-FeCrV alloys,” *Zirconium in the Nuclear Industry: Thirteenth International Symposium,* pp. 743-757, 2002.

[164] L. Sihver and L. Hallstadius, “Zero-Failure Fuel,” in *Proceeding In ENS TopFuel 99 - Topical Meeting in Nuclear Fuel*, Avignon, France, 1999.

[165] M. Limbäck, M. Dahlbäck, P. Tägtström, P. Jourdain, A. Massih, L. Sihver, T. Andersson and P. Witt, “Westinghouse optimised BWR cladding and channel materials,” in *TopFuel 2011*, Stockholm, Sweden, 2011.

[166] P. Tägtström, T. Andersson, O. Bergström, M. Dahlbäck and M. Limbäck, “The effect of secondary phase particle distribution on the in-reactor performance of BWR claddings,” in *Enlarged Halden Progr. Meeting*, Loen, Norway, 1999.

[167] P. Tägtström, M. Limbäck, M. Dahlbäck, T. Andersson and H. Pettersson, “Effects of hydrogen pickup and second-phase particle dissolution on the in-reactor corrosion performance of BWR claddings,” in *Zirconium in the Nuclear Industry: Thirteenth*

International Symposium, West Conshohocken, PA, ASTM International, 2002, pp. 96-118.

[168] P. Y. Huang, S. Mahmood and R. B. Adamson, "Effects of Thermomechanical Processing on In-Reactor Corrosion and Post Irradiation Mechanical Properties of Zircaloy-2," *Zirconium in the Nuclear Industry: Eleventh International Symposium,* pp. 726-756, 1996.

[169] S. Abolhassani, R. Restani, T. Rebac, F. Groeschel, W. Hoffelner, G. Bart, W. Goll and F. Aeschbach, "TEM Examinations of the Metal-Oxide Interface of Zirconium Based Alloys Irradiated in a Pressurized Water Reactor," *Journal of ASTM International,* vol. 2, no. 6, pp. 1-25, 2005.

[170] S. Abolhassani, G. Bart and A. Jakob, "Examination of the chemical composition of irradiated zirconium based fuel claddings at the metal/oxide interface by TEM," *Journal of Nuclear Materials,* vol. 399, no. 1, pp. 1-12, 2010.

[171] A. Garner, F. Baxter, P. Frankel, M. Topping, A. Harte, T. Slater, P. Tejland, J. Romero, E. Darby, A. Cole-Baker, M. Gass and M. Preuss, "Investigating the Effect of Zirconium Oxide Microstructure on Corrosion Performance: A Comparison between Neutron, Proton, and Nonirradiated Oxides," *Zirconium in the Nuclear Industry: 18th International Symposium,* pp. 491-523, 2018.

[172] P. Bossis, D. Pecheur, L. Hanifi, J. Thomazet and M. Blat, "Comparison of the high burn-up corrosion on M5 and low tin Zircaloy-4," *ASTM Special Technical Publication,* vol. 1467, p. 494, 2006.

[173] P. Bossis, J. Thomazet and L. Florence, "Study of the mechanisms controlling the oxide growth under irradiation: characterization of irradiated Zr-4 and Zr-1Nb-O oxide

scales," *Zirconium in the Nuclear Industry: Thirteenth International Symposium,* vol. 6, no. 4, pp. 190-221, 2002.

[174] J. S. Bryner, "The cyclic nature of corrosion of Zircaloy-4 in 633 K water," *Journal of nuclear materials,* vol. 82, no. 1, pp. 84-101, 1979.

[175] A. M. Garde, "Enhancement of aqueous corrosion of zircaloy-4 due to hydride precipitation at the metal-oxide interface," *Zirconium in the Nuclear Industry: Ninth International Symposium,* pp. 566-594, 1991.

[176] T. Kido, "A study on enhanced uniform corrosion of Zircaloy-4 cladding during high burnup operation in PWRS," in *Proceedings of the sixth international symposium on environmental degradation of materials in nuclear power systems-water reactors*, 1993.

[177] M. Blat and D. Noel, "Detrimental role of hydrogen on the corrosion rate of zirconium alloys," *Zirconium in the Nuclear Industry: Eleventh International Symposium,* pp. 563-591, 1996.

[178] Y. S. Kim, K. S. Rheem and D. K. Min, "Phenomenological study of in-reactor corrosion of Zircaloy-4 in pressurized water reactors," *Zirconium in the Nuclear Industry: Tenth International Symposium,* pp. 745-759, 1994.

[179] R. C. Asher and F. W. Trowse, "The distribution of hydrogen in zirconium alloy fuel cladding: The effects of heat flux," *Journal of Nuclear Materials,* vol. 35, no. 1, pp. 115-121, 1970.

[180] J. Godlewski, J. P. Gros, M. Lambertin, J. F. Wadier and H. Weidinger, "Raman Spectroscopy Study of the Tetragonal-to-monoclinic Transition in Zirconium Oxide Scales and Determination of Overall Oxygen Diffusion by Nuclear Microanalysis of

O18," *Zirconium in the Nuclear Industry: Ninth International Symposium,* pp. 416-, 1991.

[181] M. Dahlbäck, L. Hallstadius, M. Limbäck, G. Vesterlund, T. Andersson, P. Witt, J. Izquierdo, B. Remartinez, M. Diaz, J. L. Sacedon and A. M. Alvarez, "The Effect of Liner Component Iron Content on Cladding Corrosion, Hydriding, and PCI Resistance," *Journal of ASTM International,* vol. 2, no. 9, pp. 1-23, 2005.

[182] G. Ledergerber, W. Kaufmann, A. Ritter, D. Greiner, Y. Parmar, R. Jacot-Guillarmot and J. Krouthen, "Burnup increase and Power Uprate-Operation history of KKL," in *In Proceedings Intern. LWR Fuel Performance Meeting*, San Francisco, California, 2007.

[183] S. M. Hanlon, S. Y. Persaud, F. Long, A. Korinek and M. R. Daymond, "A solution to FIB induced artefact hydrides in Zr alloys," *Journal of Nuclear Materials,* vol. 515, pp. 122-134, 2019.

[184] L. Holzer and M. Cantoni, "Review of FIB-tomography," in *Nanofabrication Using Focused Ion and Electron Beams: Principles and Applications*, vol. 559201222, Oxford University Press, 2012, pp. 410-435.

[185] "Wavelength Dispersive X-ray Microanalysis Explained," OxfordInstruments Analytical Limited, 2002.

[186] T. Kimura, K. Nishida and S. Tanuma, "Spatial resolution of a wavelength-dispersive electron probe microanalyzer equipped with a thermal field emission gun," *Microchimica Acta,* vol. 155, no. 1-2, pp. 175-178, 2006.

[187] N. Ni, S. Lozano-Perez, J. M. Sykes, G. D. W. Smith and C. R. M. Grovenor, "Focussed ion beam sectioning for the 3D characterisation of cracking in oxide scales formed on

commercial ZIRLO™ alloys during corrosion in high temperature pressurised water," *Corrosion Science,* vol. 53, no. 12, pp. 4073-4083, 2011.

[188] P. Tejland and H. O. Andrén, "Origin and effect of lateral cracks in oxide scales formed on zirconium alloys," *Journal of Nuclear Materials,* vol. 430, no. 1, pp. 64-71, 2012.

[189] M. Chollet, S. Valance, S. Abolhassani, G. Stein, D. Grolimund, M. Martin and J. Bertsch, "Synchrotron X-ray diffraction investigations on strains in the oxide layer of an irradiated Zircaloy fuel cladding," *Journal of Nuclear Materials,* vol. 488, pp. 181-190, 2017.

[190] D. J. Cameron and R. J. Duncan, "On the existence of a memory effect in hydride precipitation in cold-worked Zr-2.5% Nb," *Journal of Nuclear Materials,* vol. 68, no. 3, pp. 340-344, 1977.

[191] B. Cox, "A mechanism for the hydrogen uptake process in zirconium alloys," *Journal of Nuclear Materials,* vol. 264, no. 3, pp. 283-294, 1999.

[192] H. Mehrer, N. Stolica and N. A. Stolwijk, Landolt–Börnstein: Diffusion in Solid Metals and Alloys, Numerical Data and Functional Relationships in Science and Technology, vol. 26, Berlin: Springer-Verlag, 1990.

[193] P. Raj, P. Suryanarayana, A. Sathyamoorthy, K. Shashikala and R. M. Iyer, "Zr2FeHx system hydrided at low temperatures: structural aspects by Mössbauer and x-ray diffraction studies," *Journal of alloys and compounds,* vol. 178, no. 1-2, pp. 393-401, 1992.

[194] F. Aubertin and S. J. Campbell, "Phase separation in hydrides of Zr2Ni," *Hyperfine Interactions,* vol. 54, no. 1, pp. 767-773, 1990.

[195] G. Sundell, M. Thuvander and H.-O. Andrén, “Tin clustering and precipitation in the oxide during autoclave corrosion of Zircaloy-2,” *Journal of Nuclear Materials,* vol. 456, pp. 409-414, 2015.

[196] K. Takeda and H. Anada, “Mechanism of corrosion rate degradation due to tin,” in *Zirconium in the Nuclear Industry: Twelfth International Symposium*, ASTM International, 2000, pp. 592-608.

[197] A. Sinhamahapatra, J. P. Jeon, J. Kang, B. Han and J. S. Yu, “Oxygen-deficient zirconia (ZrO2-x): a new material for solar light absorption,” *Scientific reports,* vol. 6, p. 27218, 2016.

[198] Y. Hatano, R. Hitaka, M. Sugisaki and M. Hayashi, “Influence of size distribution of Zr(Fe, Cr)2 precipitates on hydrogen transport through oxide film of Zircaloy-4,” *Journal of Nuclear Materials,* vol. 248, pp. 311-314, 1997.

[199] D. Shaltiel, I. Jacob and D. Davidov, “Hydrogen absorption and desorption properties of AB2 Laves-phase pseudobinary compounds,” *Journal of the Less Common Metals,* vol. 53, no. 1, pp. 117-131, 1977.

[200] R. M. Van Essen and K. H. J. Buschow, “Hydrogen absorption in various zirconium- and hafnium-based intermetallic compounds,” *Journal of the Less Common Metals,* vol. 64, no. 2, pp. 277-284, 1979.

[201] F. Pourarian and W. E. Wallace, “Hydrogen sorption characteristics of Zr1- xTix (Cr1- yFey) 2 alloys,” *Journal of the Less Common Metals,* vol. 107, no. 1, pp. 69-79, 1985.

[202] B. Cheng, P. M. Gilmore and H. H. Klepfer, “PWR Zircaloy fuel cladding corrosion performance, mechanisms, and modeling,” *Zirconium in the Nuclear Industry: Eleventh International Symposium,* pp. 137-160, 1996.

[203] X. Iltis, F. Lefebvre and C. Lemaignan, “Microstructure evolutions and iron redistribution in zircaloy oxide layers: Comparative effects of neutron irradiation flux and irradiation damages,” *Zirconium in the Nuclear Industry: Eleventh International Symposium,* pp. 242-264, 1996.

[204] C. Lemaignan, “Physical Phenomena Concerning Corrosion Under Irradiation of Zr Alloys,” *Zirconium in the Nuclear Industry: Thirteenth International Symposium,* pp. 20-29, 2002.

[205] P. Billot, J. C. Robin, A. Giordano, J. Peybernes, J. Thomazet and H. Amanrich, “Experimental and theoretical studies of parameters that influence corrosion of Zircaloy-4,” *Zirconium in the Nuclear Industry: Tenth International Symposium,* pp. 351-377, 1994.

[206] D. Pecheur, J. Godlewski, J. Peybernes, L. Fayette, M. Noe, A. Frichet and O. Kerrec, “Contribution to the Understanding of the Effect of the Water Chemistry on the Oxidation Kinetics of Zircaloy-4 Cladding,” *Zirconium in the nuclear industry: Twelfth International Symposium,* pp. 793-811, 2000.

[207] F. Garzarolli, H. Seidel, R. Tricot and J. P. Gros, “Oxide growth mechanism on zirconium alloys,” *Zirconium in the Nuclear Industry: Ninth International Symposium,* pp. 395-415, 1991.

[208] A. Baris, S. Abolhassani, Y. L. Chiu and H. E. Evans, “Observation of Crack Microstructure in Oxides and its Correlation to Oxidation and Hydrogen-uptake by 3D FIB Tomography – Case of Zr-ZrO2 in reactor,” *Materials at High Temperatures,* pp. 1-8, 2017.

[209] A. Baris, R. Restani, R. Grabherr, Y. L. Chiu, H. E. Evans, K. Ammon, M. Limbäck and S. Abolhassani, “Chemical and Microstructural Characterization of a 9 Cycle Zircaloy-2 Cladding using EPMA and FIB Tomography,” *Journal of Nuclear Materials,* vol. 504, pp. 144-160, 2018.

[210] K. Une, S. Ishimoto, Y. Etoh, K. Ito, K. Ogata, T. Baba, K. Kamimura and Y. Kobayashi, “The terminal solid solubility of hydrogen in irradiated Zircaloy-2 and microscopic modeling of hydride behavior,” *Journal of Nuclear Materials,* vol. 389, no. 1, pp. 127-136, 2009.

[211] J. Bair, M. A. Zaeem and M. Tonks, “A review on hydride precipitation in zirconium alloys,” *Journal of Nuclear Materials,* vol. 466, pp. 12-20, 2015.

[212] L. Holzer, F. Indutnyi, P. H. Gasser, B. Münch and M. Wegmann, “Three-dimensional analysis of porous BaTiO3 ceramics using FIB nanotomography,” *Journal of microscopy,* vol. 216, no. 1, pp. 84-95, 2004.

[213] A. Zielinski and S. Sobieszczyk, “Hydrogen-enhanced degradation and oxide effects in zirconium alloys for nuclear applications,” *International journal of hydrogen energy,* vol. 36, no. 14, pp. 8619-8629, 2011.

[214] J. J. Kearns, “Terminal solubility and partitioning of hydrogen in the alpha phase of zirconium, Zircaloy-2 and Zircaloy-4,” *Journal of nuclear materials,* vol. 22, no. 3, pp. 292-303, 1967.

[215] W. H. Erickson and D. Hardie, “The influence of alloying elements on the terminal solubility of hydrogen in α-zirconium,” *Journal of Nuclear Materials,* vol. 13, no. 2, pp. 254-262, 1964.

[216] G. Barbottin and A. Vapaille, New Insulators Devices and Radiation Effects, Elsevier, 1999.

[217] S. Garzarolli, H. Stehle and E. Steinberg, "Behavior and properties of Zircaloys in power reactors: a short review of pertinent aspects in LWR fuel," *Zirconium in the Nuclear Industry: Eleventh International Symposium,* pp. 12-32, 1996.